Some Recent Advances in High Temperature Photoelectron Spectroscopy

A Thesis submitted to the University of Southampton for the degree of Doctor of Philosophy.

Brian William John Gravenor

Department of Chemistry,
University of Southampton.

April, 1985.

Memorandum

This thesis is an account of original research performed by the author in the Chemistry Department, University of Southampton, between October 1981 and September 1984. Where findings of other works have been used, due reference has been given.

ACKNOWLEDGEMENTS

I wish to thank my Supervisor, Dr. J.M. Dyke for the advice and encouragement given to me throughout my time of research at Southampton. I also thank Dr. A. Morris and Professor N. Jonathan for their help in times of difficulty. Thanks also to my friends and colleagues in the Chemistry Department who helped to make my time at Southampton interesting and enjoyable. Special thanks go to the other members of the pes group: Robert Lewis, Ann Lewis, Graham Josland, Mark Hastings, Andrew Ellis, Abed Ridha, Nourredine Keddar, Colin Kirby and Julian Stevens. I also thank Ann Carroll for her excellent typing.

I am grateful to the SERC and CEGB for providing funds to enable me to carry out my research.

Lastly, I am indebted to my parents for their support, both moral and financial and their love and understanding in times of crisis.

UNIVERSITY OF SOUTHAMPTON

ABSTRACT

FACULTY OF SCIENCE

CHEMISTRY

Doctor of Philosophy

SOME RECENT ADVANCES IN HIGH TEMPERATURE PHOTOELECTRON SPECTROSCOPY

by Brian William John Gravenor

This thesis deals with the study of a number of atoms and small molecules by high temperature photoelectron spectroscopy. The experimental techniques used to study these species in the vapour phase are described in detail in Chapter Two while the theoretical methods used to assign the spectra are outlined in Chapter Three.

The work described shows that the experimental p.e. spectra of transition metals can be a valuable precursor to the study of transition metal oxides in the gas-phase. The HeI p.e. spectra of iron, cobalt and nickel are described in Chapter Six. These studies mean that all the first-row transition metals have now been studied with u.v.p.e.s. in the vapour phase and comparison of the HeI $\sigma_{4s}:\sigma_{3d}$ photoionisation cross-section ratios is given in Chapter Six. The experimental spectra for iron, cobalt and nickel as well as results previously obtained for other first-row transition metals are used to monitor the vapour above a transition metal alloy as a function of temperature. The results of this study are given in Chapter Five.

The HeI photoelectron spectra of CrO and VO are presented in Chapter Six and these are assigned with the aid of ab initio ΔSCF configuration interaction calculations (Chapter Four).

Ab initio ΔSCF CI calculations are also used in the assignment of the photoelectron spectrum of AlF. This work is described in Chapter Seven where it is shown that an ionic rather than a covalent model is qualitatively more appropriate to interpret the spectra obtained.

CONTENTS

CHAPTER PAGE

CHAPTER ONE

Introduction

Photoelectron spectroscopy (PES) is a relatively new branch of science. The technique was first performed with X-rays ($h\nu \sim 1000eV$) and used to study surfaces and later ultra-violet photoelectron spectroscopy (uvpes, $h\nu \sim 20eV$) was developed. This thesis is concerned with the latter technique. In uvpes the radiation source is much less energetic than an X-ray photon source and is generally in the region 10-50eV. This radiation is sufficiently energetic to ionise the valence electrons in atoms or molecules. The photon source most widely used in uvpes is the HeI source with an energy of 21.22eV. A more energetic source, the HeII source with an energy of 40.81eV, is sometimes useful when information is required on deeper-lying electrons.

Ultra-violet pes has developed into two separate but overlapping areas as far as the Southampton PES group is concerned. The study of transient molecules and radicals in the gas-phase was begun around ten years ago (1,2). A few years later, a radio frequency induction heater was introduced to allow vapour phase study of species generated at higher temperatures and this has grown into the High Temperature PES area with which this thesis is concerned.

The main aim of high temperature photoelectron spectroscopy is to study, in the vapour phase, the electronic structure of atoms and molecules which have negligible vapour pressures at room temperature. This means that the number of compounds available to pes investigation can be extended to include a range of inorganic compounds where an ionic bonding picture may be more appropriate than the covalent approach used for most organic systems. Relativistic effects will also be important in molecules containing elements of high atomic number. Experimental information such as photoelectron band positions, photoionisation cross-sections, and angular distributions and structure within a photoelectron band are important in probing the electronic structure of the positive ion produced on ionisation. Approximately seven years ago, Berkowitz (3) wrote a review which summarised the state of the art in high temperature pes, some 2-3 years after this method was first introduced, and this review serves as a useful summary of the interests in this area at that time. The molecules available for study were determined by the upper temperature limit of the technique which was then 1000^{o}K. This limit was

subsequently increased to 2800°K by the Southampton pes group.

In order to record photoelectron spectra of species generated at high temperature (up to 2800K), particular experimental methods are required. The methods used during the course of the work described in this thesis are described in Chapter 2.

The work to be described in the following chapters is concerned mainly with the study of metals and metal oxides with uvpes. Direct evaporation has been used to produce the metal oxides VO, BaO and SrO in the vapour phase (see chapter 6) whereas, because of dissociation of the solid oxide, Cr_2O_3, on heating, a crossed beam reaction ($Cr+O_3$) was used to produce CrO in the vapour phase (also described in chapter 6).

An important part of this work has been the use of ΔSCF CI calculations to interpret photoelectron spectra of metal oxides. The theoretical basis of these calculations is described in chapters 3 and 4. Not only do these calculations allow the photoelectron spectra of the metal oxides themselves to be assigned, they also provide a test for a theoretical model. A successful gas-phase study of an oxide with the aid of ab initio calculations will provide valuable information about the electronic structure of the molecule and fundamental information about the Metal-Oxygen bond. In principle, this information could then be used to test the theoretical model on the electronic structure of the metal oxide in the solid state. In other words, a gas-phase study is a valuable precursor to a solid state study. This approach has already been tested in the Southampton pes group with a gas-phase study on UF_4 followed by a study on the solid (4). Valuable insights may be gained into the changes in molecular and electronic structure occurring on formation of the solid from the isolated molecule.

Work on the transition metals iron, cobalt and nickel is presented in chapter 5 with the eventual aim of studying oxides of these metals. This information is, however, additionally important because it enabled test evaporations of a transition metal alloy, of importance to the nuclear programme of the CEGB, to be carried out. These studies are also described in Chapter 5. Direct comparison of the gas-phase and previous solid-state work proved useful and led to suggestions for further higher sensitivity pes experiments on alloys.

Other work has been carried out which is also of some importance to the CEGB. Magnox alloys consisting essentially of magnesium and aluminium are used for canning uranium fuel elements in the CEGB's Magnox nuclear reactors. In the case of a fire involving magnox alloys, a common extinguishant used is BF_3. It is obviously of interest to study the possible products of the reaction of BF_3 with the alloy at high temperature which may include oxides, fluorides and oxyfluorides of the constituent metals and molecular fragments of the extinguishant. A start has already been made on this study with work being carried out on AlF and AlF_3 (see Chapter 7) together with work performed by other members of the Southampton pes group, notably on BF(5) and MgF_2(6).

Other molecules studied are of importance in the earth's atmosphere. Strontium and barium monoxides have been the subject of atmospheric release experiments. An understanding of both molecules' gas phase photoelectron spectra is essential if the ion-molecule reactions occurring in the earth's atmosphere are to be understood. Some preliminary data on these molecules is presented in Chapter 6.

Further developments in the field of high temperature pes are planned. A new high sensitivity multidetector spectrometer has recently been installed in Southampton and some initial results obtained with this instrument are given in Chapter 6 of this thesis where the HeI photoelectron spectrum of vanadium is discussed.

REFERENCES

1. J.M. Dyke, N. Jonathan and A. Morris, Electron Spectroscopy: Theory, Techniques and Applications, Vol. 3, (Academic Press, London, 1979) p.189.

2. J.M. Dyke, N. Jonathan and A. Morris, Int. Rev. Phys. Chem., 2, 3 (1982).

3. J. Berkowitz, Electron Spectroscopy: Theory, Techniques and Applications, Vol. 1, (Academic Press, London, 1977) p.355.

4. G.D. Josland, Ph.D thesis, University of Southampton (1983).

5. J.M. Dyke, C. Kirby and A. Morris, J.C.S. Faraday II, 79, 483 (1983).

6. M.P. Hastings, unpublished work.

CHAPTER TWO

Experimental Methods

2.1. The Basic Spectrometer

The aim of this chapter is to outline the basic components of the photoelectron spectrometer used to perform the work described in this thesis. The general requirements are a monochromatic photon source, a sample inlet system, an ionisation chamber (where ionisation takes place), an electron energy analyser and an electron detector plus equipment for recording the resulting spectrum. The ionisation, analyser and detector regions need to be evacuated to a pressure of $<10^{-5}$ torr and a photoelectron spectrum is recorded by varying the energy of the photoelectrons allowed to reach the detector and counting the rate at which the electrons of each energy arrive. The basic components of the spectrometer used in this work will be described in detail in the following sections.

Photon Sources

For the purposes of the photoelectron spectroscopy experiment, a photon source needs to have a small linewidth, be monochromatic and have as high an intensity as possible. The most generally useful and convenient ultra-violet source is a DC discharge in pure helium. The major emission is at 58.4nm (21.22eV) and results from the transition:

$$^1P(1s2p) \rightarrow {}^1S(1s^2)$$

in the neutral helium atom. This is usually referred to as HeI radiation following the spectroscopic convention that radiation from an unionised atom is designated I, from a singly ionised atom II, and so on. Small amounts of other HeI lines are present in the discharge which arise from emission from other excited states of the type $^1P(1s\ np)$ to the $^1S(1s^2)$ state. Typical relative intensities are given in the following table:

Wavelength (Å)	Energy (eV)	Excited State	Typical Relative Intensity
584.3	21.22	2p ^1P	100.0
537.3	23.09	3p ^1P	1.3
522.2	23.74	4p ^1P	0.18
515.6	24.04	5p ^1P	0.05
512.1	24.21	6p ^1P	<0.03

The notation HeIα is sometimes used to distinguish the main emission from the others. The other HeI lines are often useful in that they can be used for purposes of spectral calibration.

For this work a DC discharge in helium along a quartz capillary tube, placed between two water cooled stainless steel electrodes, has been used. The properties of such a source are well known (1-3) and since no window materials exist which transmit photons of the required energy (2) a windowless lamp is used. The discharge takes place in flowing helium and the lamp is differentially pumped to prevent excess gas reaching the ionisation chamber.

The lamp can also be made to give a stable discharge with gases other than helium. The most useful of these is neon, giving rise to a NeIα doublet at 16.67 and 16.85eV. It is somewhat weaker than the helium source but is occasionally useful when improved resolution is required (the factors affecting resolution will be discussed later in this chapter).

Discharges in helium may also generate a series of lines from ionised helium, HeII, with the main line at 30.4nm (40.81eV) arising from the transition:

$$^2P(2p^1) \rightarrow {}^2S(1s^1)$$

HeII photons are normally present in small quantities when a helium lamp is used. A band due to the HeII ionisation of atomic helium (ip = 24.58eV) at an apparent ip of 4.98eV on the HeI scale is often seen and is a useful calibration position for HeI spectra. The proportion of HeII photons emitted from a lamp designed to emit HeI photons may be increased by reducing the helium pressure slightly.

Analyser and Detector Equipment

The electron energy analyser separates photoelectrons according to their kinetic energies. The ideal analyser provides both high resolution and high transmission but, unfortunately, these are conflicting requirements since, to achieve high resolution, some restriction must be placed on the paths of the electrons which will obviously affect transmission.

The electron energy analyser employed in this work is an electrostatic deflection analyser of the 150° hemispherical type and is shown in detail in Figure 2.1. The analyser consists of two concentric hemispherical sectors, of mean radius 10cm, mounted on an insulating material. Each hemisphere is charged to equal but opposite potentials with a potential of +V on the inner hemisphere and -V on the outer hemisphere. Electrons of a particular energy generated at the source, S, enter the analyser through the entrance slits and, by application of the correct voltage to the hemispheres, can be brought back to focus at F (see Figure 2.1). This particular design of analyser was chosen for a number of reasons which are detailed below:

(a) The electron source S, focus, F, and centre of the hemispheres, O, lie in the same plane which allows some simplification in the design and construction of the spectrometer.

(b) The 150° sector angle allows the entrance and exit slits to be placed between S, F and the hemispheres, thus enabling the hemispheres and both set of slits to be mounted on one plate (see Figure 2.1). The use of, for example, a 180° analyser would require a lens system to focus the electrons to a point source since the slits could not be positioned as simply as in the 150° case.

(c) In addition to the electron orbit shown in Figure 2.1, electrons can travel in other orbits starting as S and terminating at F but in different planes. This is the so-called 'double focussing' property of this type of analyser and results in high transmission.

In the type of analyser used in this work, electrons are usually detected by a channel electron multiplier placed at the electron focus, F. Electrons reaching the electron multiplier produce pulses which are amplified and counted by a ratemeter, the output of which is fed into a chart recorder. Spectra are recorded by sweeping the voltage applied to the hemispheres at a constant rate.

The electron trajectories inside the spectrometer are easily perturbed by stray electric and magnetic fields and care must be taken to reduce these to a minimum. The hemisphere and slit surfaces were

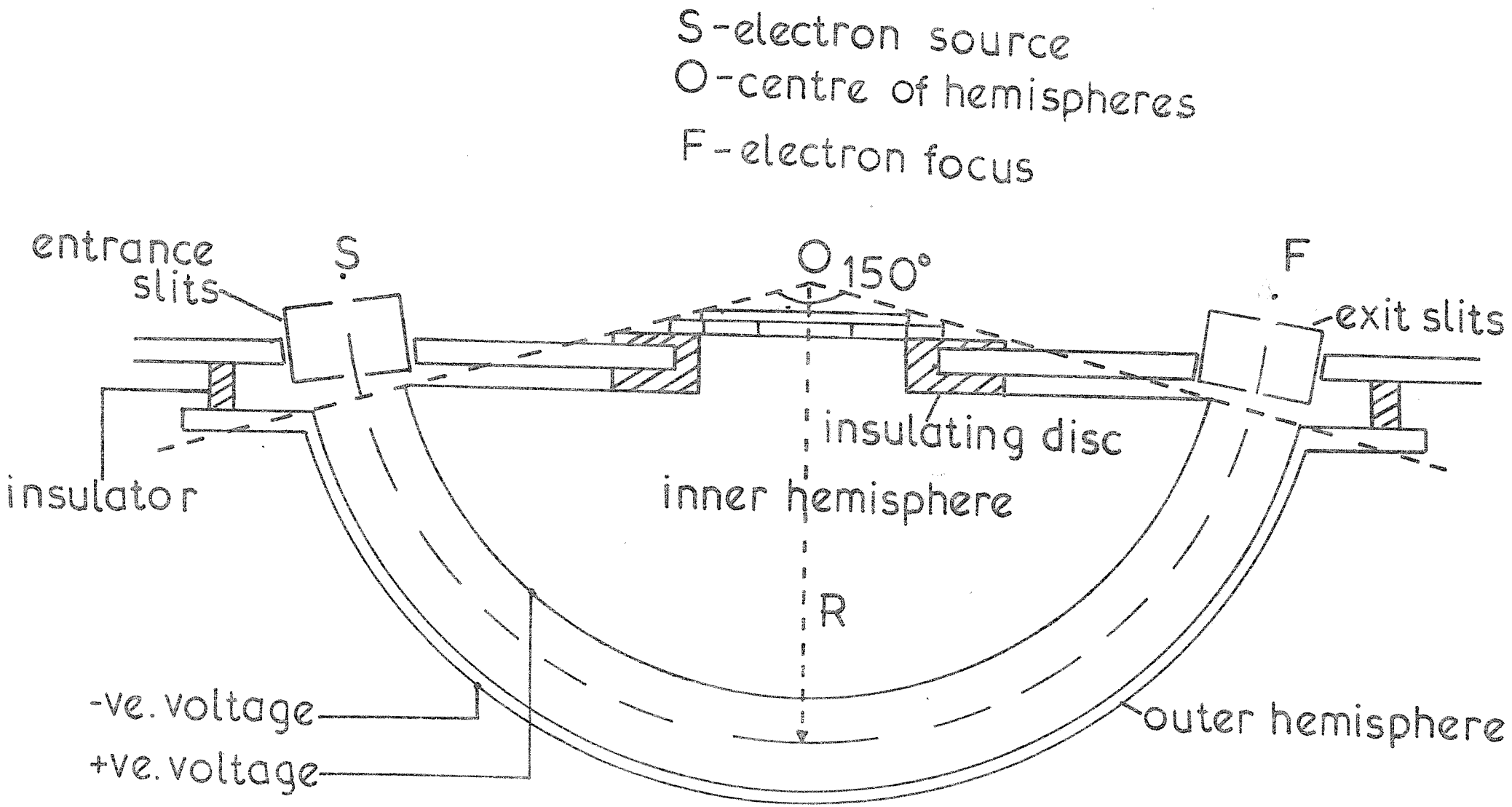
S-electron source
O-centre of hemispheres
F-electron focus
entrance slits
S
O
150°
F
exit slits
insulating disc
insulator
inner hemisphere
R
-ve. voltage
+ve. voltage
outer hemisphere

FIG 2.1

coated with graphite to reduce surface potential variations. To eliminate the earth's magnetic field, the analyser was surrounded by three sets of mutually perpendicular Helmholtz coils. A magnetometer was used to initially zero the field at the centre of the coils and any fine tuning was carried out by optimising a photoelectron signal, normally that of argon.

Some discussion of the properties of the hemispherical analyser, described above, is probably useful at this stage especially in terms of transmission and resolution. It can be shown that, for spherical sector analysers generally (4,5), the probability of transmission of an electron is proportional to the kinetic energy of that electron. The transmission function of a given analyser may be determined experimentally by making use of published data (6). This has been done for the analyser used in this work (7) and the transmission function was found to be linear except at low electron kinetic energies (<0.5eV) where electrons are particularly sensitive to slight electric and magnetic field variations with consequent poor resolution.

The resolution of a spectrometer is particularly important if, for example, vibrational structure is to be observed in experimental spectra. For the spectrometer used in this work, the typical resolution was measured as 25-30meV at F.W.H.M. for argon recorded with HeI radiation. This resolution can be thought of as being made up of an instrumental factor, plus a contribution which defines the fundamental limits of resolution.

The instrumental factor may be derived by considering the path of an electron moving in an orbit through the analyser. A stable orbit for an electron moving in an orbit of radius R will be maintained provided the electrostatic force acting on the electron is balanced by the centripetal force.

$$\text{i.e.} \qquad eF = \frac{mv^2}{R} \qquad (2.1)$$

where e, m = electron charge and mass respectively

v = electron velocity

and F = electric field between hemispheres

Since the kinetic energy of the electron will be equal to $\frac{1}{2}mv^2$, equation (2.1) gives:

$$KE = \tfrac{1}{2}\, eFR$$

and $$\Delta E = \tfrac{1}{2}\, eF\Delta R$$

Thus $$\frac{\Delta E}{E} = \frac{\Delta R}{R} \qquad (2.2)$$

The spread in energy (ΔE) of the electron beam at a given energy (E) is thus determined by the analyser geometry, being dependent on the radius of the electron orbit and the allowable variation in this, (ΔR). For an entrance slit of width dR_1 and an exit slit of width dR_2, equation 2.2 may be approximated by

$$\frac{\Delta E}{E} = \frac{(dR_1 + dR_2)}{2} \cdot \frac{1}{R} = \frac{S}{2R} \qquad (2.3)$$

This expression defines the instrumental resolution in a simplified way since the possibility of electrons entering the analyser non-tangentially is not taken into account. Two interesting points arising from equation 2.3 can be made.

(a) For a given kinetic energy, the resolution, ΔE, is proportional to the total slit width. Thus resolution may be improved by reducing the total slit width, at the expense of lower intensity.

(b) For a given analyser configuration (ie fixed S and R), the resolution is proportional to the transmission energy, E. Thus, resolution may be improved by using a less energetic photon source e.g. replacing a HeI source with a NeI source. This point is also illustrated by noting the variation in recorded band widths across a given photoelectron spectrum recorded by sweeping the analyser voltage (see for example ref. (8)). Typical slit widths used in this work were 1.0 mm for the outer slits and 1.5 mm for the inner slits for both entrance and exit slits.

As mentioned earlier, the instrumental contribution to the resolution will be the major factor, but there are other contributing factors (1,2):

(a) Thermal broadening due to the motion of the molecule being ionised. An expression for ΔE may be derived by assuming that the most probable velocity of the molecule to be ionised is

$$V = \left(\frac{2kT}{M}\right)^{\frac{1}{2}}$$

where T is the temperature (K) and M is the mass of the molecule. It can be shown (1,2) that the energy spread is given by:

$$\Delta E = 2\left(\frac{mEkT}{M}\right)^{\frac{1}{2}} = 0.723\left(\frac{ET}{M}\right)^{\frac{1}{2}} \times 10^{-3} \text{ eV}$$

where m is the electron mass.

Thus thermal broadening will increase with increasing temperature and decrease with increasing molecular mass. For example, at room temperature (300K) and a photoelectron energy of 10 eV, a photoelectron ejected from a molecule with molecular weight 20 will have a half-width of $\sim$10 meV while a photoelectron ejected from a molecule with mass 100 will have a half width of $\sim$4 meV.

(b) Line broadening in the photon source contributes approximately 3 meV to the total resolution.

A general schematic diagram of the spectrometer used in this work is shown in figure 2.2. Both the main analyser chamber and the ionisation chamber were pumped by oil diffusion pumps. A typical operating pressure of $<5 \times 10^{-6}$ torr could be attained in this way.

The sample source is dependent on the nature of the species to be studied. In this work the technique of high temperature evaporation of solid samples was used to generate the species to be studied in the vapour phase. The high temperature heating method used here will be discussed in detail in the next section.

2.2. High Temperature Methods

The design of a photoelectron spectrometer for the study of high temperature and transient species has been discussed in detail elsewhere (9,10). This thesis is only concerned with high temperature p.e.s. and

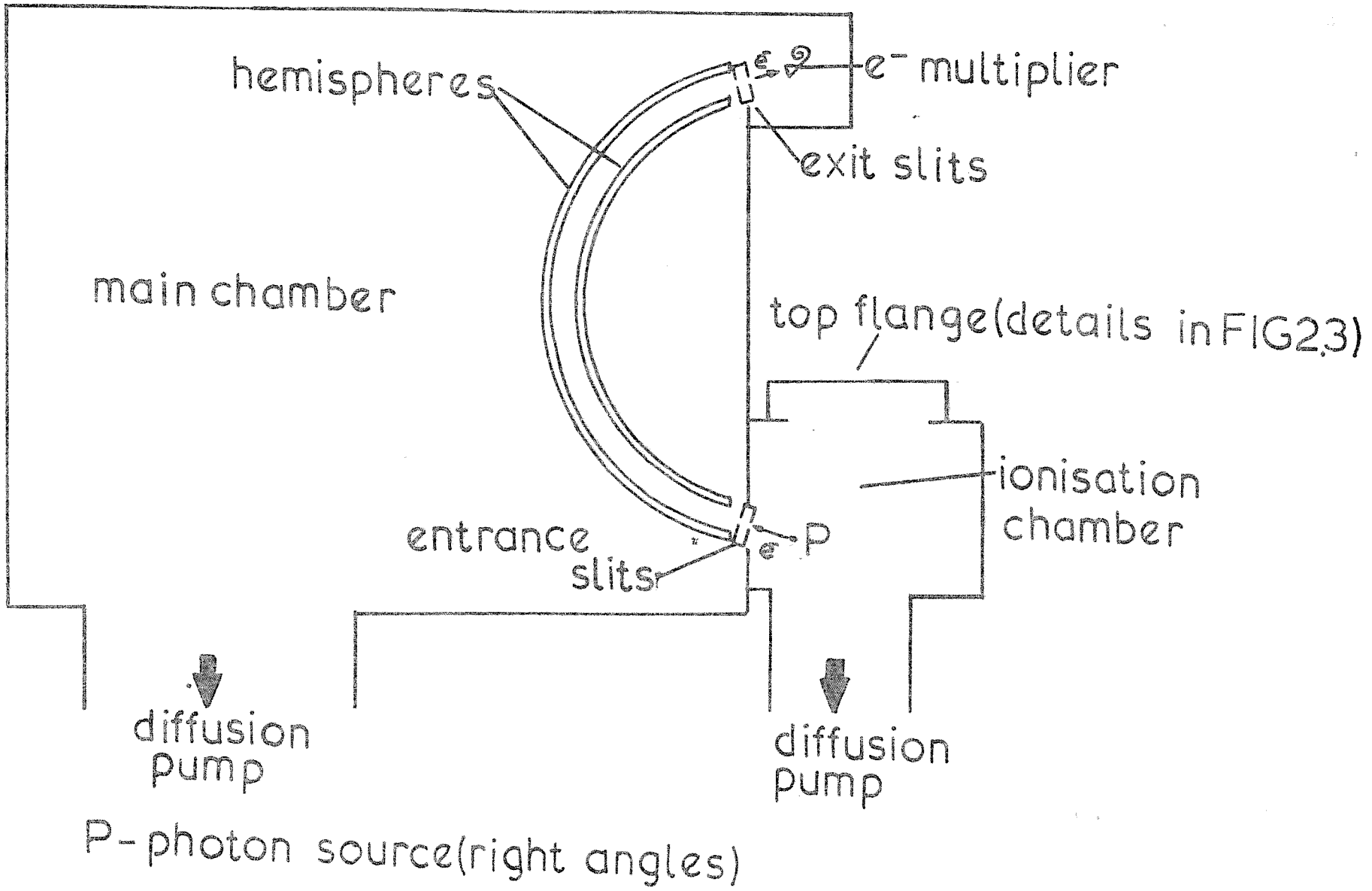
hemispheres
e⁻ multiplier
exit slits
main chamber
top flange(details in FIG2.3)
ionisation chamber
entrance slits
P
diffusion pump
diffusion pump
P-photon source(right angles)

FIG 2.2

when designing a high temperature spectrometer some important points should be borne in mind.

(a) The furnace and ionisation region should be pumped efficiently. This is particularly important since the species to be studied may be short-lived in the vapour phase, and efficient pumping is needed to ensure rapid transport of the species to the ionisation region.

(b) Considerable contamination of the ionisation chamber, particularly the analyser entrance slits and furnace components, can occur on evaporation of small quantities of material. For this reason, the ionisation chamber must be readily accessible for cleaning purposes.

These points will be discussed further in the following section.

Furnace Heating and Design

Several research groups are, at present, operating in the field of high temperature photoelectron spectroscopy using a variety of heating techniques. These techniques will be briefly discussed in terms of maximum achievable temperature and their advantages and disadvantages outlined.

(a) Electrical resistive heating is the most widely used heating technique in high temperature p.e.s. and it basically involves placing the furnace assembly inside a coil, normally of tungsten or some other refractory metal, and passing a current through the coil. The method is quite simple but, in practice, the large currents required (typically >50A to achieve furnace temperatures >1000K) would cause considerable fields in the ionisation region. This problem can be alleviated by winding the coils non-inductively. The practical upper temperature limit for this technique is $\sim$2000K and this seems to be governed by the high current requirements (which can be several hundred Amps) at which some residual field is inevitable.

The first group to publish details of a spectrometer using resistive heating was that of Berkowitz et al (11). Their spectrometer was capable of studying species at temperatures in excess of 800K. Unfortunately the residual magnetic field associated with the applied current limited the operation of the spectrometer to temperatures of 900K maximum.

Later, Potts et al (12) reported a spectrometer capable of operating at temperatures of up to 1300K. This used a resistively heated furnace similar to the Berkowitz (11) design. The non-inductive winding of the heater was improved thereby reducing residual magnetic fields. Unfortunately, contamination of the critical regions of the spectrometer led to poor resolution and hence the spectrometer was limited in its use.

Recent work has concentrated on improving furnace designs to reduce the residual magnetic fields which limit the operating temperatures of this type of heating. Berkowitz et al (13) have produced a spectrometer containing a unique "double-oven" assembly in which a conventional Knudsen cell is radiatively heated (i.e. the heating coil is not in contact with the furnace and hence heating is by radiation). The cell is extended by adding a long narrow tube to direct the sample vapour to the ionisation region. This tube is also resistively heated by a coil, hence the term "double-oven". To reduce the residual magnetic fields in the critical region of the spectrometer, both coils are arranged such that their respective residual magnetic fields cancel out. The maximum temperature obtained with this spectrometer is reported as being 1500K (13,14). This spectrometer, has been used recently in studies on B_2O_2 (14,15), atomic chlorine (16), the alkali halide monomers, dimers and trimers (17) and in a number of other studies (18,19).

Potts et al (20) have also improved their basic spectrometer and furnace design. A new resistively heated furnace (20) in which graphite or alumina tubes are heated using a double coil arrangement is employed. Each coil has a separate AC power supply operated 180° out of phase such that the magnetic field from one coil opposes that from the other. This spectrometer has been used up to temperatures of 1500K with good resolution in a number of studies, notably studies on both gas-phase and condensed phases of the tin and lead dihalides (21), gas-phase lanthanide trichlorides (22) and gas-phase and condensed phases of the bismuth and antimony halides (23). Potts et al are also interested in studying low melting point metals by gas-phase p.e.s. and have recently published details of a study on selenium and tellurium (24).

(b) Electron Bombardment heating is used by two groups, those of Bock et al and Elbel et al. Both these groups use essentially the same spectrometer (supplied by Leybold-Heraeus) which consists of an inlet system heated by electron bombardment (25) in which the furnace system is composed of a non-inductively wound tungsten coil surrounding a molybdenum inlet tube. Electrons are produced which bombard and heat the inlet tube which contains the sample. Stray electrons are prevented from entering the ionisation region by enclosing the heated area of the molybdenum tube with a stainless steel shield. This problem of stray electrons has meant that many other p.e.s. groups (including the Southampton group) have avoided the use of electron bombardment as a heating technique. The technique has, however, been used successfully in published p.e.s. studies by Elbel et al and Bock et al to achieve temperatures of 1600K (26) and 1200K (25) respectively.

(c) Laser heating seems at first sight to satisfy the requirements for a field-free ionisation region, but it too suffers from operational problems. This approach was first used by Schweitzer et al (27,28). A 50W pulsed CO_2 laser was used to heat a furnace which was thermally isolated from the spectrometer. The problem with this technique is that it produces a very localised heating effect and can produce on unstable vapour source making it difficult to record reproducible spectra. Theoretically, in laser heating, the maximum temperature attainable is dependent on the choice of materials used in furnace design and the type of laser chosen. Schweitzer et al (27) reported a maximum temperature of 1800K, but no studies have been published with temperatures greater than 1300K. This possibly represents the maximum temperature at which reliable spectra can be recorded. Laser heating was later attempted by Berkowitz et al (29). Problems were encountered in controlling sample evaporation and recorded spectra had very poor signal-to-noise ratios so Berkowitz et al had to abandon the laser heating technique in favour of the "double-oven" arrangement (13).

(d) Radio-frequency Induction heating is probably the most versatile technique and for this reason it has been chosen as the heating technique to be used by the Southampton p.e.s. group (30). Induction heating makes use of the fact that when an alternating current flows

through a conductor the associated fluctuating magnetic field can induce a current in a nearby conductor (or susceptor). The induced (or eddy) currents heat the susceptor by a normal resistive heating process. In this work radiofrequency (RF) of 1MHz was passed through an induction coil surrounding a susceptor (or furnace). Interference from the generated r.f. power in the spectrometer detection circuitry was eliminated by pulsing the RF generator output. This is done at the convenient rate of 50Hz, the frequency of the generator mains supply, i.e. for half of the 50Hz cycle the generator is transmitting and for the other half it is "off". A gating unit is used, using the 50Hz supply as a timing signal, to generate a detection window during which the signal from the detection circuit is allowed to pass through to the recording equipment. The detection window can be set to be 180° out of phase with the RF pulses and the window width adjusted to eliminate RF interference effects. Details of the radiofrequency induction heating method as used in p.e.s. have been published and can be found in references (9) and (30).

Radio-frequency induction heating has several advantages over the other three heating techniques outlined above. The most important of these are outlined below:-

(i) Potentially very high temperatures are accessible and any interference with the photoelectron signal can be eliminated by using pulsed techniques.

(ii) An inductively heated furnace is not in thermal contact with the heating supply and hence conduction heat losses are reduced.

(iii) With inductively heated furnaces, heating only occurs in the area immediately adjacent to the coil, which means that heating effects are localised to the furnace assembly region.

(iv) The sample load required (up to 1 gram) can be easily contained within the furnace assembly.

Radio-frequency induction heating was used throughout the work described in this thesis and has proved to be a very efficient heating technique.

The dimensions of the photoelectron spectrometer were such that the RF generator could not be sited closer than one meter from the ionisation chamber, so the radio frequency current was fed from the supply through leads of the required length. To reduce losses from the coil, and noting that the radio frequency current travels mainly in the surface of a conductor, the supply leads were constructed from wide copper strips. Figure 2.3 shows the location of the induction coils and furnace assembly relative to the spectrometer entrance slits. The water cooled coils are made from $^{3}/_{16}$ inch high conductivity copper tubing wound to give a coil with six turns with between 2.5 cm and 3 cm internal diameter depending on furnace requirements. The furnace assembly is supported in the RF coils by a ceramic tube which passes through an 'O'-ring vacuum seal. A carrier gas, normally helium, is passed down through the furnace support tube to aid the transport of sample vapour to the point of ionisation. The coil and furnace assembly is surrounded by a tantalum shield which serves several purposes:-

(i) to reduce radiative heat losses from the furnace and prevent radiative heating of the slit region,

(ii) to prevent any excess thermal electron emission adversely affecting the photoelectron signal, and

(iii) to collimate the sample beam and hence reduce chemical contamination of the entrance slits.

The complete furnace assembly, coils and tantalum shield are mounted on a removable flange which forms the top plate of the ionisation chamber. The fact that the top flange is removable is very advantageous since it allows easy access to the entrance slit region for cleaning purposes. A grid, positioned in front of the entrance slits further reduces sample contamination and radiative heating of the slits.

Temperatures measured during the course of this work were taken mostly using a calibrated optical pyrometer sighted down the furnace support tube onto the hottest part of the furnace. In the case of studies performed at lower temperatures (notably the AlF/AlF_3 work), a chromel-alumel thermocouple was used.

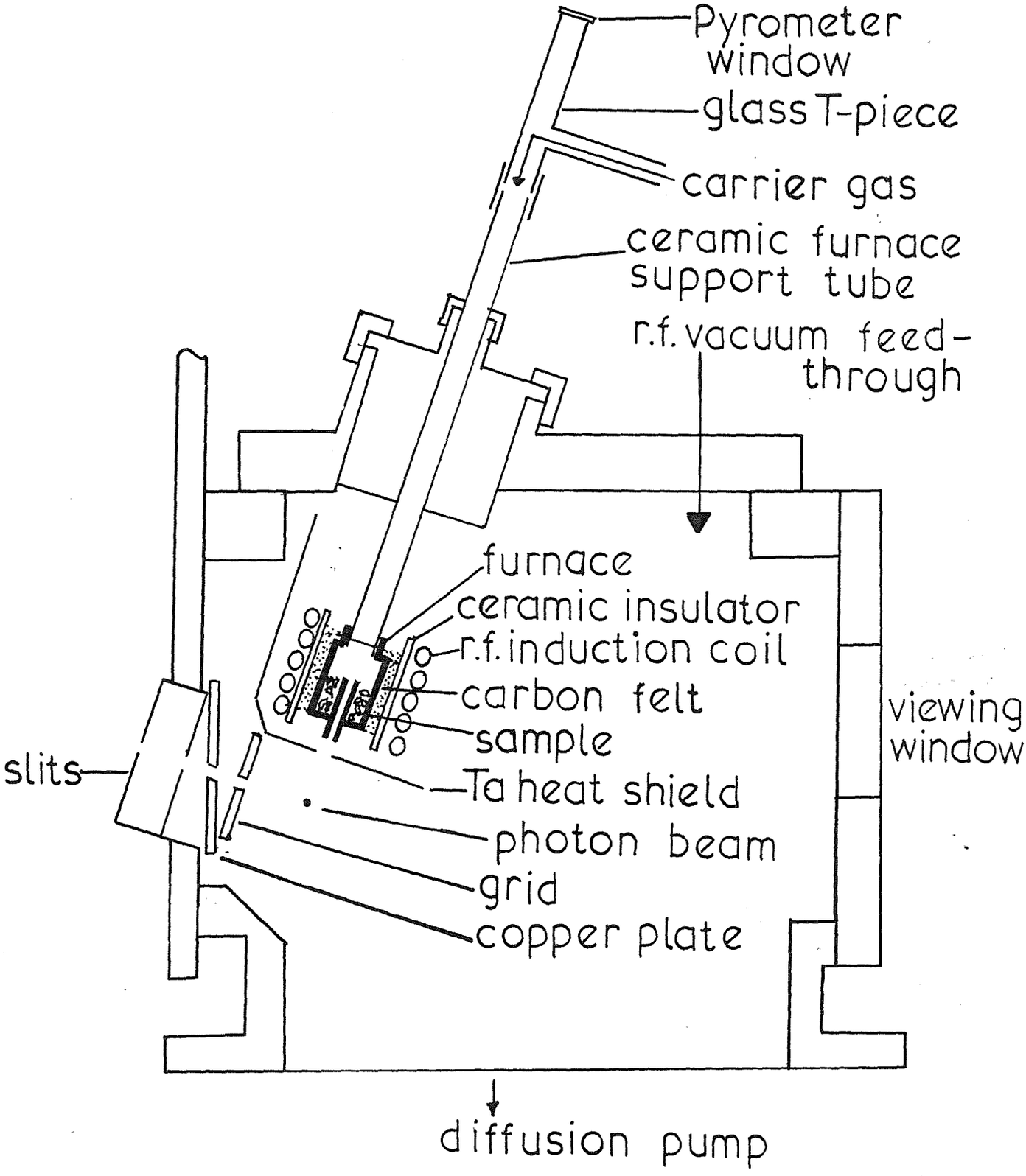
Pyrometer window
glass T-piece
carrier gas
ceramic furnace support tube
r.f. vacuum feed-through
furnace
ceramic insulator
r.f. induction coil
carbon felt
sample
Ta heat shield
photon beam
grid
copper plate
slits
viewing window
diffusion pump

FIG 2.3

Although the choice of RF induction heating has many advantages, it also imposes certain limitations on the possible furnace designs. To understand these limitations, the theory of RF induction heating needs to be understood (31-33):

For a current flowing in an electrical conductor a magnetic field is created around that conductor, the strength of the field being directly proportional to the current flowing. If the conductor is wound into a coil, then the magnetic field strength is increased, the increased strength being directly proportional to the number of turns in the coil. If an alternating current is used, then the magnetic field produced will be continually changing. Induction heating depends upon a current being induced into a second electrical conductor (known as the susceptor) by a changing magnetic field. A heating effect is produced by the current flowing in the susceptor and is given by:-

$$\text{Heat} \propto (\text{induced current})^2 X \text{ resistance of the conductor} \qquad (2.4)$$

The resistance of a conductor is given by the formula:

$$R = P\frac{L}{A} \qquad (2.5)$$

where P is the resistivity of the material
L is the length
and A is the cross-sectional area.

Therefore in using RF induction heating, it is necessary to maximise the heating effect. The large induced currents are produced by operating the generator at radio frequencies ($\sim$1 MHz) as the induced current is directly proportional to the rate of change of the magnetic field. One phenomenon that must be remembered is that high frequency current flow is restricted to the outside or "skin" of a conductor. The depth to which the currents are restricted is given by the formula (31,34):

$$d = \frac{1}{2\Pi}\sqrt{\frac{P \times 10^9}{\mu f}} \qquad (2.6)$$

where d is in cm
P is the resistivity in ohm cm
μ is the relative magnetic permeability of the susceptor material
and f is the frequency of the RF current.

This means that heat is generated within the skin depth, d, and conducted to the rest of the susceptor. Therefore, for efficient heating the magnetic flux at the surface of the susceptor should be maximised. Heating is most efficient when the susceptor is as close as possible to the induction coil. In the situation of "tight coupling" the magnetic flux density at the workpiece is a maximum. Keeping the workpiece close to the induction coil limits the amount of shielding which can be used to minimise radiative heat losses from the furnace. A balance needs to be found which optimises heating with respect to both coupling and shielding efficiencies.

For a solid cylinder, approximately 90% of the total heat is generated within a depth d from the surface, given above. For a furnace of the type shown in Figure 2.4, the entire furnace wall will be inductively heated if the wall thickness can be restricted to less than the skin depth (d). This results in rapid heating of the furnace. For wall thicknesses >d, sample heating can only take place by thermal conduction through the susceptor material which necessarily results in slower heating and, in extreme cases, a lower equilibrium temperature. In general, an optimum temperature can be achieved if the wall thickness is significantly less than the skin depth, d, when the resistance factor of equation 2.4 becomes important. For example, d for graphite is 1.8 mm at a frequency of 1 MHz. In practice, graphite furnace components can be machined with wall thicknesses down to 1 mm. In this case, the entire furnace wall can be inductively heated leading to a rapid rise in temperature.

Some commonly used susceptor materials and their corresponding properties are listed in table 2.1. On the grounds of resistivity alone, graphite appears to be the best of the susceptors listed and has been used in the work on AlF/AlF_3 described in chapter 7 of this thesis.

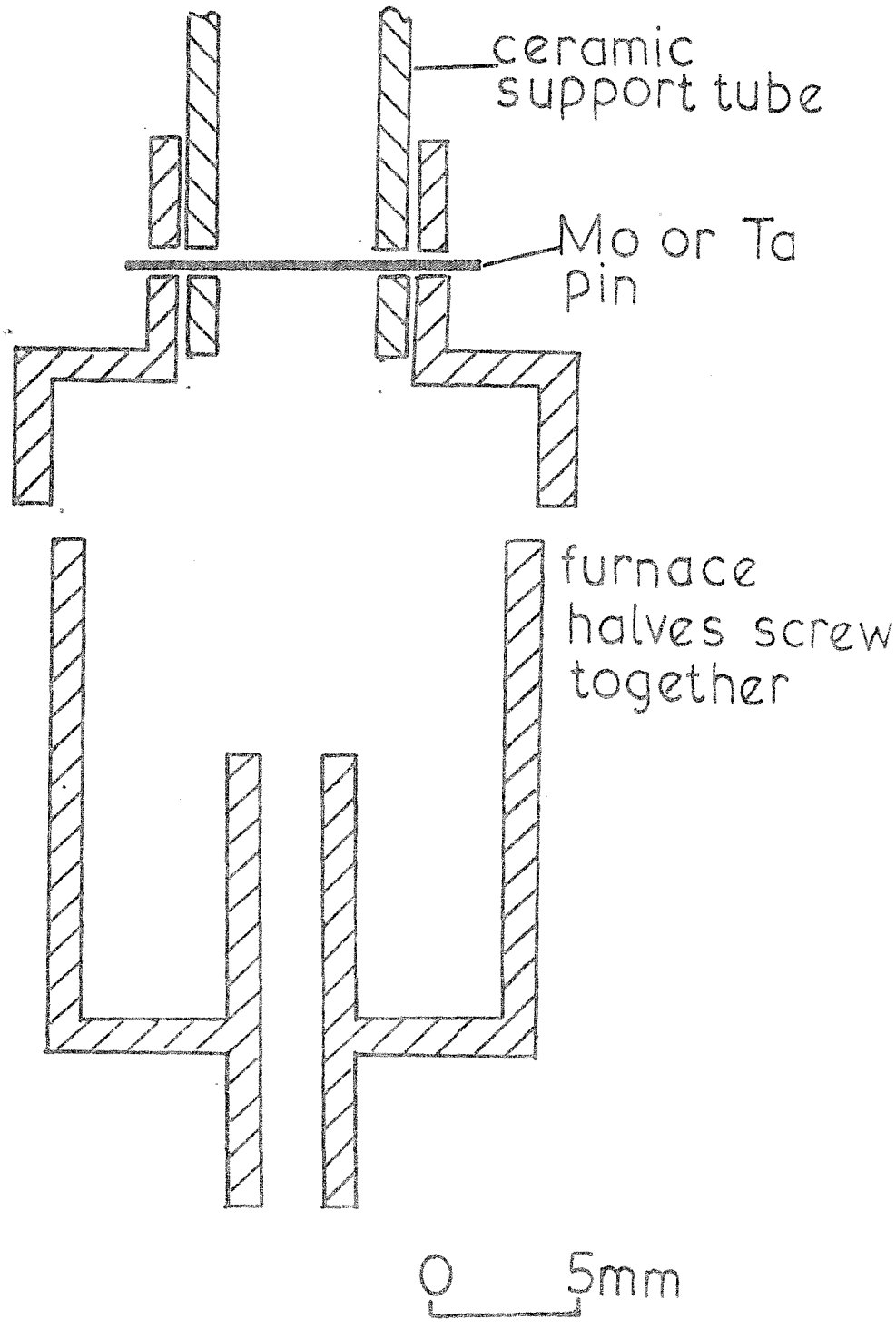
ceramic
support tube
Mo or Ta
pin
furnace
halves screw
together
0
5mm

FIG 2.4

Table 2.1 Properties of some Refractory materials*

Material	Resistivity (2000K) x 10^6/ohm cm	Max. temp(K) (a)
C	1375	3500
W	60	3100
Mo	53	2700
Ta	87	2900
Al_2O_3	$>10^7$	2400
ZrO_2	$>10^7$	2400
BN	$>10^7$	2600

*Data taken from references (34) and (35).

(a) Maximum workable temperature for a furnace manufactured from the material.

A typical arrangement for a graphite furnace is shown in Figure 2.5. Of the three susceptor metals listed (tungsten, tantalum and molybdenum), tungsten has been used in experiments on vanadium and vanadium monoxide described in chapter 6 of this thesis.

The simplest furnace arrangement possible is when the furnace is also the susceptor. This is shown in Figure 2.5. Carbon felt is placed around the furnace to reduce radiative heat losses. Carbon felt has a low thermal conductivity and is used as a thermal insulator capable of resisting temperatures of 3800K in a vacuum. It also has the advantage of low inductive pickup due to its fibrous nature and can be used in conjunction with inductively heated furnaces. A ceramic ring is pushed onto the carbon felt to ensure that the furnace arrangement does not short circuit to the coils. The ceramic therefore, has to be electrically non-conducting, have a negligible vapour pressure at high temperatures and be stable to carbon felt at high temperatures. Other desirable features are low thermal conductivity and good thermal shock properties. Ideally, it should also be relatively inexpensive, be readily available commercially and easily machinable. The limiting temperatures at which various ceramics can be used are shown in table 2.2. The choice of ceramic is largely governed by the reaction at the ceramic carbon junction.

Zirconia with a low thermal conductivity and high melting point is an excellent high temperature material. However, zirconia has not been used as a ceramic ring in this work because it becomes a conductor at high temperatures and it reacts with carbon at $\sim$1900K. It also has poor thermal shock properties. Although zirconia is unsuitable for use as a ceramic ring, it has been used successfully as a support rod for all the experimental work described in this thesis. It has also been used as a furnace material in the cases of the work on Fe, Co, Ni and CrO.

Alumina, with a melting point of approximately 2300K is chemically one of the most inert and one of the strongest of the refractory oxides. The principal limitation of alumina is its reactivity with carbon at $\sim$2000K. Alumina was used as ceramic ring for some of the lower temperature studies described in this thesis, notably Fe, Co, Ni, CrO and AlF/AlF_3.

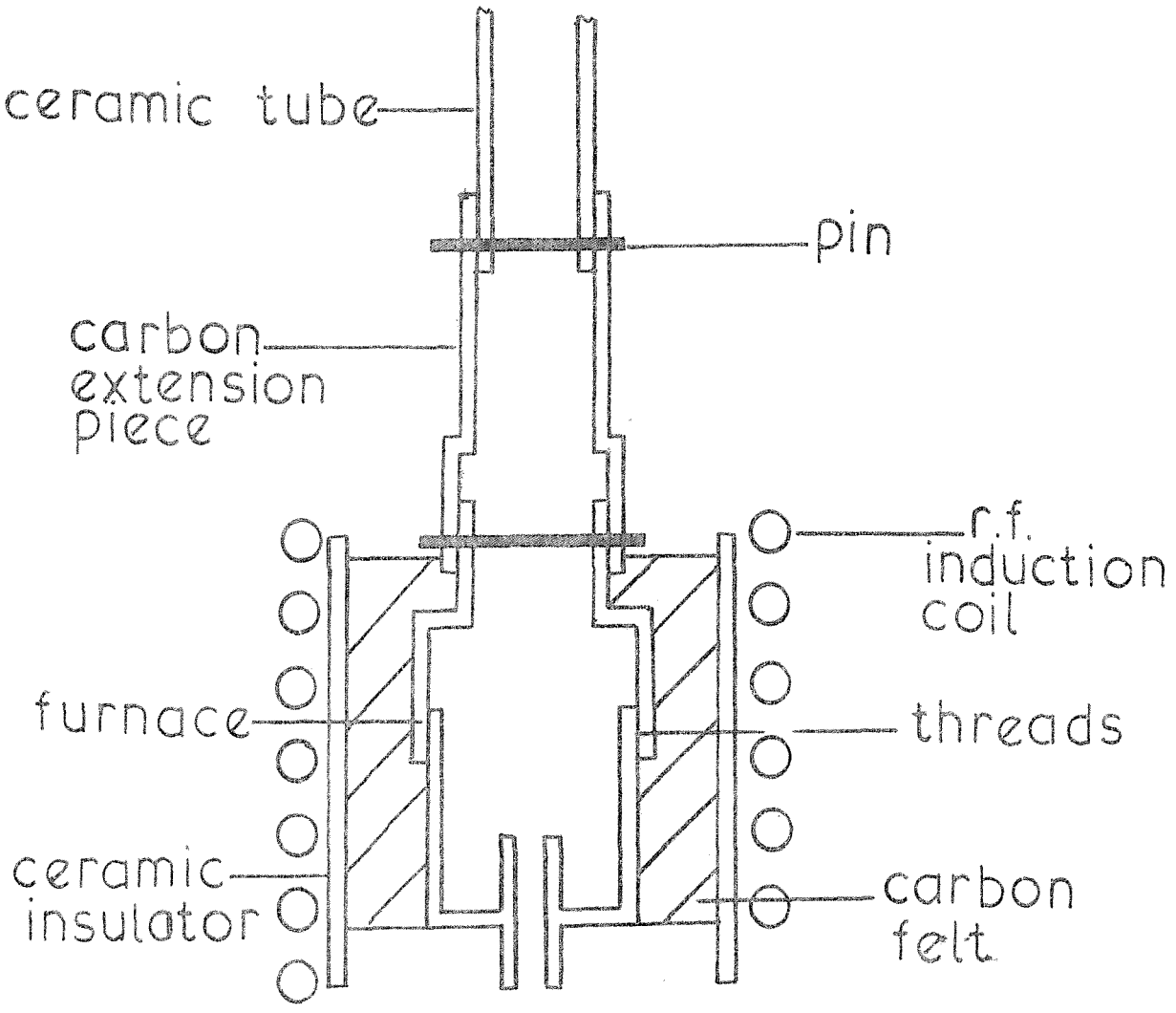
ceramic tube
pin
carbon extension piece
r.f. induction coil
furnace
threads
ceramic insulator
carbon felt
5mm

FIG 2.5

Table 2.2. Maximum workable Temperature (K) of various refractory material junctions

	C	W	Ta
ZrO_2	1900	1900	2000[a]
Al_2O_3	2000[a]	2000	2000[a]
BN	2200[a]	-	1800[a]

(a) Estimated in this work from known furnace temperatures.
(Data taken from references (36) and (37).

Boron nitride is a relatively cheap, commercially available ceramic material. The high maximum usable temperature and its ease of machining has made boron nitride the ideal ceramic for study of higher temperature species, such as V and VO, in this work.

The ceramic rod used to support the furnace assembly is normally zirconia. To avoid any high temperature reaction between the rod and the furnace, a carbon extension piece is used to 'cap' the furnace. This has the effect of removing the carbon-ceramic junction to a cooler part of the spectrometer where a reaction at the junction is less likely to occur.

Normally a furnace material is chosen on the basis of its lack of reactivity with the sample and the temperature required to generate a suitable vapour pressure of the sample in the furnace. When a furnace arrangement of the type shown in Figure 2.5 is used, a problem sometimes arises where the ideal furnace material in terms of sample compatibility may not be a good susceptor and hence it may be difficult to obtain the high temperatures necessary for evaporation of the sample to occur. Other problems may arise when a furnace must be kept completely separate from the carbon felt due to problems of reactivity (this was, in fact, found for tungsten furnaces where reaction of tungsten with carbon causes formation of a low melting point carbide). Problems such as these were encountered in the studies of Fe, Co, Ni and CrO. For Fe, Co and Ni and for Cr, zirconia was chosen as the furnace material which is known not to be a good susceptor at high temperatures (>1800K) (see table 2.1). For a high furnace temperature to be obtained, a heating method other than direct induction heating was required. It was found that a "radiator" surrounding the furnace (but not in contact with it), made from a good susceptor, could be heated up in the normal way and its heat transferred radiatively to the furnace. A typical example of this type of furnace arrangement is shown in Figure 2.6.

The radiative heating method provides greater flexibility than the direct inductive heating method because the furnace need only be designed for sample containment and the radiator designed specifically for attainment of high temperatures. Carbon felt and a ceramic are still used to reduce radiative heat losses and to insulate the furnace assembly from the coils.

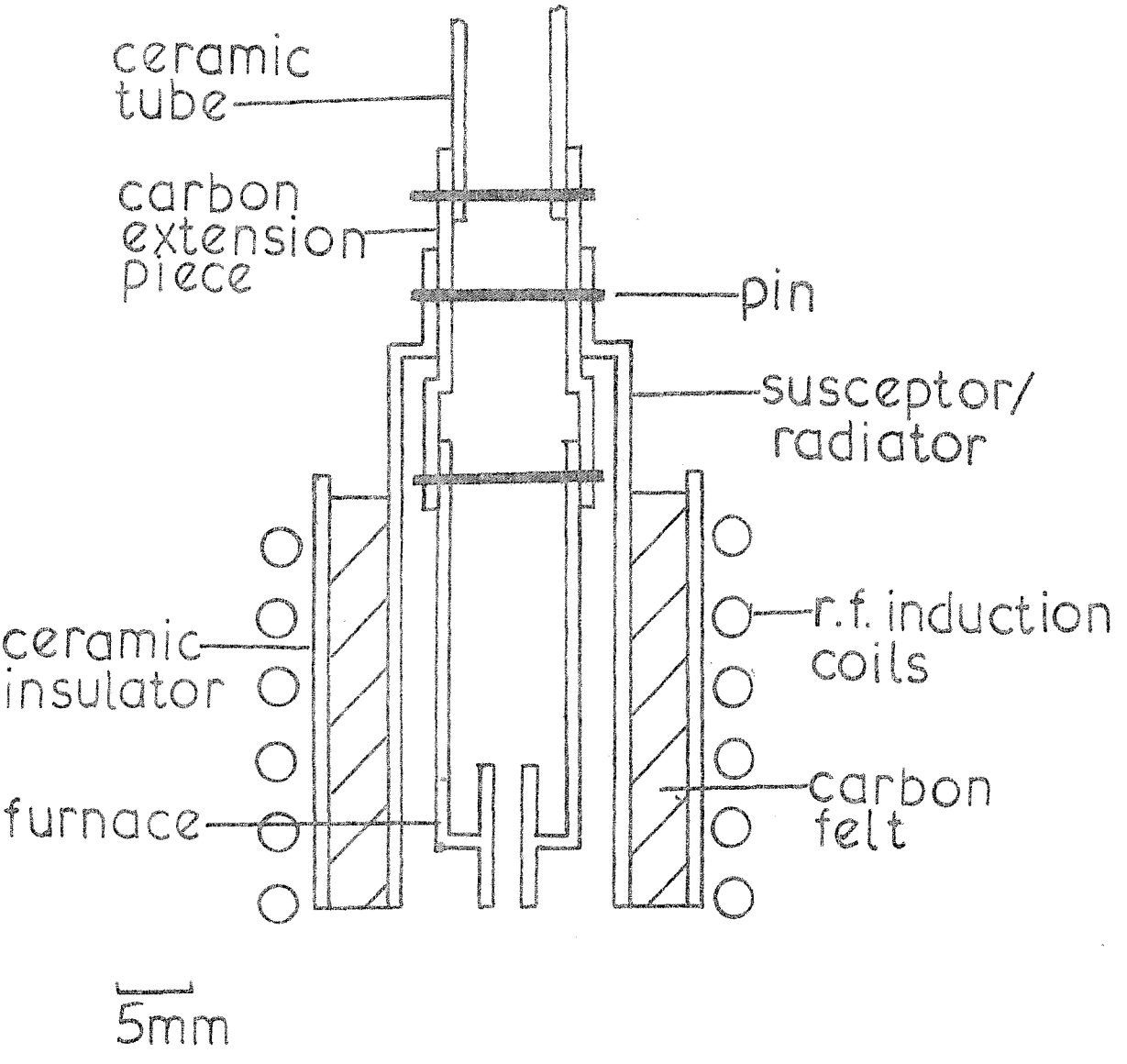
ceramic tube
carbon extension piece
pin
susceptor/ radiator
r.f. induction coils
ceramic insulator
carbon felt
furnace
5mm

FIG 2.6

A graphite radiator was chosen for the experiments on Fe, Co and Ni and on Cr + O_3 and was found to give sufficiently high temperatures to effect evaporation of the transition metals Fe, Co, Ni and Cr from zironia. An alumina ceramic was found to be adequate and little reaction was observed at the carbon-alumina junction.

In the case of vanadium and vanadium monoxide, a tungsten furnace was chosen in view of the expected high temperatures required for evaporation. At temperatures >2400K it was found that a graphite radiator would deposit small amounts of carbon on the tungsten furnace, producing a low melting point carbide and causing premature melting of the furnace. This effect obviously also prevented direct inductive heating from being used since reaction of the tungsten furnace with the carbon felt would lower the maximum usable temperature of the furnace and decrease the working life of the furnace. The material chosen for construction of the radiator for use with experiments involving tungsten furnaces was tantalum. This metal is a good susceptor, easily workable and is reasonably cheap to buy. It was found that in tests, for the same RF power, a tantalum radiator gave temperatures up to 200K higher than those obtainable with a graphite radiator. This is because the tantalum sheet used is supplied at a thickness less than the "skin depth" of tantalum and hence a radiator made from the metal will heat up very efficiently. Again, carbon felt was used as an insulator, surround by a BN ceramic. This was necessary because of the higher temperatures involved in the V/VO experiment. The only drawback with using tantalum radiators is that formation of a brittle tantalum carbide at the carbon-tantalum junction sometimes causes the radiator to crack at junction temperatures >2600K. However in the case of the V/VO system this was not found to be a problem.

2.3 The Photoelectron signal at high temperatures

The loss of signal intensity and resolution in high temperature photoelectron spectroscopy is a well known but, unfortunately, only partially understood experimental problem (13). Signal loss at high temperature can be easily demonstrated by monitoring the photoelectron signal from a constant pressure of a rare gas, such as argon, as a function of temperature. When the first study described in this thesis

was undertaken (that of Fe, Co and Ni - chapter 5) few precautions were taken to reduce signal loss. Loss of signal intensity and resolution began at furnace temperatures of approximately 1600K and increased rapidly. At 2300K only 3%-6% of the initial argon signal remained (measured from peak heights) with a resolution of approximately 150meV. Three possible mechanisms to account for signal loss may be identified:

(a) Residual R.F. interference effects. On increasing R.F. power there is an instantaneous reduction in the signal intensity and resolution which is attributed to R.F. interference.

(b) Heating of electron optics. There is a gradual deterioration in signal intensity and resolution which seems to be due to heating of the slit regions.

(c) Contamination of electron optics. Chemical contamination of the slits can lead to a build-up of a localised charge and hence a reduction in the photoelectron signal. Similar effects are observed if the entrance slits are inadequately coated in graphite following cleaning of the instrument.

Contributions from each of these three effects on the overall signal can, in principle, be estimated from the characteristics of the signal loss. Effect (a) should occur instantaneously as r.f. power is increased. It should also disappear instantaneously as r.f. power is decreased. If effect (a) was the only mechanism governing signal loss, 100% signal intensity should be re-attained on reducing the r.f. power to zero. Effect (b) would take a little longer to take effect since the system will take some time to come to equilibrium but would be expected to disappear completely when the system is allowed to cool. Effect (c) would increase with increasing temperature but would be irreversible.

At lower temperatures (<1600K) only chemical contamination has any effect on the photoelectron signal. Chemical contamination is minimised by the tantalum shield, which helps to collimate the sample beam, and the protective "grid" in front of the slits. If the sample is a well collimated beam chemical contamination below 1600K will be minimal. At temperatures >1600K all three mechanisms outlined above become important.

It is not quite clear why r.f. interference can be present when pulsed r.f. and signal gating is used. It has been found, however, that narrowing the signal window at 2300K produced a significant improvement in the resolution and some improvement in the signal intensity. Because of the use of the gating technique, up to 75% of signal intensity may be lost initially, but on reducing the gating window it has been found that signal retention has increased markedly.

Heating and contamination effects will clearly be most apparent at the analyser entrance slits. Some attempt has been made to reduce these effects by means of the tantalum shield surrounding the furnace. However, in some furnace arrangements, a "direct line of sight" between the furnace and the entrance slits can be identified by bright illumination of the slit region. This illumination is partly due to the position of the furnace in the induction coils. e.g. in fig. 2.7(a) it should be apparent that the lower the furnace is in the coils, the more likely it is that there will be a "direct line of sight" between furnace and slits. Experiments have shown that raising the furnace in the coils, thereby keeping the entrance slits in shadow, will reduce entrance slit heating and lead to an improvement in signal retention. The entrance slits may also be heated by an alternative method, that of thermal emission from the tantalum heat shield. In the original set-up shown in fig. 2.7(a), heating by thermal emission from the shield was found to be a problem, especially at temperatures greater than 2000K. A simple solution was found to this problem which is shown in fig. 2.7(b). The original slits were machined with a smaller overall length, such that they did not protrude into the ionisation chamber, and a thick copper plate containing a 4mm slit placed in front of them. This had the effect of isolating the slits completely from the ionisation chamber and drastically reducing any heating effects. Problems associated with contamination are also minimised in the same way. The combination of isolation of the slits and an optimised r.f. detection window has led to an overall improvement in signal retention. Before these improvements were made only 6% of the signal was retained at 2300K with typical resolution of 150meV (measured for argon at F.W.H.M.) whereas, after the improvements, the corresponding figures are 30% for signal retention and 60meV for typical resolution.

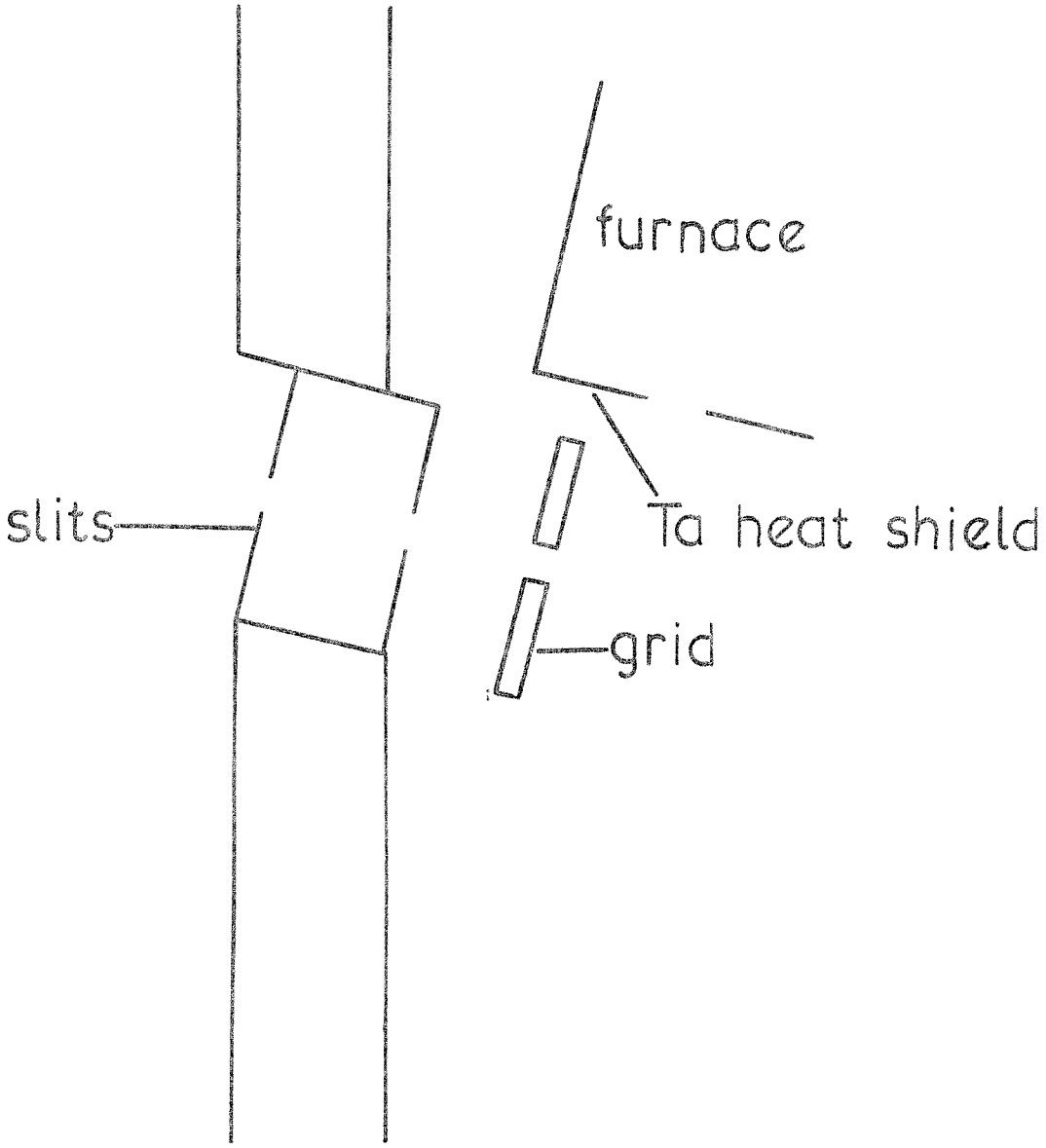

FIG 2.7(a): isolated slit arrangement – original

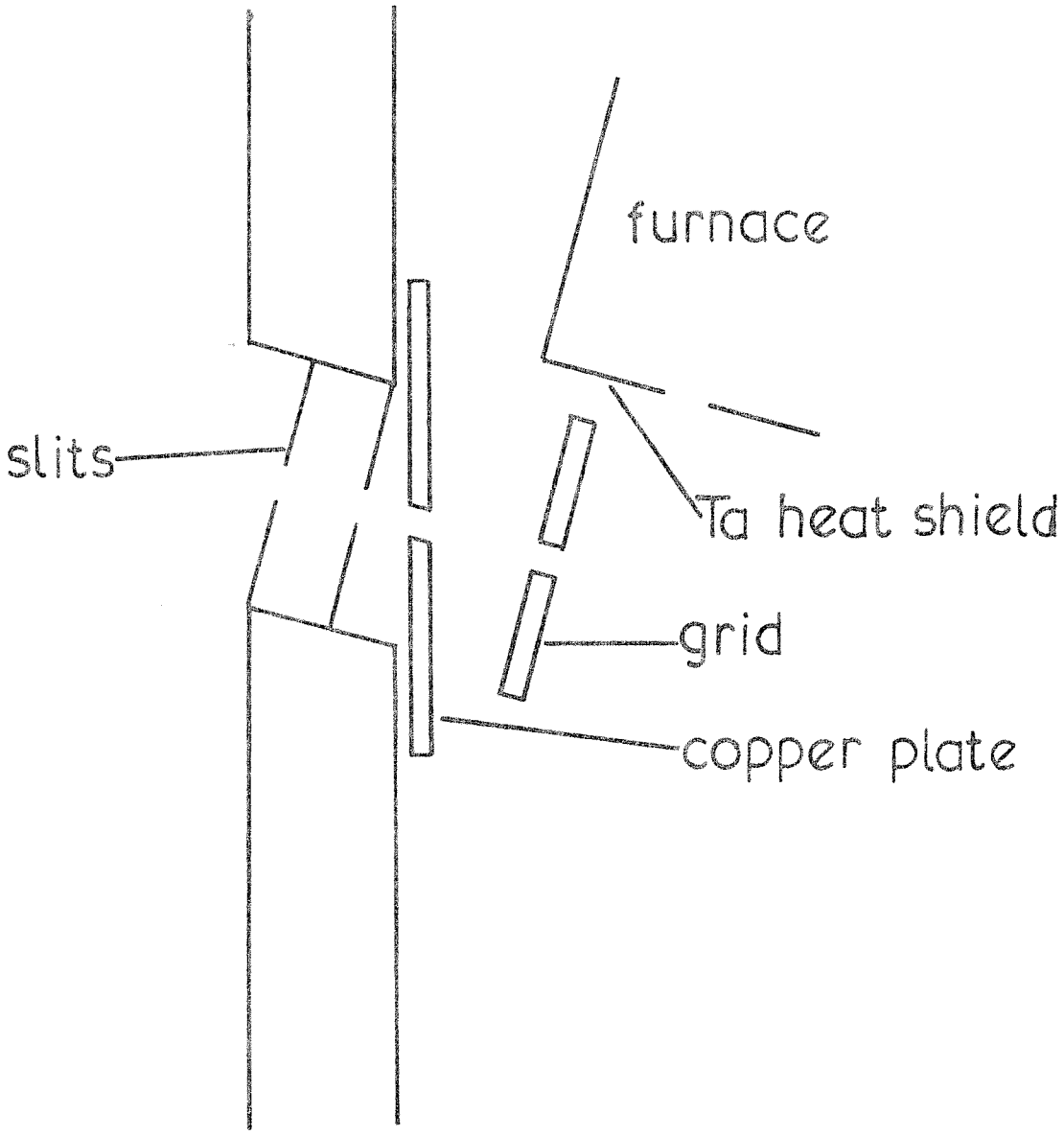

FIG 2.7(b): isolated slit arrangement – updated

Further improvements may be made to the performance of the photoelectron spectrometer depending on the species to be studied. Obviously, lowering the furnace assembly in the coils will increase the concentration of the species of interest at the ionisation region. Correspondingly, a loss of signal may result. Signal loss characteristics also depend on the type of furnace arrangement used and the optimum furnace position must be found by experimentation for each species of interest.

2.4. Further developments in High Temperature p.e.s. Instrumentation

One of the inherent drawbacks of p.e.s. is its susceptibility to perturbing electric and magnetic fields. Problems of contamination of the ionisation chamber and slit region limit the useful time of any experiment. These problems result in a loss of spectral resolution and instability in peak position. It would clearly be an advantage to have a spectrometer capable of operating at a higher photoelectron count rate such that the time needed for recording a spectrum is reduced and spectral drift minimised. Such a spectrometer has recently been constructed at Southampton (38). It features a microchannel plate detector which allows rapid acquisition of spectral data with much improved signal-to-noise ratios when compared with the conventional single detector instrument used throughout this thesis. It is hoped that the new spectrometer will allow studies to be made of species which are too low in concentration to be observed with a single detector spectrometer. An example of its use may be found in chapter 6 of this thesis where spectra of vanadium recorded by single and multi detector spectrometers are compared.

REFERENCES

1. J.H.D. Eland, 'Photoelectron Spectroscopy', Butterworths (1974).

2. J.W. Rabalais, 'Principles of Ultraviolet Photoelectron Spectroscopy', Wiley-Interscience (1977).

3. J.A.R. Samson, Rev. Sci. Inst., 40, 1174 (1969).

4. E.M. Purcell, Phys. Rev., 54, 818 (1938).

5. P.R. Woodruff, L. Torop and J.B. West, J. El. Spec. Rel. Phen., 12, 133 (1977).

6. J.L. Gardner and J.A.R. Samson, J. El. Spec. Rel. Phen., 8, 469 (1976).

7. A. Fackerell, B.Sc. (Hons.) 3rd Year Project, University of Southampton (1978).

8. D.W. Turner, C. Baker, A.D. Baker and C.R. Brundle, 'Molecular Photoelectron Spectroscopy', Wiley-Interscience (1970).

9. J.M. Dyke, N. Jonathan and A. Morris, "Electron Spectroscopy, Theory Techniques and Applications", Vol. 3, 189 (1979, Academic Press).

10. J.M. Dyke, N. Jonathan and A. Morris, Int. Rev. Phys. Chem., 2, 3 (1982).

11. J. Berkowitz, J. Chem. Phys., 56, 2766 (1972).

12. A.W. Potts, T.A. Williams and W.C. Price, Proc. R. Soc. Lond., A341, 147 (1974).

13. J. Berkowitz, C.H. Batson and G.L. Goodman, J. Chem. Phys., 71, 2624 (1979).

14. J. Berkowitz et al, J. Chem. Phys., 80, 3962 (1984).

15. J. Berkowitz et al, Ann. Isr. Phys. Soc., 6, 170 (1984).

16. J. Berkowitz et al, Ann Isr. Phys. Soc., 6, 100 (1984).

17. J. Berkowitz, C.H. Batson, G.L. Goodman; ACS. Symp. Ser., 179, 275 (1982).

18. J. Berkowitz et al, Ann Isr. Phys. Soc., 6, 167 (1984).

19. J. Berkowitz et al, Ann Isr. Phys. Soc., 6, 173 (1984).

20. E.P.F. Lee, D. Law and A.W. Potts, J.C.S. Faraday II, 76, 1314 (1980).

21. (a) I. Novak and A.W. Potts, J. Chem. Soc. Dalton Trans., 1983, 2211.

(b) I. Novak and A.W. Potts, J.El. Spec. Rel. Phen., 33, 1 (1984).

22. E.P.F. Lee, A.W. Potts and J.E. Bloor, Proc. R. Soc. Lond., A381, 373 (1982).

23. I. Novak and A.W. Potts, J. Chem. Soc. Dalton Trans., 1983, 635.

24. A.W. Potts and I. Novak, J. El. Spec. Rel. Phen., 28, 267 (1983).

25. B. Solouki, H. Bock, R. Appel, A. Westerhaus, G. Becker and G. Uhl, Chem. Ber., 115, 3747 (1982).

26. S. Elbel, H.T. Dieck, H. Walther and J. Krizek, Inorg. Chim. Acta, 53, L101 (1981).

27. G.K. Schweitzer, W.E. Bull and F.A. Grimm; Tech. Dept. U.S. Air Force Materials Laboratory (1973).

28. J.D. Allen, G.W. Boggess, T.D. Goodman, A.S. Wachtel and G.K. Schweitzer, J. El. Spec. Rel Phen., 2, 289 (1973).

29. D.G. Streets and J. Berkowitz, J. El. Spec. Rel. Phen., 9, 269 (1976).

30. D. Bulgin, J.M. Dyke, F. Goodfellow, N. Jonathan, E. Lee and A. Morris, J. El. Spec. Rel. Phen., 12, 67 (1977).

31. E. May, 'Industrial High Frequency Electric Power'. Chapman and Hall Ltd., (1949).

32. F.W. Curtis, 'High Frequency Induction Heating'. McGraw-Hill (1950).

33. C.A. Adams, J.C. Hodge and M.H. Mackusick, Elec. Eng., 53, 194 (1934).

34. I.E. Campbell and E.M. Sherwood (Ed.), 'High Temperature Materials and Technology'. John Wiley and Sons Inc. (1967).

35. C.J. Smithells, "Materials Reference Book", Vols. 1 and 2, 3rd Edn, International London and Sheffield Publ. Co. (1976).

36. P.D. Johnson, J. Am. Ceram. Soc., 33, 168 (1950).

37. G. Economos and W.D. Kingery, J. Am. Ceram. Soc., 36, 403 (1953).

38. A. Morris, N. Jonathan, J.M. Dyke, P.D. Francis, N. Keddar and J.D. Mills, Rev. Sci. Instrum., 55, 172 (1984).

CHAPTER THREE

THEORETICAL METHODS

3.1. Introduction

Photoelectron spectroscopy (p.e.s.) involves the measurement of the kinetic energies of electrons ejected from an atom or molecule by photons of energy $h\nu$. The basic photoionisation process can be summarised by the following equation:

$$M + h\nu \rightarrow M^+ + e \qquad (3.1)$$

where M is the atom or molecule under investigation. Ionisations to several ionic states may be observed and, generally, some form of theoretical calculation is needed in order that these ionisations can be assigned.

The most readily calculated quantity is the vertical ionisation potential and methods of calculating this will be the subject of most of this Chapter. Examples of the use of these methods will be found in the following experimental Chapters. In addition, for diatomic molecules neutral and ionic vibrational frequencies, equilibrium bond lengths and photoelectron band envelopes may be calculated. These quantities will be discussed in the Chapters describing work on VO, CrO and AlF.

3.2. Selection rules in p.e.s.

The probability of photoionisation occuring from a molecular ground state characterised by the wavefunction, Ψ'', to a final state (consisting of the ion and photoelectron) characterised by the wavefunction, Ψ', is proportional to the square of the modulus of the transition moment integral, M, where M is given by (1):

$$M = \Psi'^* \sum_{i,j} \underline{P}\, \Psi'' \, d\tau \qquad (3.2)$$

In the above equation, $\underline{P}$ is the electric dipole operator and the summation extends over all electrons, i, and nuclei, j. In the molecular case (j>1), use can be made of the Born-Oppenheimer approximation (2) which states that electrons can be considered as moving within a field of fixed nuclei, thus allowing the dipole operator to be split up into electronic $\underline{P_e}$, and nuclear, $\underline{P_n}$, parts. i.e.

$$\sum_{ij} \underline{P} = \sum_{i} \underline{P_e} + \sum_{j} \underline{P_n} \qquad (3.3)$$

The wavefunctions Ψ' and Ψ'' can be similarly separated into a product of electronic Ψ_e (r, R) and nuclear functions. Rotational motion can be neglected since the motion of the molecule can be referred to a rotating, molecule fixed-axis system. This allows the nuclear wavefunction to be considered solely as the vibrational wavefunction Ψ_v (R). Here, r and R are the electronic and nuclear coordinates respectively. It should also be noted that Ψ_e is generally only a weak function of R. The orthogonality of electronic wavefunctions of different electronic states allows the transition moment integral to be written as (3):

$$M = \int \Psi_v'^{*}(R)\ \Psi_v''(R)dR \int \Psi_e'^{*}(r,R) \sum_{i} \underline{P_e}\ \Psi_e''\ (r,R)dr \qquad (3.4)$$

The first integral of equation 3.4 leads to the derivation of vibrational selection rules while the second will yield the corresponding electronic selection rules.

(a) Vibrational Selection Rules (3,4)

The probability of a vibrational transition between two electronic states is proportional to the square of the first integral of equation 3.4 i.e.

$$I_{v' \leftarrow v''} \alpha \left| \int \Psi_v'^{*}(R)\ \Psi_v''(R)dR \right|^2 \qquad (3.5)$$

Equation (3.5) is known as the Franck-Condon factor and will be discussed further at the end of this chapter. v' is the vibrational quantum number in the ionic state while v'' is the corresponding vibrational quantum number in the neutral state.

For a vibrational transition to take place, the Franck-Condon factor must be non-zero which implies that the product $\Psi_v'^{*}\ \Psi_v''$ must be totally symmetric. This statement leads to the following four vibrational selection rules:

(i) Totally symmetric vibrations may assume any quantum number in the ionic state.

(ii) Assuming transitions take place from the totally symmetric v''=0 level in the molecule, non-totally symmetric vibrations only assume zero or even quantum numbers in the ion whose wavefunctions are then totally symmetric.

(iii) For a combination band (i.e. simultaneous excitation of two or more non-totally symmetric vibrations), the transition is allowed if the total wavefunction is symmetric.

(iv) If ionisation causes a change in equilibrium geometry between molecule and ion, the preceding rules still apply but only in respect of symmetry elements which are common to both states.

Examples of the experimental observation of vibrational structure will be discussed in chapters 6 and 7.

(b) Electronic Selection Rules

For a photoelectron transition to be allowed, the second integral of equation 3.4 must be non-zero,

$$\text{i.e. } \int \Psi_e'^*(r,R) \sum_i \underline{P_e}\, \Psi_e''(r,R)\,dr \neq 0$$

If spin-orbit interactions are assumed to be small, the wavefunctions Ψ_e' and Ψ_e'' can be considered to be made up of products of orbital and spin functions. Since the dipole operator does not affect spin functions, an integral of the form $\langle \Psi_S'' | \Psi_S' \rangle$, where Ψ_S is the spin wavefunction, can be factorised out (3) from equation (3.4). Spin functions corresponding to different spin values are orthogonal so that for an allowed transition there can be no change in total spin between initial and final states. Since the free electron can have spin $\pm \frac{1}{2}$ it follows that the final ionic state must differ in spin from the neutral state by $\pm \frac{1}{2}$ (in units of $\bar{h}$). This is the first electronic selection rule.

Now consider the example of the spin allowed ionisation of a closed shell singlet molecular state to a doublet ionic state as follows:

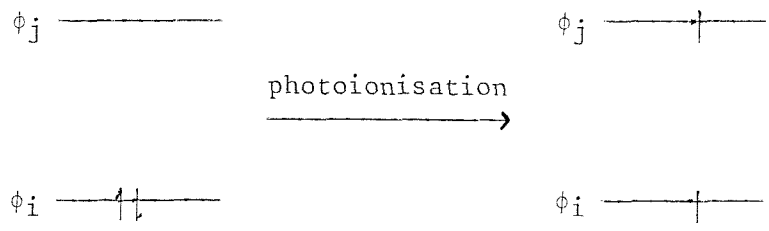

ϕ_i is a molecular orbital and ϕ_j is the wavefunction for the free electron. The wavefunction for the initial singlet state and the final singlet/triplet state are given in equations 3.6 and 3.7 respectively.

$$\Psi_e'' = |i\ \bar{i}| \tag{3.6}$$

$$\Psi_e' = \frac{1}{\sqrt{2}} \{|i\ \bar{j}| \pm |\bar{i}\ j|\} \tag{3.7}$$

The determinants used, known as Slater determinants are defined in the next section. Using the singlet ionic state (lower '-' sign in (3.7)), the second integral of equation (3.4) can be re-expressed as:

$$M_e = \int \frac{1}{\sqrt{2}} \{|i\ \bar{j}| - |\bar{i}\ j|\}^* \sum \underline{P_e}\ |i\ \bar{i}|\ dr \tag{3.8}$$

Expanding the determinants in terms of space and spin parts gives:

$$M_e = \frac{1}{2\sqrt{2}} \int [\phi_i^*(1)\ \bar{\phi}_j^*(2) - \phi_i^*(2)\ \bar{\phi}_j^*(1) - \bar{\phi}_i^*(1)\ \phi_j^*(2) + \bar{\phi}_i^*(2)\ \phi_j^*(1)]$$

$$\times\ (\underline{P_e}(1) + \underline{P_e}(2))[\phi_i(1)\ \bar{\phi}_i(2) - \phi_i(2)\ \bar{\phi}_i(1)]\ dr(1)\ dr(2) \tag{3.9}$$

Assuming the spatial orbitals are orthonormal and integrating over spin, equation 3.9 reduces to

$$M_e = \sqrt{2} \int \phi_j^*(1)\ \underline{P_e}(1)\ \phi_i(1)\ dr(1)$$

$$= \sqrt{2} \int \phi_j^*(2)\ \underline{P_e}(2)\ \phi_i(2)\ dr(2) \tag{3.10}$$

If the triplet ionic state (upper '+' sign in (3.7)) is used, M_e will be equal to zero and this implies that there can be no change in the overall electron spin of the system between initial and final states. i.e. $\Delta S = 0$. Therefore ΔS between the neutral molecule and ion must be $\pm\frac{1}{2}\hbar$.

On further consideration of equation 3.8, it is apparent that if Ψ_e' had differed from the ground state molecular wavefunction Ψ_e'' by more than one orbital, M_e would be zero. This leads to the selection rule that only one electron ionisations are allowed in pes. The derivation of this rule makes use of the orthonormality of the spatial orbitals which assumes that the orbitals are unchanged on ionisation. Allowance for this reorganisation and for electron correlation, may cause this rule to break down. These arguments can be extended so that they apply to all closed and open-shell systems.

For an allowed transition, the integral of equation 3.10 must be non-zero. This will be true if the product of the irreducible representations, Γ, of the species in equation 3.10, $\Gamma(\Phi_i) \times \Gamma(\underline{P_e}) \times \Gamma(\Phi_j)$ is totally symmetric with respect to all symmetry elements of the molecular point group. For at least one component of $\underline{P_e}$, the product $\Gamma(\Phi_i) \times \Gamma(\Phi_j)$ must contain the same symmetry species as one of the components of $\Gamma(\underline{P_e})$. Since $\underline{P_e} = e\underline{r_i}$, where $\underline{r_i}$ is the position vector of the ith electron, $\underline{P_e}$ transforms in the molecular point group as the cartesian vectors x, y and z. If the equilibrium geometries of the molecule and ion have different symmetries, then only symmetry elements common to both point groups are considered.

The selection rule governing changes in orbital angular momentum between the initial and final state applicable to optical spectroscopy is still valid in pes. In pes, the final state is the ion plus the free electron implying that the free electron may leave carrying the angular momentum necessary to satisfy this rule.

3.3. Hartree-Fock-Roothaan formalism for closed shell molecules (5,6)

The Hartree-Fock-Roothaan formalism allows a solution to the time-independent Schrodinger equation to be found. It proceeds by making an approximation to the molecular wavefunction, Φ, subject to the constraint that it should be composed of one electron functions and satisfy the Pauli Principle. The total energy, E, of the system also has to be minimised. The approximation must be made because, as is well known, the Schrodinger equation can only be solved exactly for the hydrogen atom.

In the derivation of the Hartree-Fock-Roothaan Method, the first step involves the Born-Oppenheimer approximation (2). Use of this approximation means that the total wavefunction, Ψ_{tot}, and the total energy, E_{tot}, can be split up into electronic (e) and nuclear (n) parts as follows:

$$\Psi_{tot} = \Psi_e \cdot \Psi_n \tag{3.11}$$

$$E_{tot} = E_e + E_n \tag{3.12}$$

The approximation is now used to solve the fixed nucleus time-independent Schrodinger equation:

$$H_e \Psi_e = E_e \Psi_e \tag{3.13}$$

The 'e' subscripts may be dropped for reasons of simplicity and convenience. The Hamiltonian operator $H(\equiv H_e)$ for the n-electron system has the form

$$H(1,2,\ldots n) = \sum_{\xi} H_N(\xi) + \sum_{\xi<\eta} (1/r_{\xi\eta}) \tag{3.14}$$

where the indices ξ and η run over all n electrons. The $r_{\xi\eta}$ parameter is the interelectronic distance which means that the $1/r_{\xi\eta}$ terms represent electron-electron interactions. To simplify matters, atomic units are used (i.e. electron mass, electron charge = 1) and any nuclear-nuclear interaction terms have been omitted. These can, if necessary, be added to the total energy of the molecule at the end of the calculation. The one electron operators $H_N(\xi)$ are the Hamiltonian operators for the electrons ξ moving in the field of the bare nuclei and consist of a kinetic energy term and an electron-nuclear attraction term:

$$H_N(\xi) = -\tfrac{1}{2}\nabla_\xi^2 - \sum_{\alpha} \frac{Z_\alpha}{r_{\xi\alpha}} \tag{3.15}$$

In equation 3.15, Z_α is the charge on nucleus α and $r_{\xi\alpha}$ is the electron-nuclear separation.

It is well known that the Schrodinger equation (3.13) cannot be solved exactly. Hence an approximate molecular wavefunction, Φ, must be found subject to the constraints that it is composed of one-electron

functions, satisfies the Pauli Principle and minimises the total energy, E_{tot}, of the system. To satisfy the Pauli Principle it is necessary that Φ is antisymmetric with respect to interchange of two electrons. For a system with n electrons, this can be achieved by writing the total wavefunction in the form of a determinant, known as a Slater determinant:

$$\Phi = \frac{1}{\sqrt{n!}} \begin{vmatrix} \lambda_1(1) & \lambda_2(1) & \cdots & \lambda_n(1) \\ \lambda_1(2) & & & \\ \vdots & & & \\ \lambda_1(n) & \cdots & & \lambda_n(n) \end{vmatrix} \qquad (3.16)$$

where the one electron functions $\lambda_i(\xi)$ are known as molecular spin orbitals (MSO's) and i defines the different orbitals and ξ identifies the different electrons. $1/\sqrt{n!}$ is a normalisation constant. This is the simplest case of a determinantal wave function and it should be apparent that Φ will satisfy the Pauli Principle since the interchange of two rows or columns of a determinant causes it to change to -1 times itself. More generally, Φ can be written as a linear combination of Slater determinants which will also satisfy the Pauli Principle.

The MSO's from equation 3.16 are assumed to be orthonormal

$$\text{i.e.} \int \lambda_i^* \lambda_j \, d\tau = \delta_{ij} \qquad (3.17)$$

where $d\tau$ denotes integration over all space and spin coordinates. The MSO's can be expressed as products of spin and space functions,

$$\text{e.g.} \quad \lambda_1 = \phi_1\alpha, \; \lambda_2 = \phi_2\beta$$

The spin functions α or β are clearly orthonormal while the space function can be assumed to be orthonormal. These two conditions will satisfy equation 3.17.

Using a different notation, the determinant of equation 3.16 can be expressed as:

$$\Phi = |\phi_1 \bar{\phi}_1 \phi_2 \bar{\phi}_2 \text{ ------ } \phi_m \bar{\phi}_m \phi_n \bar{\phi}_n|$$

For a closed shell system, v = n/2 where n= the number of electrons. If it is assumed that $\lambda_1 = \phi_1$, $\lambda_2 = \bar{\phi}_1$, $\lambda_3 = \phi_2$ ------ $\lambda_{n-1} = \phi_v$ and $\lambda_n = \bar{\phi}_v$, where the bar ('-') denotes β spin and no bar denotes α spin, the expression for Φ becomes,

$$\Phi = |\phi_1 \bar{\phi}_1 \phi_2 \bar{\phi}_2 \text{ ..... } \phi_v \bar{\phi}_v| \qquad (3.18)$$

Having done this, an expression for the expectation value of the electronic energy can be derived. Equation 3.13 is multiplied on the left by Ψ* and integrated over all space to give

$$\int \Psi^* H_e \Psi d\tau = E_e \int \Psi^* \Psi d\tau$$

which yields an expression for E_e.

$$E_e = \frac{\int \Psi^* H_e \Psi d\tau}{\int \Psi^* \Psi d\tau} \quad .$$

If Ψ is replaced by Φ, the following expression can be obtained (note that the 'e' subscripts have been dropped for simplicity),

$$E = \frac{\int \Phi^* H \Phi d\tau}{\int \Phi^* \Phi d\tau} \qquad (3.19)$$

The denominator is equal to 1 since Φ will be normalised from the orthonormalisation conditions on the MSO's . The variation theorem (1) requires that the expression for E in equation 3.19 should be minimised with respect to Φ. An expression for E of the form HΦ/Φ cannot be used since it has no associated minimum property (7).

An expression for the energy E can now be derived by substituting expressions for the wavefunction, Φ, and the operator, H, into equation 3.19. The wavefunction Φ is given by the determinant in equation 3.16

but can be re-expressed as:

$$\Phi = \frac{1}{\sqrt{n!}} \sum_{P} (-1)^{P} P(\lambda_1(1)\ \lambda_2(2), \ldots . \lambda_n(n)). \qquad (3.20)$$

The summation is over all n! distinct permutations, P, and the value of $(-1)^P$ is +1 or -1 if the permutation involves an even or odd number of pairwise permutations respectively. Substituting equations 3.14 and 3.20 into equation 3.19 will give two types of integrals, one involving the one electron operators, $H_N(\xi)$ and the other involving the two electron operators $1/r_{\xi\eta}$. The one electron integrals have the form:

$$I_{IJ} = \frac{1}{n!} \int \sum_{P} (-1)^{P} P(\lambda_1(1) \ldots . \lambda_n(n))^* \sum_{\xi} H_N(\xi)\ x$$

$$\sum_{Q} (-1)^{Q} Q(\lambda_1(1) \ldots . \lambda_n(n)) d\tau(1)\ d\tau(2) \ldots . d\tau(n) \qquad (3.21)$$

By considering a given permutation, P, and then considering the effect of each of the one electron operators, $H_N(\xi)$, on each of the permutations, Q, it can be seen that the integral of equation 3.21 is non-vanishing only when the permutation, Q, is equal to the specific permutation, P, under consideration. When summed over all n! permutations, equation 3.21 is reduced to a sum of one electron integrals, $\Sigma I_i'$, where the ''' superscript denotes integration over space and spin. The two electron integrals may be similarly reduced to a sum of coulomb and exchange integrals, J_{ij}' and K_{ij}'. This leads directly to an expression for E as follows:

$$E = \sum_{i} I_i' + \sum_{i<j} (J_{ij}' - k_{ij}') \qquad (3.22)$$

This is a general result where:

$$I_i' = \int \lambda_i^*(1)\ H_N(1)\ \lambda_i(1)\ d\tau(1) \qquad (3.23)$$

$$J_{ij}' = \iint \lambda_i^*(1)\ \lambda_j^*(2)\ \frac{1}{r_{12}}\ \lambda_i(1)\ \lambda_j(2)\ d\tau(1) d\tau(2) \qquad (3.24)$$

$$K_{ij}' = \iint \lambda_i^*(1)\ \lambda_j^*(2)\ \frac{1}{r_{12}}\ \lambda_j(1)\ \lambda_i(2)\ d\tau(1) d\tau(2) \qquad (3.25)$$

For a closed shell system, these integrals may be reduced further to involve space coordinates only. It is assumed that no spin-orbit coupling occurs allowing the space and spin variables to be separated. The spin parts of the MSO's in I_i', J_{ij}' and K_{ij}' are integrated out and the summation variable redefined to run over all $\mathbf{V}$(=n/2) occupied space orbitals. Use of the identity

$$J_{ii} = K_{ii} \tag{3.26}$$

yields new expressions

$$I_i = \int \phi_i^*(1)\ H_N(1)\ \phi_i(1)\ dv(1) \tag{3.27}$$

$$J_{ij} = \iint \phi_i^*(1)\ \phi_j^*(2)\ \frac{1}{r_{12}}\ \phi_i(1)\ \phi_j(2)\ dv(1)\ dv(2) \tag{3.28}$$

$$K_{ij} = \iint \phi_i^*(1)\ \phi_j^*(2)\ \frac{1}{r_{12}}\ \phi_j(1)\ \phi_i(2)\ dv(1)\ dv(2) \tag{3.29}$$

The expression for E for a closed shell system becomes

$$E = 2 \sum_{i}^{n} I_i + \sum_{ij}^{n} (2J_{ij} - K_{ij}) \tag{3.30}$$

Equation 3.30 is the most useful and widely used form of the energy expression for a closed shell determinantal function. It can be written in a different way as:

$$E = \sum_{i} (I_i + \varepsilon_i)$$

where $\varepsilon_i = I_i + \sum_{j} (2J_{ij} - K_{ij})$

A physical interpretation will be given later in the discussion of Koopmans' theorem (ε_i is, in fact, the Hartree-Fock orbital energy).

The energy terms I_i, J_{ij} and K_{ij} can be interpreted qualitatively. I_i is the energy of an electron in orbital i moving in the field of the bare nuclei. J_{ij}, known as the coulomb integral, is simply the electronic interaction between electrons in orbitals i and j. Classically

it can be interpreted as the coulomb interaction between two charged particles (electrons). The exchange integrals, K_{ij}, though having no classical analogue, can be interpreted as interactions between pairs of electrons having parallel spins.

Having obtained equation 3.30, the variation Theorem (7) may now be used to determine an approximate total determinantal wavefunction, Φ. The next step in the process is to define coulomb and exchange operators, J_i and K_i as follows:

$$J_{ij} = \int \phi_i^*(1)\ J_j(1)\ \phi_i(1)\ dv(1) \equiv \int \phi_j^*(2)\ J_i(2)\ \phi_j(2)\ dv(2) \quad (3.31)$$

$$K_{ij} = \int \phi_i^*(1)\ K_j(1)\ \phi_i(1)\ dv(1) \equiv \int \phi_j^*(2)\ K_i(2)\ \phi_j(2)\ dv(2) \quad (3.32)$$

Equation 3.30 can now be written in the form:-

$$E = 2 \sum_i \int \phi_i^*\ H_N\ \phi_i\ dv + \sum_{ij} \int \phi_i^*\ (2J_j - K_j)\ \phi_i\ dv \quad (3.33)$$

According to the Variation Theorem, the total energy, E, must now be minimised subject to the constraint

$$S_{ij} = \int \phi_i^*\ \phi_j\ dv = \delta_{ij} \quad (3.34)$$

The method of undetermined multipliers, due to Lagrange, is applied to equations 3.34 in which each equation is multiplied by the Lagrange multiplier, $-2\varepsilon_{ij}$, and added to the total energy to give:

$$E' = E - 2 \sum_{ij} \varepsilon_{ij}\ S_{ij} \quad (3.35)$$

E' must now be minimised for constant ε_{ij}'s

$$\text{i.e.}\quad \delta E' = \delta E - 2 \sum_{ij} \varepsilon_{ij} \delta S_{ij} = 0 \quad (3.36)$$

where the δ's represent changes induced by small variations in the molecular space-orbitals, $\delta\phi_i$. The variation in S_{ij} is then:

$$\delta S_{ij} = \sum \delta\phi_i^* \, \phi_j \, dv + \sum \phi_i^* \, \delta\phi_j \, dv \tag{3.37}$$

From equation 3.33, δE can be written as:

$$\delta E = 2\sum_i \int \delta\phi_i^* \, H_N \, \phi_i \, dv + 2\sum_i \int \phi_i^* \, H_N \, \delta\phi_i \, dv$$
$$+\sum_{ij} \left[\int \delta\phi_i^* \, (2J_j - K_j)\phi_i \, dv + \int \delta\phi_j^* \, (2J_i - K_i) \, \phi_j \, dv \right]$$
$$+\sum_{ij} \left[\int \phi_i^* \, (2J_j - K_j)\delta\phi_i \, dv + \int \phi_j^* \, (2J_i - K_i)\delta\phi_j \, dv \right] \tag{3.38}$$

The indices i and j run over the same ranges. It should be noted that, since the operators H_N, J_i and K_i are hermitian*, the expression for δE reduces to:

$$\delta E = 2\sum_i \int \delta\phi_i^* \, [H_N + \sum_j 2J_j - K_j]\phi_i \, dv$$
$$+ 2\sum_i \int \delta\phi_i \, [H_N^+ + \sum_j 2J_j^+ - K_j^+]\phi_i^* \, dv \tag{3.39}$$

The results of equations 3.37 and 3.39 can now be substituted into equation 3.36 to give:

$$\delta E' = 2\sum_i \int \delta\phi_i^* \, [\{H_N + \sum_j (2J_j - K_j)\}\phi_i - \sum_j \varepsilon_{ij}\phi_j] dv$$
$$+ 2\sum_i \int \delta\phi_i \, [\{H_N^+ + \sum_j (2J_j^+ - K_j^+)\}\phi_i^* - \sum_j \varepsilon_{ji}\phi_j^*] dv \tag{3.40}$$

The condition for minimisation of $\delta E'$ is that the coefficients associated with the $\{\delta\phi_i^*\}$ and $\{\delta\phi_i\}$ in the integrands of equation 3.40 should identically vanish

$$\text{i.e.} \quad [H_N + \sum_j (2J_j - K_j)]\phi_i = \sum_j \varepsilon_{ij} \, \phi_j \tag{3.41}$$

$$\text{and} \quad [H_N^+ + \sum_j (2J_j - K_j^+)]\phi_i^* = \sum_j \varepsilon_{ij} \, \phi_j^*$$

*A hermitian operator A is defined by $\int f_i^* A f_j \, dv = \int f_j A^+ f_i^*, \, dv$, where the $^+$ denotes the hermitian conjugate of that operator, and f_i and f_j are arbitrary functions.

The set of most flexible molecular orbitals, ϕ_i, must satisfy these expressions. Taking the complex conjugate of equation 3.41 and comparing it with equation 3.40, it can easily be shown that the matrix elements ε_{ij}^* are equal to the ε_{ij}. The total electron interaction operator, G, and the Hartree-Fock Hamiltonion, F, are defined as follows:

$$G = \sum_j (2J_j - K_j) \tag{3.42}$$

$$\text{and } F = H_N + G \tag{3.43}$$

These definitions allow equation 3.41 to be written as:

$$F\,\phi_i = \sum_j \varepsilon_{ij}\,\phi_j \tag{3.44}$$

or, in matrix form

$$\underline{F}\,\underline{\phi} = \underline{\varepsilon}\,\underline{\phi} \tag{3.45}$$

where $\underline{F}$ and $\underline{\varepsilon}$ are $\underline{m}$ x $\underline{m}$ matrices (m = the number of mo's) and $\underline{\phi}$ is a column vector. There is no loss of generality if it is assumed at the outset that the most flexible set of mo's satisfy the equation below:

$$F\,\phi_i = \varepsilon_i\,\phi_i \tag{3.46}$$

i.e. the $\underline{\varepsilon}$ matrix is diagonal with elements ε_i (this amounts to subjecting the initial determinant to an arbitrary linear transformation without affecting its physical significance).

The set of equations 3.46 are known as the Hartree-Fock equations and state that, for a closed shell molecule, the mo's giving the "best" single determinantal wavefunction, ϕ, are all eigen functions of the same hermitian operator F which is, in turn, defined in terms of these mos. The operator, F, is dependent on the orbitals, ϕ_i, by virtue of the dependence of F on J_i and K_i. To solve the problem, a self-consistent field (SCF) method is used in which a trial set of ϕ_i

is assumed from which a trial F can be determined. Equation (3.46) can be solved to give a new set of ϕ_i and the process repeated until a convergence criterion placed on the ϕ_i or on the total energy is reached.

The most commonly used technique is the Linear Combination of Atomic Orbitals (LCAO) SCF method first introduced by Roothaan (5) in which the molecular space orbitals are approximated by:

$$\phi_i = \sum_q C_{iq} \chi_q \tag{3.47}$$

Here the χ_q are normalised atomic orbitals (AO's) and the C_{iq} are a set of coefficients. Substituting equation 3.47 into equation 3.46, multiply both sides by χ_p and integrate gives (8):

$$\sum_q C_{iq}(F_{pq} - S_{pq}\,\varepsilon_i) = 0 \tag{3.48}$$

where

$$F_{pq} = \langle \chi_p | F | \chi_q \rangle \tag{3.49}$$

$$S_{pq} = \langle \chi_p | \chi_q \rangle \tag{3.50}$$

A more rigorous approach uses a variational treatment similar to that used for the derivation of the Hartree-Fock equations, such that the total energy is minimised with respect to the LCAO coefficients. This yields the result (5),

$$\underline{F}\,\underline{C} = \underline{\varepsilon}\,\underline{S}\,\underline{C} \tag{3.51}$$

where $\underline{F}$ and $\underline{S}$ are matrices with elements F_{pq} and S_{pq} defined in equations 3.49 and 3.50, $\underline{\varepsilon}$ is the matrix of Lagrangian multipliers, ε_{ij}, and $\underline{C}$ is the matrix of coefficients. Since an arbitrary linear transformation of the initial determinant can be chosen which makes $\underline{\varepsilon}$ diagonal, the following holds for the ith mo:

$$\underline{F}\,\underline{C}_i = \varepsilon_i\,\underline{S}\,\underline{C}_i \tag{3.52}$$

where $\underline{C_i}$ is the column vector with m components $C_{i1}.....C_{im}$ and $\underline{S}$ and $\underline{F}$ are matrices of dimension $\underline{m}$ x $\underline{m}$.

The SCF process now involves estimating an initial set of coefficients C_{iq} and computing the trial F_{pq}. Equation 3.48 is then solved to determine the new C_{iq} which in turn allows another set of F_{pq} to be calculated. The process is applied repeatedly until convergence is reached i.e. the total energy becomes lower on each successive iteration and the energy difference between successive iterations is within a pre-set tolerance.

In theory, the most accurate wavefunction for the system would require an infinite number of AO's in the MO expansion or a sufficient number of AO's such that the total energy is at the "Hartree-Fock limit" i.e. further addition of any AO's does not lead to a further lowering of the total energy. Clearly this cannot always be achieved because of the computational problems involved. Hence in practice a compromise is achieved by using a truncated basis set which gives the most accurate results consistent with the available computer time.

Koopmans' Theorem

Koopmans' Theorem offers a method of predicting vertical ionisation potentials (VIPs) of closed shell molecules. It can be derived from the Hartree-Fock method as follows:

Consider the photoionisation of an electron in the i^{th} orbital of a closed shell molecule consisting of v doubly occupied MO's, $\phi_1.....\phi_v$, represented as:

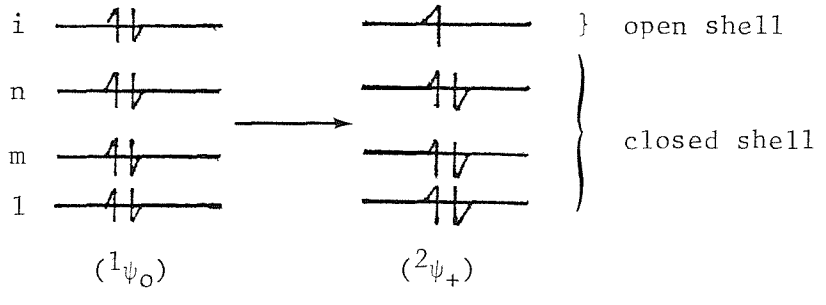

The initial molecular state is labelled $(^1\psi_o)$ and the final ionic state is labelled $(^2\psi_+)$. The total energy of the initial state, $E(^1\psi_o)$ is given directly by equation 3.30:

$$E(^1\psi_o) = 2\sum_{j}^{v} I_j + \sum_{jk}^{v} (2J_{jk} - K_{jk}) \tag{3.53}$$

The total energy of the ionic state will be made up of an expression similar to equation 3.30 consisting of the total energy of the (v-1) closed shells, the one electron integral for the single open shell and a term representing the total interaction energy of the open shell with the closed shell. Assuming no electronic reorganisation takes place on ionisation, this can be written:

$$E(^2\psi_+) = 2\sum_{j\neq i}^{v} I_j + \sum_{j,k\neq i} (2J_{jk} - K_{jk})$$

$$+ I_i + \sum_{j(\neq i)} (2J_{ij} - K_{ij}) \tag{3.54}$$

energy of closed shell

open-closed shell interaction energy

When the summations over the closed shells are redefined to include the open shell, i, the expression becomes:

$$E(^2\psi_+) = 2\sum_{j}^{v} I_j + \sum_{j,k}^{v} (2J_{jk} - K_{jk})$$

$$- I_i - \sum_{j} (2J_{ij} - K_{ij}) \tag{3.55}$$

The first two terms are simply the energy of the initial molecular state, $E(^1\psi_o)$. Hence the ionisation energy for the process $E(^2\psi_+) \leftarrow E(^1\psi_o)$ is given by:

$$E(^2\psi_+) - E(^1\psi_o) = - I_i - \sum_{j} (2J_{ij} - K_{ij}) \tag{3.56}$$

From equation 3.52 this expression reduces to:

$$E(^2\psi_+) - E(^1\psi_o) = - \varepsilon_i \tag{3.57}$$

The left hand side of this equation is the vertical ionisation potential, IP_i, which corresponds to ionisation of an electron in orbital i, such that:

$$IP_i = - \varepsilon_i \qquad (3.58)$$

ε_i is the negative of the orbital energy obtained from a molecular orbital calculation on the neutral molecule at the Hartree-Fock limit. This is the approximation proposed by Koopmans (9) and is known as Koopmans' Theorem. The theorem is applicable only to closed-shell molecules and any calculation should preferably be performed at the Hartree-Fock limit to minimise errors arising from truncation of the basis set.

Relaxation and Correlation Energy

Some important factors are ignored when deriving Koopmans' Theorem (equation 3.58). Firstly, in writing down the expression for the total energy of the ionic state, it was assumed that the orbitals, ϕ_i, remain unchanged on ionisation. In reality, when ionisation occurs the orbitals will reorganise to some extent, resulting in a lowering of the total energy of the ion. This is known as the reorganisation, or relaxation, effect. As a result, the Koopmans' Theorem ionisation energy needs a negative correction to take account of this. This correction is known as the Reorganisation Energy.

Secondly, the other major effect is that of neglect of Electron Correlation. This arises from the fact that, in the Hartree-Fock method (on which the derivation of Koopmans' theorem is based), electron-electron interaction is evaluated as an interaction of each electron with an averaged-out charge of all the other electrons. This error occurs in the evaluation of the coulomb terms in the Hartree-Fock Hamiltonian. The exchange terms are evaluated correctly and considered as the instantaneous interaction between electrons having parallel terms. These terms only account for some of the error which is known as the Correlation energy. Hence, an error in the total energy calculated by the Hartree-Fock method is introduced such that the total energy will be more positive than the true experimental energy by an amount equal to the correlation energy.

Allowance for reorganisation and correlation errors in Koopmans' theorem can be written as follows:

$$IP_i = IP_i^o - R + C \qquad (3.59)$$

(where in (3.59) R and C are usually +ve quantities).

As mentioned above, allowance for orbital relaxation in the ion requires a negative correction, -R, to the Koopmans' Theorem i.p. Electron correlation will lower the Hartree-Fock total energy of both the molecule and the ion but this usually introduces a positive contribution, +C, since the correlation energy in a n-electron molecule will usually be greater than in the corresponding (n-1) electron ion (10). It is obvious from equation 3.59 that if R and C are approximately equal, the IP_i^o will be good estimates for IP_i. This does sometimes happen though such a balance is fortuitous and it is usually found, for calculations performed at the Hartree-Fock limit, that the Koopmans' Theorem value is too high implying that R>C. In some cases, Koopmans' Theorem fails to predict the correct ordering of states in the ion (11,12) and such discrepancies are only remedied on subsequent accurate calculation of the correlation energy in both the molecule and the ionic states.

The ΔSCF Method

In this method separate SCF calculations are performed on both the molecule and the ion at the equilibrium geometry of the neutral molecule. The difference in the total energies of the molecule and ion in a particular state will be an estimate of the vertical ionisation potential for that ionisation (definitions of both vertical and adiabatic ionisation potentials may be found in section 3.4 of this thesis). The fact that a separate calculation has been performed on both molecule and ion means that the effects of orbital relaxation will have been included. Unfortunately, since non-allowance for correlation energy is a defect in the Hartree-Fock SCF method, the ΔSCF method itself will also suffer from the same deficiency. As a result, vertical

ionisation potentials predicted by the ΔSCF method are frequently too low when compared with experimental vertical ionisation potentials. Since the corresponding Koopmans' theorem vertical ionisation potentials are often too high it is fairly common to find that the true experimental vertical ionisation potential lies somewhere between the calculated ΔSCF and Koopmans' Theorem values. Methods of estimating the correlation energy correction required in a ΔSCF calculation will be described later in this Chapter and include the Multi-Configuration SCF (MCSCF) method and the method of Configuration Interaction (CI).

Open Shell Theory and the ATMOL Method

Koopmans' Theorem is only useful for closed-shell molecules and sometimes predicts an incorrect ordering of ionic states. To circumvent this problem an SCF calculation needs to be performed for the neutral molecule and for each ionic state. It is obvious that, if the neutral molecule is a closed shell species, then the ion must be an open shell species. Thus closed-shell theory must be extended in some way to take account of this. Also it is very desirable to have a method of studying molecules where the neutral molecule itself is an open shell species (this thesis describes studies of several open shell molecules).

Several SCF studies on open shell systems have been performed (13-16) with the general starting point being the method of Roothaan (5).

Roothaans open shell method (6) is an extension of the closed shell theory (5). It involves no further approximations, and can be applied to systems with more than one unpaired electron.

In the Roothaan Formalism (6) an energy expression of the following type is derived:

$$E = 2\sum_{k} I_k + \sum_{kl} (2J_{kl} - K_{kl}) + f[2\sum_{m} I_m + f\sum_{mn} (2aJ_{mn} - bK_{mn}) + 2\sum_{km} (2J_{km} - K_{km})] \qquad (3.60)$$

where a, b and f are numerical constants depending on the specific case

under study. The first two summations are familiar as those over the closed shells (given in equation 3.30), the second two are over the open shells and the last is over all open-closed shell interactions. Application of the Variation Theorem to this expression yields two sets of Hartree-Fock type SCF equations, which involve two different Hartree-Fock operators, one for the closed and one for the open shells. Unfilled, or virtual, molecular orbitals are undefined in this double Hamiltonian method, but can be included by combining these two equations in such a way as to give one resultant operator which operates on all of the molecular orbitals. This method is known as the combined Hamiltonian method (6).

The Roothaan combined Hamiltonian method (6) has a number of deficiencies. For example, it only gives correct wavefunctions for configurations of maximum multiplicity and it cannot cope with cases where the open shells have different fractional occupation. These problems can, however, be overcome by using a more general energy expression due to Huzinaga (13). The most serious problem associated with the Roothaan method is that of achieving convergence in the SCF process. Such problems can even occur for closed shell calculations (17) and this is the result of an initial poor choice of trial wavefunction. Divergence or oscillation may occur in the SCF process, particularly when a highly excited state or a state with a near degenerate neighbour of the same symmetry is being considered.

Roothaan (6) demonstrated that, by going from a double-Hamiltonian method to a single Hamiltonian method, the number of Hamiltonians required to correctly solve the open-shell problems was not unique. Later, a method involving three basic Hamiltonians, one for the closed shell, one for the open shell and one for the virtual shell was developed by McWeeny and coworkers (18,19). This was unfortunately limited in its application because of difficulties encountered in obtaining convergence. This led to the development of the ATMOL method (17, 20-23) which has proved to be very successful in performing molecular orbital calculations on both open and closed shell molecules and ions. The ATMOL method is very flexible and allows SCF calculations to be performed on closed shell and open shell molecules (up to ten open

shells can be handled). For simplicity, the method used for an SCF calculation on a molecule with just one unpaired orbital will be described here, though this can easily be extended to cover molecules with a number of open shells. The purpose of the ATMOL method for systems with one unpaired electron is to make stationary the energy of a single determinantal wavefunction (for a given choice of basis set) constructed from M1 orthonormal doubly occupied molecular orbitals (DOMOs) and M2 orthonormal singly occupied molecular orbitals (SOMOs), the latter being of common spin factor. From M linearly independent basis functions, M3 virtual molecular orbitals (VMOs) can be constructed (M=M1+M2+M3), such that all the MO's form an orthonormal set. Let ψ_1, ψ_2, ψ_3 and ϕ denote row vectors of the DOMOs, SOMOs, VMOs and basis functions respectively, then:

$$(\psi_1 : \psi_2 : \psi_3) = \phi(Q_1 : Q_2 : Q_3) = \phi Q \tag{3.61}$$

where each column of Q contains the basis function coefficients of a given molecular orbital. The following density matrices may now be defined:

$$R_1 = Q_1 Q_1^T \tag{3.62}$$

$$R_2 = Q_2 Q_2^T \tag{3.63}$$

where T denotes a transposed matrix. The electronic energy expression for the "half closed" shell case considered here is given by:

$$E = 2trR_1F + trR_2F + 2trR_1J[R_1] - trR_1K[R_1] + \tfrac{1}{2}trR_2J[R_2]$$
$$- \tfrac{1}{2}trR_2K[R_2] + 2trR_2J[R_1] - trR_2K[R_1] \tag{3.64}$$

where F is the matrix representation of the one electron Hamiltonian and J[R] and K[R] denote the coulomb and exchange matrices respectively for a given density matrix R. i.e.

$$J_{pq} = \sum_{rs} R_{rs}(pq/rs) \tag{3.65}$$

$$K_{pq} = \sum_{rs} R_{rs}(pr/qs) \tag{3.66}$$

$$\text{and } (pq/rs) = \iint \phi_p^*(1)\phi_s^*(2) \frac{1}{r_{12}} \phi_q(1)\phi_r(2)d\tau(1)d\tau(2) \tag{3.67}$$

Note that equation 3.64 is exactly analogous to equation 3.60 with $f = \frac{1}{2}$, $a = 1$ and $b = 2$ (21).

The following matrices may now be defined:-

$$R = 2R_1 + R_2 \tag{3.68}$$

$$P = \tfrac{1}{2}R_2 \tag{3.69}$$

$$G = J[R] - \tfrac{1}{2}K[R] \tag{3.70}$$

$$Z = K[P] \tag{3.71}$$

It is now convenient to make the following definition of a Fock operator

$$H_n = F + G + C_nZ \tag{3.72}$$

where the values of C_n of interest are given in the following table:

n	C_n
1	0
2	-1
3	+1
4	+2
5	-2

The energy expression may now be written in a form convenient for computational purposes as:-

$$E = \tfrac{1}{2}trR(F + H1) - trPZ \tag{3.73}$$

In order to examine the conditions for a stationary energy, physically significant variations in the molecular orbitals can be considered as:

(a) mixing of DOMOs with VMOs

(b) mixing of SOMOs with VMOs

(c) mixing of DOMOs and SOMOs.

Small variations of these types, while preserving the orthonormality of the DOMOs to first order, may be written:-

$$(a)\quad \psi_1{}^1 = (\psi_1 : \psi_3) \begin{bmatrix} I_1 \\ \hline A \end{bmatrix} \tag{3.74}$$

$$(b)\quad \psi_2{}^1 = (\psi_2 : \psi_3) \begin{bmatrix} I_2 \\ \hline B \end{bmatrix} \tag{3.75}$$

$$(c)\quad (\psi_1 : \psi_2)^1 = (\psi_1 : \psi_2) \left[\begin{array}{c:c} I_1 & -C^T \\ \hdashline C & I_2 \end{array}\right] \tag{3.76}$$

where I_1 and I_2 are identity matrices of order M1 and M2 respectively and A, B and C are matrices of mixing coefficients of order M3 x M1, M3 x M2 and M2 x M1 respectively. Equations 3.74, 3.75 and3.76 can be combined to give:

$$(\psi_1 : \psi_2)^1 = (\psi_1 : \psi_2 : \psi_3) \left[\begin{array}{c:c} I_1 & -C^T \\ \hdashline C & I_2 \\ \hdashline A & B \end{array}\right] \tag{3.77}$$

It should be noted that the density matrices R_1 and R_2, and hence the energy, are invariant under unitary transformations which mix MOs within the same category (i.e. DOMO or SOMO). Thus a unique specification of the self-consistent DOMOs and SOMOs requires extra sets of $\frac{1}{2}$M1(M1 - 1) and $\frac{1}{2}$M2(M2 - 1) conditions respectively. These extra conditions may be supplied by requiring that:

$$Q_L^T Z Q_L = \Lambda \tag{3.78}$$

where Z is an arbitrary M x M hermitian matrix. Λ is a diagonal matrix and L denotes a particular category of molecular orbital. The perturbed molecular orbitals are orthonormal only to first order. The expansion of the energy, correct to first order in the elements of the matrices

A, B and C is given by (21, 23):

$$E = E_o + 4\sum_{k}^{M3}\sum_{i}^{M1} A_{ki}\, H1_{ki} + 2\sum_{k}^{M3}\sum_{j}^{M2} B_{kj}\, H2_{kj}$$
$$+ 2\sum_{i}^{M1}\sum_{j}^{M2} C_{ji}\, H3_{ji} \qquad (3.79)$$

where the summation variables i, j and k refer to DOMOs, SOMOs and VMOs respectively, and H_{npq} is the matrix element of the pth MO with the qth MO over the operator H_n. The conditions for a stationary state are satisfied when all the matrix elements $H1_{ki}$, $H2_{kj}$ and $H3_{ji}$ in equation 3.79 are zero. Thus:

$$\left(\frac{\partial E}{\partial A_{ki}}\right)_{A_{ki}=0} = 4H1_{ki} \qquad (3.80)$$

$$\left(\frac{\partial E}{\partial B_{kj}}\right)_{B_{kj}=0} = 2H2_{kj} \qquad (3.81)$$

$$\left(\frac{\partial E}{\partial C_{ji}}\right)_{C_{ji}=0} = 2H3_{ji} \qquad (3.82)$$

The first order analysis will be valid if the elements of A, B and C are small (i.e. the "higher terms" of equation 3.79 will be negligible). The general philosophy of the minimisation procedure is as follows: A suitable Fock operator is defined in the basis of the trial molecular orbitals (rather than in the atomic basis function representation) and this Fock operator is diagonalised. The resulting eigenvectors, after suitable ordering, define iterated molecular orbitals as linear combinations of the trial molecular orbitals.

If $Q^{(k)}$ denotes the eigenvector array defining trial molecular orbitals as a linear combination of basis functions for the k'th iterative cycle and $T^{(k)}$ denotes the eigenvectors resulting from the diagonalisation of the Fock operator in the trial molecular orbital basis, then iterated molecular orbitals are defined as linear combinations of the trial molecular orbitals. Then,

$$Q^{(k+1)} = Q(k)_T(k) \qquad (3.83)$$

where $Q^{(k+1)}$ is to be used as the input for the $(k+1)^{th}$ cycle. The general form of the Fock operator is:

$$\begin{bmatrix} (HD)_{dd} & \lambda_{ds}(H3)_{ds} & \lambda_{dv}(H1)_{dv} \\ \lambda_{ds}(H3)_{sd} & (HS)_{ss} + \alpha I_2 & \lambda_{sv}(H2)_{sv} \\ \lambda_{dv}(H1)_{vd} & \lambda_{sv}(H2)_{vs} & (HV)_{vv} + (\alpha + \beta)I_3 \end{bmatrix} \qquad (3.84)$$

where $(HD)_{dd}$, $(HS)_{ss}$ and $(HV)_{vv}$ each denote a block of one of the operators H1 to H3 in the basis of the DOMOs, SOMOs and VMOs respectively.

λ_{ds}, λ_{dv} and λ_{sv} are the DOMO-SOMO, DOMO-VMO and SOMO-VMO "damp factors" respectively and are often set to unity. These "damp factors" have the effect of preventing any wild oscillations between neighbouring states of the same symmetry. $(H3)_{ds}$ denotes a block of H3 connecting all DOMOs with all SOMOs. $(H3)_{sd}$ is the transpose of $(H3)_{ds}$ and $(H1)_{dv}$, $(H1)_{vd}$, $(H2)_{sv}$ and $(H2)_{vs}$ are defined in a similar way. Lastly, α and β denote the DOMO-SOMO and SOMO-VMO level shifters respectively. Level shifters have the effect of separating the DOMOs, SOMOs and VMOs thus ensuring that the stationary state obtained in the calculation is the one actually required. Also, any interactions between VMOs and DOMOs, which may affect the overall result, are avoided.

It can be seen that if the above Fock operator is diagonal, the conditions for a stationary energy will be satisfied (equations 3.79 to 3.82) so that the total wavefunction will be self-consistent. The use of first order perturbation theory to monitor the diagonalisation of the Fock operator (21) yields the results:

$$A_{ki} = \lambda_{dv}H1_{ki}/(HD_{ii} - HV_{kk} - \alpha - \beta) \qquad (3.85)$$

$$B_{kj} = \lambda_{sv}H2_{kj}/(HS_{jj} - HV_{kk} - \beta) \qquad (3.86)$$

$$C_{ji} = \lambda_{ds}H3_{ji}/(HD_{ii} - HS_{jj} - \alpha) \qquad (3.87)$$

Assuming that the damp factors λ_{dv}, λ_{sv} and λ_{ds} are set to unity and if α and β are chosen to be positive and with a sufficiently large magnitude then:

(a) the first order analysis will be valid irrespective of the magnitude of the elements of the Fock operator;

(b) the trial MO's can be forced to obey the "aufbau" principle so that large scale inter-shell swapping of molecular orbitals is inhibited. Such large scale swapping would correspond to large perturbations in the wavefunction;

(c) the matrix elements of A, B and C can be made arbitrarily small and of opposite sign to the elements $H1_{ki}$, $H2_{kj}$ and $H3_{ji}$ (equations 3.79 to 3.82).

Thus, for a suitable choice of level shifters, the iterated total energy will be lower than the starting total energy value given any trial set of molecular orbitals and iteration will always proceed down the energy surface.

The level shifted eigenvalues of the Fock operator are corrected by $(\alpha + \beta)$ and α for the VMOs and SOMOs respectively, to give the non-level shifted eigenvalues which can then be used for further calculation (see section on CI calculations). Thus, generally speaking, convergence to a given state can nearly always be achieved by choosing a sufficiently high value of the level shifters.

The ATMOL method is noted for its lack of complication, ease of use and flexibility in forcing convergence to most states of molecules or ions, though problems are sometimes encountered when a highly excited state or a state with a near degenerate neighbour of the same symmetry are being considered. Also, sometimes the need to use excessively large level shifters in forcing convergence can be wasteful of computer time since the rate of convergence can be drastically reduced. The ATMOL method has been used widely throughout this thesis for computing wavefunctions of molecules and ions and the prediction of vertical ionisation potentials. The results of these calculations are given in Chapters 6 (TiO, VO and CrO) and 7 (AlF and AlF_3). [It should be noted that the vector coupling coefficients required for calculations on systems with more than one open shell are given in an appendix at the end of this Chapter].

Configuration Interaction (CI)

The method of configuration interaction involves a straightforward variational solution (24) of the Ritz linear expansion of electronic wavefunctions. The method uses a linear expansion of the trial functions, expressed as:

$$\Psi = \sum_{s=1}^{n} C_s \Phi_s \tag{3.88}$$

where the Φ_s are predetermined expansion functions and the linear expansion coefficients C_s are the parameters which are varied to make $E(\Psi)$ stationary. The obvious difference between this method and the SCF method lies in the fact that the latter relies on a single Slater determinant while the CI method relies on several determinants depending on the number of configuration functions (Φ_s) generated. As before, application of the Variation Theorem leads to the generalised matrix eigenvalue equation.

$$\underline{H}\,\underline{c} = E\,\underline{S}\,\underline{c} \tag{3.89}$$

where $\underline{H}$ and $\underline{S}$ are Hermitian matrices defined by

$$H_{st} = \langle \Phi_s | \hat{H} | \Phi_t \rangle \tag{3.90}$$

$$S_{st} = \langle \Phi_s | \Phi_t \rangle \tag{3.91}$$

and the column vector, $\underline{c}$ has the desired coefficients, C_s, as components. The set of expansion functions, $\{\Phi_s\}$, is normally chosen to be orthonormal, in which case $\underline{S}$ becomes a unit matrix and equation 3.89 reduces to

$$\underline{H}\,\underline{c} = E\,\underline{c} \tag{3.92}$$

The eigenvalues, E_p, will be numbered such that

$$E_1 \leq E_2 \leq \ldots\ldots\ldots \leq E_n \tag{3.93}$$

Each eigenvalue, E_p, of equation 3.89 is an upperbound to the corresponding

eigenvalue of $\hat{H}$ and, as additional terms are added to the expansion, each eigenvalue, $E_p^{(n+1)}$ of the $(n+1)$-term expansion satisfies the inequalities

$$E_{p-1}^{(n)} \leq E_p^{(n+1)} \leq E_p^{(n)} \tag{3.94}$$

and as the expansion set $\{\Phi_s\}$ approaches completion, each eigenvalue $E_p^{(n)}$ of equation 3.89 will approach the corresponding eigenvalue, E_p, of $\hat{H}$ from above.

In general, a configuration interaction (CI) calculation proceeds through several steps which will be described in detail later. These can be summarised as:

(a) Construction of configuration functions (CF_s).
(b) Selection of configuration functions.
(c) Matrix element evaluation.
(d) CI Matrix eigenvalue evaluation.
(e) Wavefunction analysis.

A configuration interaction calculation is a very effective method of accounting for the correlation energy neglected by the Hartree-Fock SCF method. The method is more likely to take account of all the electron correlation in a particular molecular or ionic state if the preceding SCF calculation is carried out at the Hartree-Fock limit and if all configuration functions of the correct symmetry are included in the final CI expansion. Unfortunately, the number of configuration functions, which can number thousands for a molecule of the type studied in this thesis, makes a CI calculation very expensive in terms of computer time. This problem may be partially remedied by only including certain configuration functions in the final CI expansion. The methods of achieving this will be discussed in section b).

The various stages of a CI calculation will now be described in detail with reference to the SPLICE CI program (25) used throughout this thesis. This program was designed to be run in conjunction with the ATMOL3 suite of programs (23).

(a) Construction of Configuration Functions (CF_S)

Configuration functions are constructed from products of one-electron functions (spin-orbitals) such that each Φ_s satisfies the same symmetry conditions that ψ is required to satisfy. The main symmetry condition is that the CFs should be antisymmetric with respect to interchange of two electrons and this can be easily satisfied by collecting the products of spin-orbitals in Φ_s into Slater determinants. A linear combination of Slater determinants is still required in the general case to satisfy spin and space symmetry conditions. This can be done by choosing CFs which are eigen functions of the spin operators, $\hat{S}^2$ and $\hat{S}_Z$, since the Hamiltonian is spin-free.

A bonded function for a n-electron system corresponding to p spin-coupled pairs and n-2p unpaired orbitals is defined as follows:

$$\Phi = \hat{A}[\phi_1\phi_2][\phi_3\phi_4].....[\phi_{2p-1}\phi_{2p}][\phi_{2p+1}.....[\phi_n \qquad (3.95)$$

where the spin coupled pairs are defined as:

$$[\phi_i\phi_j] = \phi_i(i)\ \phi_j(j)\ \frac{1}{\sqrt{2}}\ \{\alpha(i)\ \beta(j)-\beta(i)\ \alpha(j)\} \text{ if } \phi_i \neq \phi_j$$

$$= \sqrt{2}\ \phi_i(i)\ \phi_j(j)\ \alpha(i)\ \beta(j) \qquad (3.96)$$

and the unpaired orbitals are defined as:

$$[\phi_i = \phi_i(i)\ \alpha(i)] \qquad (3.97)$$

The symbol $\hat{A}$ denotes an antisymmetrising operator which produces a normalised, completely antisymmetric wavefunction. Configuration function generation proceeds by two simple rules which correspond to the Rumer bonded function scheme (26).

(i) In each bonded function identical orbitals must be bracketed together i.e. any repeated spatial orbital must occur once with α spin and once with β spin.

(ii) From the remaining orbitals, all bracket patterns are constructed which preserve an excess, if any, of left brackets. The SPLICE program will generate a complete set of CFs, which satisfy the spin and symmetry constraints, from a given set of reference configurations. All possible single and double excitations from the reference configurations are considered but may often give rise to a large number of CFs. In cases like this, it is necessary to introduce some form of configuration function selection.

(b) Selection of Configuration Functions

Two methods of selection are available. Firstly, since a given set of reference configurations may give rise to a very large number of configuration functions, most of which will have a negligible effect on the final CI expansion, it is prudent to use a "preselection" method. This is carried out by restricting the number of virtual orbitals to which electrons may be excited and by "freezing" some of the deeper orbitals or "core" orbitals. "Freezing" the core orbitals will completely neglect correlation effects in the inner shell, but this is an acceptable approximation since the purpose of this work is to calculate total energies of molecules and their valence ionic states and hence determine vertical ionisation potentials for valence electron ionization. Subtraction of the total energies of an ion in a particular state from the neutral molecule will cancel this error since the inner shell will be essentially identical for both molecule and ion. For a CI calculation to be effective, all the CFs likely to make an appreciable contribution to the CI energy must be included. In general terms, the most important CFs are likely to be those which involve excitation of electrons from the uppermost occupied orbitals to the lowermost virtual orbitals. Excitations from the "frozen" (or core orbitals) to "frozen" virtual orbitals are unlikely to generate states which make large contributions to the energy lowering because of the large energy differences between the orbitals involved. Examples of the use of this method are given in Chapter 4 (TiO, VO and CrO).

Secondly, individual configuration selection may be carried out. This is a way of either estimating the contribution to the lowering of the total energy for each CF or by estimating the CI coefficient of an individual CF in the final CI wavefunction. To achieve this, first order perturbation theory is applied to give

$$C_s = \frac{\langle\phi_s|\hat{H}|\phi_o\rangle}{\langle\phi_o|\hat{H}|\phi_o\rangle - \langle\phi_s|\hat{H}|\phi_s\rangle} \qquad (3.98)$$

$$\text{and } \Delta E_s = \frac{|\langle\phi_s|\hat{H}|\phi_o\rangle|^2}{\langle\phi_o|\hat{H}|\phi_o\rangle - \langle\phi_s|\hat{H}|\phi_s\rangle} \qquad (3.99)$$

where ϕ_o is a zero-order wavefunction (or reference configuration). C_s is the CI coefficient and ΔE_s is the energy contribution of a CF, ϕ_s, to the CI total energy. These formulae are quite adequate for configuration selection provided that ψ_o is a good zero order wavefunction. Where this is not the case it is necessary to use a set of configuration functions known as root functions, which are a linear combination of determinants as an estimate for ψ_o. This makes the situation a little more complicated since the modified method has to take account of interactions between the root functions themselves as well as with the CFs. This can lead to problems when using a selection procedure to reduce the number of CFs to be included in the final CI expansion. To choose a set of root configurations, a full CI calculation is performed (with the required core and virtual orbitals frozen) and all configuration functions (generated by single and double excitation) with a coefficient of greater than 0.2 in the CI total energy are then used as root configurations in the final CI. However, in practice, it is unusual to find any configuration functions with a coefficient large enough to be added to the set of root configurations.

The selection of the configurations themselves proceeds by two methods: cumulative or threshold selection. Cumulative selection is achieved by specifying the number of configurations to be retained in the final CI and discarding the remainder of lower energy. Threshold selection is accomplished by specifying an energy threshold and any configurations with energy contribution below that threshold are discarded. Using either of these two methods, the computation time required can be reduced substantially with little loss of accuracy (27).

Unfortunately, in the SPLICE program, perturbation selection is only applicable to calculations involving non-degenerate states. The selection procedure will break down for a state with degeneracy and this is due to the assumptions made in perturbation theory. This can be outlined as follows:-

The Schrodinger equation is first assumed,

$$H_e^o \psi_e^o = E_e^o \psi_e^o \qquad (3.100)$$

where H_e^o, ψ_e^o and E_e^o are the zero order Hamiltonian, wavefunction and energy respectively. The Hamiltonian used in the full CI calculation is assumed to be only slightly different and can be written:

$$H_{CI} = H_e + \lambda H^{(1)} \text{ to first order} \qquad (3.101)$$

The equation which now has to be solved becomes

$$(H_e + \lambda H^{(1)})\psi_e = E_e \psi_e \qquad (3.102)$$

Since ψ_e and E_e will be functions of λ, they can be expanded in the form of a power series and written down as

$$\psi_e = \psi_e^o + \lambda\psi_e^{(1)} + \lambda^2 \psi_e^{(2)} + \ldots\ldots \qquad (3.103)$$

$$E_e = E_e^o + \lambda E_e^{(1)} + \lambda^2 E_e^{(2)} + \ldots\ldots \qquad (3.104)$$

Substituting equations 3.103 and 3.104 into equation 3.102 gives

$$(H_e + \lambda H^{(1)})(\psi_e^o + \lambda\psi_e^{(1)} + \lambda^2 \psi_e^{(2)} + \ldots\ldots)$$

$$= (E_e^o + \lambda E_e^{(1)} + \lambda^2 E_e^{(2)} + \ldots\ldots)(\psi_e^o + \psi_e^{(1)} + \lambda^2 \psi_e^{(2)} \ldots)$$

The next stage is to expand this out and equate coefficients on both sides of the equation, thus

$$H_e\ \psi_e^o + \lambda(H_e\ \psi_e^{(1)} + H^{(1)}\ \psi_e^o) + \lambda^2(H_e\ \psi_e^{(2)} + H^{(1)}\ \psi_e^{(1)}) + \ldots$$

$$= E_e^o\ \psi_e^o + \lambda(E_e^o\ \psi_e^{(1)} + E_e^{(1)}\ \psi_e^o) + \lambda^2(E_e^o\ \psi_e^{(2)} + E_e^{(1)}\ \psi_e^{(1)}$$

$$+ E_e^{(2)}\ \psi_e^o) + \ldots\ldots$$

Equating powers of λ on both sides of the equation, gives;

$$H_e\ \psi_e^o = E_e^o\ \psi_e^o \tag{3.105}$$

$$(H_e - E_e^o)\psi_e^{(1)} = E_e^{(1)}\ \psi_e^o - H^{(1)}\ \psi_e^o \tag{3.106}$$

$$(H_e - E_e^o)\psi_e^{(2)} = E_e^{(2)}\ \psi_e^o + E_e^{(1)}\ \psi_e^{(1)} - H^{(1)}\ \psi_e^{(1)} \tag{3.107}$$

Equation 3.105, by assumption, has already been solved. Solutions of equations 3.106 and 3.107 will give $\psi_e^{(1)}$ and $E_e^{(1)}$ and $\psi_e^{(2)}$ and $E_e^{(2)}$ and so on. For a first order perturbation, it is the solution of equation 3.106 that is required. To obtain the solution, it is assumed that the function, $\psi_e^{(1)}$, can be expanded in terms of the normalised and orthogonal set of functions ψ_1^o, ψ_2^o.....ψ_n^o.

$$\psi_e^{(1)} = A_1\ \psi_1^o + A_2\ \psi_2^o + \ldots\ldots + A_m\ \psi_m^o + \ldots\ldots \tag{3.108}$$

where the A_m's are to be determined. The function $H^{(1)}\ \psi_e^o$ can also be expanded into the series

$$H^{(1)}\ \psi_e^o = H_{1e}^{(1)}\ \psi_1^o + H_{2e}^{(1)}\ \psi_2^o + \ldots\ldots + H_{me}^{(1)}\ \psi_m^o + \ldots \tag{3.109}$$

where

$$H_{me}^{(1)} = \int \psi_m^{o*}\ H^{(1)}\ \psi_e^o\ d\tau \tag{3.110}$$

Equation 3.108 and 3.109 are now substituted into equation 3.106 to give

$$(H_e - E_e^o)(A_1\ \psi_1^o + A_2\ \psi_2^o + \ldots.) = E_e^{(1)}\ \psi_e^o - H_{1e}^{(1)}\ \psi_1^o$$

$$- H_{2e}^{(1)}\ \psi_2^o - \ldots\ldots \tag{3.111}$$

which can be reduced by means of equation 3.105 to

$$(E_1^o - E_e^o)A_1\ \psi_1^o + (E_2^o - E_e^o)A_2\ \psi_2^o + \ldots\ldots$$

$$= E_e^{(1)}\ \psi_e^o - H_{1e}^{(1)}\ \psi_1^o - H_{2e}^{(1)}\ \psi_2^o \qquad (3.112)$$

The coefficient of each ψ_e^o must be equal on both sides of the equation, so that

$$E_e^{(1)} - H_{ee}^{(1)} = 0 \qquad (3.113)$$

The first order perturbation energy has thus been determined to be

$$E_e^{(1)} = H_{ee}^{(1)} = \int \psi_e^{o*}\ H^{(1)}\ \psi_e^o\ d\tau \qquad (3.114)$$

By equating the coefficients of ψ_m^o $(m \neq e)$, the following equation is obtained.

$$(E_m^o - E_e^o)A_m = - H_{me}^{(1)}$$

$$\text{i.e.}\quad A_m = \frac{H_{me}^{(1)}}{E_e^o - E_m^o} \qquad (3.115)$$

It is this term which, unfortunately, causes the problems in a CI calculation involving degenerate states and the reasons are outlined below using a $^2\Pi$ state as an example. The $^2\Pi$ state can be represented in two alternative ways i.e.

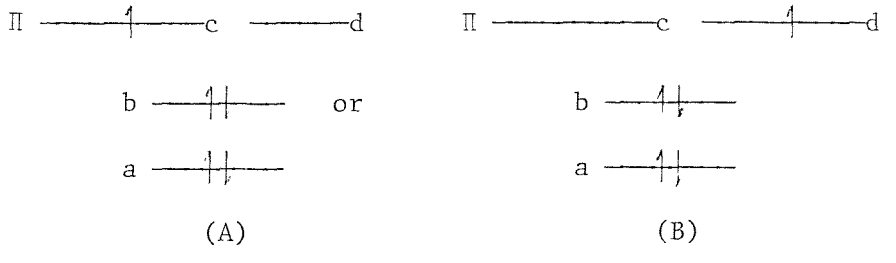

(A) (B)

The two root configurations for this state will be

(aa)(bb)(c and (aa)(bb)(d

Consider a single electron excitation c→d in (A) where $E_A^o = E_B^o$. A_m will tend to infinity as E_A^o and E_B^o approach in energy. When they are equal, A_m will equal infinity and the equation for $\psi_e^{(1)}$ will be meaningless. The SPLICE program will thus terminate with an error and proceed no further. For this reason, all the CI calculations outlined in Chapter 4 used a preselection method rather than perturbation selection.

(c) Matrix Element Evaluation

The next step in a CI calculation involves evaluating matrix elements of the CI Hamiltonian between the bonded functions. In general, these matrix elements can be written as sums of integrals between determinants of the two bonded functions. The matrix elements can in turn be written in terms of one- and two-electron integrals over the space orbitals, ϕ_i. The general expression is therefore:-

$$\langle\Phi_s|\hat{H}|\Phi_t\rangle = \sum_{ij} a_{ij}^{st} \langle\phi_i|\hat{h}|\phi_j\rangle + \sum_{ijkl} b_{ijkl}^{st} \langle\phi_i\phi_j|\hat{g}|\phi_k\phi_l\rangle$$

where Φ_s and Φ_t are determinants, $\Phi_i....\Phi_l$ are space orbitals, the coefficients a_{ij}^{st} and b_{ijkl}^{st} are called Projective Reduction coefficients (28,29), and $\hat{h}$ and $\hat{g}$ are one-electron and two-electron operators respectively. Once the CI Hamiltonian matrix has been constructed, the next step is to calculate the eigenvalues and eigenvectors of the matrix.

(d) CI matrix eigenvalue evaluation

This proceeds via a method developed by Shavitt (30) known as the method of optimal relaxations. This method is capable of evaluating a series of roots which are solutions to the CI secular equations. Problems sometimes occur when evaluating higher roots since the computational effort required is increased. In the case where near-degenerate eigenvalues are present, difficulties in obtaining convergence may be experienced because of swapping between states. For these reasons, the SPLICE method can only realistically evaluate the first four or five roots for any given

symmetry type. Having evaluated the roots (i.e. the eigenvectors of the CI matrix), the wavefunction can be analysed in terms of natural orbitals.

(e) Wavefunction Analysis

The analysis proceeds with the calculation of the one- and two-particle spin and spin-free density matrices in the MO and AO basis representations. The natural orbitals, in either representation, are obtained as eigenvectors of the respective density matrices with the eigenvalues being occupation numbers. Both sets of natural orbitals may be stored for later analysis by the ATMOL3 suite of programs (23). In the case of the work described in this thesis, the natural orbitals of the molecules and their respective ionic states were used in a Mulliken Analysis program (23) to give an indication of the changes in electron density which occur on ionisation.

In summary, the CI method provides a very effective way of accounting for most of the correlation energy in a state of interest but can suffer from the approximations imposed by lack of computer time or space i.e. this necessitates restricting the virtual orbital space or "freezing" core orbitals.

It is also worth mentioning that, although a CI calculation takes account of much of the correlation energy, the initial choice of basis set in an ab initio SCF calculation may lead to a poor description of the molecular wavefunction, i.e. the calculation is not close to the Hartree-Fock limit . In this case the CI calculation will be unable to give an accurate result. To circumvent this problem, it would be much better to combine the main attributes of both the SCF and the CI methods such that electron correlation is taken into account throughout a calculation. Such a method is described below.

The Multiconfiguration Self-Consistent Field Method (31)

It is intended to give an outline of the Multiconfiguration Self-Consistent Field (MCSCF) method rather than present a rigorous proof as given for the SCF method. In the MCSCF method, it is assumed that the total wavefunction is a linear combination of configurations

given by

$$\Psi^{(n)} = \sum_a A_a^{(n)} \Phi_a \qquad (3.116)$$

when the superscript (n) corresponds to the n^{th} root of the secular equation

$$|E_{ab} - E\delta_{ab}| = 0 \qquad (3.117)$$

Equation 3.116 is already familiar as that used in the CI expansion (equation 3.88). The configurations $|\Phi_a|$ are assumed to be orthonormal and E_{ab} is the matrix element of the Hamiltonian, H

$$\text{i.e.} \quad E_{ab} = \langle\Phi_a|H|\Phi_b\rangle.$$

In the SCF method, only one configuration, Φ_a, was defined. In the MCSCF method, Φ_a is written formally as:

$$\Phi_a = \sum U_{at} \Phi_t \qquad (3.118)$$

where the Φ_t are Slater determinants i.e. Φ_a is expressed as a linear combination of Slater determinants. The Φ_t are written as:

$$\Phi_t = |n_1^t, n_2^t, \ldots\ldots, n_m^t\rangle \qquad (3.119)$$

the n_i^t being occupation numbers (either 0 or 1) of the spin-orbitals i, and the U_{at} are coupling coefficients defined by the symmetry of the state represented by $\Psi^{(n)}$.

The MCSCF procedure proceeds by a process similar to that used in the SCF and CI methods and this is summarised briefly below (32):

(i) Select initial molecular orbitals from an atomic basis and configuration types via a single-determinantal SCF calculation;

(ii) set up and solve the CI problem for the required state;

(iii) using the results of (ii), set up a multi-determinantal SCF calculation;

(iv) solve the multidetermantal SCF equations.

Steps (ii) to (iv) are iterated to convergence. The method is applicable to several roots of a given symmetry with the required root being specified in (ii). Unfortunately, difficulty is sometimes encountered in obtaining convergence for the higher roots, as in the CI method, but this is not normally a problem since only the lowest roots are required for any state.

The advantages of the method are two-fold. Firstly, a more accurate description of the molecular electronic wavefunction of the molecule is obtained compared to the "single determinant" SCF method and, secondly, correlation energy is accounted for throughout the calculation. The method is superior to the SCF followed by CI approach since both SCF and CI stages are iterated to convergence. Even better results may be obtained by following up the MCSCF calculation with a further CI to include some of the less important configurations previously omitted. In practice, however, the MCSCF method is still little used because of the large computational effort required. An example of the use of this method can be found in Chapter 7 where its application to the interpretation of the photoelectron spectrum of AlF is described. These calculations were performed by Drs. Rosmus and Klein in Frankfurt.

The Pseudonatural orbital CI (PNO-CI) method (33)

The two preceding sections on the CI and MCSCF methods have generally considered only the effects of single and double excitations on the total energy of the state of interest. Inclusion of any higher excitations is prohibitive due to the enormous amount of computer time that would be required. The PNO-CI method can make some allowance for higher excitations by, firstly, reducing the number of configurations generated by single and double excitations and, secondly, making allowance for higher order excitations through the Coupled Electron Pair approximation (CEPA). The whole method is sometimes known as the PNO-CEPA method and is referred to as such in the work on AlF (see Chapter 7).

It is intended, here, to give only a brief overview of the PNO-CEPA method. (For full details, ref. (33) should be consulted). The method itself is intended as an alternative to the CI method described above. The initial wavefunction is described in the usual way as

$$\Psi_o = \sum_s C_s \Phi_s \qquad (3.120)$$

as in equation 3.88. ψ_o will be referred to as the reference wavefunction and is obtained using either the SCF or MCSCF methods described earlier in this thesis. ψ_o is usually chosen to have all the symmetry properties of the electronic state. Following the terminology of Silverstone and Sinanoglu (34), the occupied orbitals in ψ_o which play a part in the overall CI calculation will be termed "internal orbitals". Φ_s in equation (3.120) is a single determinant.

Using the reference wavefunction, other configurations must be constructed by considering one, two and higher order excitations. Since the "configuration expansion" will be dominated by those configurations contained in the reference wavefunction, ψ_o, it is useful to classify the configurations according to the number of electrons that are outside the internal space i.e. the number of internal orbitals being substituted by virtual or "external" orbitals. Since the Hamiltonian is built from one-electron and two-electron operators, configurations with more than two external orbitals have vanishing matrix elements with the reference function. Therefore, the double substitutions play the crucial role in completing the configuration expansion. The wavefunction involving single and double substitutions can be written as:

$$\Psi = \Phi_o + \sum_i \sum_a C_i^a \Phi_i^a + \sum_{i \leq j} \sum_{a \leq b} C_{ij}^{ab} \Phi_{ij}^{ab} \qquad (3.121)$$

where Φ_o is the reference determinant and Φ_{ij}^{ab} denotes a configuration obtained from Φ_o by replacing the internal spin-orbitals ψ_i and ψ_j by external spin-orbitals ψ_a and ψ_b.

The smallness of the coefficients in equation 3.121 makes it sensible to use perturbation methods to calculate the PNO-CI total energy.

The wavefunction given to first-order accuracy may be written down as follows:

$$\Psi^{(1)} = \Phi_o - \sum_{a\leq b} \sum_{i\leq j} \Phi_{ij}^{ab} <\Phi_{ij}^{ab}|\hat{H}|\Phi_o>/E_{ij}^{ab} \qquad (3.122)$$

where the energy denominators may be obtained from the eigenvalues of the Fock operator. From $\Psi^{(1)}$, the energy is calculated to second order as

$$E^{(2)} = <\Phi_o|\hat{H}|\Psi(1)> \qquad (3.123)$$

and to third order as

$$E^{(3)} = <\Phi_o|\hat{H}|\Phi_o> + <\Psi^{(1)}|\hat{H} - <\Phi_o|\hat{H}|\Phi_o>|\Psi(1)> \qquad (3.124)$$

The accuracy of the correlation energy to second order is generally no better than 10% (35) and is therefore insufficient for many purposes. The third-order energy requires calculating the Hamiltonian matrix elements between all configurations of $\Psi^{(1)}$ and is computationally time consuming. To circumvent this problem, equation 3.121 can be expressed in a more compact form before calculating the energy and other expectation values. This is done using the fact that a sum over determinants that differ in one particular column only may be expressed as a single determinant containing the sum of the differing columns:

$$\text{i.e.} \quad \sum_a C^a |\psi_1 \ldots \psi_a \ldots \psi_N| = |\psi_1 \ldots (\sum_a C^a \psi_a) \ldots \psi_N| \qquad (3.125)$$

This means that one sum of the two-electron clusters of equation 3.121 can be absorbed by defining new orbitals. For example,

$$\Psi_{a(ij)} = \sum_b \Psi_b C_{ij}^{ab}/C_{ij}^{a} \qquad (3.126)$$

can be rewritten as:

$$\sum_{ab} C_{ij}^{ab} \Phi_{ij}^{ab} = \sum_a C_{ij}^{a} \Phi_{ij}^{aaij} \qquad (3,127)$$

This has the effect of reducing the number of configurations per pair (ij) from L^2 to L (L being the dimension of the external orbital space) at the cost of having one orbital in each configuration that is not orthogonal to all the others. Because of this approximation, the natural orbitals have been termed "Pseudo-natural orbitals" and the above description illustrates the basic idea of the PNO-CI approach. Having got to this stage, it is now possible to take account of the effects of higher order excitations on the total energy of the state of interest through the coupled Electron Pair approximation (CEPA). This is outlined below:-

The configuration space is extended to all multiple substituted Φ_M possible within the given orbital set. The Schrodinger equation then has the following matrix form:-

$$E = \sum_P \sum_{ij} \langle \Phi_p^{ij} | \hat{H} | \Phi_o \rangle C_p^{ij} = \sum_P E_p \qquad (3.128)$$

where P represents a double hole state irreducible with respect to certain symmetry operations, s^1, which may be obtained by annihilating the spin orbitals ψ_a and ψ_b in determinant Φ_s (equation 3.120). Φ_p^{ij} denotes that configuration of the required symmetry which is obtained by coupling two electrons in the spin-orbitals ψ_i and ψ_j with the double hole state defined by P. Assuming $C_o = 1$ and $E_o = 0$,

$$[E - \langle \Phi_p^{ij} | \hat{H} | \Phi_p^{ij} \rangle] C_p^{ij} = \langle \phi_p^{ij} | \hat{H} | \phi_o \rangle + \sum_{kl \neq ij} \langle \Phi_p^{kl} | \hat{H} | \Phi_p^{ij} \rangle C_p^{kl}$$
$$+ \sum_{P'} \sum_{kl} \langle \Phi_{p'}^{kl} | \hat{H} | \Phi_p^{ij} \rangle C_{p'}^{kl} + \sum \langle \Phi_M | \hat{H} | \Phi_p^{ij} \rangle C_M \qquad (3.129)$$

This rather unwieldy expression may be simplified using the approximation

$$\sum \langle \Phi_M | \hat{H} | \Phi^{ij} \rangle C_M \underset{\sim}{\approx} C_P^{ij} \sum_{P' \neq P} E_{P'}, \qquad (3.130)$$

which is essentially the result of assuming that unlinked clusters are the dominant multiple substitutions. Equation 3.129 may now be rewritten as follows:

$$[E - DE_P - \langle \Phi_P^{ij} | \hat{H} | \Phi_P^{ij} \rangle] C_P^{ij} = \langle \phi_P^{ij} | \hat{H} | \phi_o \rangle$$

$$+ \sum_{kl \neq ij} \langle \Phi_P^{kl} | \hat{H} | \Phi_P^{ij} \rangle C_P^{kl} + \sum_{p'} \sum_{kl} \langle \Phi_{P'}^{kl} | \hat{H} | \Phi_P^{ij} \rangle C_{P'}^{kl} \qquad (3.131)$$

$$\text{with} \qquad DE_P = \sum_{P' \neq P} E_{P'} \qquad (3.132)$$

Equations 3.128 through to 3.132 are known as the Coupled Electron Pair Approximation (CEPA) (33). The modified eigenvalue equations 3.128, 3.131 and 3.132 are most easily solved by applying an iterative procedure (36). In every step, a set of pair energies, E_P is obtained from equation 3.128, together with approximate coefficients, C_P^{ij}, and used in equation 3.131 and 3.132 for the next step. Using such an iterative procedure, cluster corrections are taken into account to all orders. It is the sum of pair energies in equation 3.132.

As mentioned earlier, the whole method is known as the PNO-CEPA method and offers a very effective way of accounting for almost 100% of the correlation energy for a particular molecular or ionic state through the use, firstly, of the PNO-CI approach to reduce the number of single and double substitutions constructed from the reference wavefunction and, secondly, by taking account of higher order substitutions which are omitted in a standard CI calculation. Examples of the use of this method will be found in Chapter 7.

The Hartree-Fock-Slater Method (37-39)

The Hartree-Fock-Roothaan method outlined earlier in this Chapter has been used successfully on several molecules described in this thesis. Its use is confined mainly to small molecules and the reason for this is clear when the calculation of integrals involving the exchange operator are considered. The exchange operator is different for each orbital or spin orbital and, in fact, the number of exchange terms which must be calculated rises approximately as n^4, where n is the number of atomic basis functions. It is therefore apparent that calculations on molecules involving heavy atoms are not feasible due to the necessarily large basis set. The vast amount of computer time required for large molecules makes a calculation at the Hartree-Fock-Roothaan level impractical. The

simplification originally proposed by Slater (40) involves averaging the exchange operator over all spin orbitals. From studies on a homogeneous electron gas, Slater found that the exchange terms could be further approximated to a function of the charge density, P, in the system. The functional dependence is fairly simple, the exchange term being proportional to $P^{1/3}$. Replacing each exchange term by the $P^{1/3}$ term is known as Slater's exchange or $X\alpha$ approximation and this is a central approximation in the Hartree-Fock-Slater (HFS) method. Having made the approximation, the HFS equations can be set up and a method of solving them needs to be found. A numerical integration scheme is the method chosen. Two ways of calculating vertical ionisation potentials by the HFS method are commonly used - a transition state method described by Beebe (41) or a ΔSCF calculation of the type described earlier. Both these methods include orbital relaxation on ionisation and have been shown to give numerically equivalent results. Comparison of vertical ionisation potentials calculated by both the HFS and ATMOL3 ΔSCF methods has shown that the former are closest to the experimental values indicating that some allowance for correlation energy is present in the HFS predicted values. This is, perhaps, fortuitous and is due to cancellation of the errors introduced into the calculation by the Slater exchange approximation (40).

In summary, the main advantage of the HFS method lies in the fact that calculations on species involving heavy atoms become feasible. The approximations in the method also mean that larger basis sets may be used, leading to a more realistic description of the system under study and also to a reduction in the amount of computer time required by a calculation. It is hoped to perform HFS calculations on heavy molecules such as those involving the lanthanide and actinide metals in the near future in the Southampton PES group as part of the group's effort to investigate high temperature vaporisation processes associated with a nuclear environment. Such calculations will be an invaluable aid to the assignment of experimental spectra.

Choice of Atomic Basis Set in Molecular Orbital Calculations

The accuracy of an ab initio SCF calculation is determined primarily by its proximity to the Hartree-Fock limit. This desirable state of affairs is obtained when no further lowering in the total energy can be gained by increasing the size of the basis set. Two types of basis set are commonly used in molecular orbital calculations:

(i) Slater-type Orbitals (STOs)

These have the general form:

$$\chi_{n,l,m} = N\, r^{n-1} \exp(-\xi r) Y_{lm}(\theta,\phi)$$

where N is a normalisation factor and $Y_{l,m}(\theta,\phi)$ is a spherical harmonic. The exponent, ξ, may be optimised by minimising the total energy for the element in question (42) and it is then possible to represent the "true" AO quite well with one STO. This is particularly so in the core orbitals. It is unfortunate that integrals involving STOs have to be evaluated numerically which is computationally very time-consuming. In order to increase the number of variational parameters (the coefficients in the linear combination of atomic orbitals) further Slater functions can be added to provide a superior description of the atom or molecule in a particular electronic state. In particular, for molecular calculations it is generally necessary to include extra functions to describe the valence m.o.s. as these orbitals are more important when considering atomic interactions. A basis set which includes two STOs for every formally occupied atomic orbital is called a double zeta basis set (see for example ref.(42)).

(ii) Gaussian-type Orbitals (GTOs)

These have the general form:

$$\chi = N^1\, r^{n-1} \exp(-\xi r^2) Y_{lm}(\theta,\phi)$$

where N^1 is, again, a normalisation constant. GTOs were first suggested by Boys (43) in 1950 but are less appropriate for expanding the electronic wavefunctions of atoms and molecules than STOs. This necessitates the use

of a larger set of functions to obtain equivalent results.

The advantage of GTOs however, is that one- and two-electron integrals over AO's, needed in the Hartree-Fock method, can be evaluated analytically. This procedure is simpler than the numerical integration required for STOs and is more economical in terms of computer time.

Both types of basis set have been used in the work described in this thesis. STOs have been used for calculations on AlF, AlF_3, CS and SiS (see Chapters 4 and 7). It is possible to represent each AO in an atom by a single STO, giving rise to the so-called minimal basis set but use of a linear combination of STOs has been found to give improved results. The double-zeta basis set of Roetti and Clementi (42), consisting of a linear combination of two STOs for each AO, has been used to perform calculations on the four molecules listed above. To further improve the efficiency of the calculations two other refinements were introduced. Firstly, to combine the accuracy of STOs with the ease of use of GTOs, each STO was expanded as a linear combination of 3GTOs. Secondly, polarisation functions were also included in the basis set giving rise to an improved description of the outer "bonding" orbitals. Basis sets involving polarisation functions have been used in the calculations described in Chapters 4 and 7.

For the transition metal oxides described in this thesis (see Chapters 4 and 6), GTOs were used. Three basis sets are available in the literature for the first-transition series (44-46). The basis sets of Basch et al (44) and Wachters et al (45) are large being (15s, 8p, 5d) and (14s,9p, 5d) respectively. Both basis sets will lead to very accurate wavefunctions but, unfortunately, their size tends to be rather prohibitive for use in molecular calculations. For this reason, the (12s, 6p, 4d) basis set of Roos et al (46) was chosen for the calculations on transition metal oxides to be described in this thesis. When the basis set for oxygen (7s, 3p) (47) is added, it becomes clear that the basis set will still be rather large and could still be prohibitive in terms of computer time. To circumvent this problem, a technique known as "contraction" was used. In this technique, a number of functions can be grouped together

and treated as one function. The resulting functions are known as contracted GTOs (CGTOs) and are linear combinations of GTOs. Since this thesis is concerned mainly with the study of the valence orbitals of atoms and molecules, the most appropriate contraction scheme would be one where the innermost (large exponent) GTOs are contracted leaving the outermost (small exponent) GTOs uncontracted. The contraction scheme actually used was that of Raffenetti (48), the basis set having been supplemented by metal d exponents specified by Hay (49).

In the case of CrO, both STO and CGTO basis sets were used. It was found that both basis sets gave similar results in terms of total energy for the molecule and its ionic states with the CGTO basis set being the most economical in terms of computer time(for a given state of the ion or molecule, the total energy with the CGTO basis set was in fact lower than with a STO basis set). For these reasons, it was decided to use a CGTO basis set in subsequent calculations on TiO and VO.

3.4. Information to be obtained from Photoelectron Bands

The most obvious information to be derived from photoelectron spectra are the ionisation potentials (IP_s). This is summarised by the following equation,

$$KE = h\nu - IP_i \qquad (3.133)$$

which holds for atoms. KE is the kinetic energy of the ejected electron, $h\nu$ is the energy of the ionising radiation and IP_i is the i^{th} ionisation potential. Thus, if KE and $h\nu$ are known, IP_i can be very easily determined. Intensity data can be determined by measuring the relative intensities of each band in a spectrum and, after taking instrumentation factors into account, this yields a quantity known as the Relative Photoionisation Cross-Section which can be regarded as being a measure of the relative probability of ionisation to different ionic states (this quantity will be discussed again in Chapters 5 and 6).

In the case of molecules, equation (3.133) must be modified to take the vibrational change on ionisation (ΔE_v) into account

$$\text{i.e.} \quad KE = h\nu - IP_i - \Delta E_v \tag{3.134}$$

where the quantities KE, $h\nu$ and IP_i are as before. The vibrational energy levels in a molecular ion can be written approximately in terms of the anharmonic energy expression as

$$E_{vib} = \bar{w}_e(v + \tfrac{1}{2}) - \bar{w}_e x_e(v + \tfrac{1}{2})^2 \tag{3.135}$$

where $\bar{w}_e$ is the vibrational frequency, v is the vibrational quantum number and x_e is the anharmonicity constant. For the diatomic molecules studied in this thesis, long vibrational series are often observed (e.g. the first band of CrO, discussed in Chapter 6). If all the observed components arise from ionisation from the v" = 0 level in the ground state of the neutral molecule, values for $\bar{w}_e'$ and $\bar{w}_e x_e'$ may be obtained by simple measurement of the vibrational separation in a band. From equation (3.135) it can be shown that

$$\Delta E = E_{v+1} - E_v = \bar{w}_e' - 2\bar{w}_e x_e'(v + 1) \tag{3.136}$$

where $\bar{w}_e'$ and $\bar{w}_e x_e'$ are spectroscopic parameters in the ion. Thus a plot of ΔE versus (v + 1) will give a straight line with slope $-2\bar{w}_e x_e'$ and intercept $\bar{w}_e'$ with respect to the ion.

It is useful, at this point, to define two other quantities which can be measured from a vibrational series. The n^{th} vertical ionisation potential (VIP) is defined as the energy difference between the molecule in its ground electronic state and the ion in its n^{th} electronic state but with the nuclei in the ion having the same positions as they had in the molecule. Experimentally, the VIP is measured as the point of maximum intensity in a photoelectron band. The n^{th} adiabatic ionisation potential (AIP) is defined as the difference between the molecule in it's electronic and vibrational ground state and the ion in its n^{th} electronic state and its lowest vibrational level in that electronic state i.e. it corresponds to the v' = 0←v" = 0 ionisation (v' indicates ionic state while v" indicates neutral state). Experimentally, the AIP corresponds to the first vibrational component in a photoelectron band.

A relatively unused piece of information to be derived from photoelectron spectra of molecules is the relative photoionisation cross-section for different ionic states. At present, experimental intensities are just measured and tabulated. However, it is now possible to predict these quantities theoretically.

Photoelectron spectroscopy may also be used to derive estimates of dissociation energies of molecular ions. Consider the case of a diatomic ion AB^+ which undergoes an ionic dissociation process:

$$AB^+ \rightarrow A^+ + B$$

Figure 3.1 shows the potential energy curves for the molecule AB and its ion AB^+. From the Figure it is apparent that

$$AIP_{AB} + D_o(AB^+) = D_o(AB) + IP_A$$

$$\text{Hence } D_o(AB^+) = D_o(AB) + IP_A - AIP_{AB}$$

AIP_{AB} is measured experimentally by p.e.s. and IP_A and $D_o(AB)$ may normally be found from published tables (50) and elsewhere in the literature. Thus, knowing these values, it is a simple matter to calculate a value for $D_o(AB^+)$. It is assumed that the ion AB^+ dissociates to give A^+ and B in their respective ground states. On dissociation, a molecule in a particular electronic state must obey the Wigner-Witmer correlation rules (51) which state that total spin and angular momentum must be conserved. Thus the sums of the components of the total orbital angular momenta of the two atoms and of the components of the total spin angular momenta must equal the total orbital angular momentum and the total spin angular momentum in the molecule respectively. By way of illustration, consider the dissociation of the $TiO(X^3\Delta)$ state. It is expected that the dissociation products will be formed in their respective ground states, $Ti(^3F)$ and $O(^3P)$. The components of total orbital angular momentum about the internuclear direction in the molecule

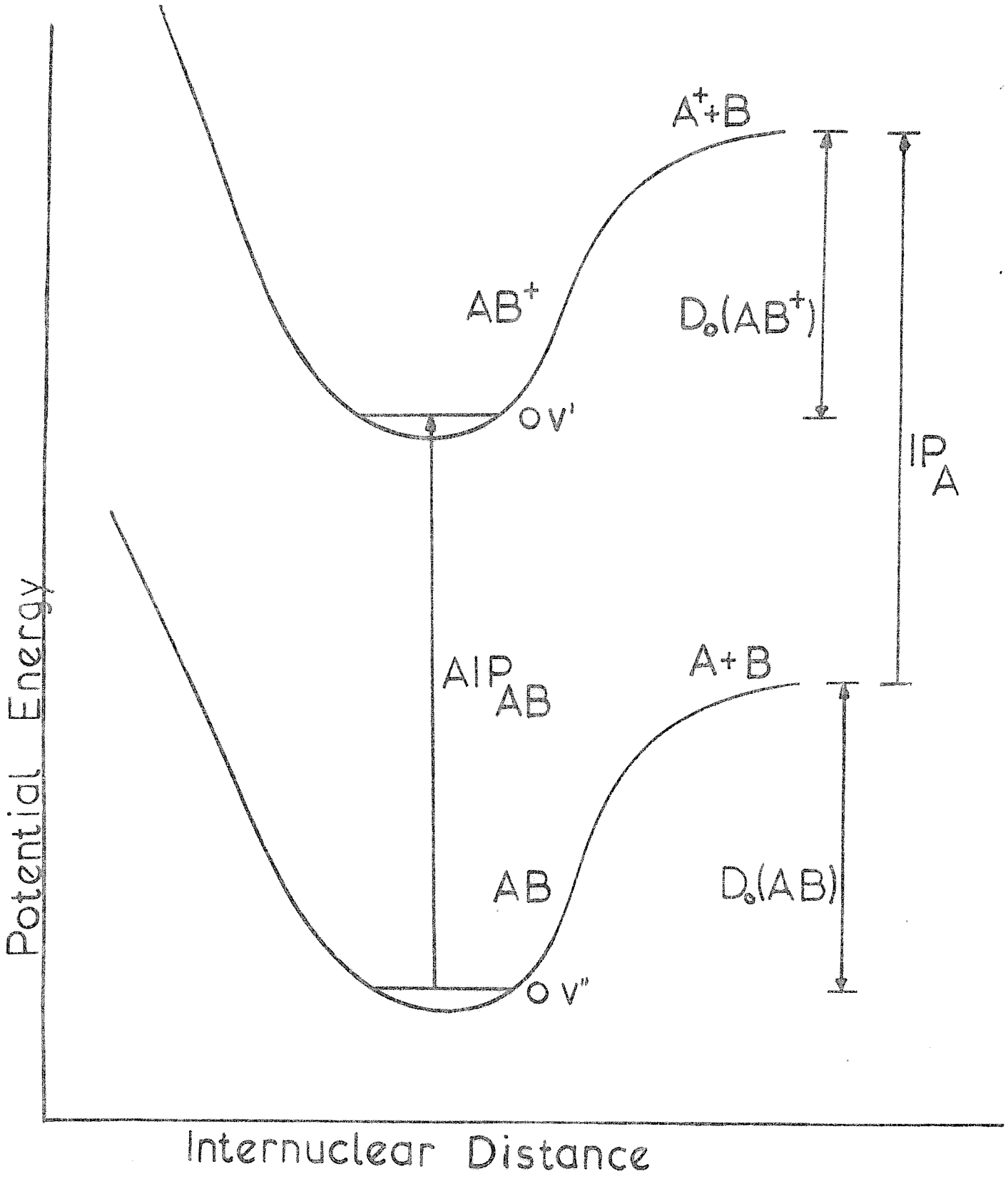
A+ + B
AB+
D₀(AB+)
IP A
v'
v''
AIP AB
A + B
AB
D₀(AB)
Potential Energy
Internuclear Distance

FIG 3.1

are given by:

$$M_n = M_{L_1} + M_{L_2}$$

where M_{L_1} and M_{L_2} are components of the total orbital angular momenta of the two atoms. All the possible values of M_n are obtained by combining all possible values of M_{L_1} and M_{L_2}. Possible values of the total spin angular momentum of the molecule are given by

$$S = (S_1 + S_2), (S_1 + S_2 - 1) .... |S_1 - S_2|$$

where S_1 and S_2 are the total spin angular momenta of the two atoms. Thus for $Ti(^3F)$ and $O(^3P)$

$$Ti(^3F);\ M_L = 3,2,1,0,-1,-2,-3;\ S = 1$$

$$O(^3P);\ M_L = 1,0,-1;\ S = 1$$

It can now be easily shown by combining values of M_L for $Ti(^3F)$ and $O(^3P)$ that possible states of the TiO molecule are Γ, ϕ, Δ, Π and Σ. Also, by combining values of S for both atoms, S can have values of 2,1 and 0 in the molecule giving rise to quintet, triplet and singlet states. Since the $^3\Delta$ state of TiO is an allowed state of the $Ti(^3F) + O(^3P)$ reaction, it is also true to say that the dissociation process

$$TiO(^3\Delta) \rightarrow Ti(^3F) + O(^3P)$$

is in accordance with the Wigner-Witmer correlation rules (51).

A further piece of information can be derived by using the Franck-Condon Principle with the experimental vibrational band envelope to estimate the equilibrium bond length for a particular molecular ionic state. The Franck-Condon Principle states that ionisation of a molecule takes place on a time-scale very much shorter than that in which a molecular vibration can occur. This means that, for the most probable vibrational transition in a photoelectron band, the geometry of a molecule is the same immediately after ionisation as it was before. The

probability and hence intensity of a transition occuring between the v" level of the ground state molecule and the v' level of the ion is given by:

$$I_{v'\leftarrow v''} = |R_e(Q_o)|^2 \left| \int \Psi'_{v'}{}^{*}(R)\ \Psi''_{v''}(R)dR \right|^2 \qquad (3.136)$$

This is similar to equation (3.5) and is derived using the Born-Oppenheimer approximation (2). The second term on the right-handside of equation (3.136) is known as the Franck-Condon factor. The factor $R_e(Q_o)$ is the electric dipole transition moment about the equilibrium nuclear position, Q_o, and is assumed to be constant over a vibrational series. Vibrational transitions are assumed to occur from the lowest vibrational level, v"=0, of the ground state molecule. This is a quite reasonable assumption provided $\bar{w}_e$">>kT. To obtain an estimate of the equilibrium bond length of a molecular ion in a particular state experimental intensities measured from a vibrational series are compared with calculated Franck-Condon factors using a least squares procedure (52). Morse potentials are assumed for both the ground and ionic states, the expression for a Morse potential being given below:

$$E = D_e[1 - \exp(a(r_e - r))]^2 \qquad (3.137)$$

The constants D_e and a are related to $\bar{w}_e$ and x_e by the following expressions:

$$a = \pi C\ \bar{w}_e \sqrt{\frac{2\mu}{D_e}} \qquad (3.138)$$

$$D_e = \frac{\bar{w}_e}{4x_e} \qquad (3.139)$$

$\bar{w}_e$", $\bar{w}_e$"x_e and r_e" for the neutral molecule are normally taken from optical spectroscopy and $\bar{w}_e$' and $\bar{w}'_e x_e$ are measured directly from the photoelectron spectrum. The vibrational wavefunctions $\Psi'_{v'}$, (R) and $\Psi''_{v''}$(R) can be calculated as numerical solutions of the radial Schrodinger equation using Morse potentials for both molecule and ion. The Franck-Condon factors are then calculated for a range of values of r_e', the equilibrium bond length in the ion, and theoretical and experimental

vibrational envelopes compared by a least-squares procedure to give the optimum value of r_e'. The method is generally held to be accurate to within $\pm 0.01\text{Å}$. Any errors arise from the fact that the electronic transition moment is assumed constant across a band and from uncertainties in measuring the component intensities of the experimental spectra. This method is obviously only applicable to those spectra where clear vibrational series may be observed. Problems may be encountered when a molecule predissociates. In this case, some fine structure may be observed which will eventually merge into a continuum. Similar spectra may also be obtained when the dissociation limit of the ion is reached.

Qualitatively, some information of the type of orbital from which ionisation takes place may be gained by considering the change in $\bar{w}_e'$ and r_e' in the ion relative to the neutral molecule. In general, if $\bar{w}_e'$ and r_e' are similar to $\bar{w}_e''$ and r_e'', ionisation will have occurred from a non-bonding orbital. A decrease in $\bar{w}_e'$ relative to $\bar{w}_e''$ shows that the bond in the ion has been weakened, with a corresponding increase in r_e' relative to r_e'', and this indicates that ionisation has occurred from a bonding orbital. Conversely, an increase in $\bar{w}_e'$ and decrease in r_e' relative to the parameters in the neutral molecule indicates ionisation from an antibonding orbital and consequent strengthening of the bond in the ion. It should be noted that this approach is approximate, makes no allowance for reorganisation and can sometimes break down e.g. in the 3rd pe band of CO and the 1st pe band of AlF.

Further evidence which may be derived from a photoelectron band involves the measurement of molecular spin-orbit coupling constants. This can be an invaluable aid to spectral assignment since spin-orbit coupling constants predicted theoretically may be fairly easily obtained using an approximate wavefunction. Spin-orbit coupling is caused by an interaction between the spin and orbital angular momentum in a molecule or ion in a particular state. It is probably useful, at this stage, to explain the origin of the interaction. For a diatomic molecule obeying Hund's case a) shown below;

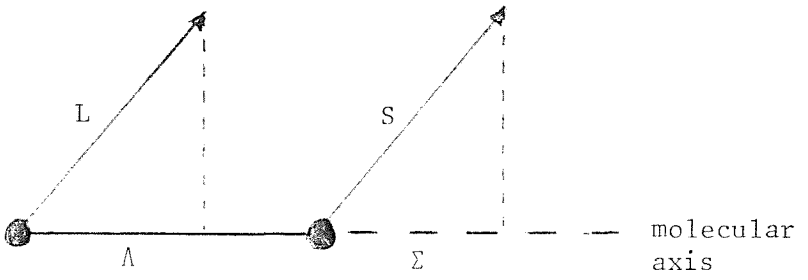

a particular electronic state is labelled $^{2S+1}\Lambda_{g,u}$. Λ refers to the total orbital angular momentum along the molecular axis and (2S+1) is the spin multiplicity. The subscripts g and u indicate the overall symmetry of the state with respect to inversion in the molecular centre of symmetry. Spin-orbit components are given by:

$$\Omega = \Lambda + \Sigma \tag{3.140}$$

where Σ takes on values S, S-1,...,-S and is the component of S along the molecular axis. As an example, consider the $^4\Pi_u$ and $^2\Pi_u$ states of the O_2^+ ion. The $^4\Pi_u$ state,

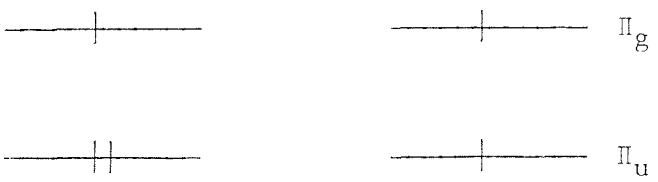

has $\Lambda = 1$ and $S = {}^3/_2$. Four spin-orbit components are expected with $\Omega = {}^5/_2$, ${}^3/_2$, $\frac{1}{2}$ and $-\frac{1}{2}$. Similarly, the $^2\Pi_u$ state has $\Lambda = 1$ and $S = \frac{1}{2}$ giving two components with $\Omega = {}^3/_2$, $\frac{1}{2}$. Each value of Ω will have a marginally different energy and the splitting can be observed providing the resolution of the photoelectron spectrometer is sufficiently good. The energies of spin orbit components are given by $E = E_o + G\Lambda\Sigma$, where E_o is the energy in the absence of spin-orbit coupling and G is the spin-orbit coupling coefficient. The observance of spin-orbit splitting shows that an observed state has a spin multiplicity greater than one and

non-zero orbital angular momentum since, for splitting to be observed, Ω must have more than one value. Furthermore, a spin-orbit coupling model may be invaluable in assigning experimental pe spectra. The magnitude of the splitting in a particular electronic state may be predicted theoretically and then compared with experiment (53,54).

Examples of the information to be derived from photoelectron spectra of atoms and molecules will be given in Chapters 5, 6 and 7. In particular, vibrational structure is observed in the experimental work on TiO, VO, CrO and AlF allowing Franck-Condon calculations to be performed and ionic equilibrium bond lengths to be estimated.

APPENDIX

Vector coupling coefficients for ATMOL3 openshell method (GRHF)

It is the purpose of this section to illustrate how the vector coupling coefficients to be used in an ATMOL3 openshell calculation on a linear molecule may be derived (55). First it is necessary to define several quantities:-

F_{mm} = the expectation value of the m'th molecular orbital over the unscreened one-particle Hamiltonian operator for the system.

$F_M = \sum_{m\epsilon M} F_{mm}$ = the sum of the one-particle expectation values for all molecular orbitals in shell M.

J_{mn} = (mm/nn) = the coulomb integral between molecular orbitals m and n.

$J_{MN} = \sum_{m\epsilon M} \sum_{n\epsilon N} J_{mn}$

K_{mn} = (mn/mn) = the exchange integral between molecular orbitals m and n.

$K_{MN} = \sum_{m\epsilon M} \sum_{n\epsilon N} K_{mn}$

Having defined these quantities it is now possible to define the type of energy expression which can be handled by the GRHF module (55) of the ATMOL3 package as follows:

$$E = \sum_{M}^{NSHELL} W_M F_M + \sum_{M}^{NSHELL} \sum_{N}^{NSHELL} X_{MN} J_{MN} + \sum_{M}^{NSHELL} \sum_{N}^{NSHELL} Y_{MN} K_{MN} \ldots (A)$$

where W_M are the one-electron energy expression parameters (which are simply equal to the number of electrons in a particular shell), X_{MN} are the coulomb energy expression parameters, Y_{MN} are the exchange energy expression parameters and NSHELL is the total number of shells in the system. It is the values of X_{MN} and Y_{MN} (the so-called "vector coupling coefficients") which need to be calculated and which are the subject of this Appendix.

The derivation proceeds via the method of Rose and McKoy (56), using real molecular orbital functions, and the coefficients thus obtained are then converted to ATMOL standards. This method is thought to be simpler than deriving the ATMOL coefficients directly since the use of complex functions is avoided (as used in refs. (58) and (59)).

Rose and McKoy (56) define the expression for the total energy of an open-shell system as:

$$E = 2\sum_{q=1}^{Q} f_q \sum_{\phi_i \varepsilon \{\phi_q\}} h_i + \sum_{q=1}^{Q}\sum_{p=1}^{Q} f_q f_p \sum_{\phi_i \varepsilon \{\phi_q\}} \sum_{\phi_i \varepsilon \{\phi_p\}} (2\, a_{qp}\, J_{ij} - b_{qp}\, K_{ij}) \quad \ldots(B)$$

The occupied spatial orbitals are divided into Q shells, each containing the set of orbitals $\{\phi_q\}$. Here f_q is the fractional occupation of shell q, a_{qp} and b_{qp} are the elements of a symmetric matrix specifying the interactions between shells q and p and h_i, J_{ij} and K_{ij} are defined as follows:

$$h_i = \langle \phi_i | h | \phi_i \rangle,$$

$$J_{ij} = \langle \phi_i(1)\ \phi_j(2) | 1/r_{12} | \phi_i(1)\ \phi_j(2) \rangle,$$

$$K_{ij} = \langle \phi_i(1)\ \phi_j(2) | 1/r_{12} | \phi_j(1)\ \phi_i(2) \rangle.$$

The expressions for J_{ij} and K_{ij} are identical to those for J_{mn} and K_{mn} in equation (A).

The first step in the calculation is to write down the energy expression in terms of the J and K interactions between the constituent shells. For example, consider a $\sigma^1\ \pi^2$ configuration:

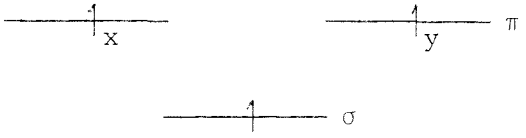

For the $^4\Sigma^-$ state, the energy expression may be written as

$$E = (J_{\sigma x} + J_{\sigma y} - K_{\sigma x} - K_{\sigma y})_{\sigma\pi} + (J_{xy} - K_{xy})_{\pi\pi}.$$

Expressionssuch as this are simple to derive. For every pair of electrons of the same spin there is one J term and one K term i.e. E = (J - K). In the case of two electrons of opposite spin, there will again be a J term but no K term since exchange integrals only exist

between electrons of like spin. Thus for the imaginary configuration $a^1\ b^1$ there are two possible energies:

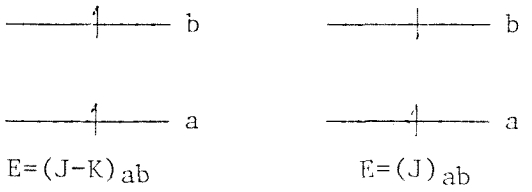

The two configurations are separated by an energy, K, which should be apparent from the above expressions. Using these simple rules, it is a trivial matter to write down an expression for any state in any electronic configuration provided that the electrons are properly counted. As another example consider the $\sigma^1\ \pi^2$, $^2\Delta$ state:

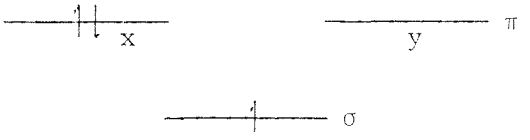

$$E=(2J_{\sigma x}-K_{\sigma x})_{\sigma\pi} + (J_{xx})_{\pi\pi}$$

Comparison of this expression with that written down previously for the $^4\Sigma^-$ state shows that there are still three J terms but only one K term since one electron now has opposite spin. To show how the vector coupling coefficients are derived from the Rose and McKoy energy expression (56) and then converted to ATMOL standards, a simple example will be considered.

Consider the $^3\Delta$ state arising from the $\pi_i^1\ \pi_j^1$ configuration. From Raftery et al (58), the correctly formulated wavefunction which is an eigen function of S^2, S_Z, and Λ is

$$\Psi = |\pi_i^+\pi_j^+|.$$

The corresponding energy is $E = (J_o - K_o)_{\pi_i\pi_j}$.

Note: page out of sequence.

$$= \tfrac{1}{4}\{2K_{xx*} + K_{xx*} - 2K_{xy*} + K_{yy*} - 2K_{yx*}\}$$

$$= K_{xx*} - K_{xy*}$$

Then $E = (J_o - K_o)_{\pi_i\pi_j}$

$$= \tfrac{1}{2}J_{xx*} - \tfrac{1}{2}J_{xy} - K_{xx*} + K_{xy*}$$

$$= 4\{\frac{1}{8}J_{xx*} + \frac{1}{8}J_{xy} - \tfrac{1}{4}K_{xx*} - \tfrac{1}{4}K_{xy*}\}$$

These vector coupling coefficients agree with those given in the ATMOL manual.

i.e. coulomb $xx* = \frac{1}{8}$

$xy* = \frac{1}{8}$

exchange $xx* = -\frac{1}{4}$

$xy* = \frac{1}{4}$

The method outlined above becomes very complicated and time-consuming when considering more intricate configuration types. Three worked examples will be discussed to illustrate how the vector coupling coefficients may be derived in a simpler way.

Example One - $\sigma^1\pi^3$

$^3\Pi$ state

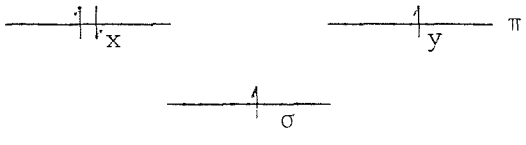

σ-σ terms

$E = 0 (= J_{\sigma\sigma} - K_{\sigma\sigma})$ since $J_{\sigma\sigma} = K_{\sigma\sigma}$ by definition. By default the ATMOL method takes values of $\frac{1}{2}$ and $-\frac{1}{2}$ for the J and K coefficients respectively.

Note: page out of sequence.

σ-π terms

$$E = 2J_{\sigma x} + J_{\sigma y} - K_{\sigma x} - K_{\sigma y}$$
$$= 2J_{\sigma y} + J_{\sigma x} - K_{\sigma y} - K_{\sigma x}$$

Both expressions on the RHS of the above will be equal since the $^3\Pi$ state has two possible configurations: $\sigma\bar{x}xy$ and $\sigma\bar{y}yx$.

Any derivation of the vector coupling coefficients will, of course, take both configurations into account:

Thus: $$E = \tfrac{3}{4}\begin{bmatrix} J_{\sigma x} \\ J_{\sigma y} \\ J_{y\sigma} \\ J_{x\sigma} \end{bmatrix} - \tfrac{1}{2}\begin{bmatrix} K_{\sigma x} \\ K_{\sigma y} \\ K_{y\sigma} \\ K_{x\sigma} \end{bmatrix}$$

The coupling coefficients for use in the ATMOL method may now be simply read off since further conversion is not required.

$$\text{coulomb term} = \tfrac{3}{4}$$
$$\text{exchange term} = -\tfrac{1}{2}$$

π-π terms

$$E = J_{xx} + 2J_{xy} - K_{xy}$$
$$= J_{yy} + 2J_{yx} - K_{yx}$$
$$= \tfrac{1}{2}\begin{bmatrix} J_{xx} \\ J_{yy} \end{bmatrix} + \begin{bmatrix} J_{xy} \\ J_{yx} \end{bmatrix} - \tfrac{1}{2}\begin{bmatrix} K_{xy} \\ K_{yx} \end{bmatrix}$$

Since the ATMOL method uses coefficients for terms such as K_{xx} and K_{yy} not given above, allowance must be made for this. Since $J_{xx} = K_{xx}$ and $J_{yy} = K_{yy}$ by definition, $\tfrac{1}{2}\begin{bmatrix} J_{xx} \\ J_{yy} \end{bmatrix}$ may be added to the first matrix on the right handside of the above equation while $\tfrac{1}{2}\begin{bmatrix} K_{xx} \\ K_{yy} \end{bmatrix}$ may be subtracted from the third matrix.

Thus: $E = \begin{bmatrix} J_{xx} \\ J_{yy} \\ J_{xy} \\ J_{yx} \end{bmatrix} - \frac{1}{2} \begin{bmatrix} K_{xy} \\ K_{yx} \\ K_{yy} \\ K_{xx} \end{bmatrix}$

The ATMOL coupling coefficients may again simply be read off:

coulomb term = 1

exchange term = $-\frac{1}{2}$

Coupling coefficients for the $\sigma^1\pi^3$, $^1\Pi$ state may be similarly derived and are given in the table at the end of this Appendix.

Example Two - $\pi_u^3\pi_g^3$

$^3\Delta$ state

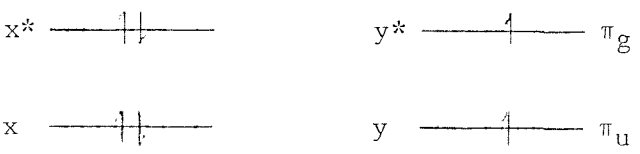

π_u-π_u terms

Note that the results for π_g - π_g will be identical.

$E = 2J_{xx} + J_{xy} - K_{xy}$

$= \begin{bmatrix} J_{xx} \\ J_{yy} \\ J_{xy} \\ J_{yx} \end{bmatrix} - \frac{1}{2} \begin{bmatrix} K_{xy} \\ K_{yx} \\ K_{yy} \\ K_{xx} \end{bmatrix}$ by analogy with the π-π terms of the $\sigma^1\pi^3$ ($^3\Pi$) configuration.

coulomb term = 1

exchange term = $-\frac{1}{2}$

π_u-π_g terms

$$E = 4J_{xx*} + 2J_{xy*} + 2J_{yx*} + J_{yy*} - K_{yy*} - K_{xy*} - 2K_{xx*}$$
$$= \frac{9}{2}J_{xx*} + \frac{9}{2}J_{x*y} - 3K_{xx*} - K_{xy*}$$

$$= \frac{9}{2}\cdot\frac{1}{4}\begin{bmatrix} J_{xx*} \\ J_{xy*} \\ J_{x*y} \\ J_{yy*} \end{bmatrix} + \frac{9}{2}\cdot\frac{1}{4}\begin{bmatrix} J_{xx*} \\ J_{xy*} \\ J_{x*y} \\ J_{yy*} \end{bmatrix} - 3\cdot\frac{1}{4}\begin{bmatrix} K_{xx*} \\ K_{xy*} \\ K_{x*y} \\ K_{yy*} \end{bmatrix} - \frac{1}{4}\begin{bmatrix} K_{xx*} \\ K_{xy*} \\ K_{x*y} \\ K_{yy*} \end{bmatrix}$$

coulomb terms: $xx^* = \frac{9}{8}$, $x^*y = \frac{9}{8}$

exchange terms: $xx^* = -\frac{3}{4}$, $x^*y = -\frac{1}{4}$.

Example Three - $\sigma^1\pi^1\delta^2$

This configuration is one used in a calculation on the CrO($X^5\Pi$) state

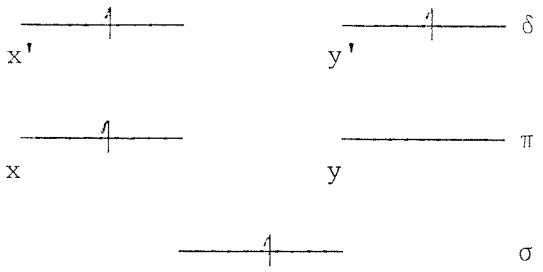

Three types of terms are involved, namely the σ-π, σ-δ and π-δ. The first two may be deduced by analogy with the $\sigma^1\pi^1$ and $\sigma^1\pi^2$ configurations tabulated in the ATMOL manual. Only the π-δ terms need to be calculated and this is done below:

$$E = J_{xx1} + J_{xy1} - K_{xx1} - K_{xy1}$$
$$= \frac{1}{4}\begin{bmatrix} J_{xx1} \\ J_{xy1} \\ J_{yx1} \\ J_{yy1} \end{bmatrix} + \frac{1}{4}\begin{bmatrix} J_{xx1} \\ J_{xy1} \\ J_{yx1} \\ J_{yy1} \end{bmatrix} - \frac{1}{4}\begin{bmatrix} K_{xx1} \\ K_{xy1} \\ K_{yx1} \\ K_{yy1} \end{bmatrix} - \frac{1}{4}\begin{bmatrix} K_{xx1} \\ K_{xy1} \\ K_{yx1} \\ K_{yy1} \end{bmatrix}$$

The ATMOL package, however, uses real functions. π_i^+, π_i^- etc can be converted to real functions as follows:-

———————x* ———————y* $\pi_j^+ = \frac{1}{\sqrt{2}}(x^* + iy^*)$

$\pi_j^- = \frac{1}{\sqrt{2}}(x^* - iy^*)$

———————x ———————y $\pi_i^+ = \frac{1}{\sqrt{2}}(x + iy)$

$\pi_i^- = \frac{1}{\sqrt{2}}(x - iy)$

Expressions for J_o and K_o in terms of real functions must now be found. i.e.

$$J_o = ((\pi_i^+)^* \pi_i^+ | (\pi_j^+)^* \pi_j^+)$$

$$= (\pi_i^- \pi_i^+ | \pi_j^- \pi_j^+)$$

Substituting in for π_i^+ etc.

$$J_o = \tfrac{1}{4}\{(x - iy)(x + iy) | (x^* - iy^*)(x^* + iy^*)\}$$

expanding out

$$J_o = \tfrac{1}{4}\{(xx + yy | x^*x^* + y^*y^*) - (yx - xy | y^*x^* - x^*y^*)$$
$$-i\ (yx - xy | x^*x^* + y^*y^*) - i\ (xx + yy | y^*x^* - x^*y^*)\}$$

$$= \tfrac{1}{4}\{2J_{xx^*} - 2J_{xy}\}$$

$$K_o = ((\pi_i^+)^* \pi_j^+ | (\pi_j^+)^* \pi_i^+)$$

$$= (\pi_i^- \pi_j^+ | \pi_j^- \pi_i^+)$$

$$= \tfrac{1}{4}\{(x - iy)(x^* + iy^*) | (x^* - iy^*)(x + iy)\}$$

expanding out

$$K_o = \tfrac{1}{4}\{(xx^* | x^*x) + (xx^* | y^*y) + (yy^* | x^*x)$$
$$+ (yy^* | y^*y) - (yx^* | y^*x) + (xy^* | y^*x)$$
$$+ (yx^* | x^*y) - (xy^* | x^*y)\}$$

coulomb terms: $xx^* = \frac{1}{4}$, $xy^* = \frac{1}{4}$

exhange terms: $xx^* = -\frac{1}{4}$, $xy^* = -\frac{1}{4}$.

Conversion from Rose and McKoy to ATMOL standards

It would be useful at this stage to show how the values tabulated by Rose and McKoy (56) can be converted to ATMOL standards. The tabulated values (56) are those of a_{qp} and b_{qp} given in equation (B) of this Appendix. Comparison of equations (A) and (B) will show that the coupling coefficients to be used by the ATMOL method may be obtained by a simple multiplication, i.e.

$$X_{MN} \equiv f_q\, f_p\, 2\, a_{qp}$$

$$Y_{MN} \equiv -f_q\, f_p\, b_{qp}$$

where f_q and f_p are the fractional occupancies. Take the $\pi_u^3\pi_g^3$ configuration ($^3\Delta$) state as an example.

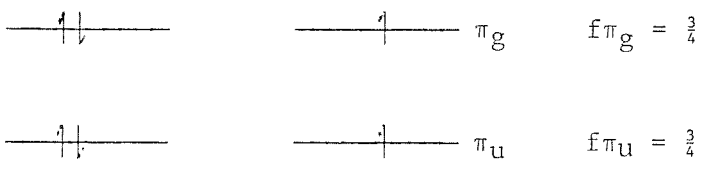

π_u-π_u terms

Coulomb term: $xx^* = \frac{3}{4} \cdot \frac{3}{4} \cdot 2.1 = \frac{9}{8}$

$xy^* = \frac{3}{4} \cdot \frac{3}{4} \cdot 2.1 = \frac{9}{8}$

Exchange term: $xx^* = -\frac{3}{4} \cdot \frac{3}{4} \cdot \frac{4}{3} = -\frac{3}{4}$

$xy^* = -\frac{3}{4} \cdot \frac{3}{4} \cdot \frac{4}{9} = -\frac{1}{4}$

These values agree with those calculated in this Appendix from first principles.

The paper by Rose and McKoy tabulates values for all the states arising from the $\pi_u^3\pi_g^3$ and $\pi_u^3\pi_g^1$ configurations allowing coupling coefficients for these configurations to be very simply calculated.

Coupling Coefficients derived from $\sigma^1\pi^n$ configurations

Configuration	State	Coulomb			Exchange		
		$\sigma\sigma$	$\sigma\pi$	$\pi\pi$	$\sigma\sigma$	$\sigma\pi$	$\pi\pi$
$\sigma^1\pi^1$	$^1\Pi$	$\frac{1}{2}$	$\frac{1}{4}$	0	$-\frac{1}{2}$	$\frac{1}{4}$	0
	$^3\Pi$	$\frac{1}{2}$	$\frac{1}{4}$	0	$-\frac{1}{2}$	$-\frac{1}{4}$	0
$\sigma^1\pi^2$	$^2\Sigma^+$	$\frac{1}{2}$	$\frac{1}{2}$	0	$-\frac{1}{2}$	$-\frac{1}{4}$	$\frac{1}{2}$
	$^2\Sigma^-$	$\frac{1}{2}$	$\frac{1}{2}$	$\frac{1}{2}$	$-\frac{1}{2}$	$\frac{1}{4}$	$-\frac{1}{2}$
	$^2\Delta$	$\frac{1}{2}$	$\frac{1}{2}$	$\frac{1}{4}$	$-\frac{1}{2}$	$-\frac{1}{4}$	0
	$^4\Sigma^-$	$\frac{1}{2}$	$\frac{1}{2}$	$\frac{1}{2}$	$-\frac{1}{2}$	$-\frac{1}{2}$	$-\frac{1}{2}$
$\sigma^1\pi^3$	$^1\Pi$	$\frac{1}{2}$	$\frac{3}{4}$	1	$-\frac{1}{2}$	0	$-\frac{1}{2}$
	$^3\Pi$	$\frac{1}{2}$	$\frac{3}{4}$	1	$-\frac{1}{2}$	$-\frac{1}{2}$	$-\frac{1}{2}$

Identical parameters are obtained for the corresponding $\sigma^1\delta^n$ configurations and their constituent states.

Coupling Coefficients derived from $\pi^n\delta^n$ configurations

Configuration	State	Coulomb			Exchange		
		$\pi\pi$	$\pi\delta$	$\delta\delta$	$\pi\pi$	$\pi\delta$	$\delta\delta$
$\pi^1\delta^2$	$^4\Pi$	0	$\frac{1}{4}$	$\frac{1}{2}$	0	$-\frac{1}{4}$	$-\frac{1}{2}$
$\pi^3\delta^2$	$^4\Pi$	1	$\frac{3}{4}$	$\frac{1}{2}$	$-\frac{1}{2}$	$-\frac{1}{2}$	$-\frac{1}{2}$
$\pi^3\delta^1$	$^3\Phi$	1	$\frac{3}{8}$	0	$-\frac{1}{2}$	$-\frac{1}{4}$	0

Only the lowest energy state is given here (58, 59).

Coupling coefficients for other configurations have been listed in the ATMOL manual (55).

References

1. H. Eyring, J. Walters and G.E. Kimball, "Quantum Chemistry", Wiley (1960).

2. M. Born and R. Oppenheimer, Ann. Phys., 84, 457 (1927).

3. J.W. Rabalais, "Principles of Ultraviolet Photoelectron Spectroscopy", Wiley-Interscience (1977).

4. J.H.D. Eland, "Photoelectron spectroscopy", Butterworths (1974).

5. C.C.J. Roothaan, Rev. Mod. Phys., 23, 161 (1951).

6. C.C.J. Roothaan, Rev. Mod. Phys., 32, 179 (1960).

7. C.A. Coulson, "Valence", 2nd Edn., Oxford University Press (1961).

8. R.G. Parr, "Quantum Theory of Molecular Electronic Structure," W.A. Benhamin (1963).

9. T. Koopmans, Physica, 1, 104 (1934).

10. W.G. Richards, Int. J. Mass Spectrom. Ion. Phys., 2, 419 (1969).

11. P.E. Cade, K.D. Sales and A.C. Wahl, J. Chem. Phys., 44, 1973 (1966).

12. A.B. Cornford, D.C. Frost, C.A.M. McDowell, I.L. Ragle and F.A. Stenhouse, J. Chem. Phys., 54, 2651 (1971).

13. S. Huzinaga, Phys. Rev., 120, 866 (1960).

14. R. McWeeny, Proc. Roy. Soc. (London)., A235, 496 (1956).

15. R. McWeeny, Proc. Roy. Soc. (London), A241, 239 (1957).

16. R. McWeeny, Phys. Rev. 126, 1028 (1962).

17. V.R. Saunders and I.H. Hillier, Int. J. Quant. Chem., 7, 699 (1973).

18. J.L. Dodds and R. McWeeny, Chem. Phys. Lett., 13, 9 (1972).

19. R. McWeeny, "Molecular Orbitals in Chemistry, Physics and Biology", Ed. P-O Lowdin and B. Pullman, Academic Press (1964).

20. I. Hillier and V.R. Saunders, Int. J. Quant. Chem., 4, 503 (1970).

21. M.F. Guest and V.R. Saunders, Mol. Phys., 28, 819 (1974).

22. M.F. Guest and V.R. Saunders, Mol. Phys., 29, 873 (1975).

23. ATMOL3 Manual, Rutherford Appleton Laboratory, Didcot, Oxon (1976).

24. W. Ritz, J. Reine Angew. Math., 135, 1 (1909).

25. M.F. Guest and W.R. Rodwell, SPLICE Parts 1-4, users manual, Rutherford Appleton Laboratory, Didcot, Oxon (1977).

26. G. Rumer, Gottinger Nachr. 377 (1932).

27. R.C. Raffenetti, K. Hsu and I. Shavitt, Theor. Chim. Acta., 34, 105 (1974).

28. S.F. Boys, C.M. Reeves and I. Shavitt, Nature 178, 1207 (1956).

29. B.T. Sutcliffe, J. Chem. Phys., 45, 235 (1966).

30. I. Shavitt, C.F. Bender, A. Pipano and R.P. Hosteny, J. Comput. Phys., 11, 90 (1973).

31. A.C. Wahl and G. Das, "Methods of Electronic Structure Theory", vol. 3, Ed. H.F. Schaefer III, Plenum Press, New York (1977).

32. A.C. Hurley, "Electron Correlation in Small Molecules", Academic Press, London (1976).

33. W. Meyer, J. Chem. Phys., 58, 1017 (1973).

34. H.J. Silverstone and O. Sinanoglu, J. Chem. Phys., 44, 1899, 3608 (1966).

35. W. Meyer, "Methods of Electronic Structure Thoery", vol. 3, Ed. H.F. Schaefer III, Plenum Press, New York (1977).

36. R.K. Nesbet, J. Chem. Phys., 43, 311 (1965).

37. E.J. Baerends and P. Ros, Int. J. Quantum Chem., 12, 169 (1978).

38. E.J. Baerends, D.E. Ellis and P. Ros, Chem. Phys., 2, 41 (1973).

39. E.J. Baerends and P. Ros, Chem. Phys., 2, 52 (1973).

40. J.C. Slater, Phys. Rev., 81, 385 (1951).

41. N.H.F. Beebe, Chem. Phys. Lett., 19, 290 (1973).

42. C. Roetti and E. Clementi, J. Chem. Phys., 60, 4725 (1974).

43. S.F. Boys, Proc. R. Soc. London Ser. A, 200, 542 (1950).

44. H. Basch, C.J. Hornback and J.W. Moskowitz, J. Chem. Phys., 51, 1311, (1969).

45. A.J.H. Wachters, J. Chem. Phys., 52, 1033-1036 (1970).

46. B. Roos, A. Veillard and G. Vinot, Theor. Chim. Acta, 20, 1 (1971).

47. B. Roos and P. Siegbahn, Theor. Chim. Acta, 17, 209 (1970).

48. R.C. Raffenetti, J. Chem. Phys., 58, 4452 (1973).

49. P.J. Hay, J. Chem. Phys., 66, 4377 (1977).

50. See for example:

(a) C.E. Moore, Atomic Energy Levels, Nat. Bur. Stand., Circ. 467 (US Govt. Printing Office, Washington D.C., 1949) vols. 1-3.

(b) JANAF Thermochemical Tables, Ed. D.R. Stull and H. Prophet (Nat. Bur. Stand., Washington D.C., 2nd Edn. 1971), vol. 37.

51. G. Herzberg, Molecular Spectra and Molecular Structure:I. Spectra of Diatomic Molecules, 2nd. Edn. Van Nostrand (1961).

52. M.P. Hastings, 3rd year project, University of Southampton (1981).

53. S.J. Dunlavey, J.M. Dyke and A. Morris, J. El. Spec. Rel. Phen., 12, 259 (1977).

54. E.A. Colbourn, J.M. Dyke, N.K. Fayad and A. Morris, J. El. Spec. Rel. Phen., 14, 443 (1978).

55. V.R. Saunders and M.F. Guest, ATMOL3 Manual (Part 9), Rutherford Appleton Laboratory, Didcot, Oxon. No. RL-76-106 (August 1976).

56. J.B. Rose and V. McKoy, J. Chem. Phys., 55, 5435 (1971).

57. J.M. Dyke, B.W.J. Gravenor, R.A. Lewis and A. Morris, J. Chem. Soc. Faraday Trans. 2, 79, 1083 (1983).

58. J. Raftery, P.R. Scott and W.G. Richards, J. Phys. B, 5, 1293 (1972).

59. P.R. Scott, J. Raftery and W.G. Richards, J. Phys. B, 6, 881 (1973).

CHAPTER FOUR

The Use of Configuration Interaction Calculations to Interpret the Photoelectron Spectra of AlF, CS and SiS

4.1. Introduction

In recent years, the use of configuration interaction (CI) calculations in the study of the electronic structure of molecules has increased quite considerably. The advent of faster and more efficient computers has made it possible to study systems previously considered too large to handle. CI calculations have been used on several occasions to assign experimental spectra recorded during the course of this work, notably in assigning the photoelectron spectra of titanium monoxide, vanadium monoxide and chromium monoxide (Chapter 6) and aluminium monofluoride (Chapter 7).

The aim of the work described in this chapter was to study, via configuration interaction calculations, the molecules AlF, CS and SiS. The work on AlF described here is discussed with reference to experimental work performed at Southampton and described in Chapter 7 of this thesis. Experimental work on CS performed previously (1-5) and recent calculations on SiS (6) are used for purposes of comparison. CS was one of the first short-lived molecules to be studied in the gas-phase with u.v. pes and it is notable in that Koopmans' theorem fails to predict the correct number of bands in the HeI photoelectron spectrum. It is also worth mentioning that a preliminary experimental study on SiS has been performed at Southampton (7) and it is intended that the present configuration - interaction calculations will be used in the eventual assignment of the spectrum when a better experimental spectrum is obtained. Before the present calculations were commenced and while the experimental work on AlF was in progress, it was thought that the isoelectronic molecules AlF and CS would have very similar experimental spectra while the spectrum of the valence isoelectronic molecule SiS would also bear some similarities to those of AlF and CS.

The method of configuration interaction has been outlined in Chapter 3 of this thesis and this should be consulted for further details of the method. In Chapter 3 only single and double excitations from the reference configuration or configurations are allowed with some constraint over which occupied orbitals are deemed "frozen" and which virtual orbitals are open to substitution. It should be noted that this is an approximation which means that only a part of the total correlation energy can be taken

into account for a given state of a molecule or ion. Higher excitations (triple and quadruple) also will improve the accuracy of the CI calculations although this is not possible when using the present method at Southampton because of restrictions on the use of computing time and storage space. Sinanoglu (8) has explained that the effect of triple excitations from the reference configuration on both closed and open shell systems is generally negligible while the effect of quadruple excitations can be quite important because of simultaneous electron pair correlations. Davidson (9) has described an approximate method to allow for the effect of quadruple excitations on the total correlation energy. The fraction of the correlation energy which comes from quadruple excitations was found to be roughly $1-Co^2$ where Co is the coefficient of the reference configuration in the total CI expansion when only single and double excitations are considered. For a molecule such as N_2 this was found to be approximately 7% of the total correlation energy. It was decided, however, not to correct for the effect of quadruple excitations in the present calculations by this method because of its lack of theoretical justification plus the fact that the calculations performed at Southampton involve subtraction of the total energy of the molecule and ion, after allowance for some correlation energy in each state and hence there will be some cancellation of the small contributions arising from quadruple excitations. A more accurate estimation of the correlation energy in a given state could be obtained by increasing the number of single and double excitations allowed in the CI expansion or by performing calculations using the PNO-CEPA method which takes the effect of higher excitations into account (10,11).

To sum up, the calculations described in this chapter proceed with the determination of the SCF total energy for both molecule and ion both at the molecular equilibrium geometry and then correlation energy in each state is allowed for by a separate CI calculation on both molecule and ion. Subtraction of the corrected total energy of the ion from that of the molecule gives an estimate of the correlation corrected vertical ionisation potential. This process is carried out for all allowed bands with several excited states of each molecular or ionic state being generated. The coefficients of allowed contributions to formally forbidden bands may then simply be read off from the computer output for these excited states.

4.2. Computational Details

In this chapter, ab initio SCF calculations were performed on the three molecules AlF, CS and SiS using the ATMOL 3 suite of programs (12). The respective ground state configurations of the three molecules may be written as:

$$AlF(X^1\Sigma^+) \text{ ---------- } (5\sigma)^2(6\sigma)^2(2\pi)^4(7\sigma)^2$$

$$CS(X^1\Sigma^+) \text{ ---------- } (5\sigma)^2(6\sigma)^2(2\pi)^4(7\sigma)^2$$

$$SiS(X^1\Sigma^+) \text{ ---------- } (7\sigma)^2(8\sigma)^2(3\pi)^4(9\sigma)^2$$

Ionisations from the three outermost molecular orbitals of the three molecules were to be studied corresponding to two $^2\Sigma^+$ states and one $^2\Pi$ state in the ion.

The basis set used for all SCF calculations was a double-zeta STO basis set taken from those of Roetti and Clementi (13) with added STO polarisation functions.

(i) For AlF the polarisation function exponents used were Al 4s (1.00), 4p (1.00), 3d (1.35) and F3d (2.01). All of the SCF calculations on AlF were performed at the experimental equilibrium bond length of AlF $X^1\Sigma^+$ of 1.6544Å (14-17).

(ii) For CS the polarisation function exponents used were C 3d (2.27) and S 4s (1.00), 4p (1.00) and 3d (1.40). All of the SCF calculations on CS were performed at the experimental equilibrium bond length of CS $X^1\Sigma^+$ of 1.5349Å (18), and

(iii) Finally for SiS the polarisation function exponents used were Si 4s (1.00), 4p (1.00) and 3d (1.35) and S 4s (1.00), 4p (1.00) and 3d (1.40). All of the SCF calculations on SiS were performed at the experimental equilibrium bond length of SiS $X^1\Sigma^+$ of 1.9293Å (18).

The above calculations have been supplemented by configuration interaction calculations on the neutral molecules and a number of ionic states. These calculations were performed using the SPLICE suite of programs (19). The calculations applied the same criteria to each molecule i.e. in each case the same number of occupied orbitals and valence orbitals were open to substitution. In the case of CS and AlF only the orbitals 5σ to 13σ and 2π to 6π were open to substitution. The frozen orbitals for CS corresponded to contributions from the 1s, 2s and 2p orbitals of S and from the 1s orbital of C. Similarly the frozen orbitals for AlF corresponded to contributions from the 1s, 2s and 2p orbitals of Al and the 1s orbital of F. In both cases the energy of the lowermost active orbital was -1.6au while that of the uppermost active orbital was +1.6au. In the case of SiS, the corresponding orbitals open to substitution were 7σ to 15σ and 3π to 7π. The frozen orbitals corresponded to contributions from the 1s, 2s and 2p orbitals of both S and Si. The energy of the lowermost active orbital for SiS was -0.9au while that of the uppermost active orbital was +0.92au. It can be seen that, for each of the three molecules, there are 9 active σ orbitals and 5 active π orbitals. The CI calculations proceeded by entering a single reference configuration for states generated from $a(\sigma)^{-1}$ configuration and considered all single and double excitations from that reference configuration subject to the constraints outlined above. In the case of states generated from a $(\pi)^{-1}$ ionisation, two degenerate reference configurations were used and single and double excitation were generated from both these configurations, again subject to the constraints outlined above. For the neutral molecules, one reference configuration was used, corresponding to the ground state configuration of each molecule ($X^1\Sigma^+$ state). The results of the SCF calculations and these CI calculations are given in table 4.1. In all cases CI in the initial $X^1\Sigma^+$ ground state was negligible with the major contribution coming from the ground state configuration.

The figures in brackets in the fourth column of table 4.1. are the sum of coefficients of formally allowed contributions to the final CI wavefunction in the ion. Some explanation of the theoretical basis of this is required. The intensity of a photoelectron band is given by $|Q|^2$

where

$$Q = \int \psi_e^i (N) \sum_i \vec{eR}_i \psi_e^f (N) \, dt$$

where $\psi_e^i (N)$ and $\psi_e^f (N)$ are initial and final determinantal wavefunctions. Considering CI in the final wavefunction (CI is negligible in the initial state), then

$$\psi_e^f (N) = \sum_i C_i^f \psi_e^f (N)$$

Q can now be written as

$$Q = \int \psi_e^i (N) \sum_i \vec{eR}_i \sum_i C_i \psi_e^f (N) \, dt$$

$$= \sum_{l_1} C_{l_1} \int \psi_e^i (N) \sum_i \vec{eR}_i \psi_e^f (N)' dt \quad \text{---------- (A)}$$

$$+ \sum_{k_2} C_{k_2} \int \psi_e^i (N) \sum_i \vec{eR}_i \psi_e^f (N)'' dt$$

where $\psi_f (N)'$ are final determinantal wavefunctions which differ from $\psi_e^i (N)$ by only one spin orbital and $\psi_f (N)''$ differ from $\psi_e^i (N)$ by more than one spin orbital (note that $i = l_1 + k_2$). If there is no reorganisation in the final state i.e. the same space orbitals can be used to construct $\psi_e^i (N)$ and $\psi_e^f (N)$, then terms in the second summation go to zero.

i.e. $$Q = \int \psi_e^i (N) \sum_i \vec{eR}_i \sum_i C_i \psi_e^f (N)' dt$$

$$= \sum_{l_1} C_{l_1} (\sqrt{2} \, m_{ph,i})$$

where $m_{ph,i} = \int \phi_i^* (1) \, \vec{eR}(1) \, \phi_{ph}(1) \, dt(1)$

In this case, the initial and final determinants in (A) differ by the space function ϕ_i in $\psi_e^i (N)$ and ϕ_{ph}, the free electron wave function in $\psi_e^f (N)'$.

The intensity of a band is determined by $|Q|^2$, hence

$$|Q|^2 = \sum_{l_1} C_{l_1}^2 \; (\sqrt{2}\; m_{ph,i})^2 + 4 \sum_{l_1 \geq k_1} \sum C_{k_1} \; C_{l_1} \; m_{ph_1,i}, m_{ph_k,j}$$

In the treatment presented in this thesis, the term in brackets is set to unity and the double summation is neglected. i.e. band intensities are estimated purely on the basis of the terms $\sum_{l_1} C_{l_1}^2$ and terms involving the free electron wavefunction are ignored. This treatment obviously also neglects reorganisation in the final state which will always occur. Hence the square of coefficients $C_{l_1}^2$ corresponds to the quantity quoted in table 4.1. To determine this, it is simply a matter of reading off the coefficients of the individual formally allowed configurations from the CI computer output and squaring them.

Manson (21) has identified three mechanisms which describe the breakdown of the one-electron picture in photoelectron spectroscopy. These are:

(i) initial-state configuration interaction (ISCI)
(ii) final ionic state configuration interaction (FISCI) and
(iii) interchannel coupling.

The CI calculations performed in this work can only take ISCI and FISCI into account. However, in the ground states of the neutral molecules CS, AlF and SiS the calculations indicate that one determinant is the main contributor to the CI expansion i.e. essentially FISCI calculations are being performed here.

4.3. Results and Discussion

The results of the SCF and CI calculations together with a table of computed electron density changes on ionisation for the three molecules under study are shown in tables 4.1 and 4.2. Table 4.1 shows that the calculations on all three molecules give very similar results with two $(\sigma)^{-1}$ ionisations giving rise to the $X^2\Sigma^+$ and $B^2\Sigma^+$ states in the ion and one $(\pi)^{-1}$ ionisation giving rise to the $A^2\Pi$ state in the ion. In addition in all three cases a fourth band, due to configuration interaction, is calculated to be approximately 3eV higher in ionisation energy than the $B^2\Sigma^+$ state.

The experimental HeI photoelectron spectrum recorded for AlF may be seen in figure 7.1 of chapter 7 of this thesis. It shows three bands as well as a broad weak feature centred at 16.10eV. This broad weak feature was subsequently assigned on experimental evidence to ionisation of aluminium trifluoride, AlF_3, present in the vapour over Al/AlF_3 mixtures. The first band of AlF, experimental v.i.p. 9.73±0.01eV can be assigned to the AlF^+ $X^2\Sigma^+$ state, derived from ionisation of the 7σ orbital, by comparison with the ΔSCF and ΔSCF plus CI calculated ips. The sum of the coefficients of formally allowed contributions totals to 0.96 which shows that there are practically no contributions to the CI wavefunction from other, formally forbidden, configurations.

The second band of AlF is more complicated. Experimentally it appears as a broad feature with band onset of 13.65eV and band maxima of 14.75eV. Both ΔSCF and ΔSCF plus CI calculations indicate that this band is made up of contributions from both $(2\pi)^{-1}$ and $(6\sigma)^{-1}$ ionisations i.e. both AlF^+ $A^2\Pi$ and $B^2\Sigma^+$ states. In the case of the AlF^+ $A^2\Pi$ state, the sum of coefficients of allowed contributions totals to 0.92. However, the CI calculation on the AlF^+ $B^2\Sigma^+$ state points to the existence of a configuration interaction band at 18.34eV with sum of coefficients of 0.09. This is sufficiently large for the band to be observed experimentally and is thus assigned to the experimental band at 15.33eV. This assignment is also supported by the PNO-CEPA calculations in chapter 7. The AlF^+ $B^2\Sigma^+$ state CI calculations showed that the CI band is due to the $(2\pi)^{-1}(7\sigma)^{-1}(3\pi)^{+1}$ configuration. This configuration gains intensity by interaction with the root configuration of the AlF^+ $B^2\Sigma^+$ state i.e. a configuration derived by one-electron ionisation from the neutral molecule. The relative intensity of the CI band and the band due to the AlF^+ $B^2\Sigma^+$ state may be estimated from squares of coefficients of formally allowed contributions to the CI wavefunction as 0.09:0.87 or 1:9.67. This relative intensity will be discussed further with reference to the calculations on CS and SiS.

The experimental spectrum of CS(1-5) is very similar to that of AlF in that it contains four bands, three due to one-electron ionisation from the neutral molecule and one due to configuration interaction.

The first band of CS has an experimentally measured v.i.p. of 11.33eV. The ΔSCF plus CI calculated value is 11.00eV with a sum of coefficients of 0.87 slightly reduced from the 0.96 of the AlF^+ $X^2\Sigma^+$ state. Ten higher roots of the CI wavefunction, starting with the determinant derived from the $(7\sigma)^{-1}$ ionisation as root function, were calculated but no roots corresponding to possible allowed bands were seen. Similarly, the second band of CS corresponding to the $(2\pi)^{-1}$ ionisation with an experimental v.i.p. of 12.90eV showed good agreement with a ΔSCF plus CI i.p. of 12.55eV. The sum of coefficients of allowed contributions in this case was 0.90 compared with the corresponding value of 0.92 in the case of AlF. The changes in electron density on ionisation for AlF and CS are shown in tables 4.2(a) and 4.2(b). Considering the first band of AlF and CS, the $X^2\Sigma^+ \leftarrow X^1\Sigma^+$ ionisation, it can be seen that, for AlF, the main change in electron density is in the Al(s) orbitals with small contributions from Al(p), F(p) and Al(d). The changes in electron density for the first band of CS are quite different. The main changes are in the C(s), S(s) and S(p) orbitals with small contributions from the C(p), C(d) and S(d) orbitals. The sum of squares of allowed contributions are 0.96 and 0.87 for the first bands of AlF and CS respectively. For the second bands of AlF and CS, the corresponding coefficients are 0.92 and 0.90 respectively. Tables 4.2(a) and 4.2(b) show that the main changes in electron density on ionisation are in Al(p) and F(p) for AlF and C(p) and S(p) for CS.

The third and fourth bands of CS bear some similarity with those of AlF. The calculated ΔSCF plus CI i.p. of 17.05eV for the $CS^+B^2\Sigma^+ \leftarrow CSX^1\Sigma^+$ ionisation compares reasonably well with the experimentally measured value of 16.06eV. Examination of the CI output for the $CS^+B^2\Sigma^+$ state showed the existence of a band at a calculated value of 20.26eV. A band at 18.03eV was in fact observed in the experimental spectrum. The calculation showed that this configuration interaction band is due to the $(2\pi)^{-1}(7\sigma)^{-1}(3\pi)^{+1}$ configuration which gains intensity by interaction with the root configuration of the $CS^+B^2\Sigma^+$ state i.e. a configuration derived by one-electron ionisation from the neutral molecule. This is the same configuration that gives rise to the configuration-interaction band in the AlF spectrum. The relative intensity of the CI band of CS and the band due to the $CS^+B^2\Sigma^+$

state may be estimated from the squares of coefficients of formally allowed contributions to the CI eigenvectors as 0.11:0.73 or 1:6.64, a substantial change compared to that of AlF. Unfortunately, the eigenvectors produced by the AlF CI calculations were not stored and it was then not possible to calculate changes in electron density on ionisation in this case.

Clearly, because AlF and CS have the same ground state electronic configuration, both molecules might be expected to show similar characteristics in their experimental photoelectron spectra. The present calculations have proved this to be so although there is scope for improvement in the calculated values. The present method only takes single and double excitations into account in the CI expansion. As mentioned earlier, triple and quadruple excitations can also be quite important and improved results could be obtained if these were included. Some attempt has been made to do this in the case of AlF (see chapter 7 of this thesis) using the PNO-CEPA method. This proved especially useful in the analysis of the second and third bands of AlF. Unfortunately, it was not possible to calculate a vertical ionisation potential for the fourth AlF band using the PNO-CEPA method.

In view of the fact that SiS is valence isoelectronic with CS and AlF, it is to be expected that the experimental pe spectra of SiS would be similar to that of CS and AlF. Unfortunately no experimental data on the pe spectrum of SiS is yet available so for the purposes of the present study comparison of calculated results must be discussed with reference to previous calculations performed by Von Niessen et al using a Green's Function method (6). As in the cases of CS and AlF, three one-electron ionisations from neutral SiS were considered i.e. $(9\sigma)^{-1}$, $(3\pi)^{-1}$ and $(8\sigma)^{-1}$ ionisations to give the $X^2\Sigma^+$, $A^2\Pi$ and $B^2\Sigma^+$ states in the ion respectively. Previous calculations showed (6) that the $^2\Sigma^+$ state was the ground state of the ion. However, the present ΔSCF calculations show (table 4.1(c)) that the SiS^+ $^2\Pi$ state would appear at lower i.p. than the SiS^+ $^2\Sigma^+$ state. Hence, on the evidence of the ΔSCF calculations the ground state of SiS^+ would be assigned as $X^2\Pi$. This assumption would be made without taking correlation energy changes on ionisation into account. However, on performing CI calculations on both states, this assignment must

be thrown into doubt. There is a negligible difference in computed vertical i.p. for the two states of 0.01eV. If a fuller CI had been performed for both states it would have been possible to assign the ground state of SiS^+ with greater confidence. Both bands appear from the CI calculations to be equally intense, as estimated as the sum of coefficients of formally allowed contributions to the final CI wave-functions, a situation essentially analogous to that of AlF and CS. Experimentally these two bands should be easy to distinguish since the $(\sigma)^{-1}$ ionisation will be sharp while the $(\pi)^{-1}$ ionisation will be broad. It is interesting to note that similar behaviour was observed for SiO(20). ΔSCF calculations failed to predict the correct ordering of the first two ionic states of SiO but subsequent CI calculations showed that the $^2\Sigma^+$ state derived by $(7\sigma)^{-1}$ ionisation was, in fact, the ground state of the ion.

The third band of SiS derived by $(8\sigma)^{-1}$ ionisation to give the $B^2\Sigma^+$ state in the ion shows good agreement with the previous calculated result (6). Several roots were calculated for the SiS^+ $B^2\Sigma^+$ state in the CI calculation and these calculations pointed to the existence of a configuration-interaction band at approximately 3eV higher in v.i.p. than the main SiS^+ $B^2\Sigma^+$ band. This CI band had an apparent intensity of 0.10 (table 4.1(c)) relative to an intensity of 0.71 for the main SiS^+ $B^2\Sigma^+$ ionisation as estimated from sums of squares of allowed contributions i.e. a relative intensity of 1:7.10, very similar to the value found for the same two bands in CS. The CI calculation showed that this configuration-interaction band is due to the $(3\pi)^{-1}(9\sigma)^{-1}(4\pi)^{+1}$ configuration which gains intensity by interaction with the root configuration of the SiS^+ $B^2\Sigma^+$ state i.e. a configuration derived by one electron ionisation from the neutral molecule. Table 4.2(b) shows that the electron density changes on ionisation for the $B^2\Sigma^+$ and CI bands for CS and SiS are very similar. For the $B^2\Sigma^+$ and CI bands the main changes in electron density in CS are in the C(s) and S(p) orbitals. By direct analogy it would be expected that similar changes in the Si(s) and S(p) orbitals would be observed. Reference to table 4.2(c) shows that this is indeed the case. To confirm the present calculations on SiS it would be useful to perform an experimental study on this molecule. Such a study has already been started in Southampton (7) and it is hoped that this work will stimulate further interest.

In conclusion, several points should be made:

(i) The results of the SCF calculations could be improved by using a larger basis set nearer to the Hartree-Fock limit. It was mentioned in chapter 3 of this thesis that a CI calculation can only be as good as its preceding SCF calculations. If the SCF calculations are improved there will be a consequent increase in accuracy in the CI results.

(ii) To take more account of correlation energy changes on ionisation a fuller CI calculation for each molecule needs to be performed. At present, the number of electron excitations to be included in a CI calculation needs to be severely curtailed due to limitations in computer time and data storage facilities. The advent of faster and more efficient computers should soon allow a more complete CI to be performed by including every possible single and double excitation.

(iii) The effect of triple and quadruple excitations may be quite important (8). Inclusion of these in a CI calculation is, at present, prohibitive. However, as in the case of AlF (see chapter 7 of the thesis) the PNO-CEPA method can take some account of triple and quadruple excitations. It has been estimated that $\sim$75% of correlation energy can be accounted for by the PNO-CEPA method (see chapter 3 for further details of this method).

Table 4.1.(a) Computed Vertical Ionisation Potentials of $AlF(X^1\Sigma^+)$[a]

Orbital Ionised	Ionic State	ΔSCF IP/eV	ΔSCF plus CI IP/eV	Experimental Value[d]	No. of Configurations[c]
7σ	$X^2\Sigma^+$	8.51	9.24 (0.96)[b]	9.73±0.01	2957
2π	$A^2\Pi$	12.99	13.44 (0.92)	13.6 -15.2	4826
6σ	$B^2\Sigma^+$	15.28	15.13 (0.87)		2957
-	$(C^2\Sigma^+)$	-	18.34 (0.09)	15.33±0.01	

(a) All calculations were performed at the experimental equilibrium bond length of $AlF(X^1\Sigma^+)$ of 1.6544Å (14-17).

(b) Values in brackets are the sum of coefficients of formally allowed contributions to the final CI wavefunctions.

(c) The CI calculation on $AlF(X^1\Sigma^+)$ produced 1567 configurations.

(d) See chapter seven of this thesis.

Table 4.1(b) Computed Vertical Ionisation Potentials of $CS(X^1\Sigma^+)$[e]

Orbital Ionised	Ionic State	ΔSCF IP/eV	ΔSCF plus CI IP/eV	Experimental Value[g]	No. of Configurations[h]
7σ	$X^2\Sigma^+$	11.01	11.00 (0.87)[f]	11.33	2957
2π	$A^2\Pi$	11.89	12.55 (0.90)	12.90	4826
6σ	$B^2\Sigma^+$	18.12	17.05 (0.73)	16.06	2957
-	$(C^2\Sigma^+)$	-	20.26 (0.11)	18.03	

(e) All calculations were carried out at the equilibrium bond length of $CS(X^1\Sigma^+)$ of 1.5349Å (18).

(f) Values in brackets are the sum of coefficients of formally allowed contributions to the final CI wavefunctions.

(g) Experimental results taken from refs. (1-5).

(h) The CI calculation on $CS(X^1\Sigma^+)$ produced 1567 configurations.

Table 4.1.(c) Computed Vertical Ionisation Potentials of $SiS(X^1\Sigma^+)$[i]

Orbital Ionised	Ionic State	ΔSCF IP/eV	ΔSCF plus CI IP/eV	Previous calculated Value[k]	No. of Configurations[1]
9σ	$X^2\Sigma^+$	10.00	9.98 (0.89)[j]	9.79	2957
3π	$A^2\Pi$	9.48	9.97 (0.90)	10.73	4826
8σ	$B^2\Sigma^+$	14.92	13.93 (0.71)	13.28	2957
-	$(C^2\Sigma^+)$	-	16.91 (0.10)	20.72	

(i) All calculations were performed at the experimental equilibrium bond length of $SiS(X^1\Sigma^+)$ of 1.9293Å (18).

(j) Values in brackets are the sum of coefficients of formally allowed contributions to the final CI wavefunctions.

(k) No experimetnal data available. Calculated values taken from ref. (6).

(l) The CI calculation on $SiS(X^1\Sigma^+)$ produced 1567 configurations.

Table 4.2.(a) Changes in Electron Density on Ionisation Calculated from AlF Converged SCF Wavefunctions

State	Atomic Orbital					
	Al(s)	F(s)	Al(p)	F(p)	Al(d)	F(d)
$AlF^+ X^2\Sigma^+$	0.8687	-0.0021	0.0552	0.0745	0.0105	-0.0068
$AlF^+ A^2\Pi$	-0.1252	-0.0287	0.3750	0.6849	0.0913	-0.0027
$AlF^+ B^2\Sigma^+$	0.1467	-0.0041	0.2813	0.5139	0.0572	-0.0051
$AlF^+ C^2\Sigma^+$	-	-	-	-	-	-

Table 4.2.(b) Changes in Electron Density on Ionisation Calculated from CS Converged SCF Wavefunctions[a]

State	Atomic Orbital					
	C(s)	S(s)	C(p)	S(p)	C(d)	S(d)
CS^+ $X^2\Sigma^+$	0.5997 (0.5932)	-0.1371 (-0.1267)	-0.0694 (-0.0769)	0.6231 (0.5933)	-0.0695 (-0.0776)	0.0529 (0.0948)
CS^+ $A^2\Pi$	0.1254 (0.1355)	-0.1646 (-0.1387)	0.3260 (0.3286)	0.6973 (0.6658)	-0.1207 (-0.1177)	0.1366 (0.1286)
CS^+ $B^2\Sigma^+$	0.2808 (0.3141)	0.2373 (0.1654)	0.0012 (0.0734)	0.3030 (0.3052)	0.0565 (-0.0382)	0.1213 (0.1803)
CS^+ $(C^2\Sigma^+)$	- (0.3203)	- (-0.0620)	- (0.1321)	- (0.5769)	- (-0.0344)	- (0.0669)

(a) Figures in brackets are the electron density changes derived from analysis of the CI Natural Orbitals.

Table 4.2.(c) Changes in Electron Density on Ionisation Calculated from SiS Converged SCF Wavefunctions[b]

State	Atomic Orbital					
	Si(s)	S(s)	Si(p)	S(p)	Si(d)	S(d)
SiS^+ $X^2\Sigma^+$	0.1738 (0.1631)	-0.1393 (-0.1415)	0.2706 (0.2474)	0.4739 (0.4765)	0.1081 (0.1128)	0.1129 (0.1417)
SiS^+ $A^2\Pi$	-0.0672 (-0.0327)	-0.1743 (-0.1540)	0.4801 (0.5026)	0.5620 (0.5102)	0.0551 (0.0425)	0.1443 (0.1313)
SiS^+ $B^2\Sigma^+$	0.2765 (0.4828)	0.2359 (-0.0099)	0.0018 (-0.0046)	0.2937 (0.4268)	0.0580 (-0.0136)	0.1341 (0.1185)
SiS^+ ($C^2\Sigma^+$)	- (0.2515)	- (-0.1217)	- (0.0129)	- (0.6639)	- (0.1400)	- (0.0534)

(b) Figures in brackets are the electron density changes derived from analysis of the CI natural orbitals.

REFERENCES

1. N. Jonathan, A. Morris, M. Okuda, D.J. Smith and K.J. Ross, Chem. Phys. Letts., 13, 334 (1972).

2. N. Jonathan, A. Morris, M. Okuda, K.J. Ross and D.J. Smith, Disc. Faraday Soc., 54, 48 (1972).

3. G.H. King, H.W. Kroto and R.J. Suffolk, Chem. Phys. Letts., 13, 457 (1972).

4. D.C. Frost, S.T. Lee and C.A. McDowell, Chem. Phys. Letts., 17, 153 (1972).

5. J. Schirmer, W. Domcke, L.S. Cederbaum and W. von Niessen, J. Phys. B., 11, 1901 (1978).

6. W. von Niessen, L.S. Cederbaum, J. Schirmer, G.H.F. Diercksen and W.P. Kraemer, J. El. Spec. Rel. Phen., 28, 45 (1982).

7. M.P. Hastings (unpublished data).

8. O. Sinancglu, J. Chem. Phys., 36, 706 (1962).

9. E.R. Davidson in 'The World of Quantum Chemistry' eds. R. Daudel and B. Pullman (D. Reidel Publ. Co., Dordrecht, Holland, 1974).

10. W. Meyer, J. Chem. Phys., 58, 1017 (1973).

11. W. Meyer in "Methods of Electronic Structure Theory", Vol. 3 ed. H.F. Schaefer III (Plenum Press, New York, 1977).

12. V.R. Saunders and M.F. Guest, ATMOL 3 Reference Manual (SERC, Rutherford Appleton Laboratory, 1976).

13. C. Roetti and E. Clementi, J. Chem. Phys., 60, 4725 (1974).

14. (a) D.R. Lide, J. Chem. Phys., 38, 2027 (1963).

    (b) D.R. Lide, J. Chem. Phys., 42, 1013 (1965).

15. A.G. Maki and F.J. Lovas, J. Mol. Spectry., 95, 80 (1982).

16. F.C. Wyse, W. Gordy and E.F. Pearson, J. Chem. Phys., 52, 3887 (1970).

17. J. Hoeft, F.J. Lovas, E. Tiemann and T. Torring, Z. Naturforsch, 25A, 1029 (1970).

18. K.P. Huber and G. Herzberg, 'Constants of Diatomic Molecules', (Van Nostrand Reinhold Co., New York, 1979) and references therein.

19. M.F. Guest and W.R. Rodwell, RL-77-110B. The Bonded Function CI Program, SERC, Rutherford Appleton Laboratory (1977).

20. E.A. Colbourn, J.M. Dyke, E.P.F. Lee, A. Morris and I.R. Trickle, Molec. Phys., 35, 873 (1978).

21. S.T. Manson, J. El. Spec. Rel. Phen., 9, 21 (1976).

CHAPTER FIVE

5.A. AN INVESTIGATION OF THE TRANSITION METALS IRON, COBALT AND NICKEL

5.A.1. Introduction

Although photoelectron spectroscopy (PES) has been used to investigate the electronic structure of transition metals and oxides in the solid state (1-5), very few studies of this type exist on these metals and their oxides in the gas phase. Such experiments are nevertheless important because they provide valuable reference data for the understanding of the changes in electronic structure which take place upon formation of polymeric species and solids from the isolated atoms or molecules. A secondary but important consideration is that one possible way of producing a transition metal oxide in the vapour phase is via gas-phase oxidation of a transition metal. Hence a gas-phase PES investigation of a transition metal will be an important precursor to the study of the corresponding transition metal oxide in the vapour phase.

As discussed in earlier work (6), gas-phase metal photoelectron spectra are also important because the relative photoionisation cross-section of the outermost ns and (n-1)d shells may be obtained from the spectra at the photon energy used. Moreover, by observing bands which derive their intensity from configuration interaction and by measuring relative band intensities, PES provides a sensitive probe of correlation and relativistic effects in the particular atom under study (7,8).

5.A.2. Experimental

Atomic vapours were obtained by vapourising the solids (>99.9% purity) into flowing helium from a zirconia-lined molybdenum furnace of similar design to that described in Chapter two of this thesis. Vapour pressures of the metals under study (9-11) were high enough to allow spectra to be recorded at furnace temperatures of (1980±30)K for iron, (1925±30)K for cobalt and (2140±30)K for nickel. These temperatures were measured by focusing a calibrated optical pyrometer onto the hottest part of the furnace.

Details of the photoelectron spectrometer and of the furnace used for the study of these three metals may be found in Chapter two of this thesis. The HeI(21.21eV) photoelectron spectra of methyl iodide, water,

carbon monoxide and nitrogen were used for calibration purposes. The transmission function of the analyser has been calibrated by a standard method (see Chapter 2) and found to be linear within ±5% of the electron kinetic energy for electron energies greater than 0.5eV. Observed metal ionisation energies agreed well with those obtained from optical spectroscopy (12) and are quoted to an estimated accuracy of ±0.01eV.

5.A.3. Results and Discussion

The HeI photoelectron spectra of iron, cobalt and nickel are shown in figures 5.A.1. to 5.A.7. In each case, evidence was obtained for ionisation from both the 4s and 3d shells.

The ground state of neutral iron is a $^5D_4$ state arising from the electronic configuration ....$3d^64s^2$. At the temperatures used for evaporation it is expected that other J components (J=3, 2, 1, 0) of this ^5D state will be populated and it is expected that the spectra obtained will contain contributions arising from population of the excited J components. From optical spectroscopy (12), it is known that there will be two formally allowed 4s one-electron ionisations corresponding to the processes $(3d^64s;\ ^6D)Fe^+ \leftarrow (3d^64s^2;\ ^5D)Fe$ and $(3d^64s;\ ^4D) \leftarrow (3d^64s^2;\ ^5D)Fe$ as well as two formally allowed 3d one-electron ionisations corresponding to $(3d^54s^2;\ ^6S)Fe^+ \leftarrow (3d^64s^2;\ ^5D)Fe$ and $(3d^54s^2;\ ^4D)Fe^+ \leftarrow (3d^64s^2;\ ^5D)Fe$. The HeI photoelectron spectrum of iron (figure 5.A.1. (a)) showed clear evidence for three of these bands but the band associated with the $(3d)^{-1}$ ionisation $Fe^+\ ^4D \leftarrow Fe\ ^5D$ was not observed. The three observed bands are shown more clearly in figure 5.A.1. (b). The two bands associated with the $(4s)^{-1}$ ionisations showed no resolvable structure and this almost certainly arises because they are made up of a complex pattern of ionisations from the five J components in the initial ^5D state to a number of J components in the ionic state. For the first band, the $Fe^+(^6D)$ state has five components whereas for the second band, the $Fe^+(^4D)$ state has four components. The peak maxima of these bands were measured as 7.90eV and 8.89eV respectively in good agreement with the expected energies for the $^6D_{9/2}\ Fe^+ \leftarrow {}^5D_4Fe$ and $^4D_{7/2}Fe^+ \leftarrow {}^5D_4Fe$ ionisations (12), consistent with these ionisations being the main contributions to the observed bands.

The bands associated with the $(3d)^{-1}$ ionisation consisted of one sharp peak with two smaller features on the low ionisation energy side (figure 5.A.2. (a)). The measured positions of these peaks were 10.79, 10.74 and 10.71eV respectively in agreement with ionisation energies estimated from optical spectroscopy for ionisation from the $^5D_4$, $^5D_3$ and $^5D_2(3d^64s^2)Fe$ neutral states to the $^6S_{5/2}(3d^54s^2)Fe^+$ ionic state. The components arising from ionisation of the $^5D_1$ and $^5D_0$ neutral atom states were not resolved experimentally. As the ionic state associated with this band has only one J component, it is convenient to use the observed band envelope to estimate the temperature of the atomic beam when photoionisation occurs. The method assumes that each component is Gaussian in shape with a half width of 45meV, the estimated experimental half width. Simulated spectra at Boltzmann temperatures for the initial atomic ^5D state at 300, 1400, 1500, 1600 and 1800K, as well as the experimental envelope for the ^6S, $Fe^+ \leftarrow ^5D$, $Fe(3d)^{-1}$ ionisation are shown in figure 5.A.2.(b). The agreement between experimental and computed band envelopes is good for temperatures in the region 1400-1800K and, when experimental errors in the measured band intensities are taken into account, the effective temperature of electronically excited iron is estimated as (1500±200)K. As observed in other cases (7,8), this temperature is less than the furnace temperature at which spectra were recorded and indicates that the excited atoms lose electronic excitation energy, probably by collision with the helium carrier gas, before being ionised.

The experimental intensity ratio of the three observed bands associated with the ^6D, ^4D and ^6S ionic states has been measured, after correction for the analyser transmission function, as (1.4±0.2):1.00:(7.3±0.7). The bands associated with the ^6D and ^4D ionic states are, within experimental error, in the expected ratio of 3:2 calculated on the basis of the total number of components in the ionic state. Also, by dividing the corrected experimental intensities by the number of components in the corresponding ionic state, a value of (25.5±1.5) is obtained for the iron $\sigma_{3d}:\sigma_{4s}$ relative HeI photoionisation cross section , measured at right angles to the photon beam. The measurements made from the HeI photoelectron spectrum of iron are summarised in table 5.A.1.

One remaining problem exists with the iron spectrum. As indicated earlier, one other allowed $(3d)^{-1}$ ionisation corresponding to the process $(3d^5\ 4s^2;\ ^4D)Fe^+ \leftarrow (3d^6 4s^2;\ ^5D)Fe$ should be observed in the HeI region with the most intense component corresponding to the $^5D_4 \leftarrow {}^4D_{7/2}$ ionisation at 15.37eV. However, despite a careful search of the 14.0-16.0eV ionisation energy region, no evidence of this band was obtained. This probably arises because the 3d photoionisation cross-section curve as a function of free-electron kinetic energy is very low at threshold and rises steeply to a maximum above threshold (13,14). For the band associated with the $(3d)^{-1}$ ionisation at 15.37eV the electron kinetic energy will be approximately half that for the $(3d)^{-1}$ band at 10.79eV ionisation energy and, from the calculated shape of the 3d photoionisation cross-section curve (13,14) it is expected that the cross-section for the band at 10.79eV will be much greater than the band at 15.37eV.

A recent study by Schmidt et al (24) has presented gas-phase vacuum ultra-violet photoelectron spectra of the three transition metals iron, cobalt and nickel. Synchrotron radiation of between 40eV and 80eV energy was used with experimental resolution varying from 150meV at 40eV photon energy to 500meV at 80eV photon energy. In the work on iron (24), spectra were recorded at the position of the dominant $3p^5(3d^7\ ^4F)4s^2\ ^5D \leftarrow 3p^6 3d^6 4s^2\ ^5D$ resonance transition at 56.65eV. Bands associated with ionisations from the 3d and 4s orbitals of the ground ^5D state were observed. Three bands with ionisation energies at 8.1±0.15eV, 9.0±0.1eV and 10.8eV were seen, which correspond to autoionisation from the excited ^5D state to the Fe^+ ^6D, ^4D and ^6S states observed in the work on iron described in this Chapter. The assignment of these bands and their measured ionisation energies agree well with those derived in the work described in this Chapter and quoted in table 5.A.1. Because of the experimental resolution of the technique used by Schmidt et al (24); it was not possible to observe any structure on the Fe^+ ^6S band. The poorer resolution also accounts for the higher error bounds on the measured values of the positions of the bands in question. It is interesting to note that, while the expected $(3d^6 4s^2\ ^4D)Fe^+ \leftarrow (3d^6 4s^2\ ^5D)Fe$ ionisation at 15.37eV (12) was not observed in the present work, evidence

of a band at 15.3±0.2eV was seen in reference (24). This was assigned by Schmidt et al (24) to the $(3d^6 4s^2\ ^4D)Fe^+ \leftarrow (3d^6 4s^2\ ^5D)Fe$ ionisation. The fact that this band was observed is probably due to the use of a higher incident photon energy than that used in the present HeI photoelectron spectroscopic study plus the fact that the $Fe^+\ ^4D$ state is obtained via a one-electron excitation followed by one-electron autoionisation.

The relative intensities of the $Fe^+\ ^6D$(8.1eV), $Fe^+\ ^4D$(9.0eV), $Fe^+\ ^6S$(10.8eV) and $Fe^+\ ^4D$(15.3eV) states can be measured directly from the work of Schmidt et al (24). After correction for the transmission function of the analyser the measured values were 1.00(^6D):1.88(^4D): 2.83(^6S):13.86(^4D). Although these values would be affected by autoionisation effects these could not be quantitatively taken into account for the purposes of this measurement. The relative intensity of the ^6D(8.1eV) and ^4D(9.0eV) bands, expected to be 1.5:1 on the basis of the number of components in the ionic state, was measured as 1:1.88, a discrepancy which must be due to autoionisation effects. However the measured value of 1:4.90 for the relative intensity of the ^6S(10.8eV) and ^4D(15.3eV) states was in qualitative agreement with the expected value of 1:3.33 calculated on the basis of the number of components in the ionic state.

The measured intensities of all four bands may be used to calculate a value for the $\sigma_{3d}:\sigma_{4s}$ relative photoionisation cross-section at 54°44' to the photon beam. Because of the discrepancy in the relative intensities of the ^6D(8.1eV) and ^4D(9.0eV) bands, the s ionisation intensity will be taken to be a sum of these two bands. The $\sigma_{3d}:\sigma_{4s}$ relative photoionisation cross-section may now be calculated using either $(d)^{-1}$ ionisation to the ^6S(10.8eV) or ^4D(15.3eV) states. Using the intensity of the ^6S state will give a value of approximately (8.2:1) while using the intensity of the ^4D state will give a value of approximately (12.0;1) for the $\sigma_{3d}:\sigma_{4s}$ relative photoionisation cross-section ratio. Because autoionisation effects play a major part in the spectra recorded by Schmidt et al (24) the best estimate for the $\sigma_{3d}:\sigma_{4s}$ relative photoionisation cross-section ratio would probably be an average of the two calculated values i.e. (10.1:1) in qualitative agreement with the value of (25.5:1) determined in the HeI study.

The HeI photoelectron spectrum recorded for cobalt is shown in figure 5.A.3. The ground electronic state of atomic cobalt is a ^4F state arising formally from the $3d^74s^2$ configuration and in the HeI region, three bands associated with one-electron ionisation from this state are expected from optical data (12). These consist of two $(4s)^{-1}$ ionisations and one $(3d)^{-1}$ ionisation corresponding to the processes $(3d^74s;\ ^5F)Co^+ \leftarrow (3d^74s^2;\ ^4F)Co$, $(3d^74s;\ ^3F)Co^+ \leftarrow (3d^74s^2;\ ^4F)Co$ and $(3d^64s^2;\ ^5D)Co^+ \leftarrow (3d^74s^2;\ ^4F)Co$. These three bands were observed experimentally (at peak maxima of 8.27, 9.08 and 12.91eV respectively) and, in addition, one other band was observed at 7.86eV which could be identified with the formally forbidden ionisation $(3d^8;\ ^3F)Co^+ \leftarrow (3d^74s^2;\ ^4F)Co$ (12) (figure 5.A.3). Detailed inspection of the ionisation energy range 7.0-10.0eV showed that of the three bands assigned to ionisation of atomic cobalt in this region the first and third bands showed resolvable structure whereas the band assigned to the $(3d^74s;\ ^5F)Co^+ \leftarrow (3d^74s^2;\ ^4F)Co$ process showed no such structure (figure 5.A.3.(b) and 5.A.4.). As discussed previously for iron, this probably arises because of overlapping contributions arising from population of the four J levels in the initial ^4F state and ionisation to the five J components in the ionic state. However, the measured peak maximum of the observed band (8.27eV) was in good agreement with that expected (12) for the ionisation $^5F_5Co^+ \leftarrow {}^4F_{9/2}Co$, the most intense contributor to the observed band. For the first band, peak maxima could be identified at 7.86, 7.98, 8.06 and 7.76eV and these could be assigned to the four ionisations $Co^+(a^3F_4,\ ^3F_3,\ ^3F_2) \leftarrow Co(^4F_{9/2})$ and $Co^+(a^3F_4) \leftarrow Co(^4F_{7/2})$ respectively (figure 5.A.4.(a)). In the third band, a component was resolved on the low ionisation energy side of the main band and is attributed to the $Co^+(b^3F_4) \leftarrow Co(^4F_{7/2})$ transition, whereas the remainder of the band arises from unresolved $Co^+(b^3F_{4,3,2}) \leftarrow Co(a^4F_{9/2})$ and $Co^+(b^3F_{3,2}) \leftarrow Co(a^4F_{7/2})$ contributions (figure 5.A.4.(b)).

The experimental intensities (corrected for analyser transmission function) of the three bands associated with the $(4s)^{-1}$ ionisations corresponding to ionisation to the a^3F, a^5F and b^3F ionic states were measured as $(1.9\pm0.2):(1.9\pm0.2):1.0$ respectively (table 5.A.2.). Clearly, the band associated with ionisation to the $(3d^8)a^3FCo^+$ state has appreciable intensity and it is worth considering the possible ways by

which this formally forbidden band gains intensity. Three mechanisms have been identified which describe the breakdown of the one-electron picture in photoelectron spectroscopy (15); initial-state configuration interaction (ISCI), final-ionic-state configuration interaction (FISCI) and continuum-state configuration interaction (CSCI) or inter-channel coupling. Because, in neutral cobalt, the ground state is a ^4F state formally arising from the $3d^74s^2$ configuration and as there is another ^4F state arising from the $3d^84s$ configuration approximately 3500cm^{-1} higher in energy, interaction between these states (i.e. ISCI) seems an obvious possibility by which the band associated with the $(3d^8; a^3F)Co^+$ state could gain intensity. However, recent configuration interaction calculations on neutral cobalt (16) have shown that the interaction between the $(3d^74s^2)^4F$ and $(3d^84s)^4F$ cobalt states is very small and this result indicates that ISCI can be ruled out in this case. Although interaction between the $(3d^8)a^3F$ and $(3d^74s)b^3F$ states in Co^+ is also possible (i.e. FISCI) no calculations have been performed to quantify the extent of this effect. However, as indicated in table 5.A.2., the relative intensity of the two bands associated with the processes $(3d^74s; {}^5F, {}^3F)Co^+ \leftarrow (3d^74s^2; {}^4F)Co$ is greater than the expected 5:3 ratio (corrected experimental ratio (3.8±0.4):2) and this would be consistent with the band associated with the $(3d^74s)b^3F$ Co^+ state losing intensity while that associated with the $(3d^8)a^3F$ Co^+ state gains intensity. Obviously, however, interchannel coupling or even autoionisation cannot be eliminated at this stage.

The band associated with the $(3d)^{-1}$ ionisation of cobalt is shown in figure 5.A.3.(c). It shows components arising from the $Co^+({}^5D_{4,3,2}) \leftarrow Co({}^4F_{9/2})$ and $Co^+({}^5D_4) \leftarrow Co({}^4F_{7/2})$ processes at 12.91, 12.98, 13.03 and 12.81eV respectively, in agreement with the expected ionisation energies derived from optical spectroscopy (12). The intensity of this band relative to the $(4s)^{-1}$ band at 8.27eV associated with the ^5F, $Co^+ \leftarrow {}^4F$, Co ionisation has been measured experimentally as (6.4±0.6) after correction for the analyser transmission function and this leads, after allowance for the number of components in the upper state, to a 3d:4s photoionisation cross section ratio of (9.0±1.0).

Of the four bands assigned to ionisation of cobalt, three show components arising from ionisation of electronically excited cobalt. However, unlike iron where one band corresponds to ionisation to an ionic state with only one J component, in cobalt each band corresponds to ionisation from the initial ^4F state with a maximum of four occupied J components to an ionic state also with several J components. The resulting heavily overlapped structure in each band makes it impossible to use the observed envelopes to estimate the extent of electronic excitation in cobalt due to photoionisation.

Five additional bands were observed in the 8.0-12.0eV ionisation energy region with ionisation potentials of (8.64±0.03)eV, (9.68±0.02)eV, (10.09±0.02)eV, (10.81±0.03)eV and (11.11±0.03)eV (these bands are marked 'X' in figures 5.A.3.(a) and 5.A.3.(b)). These features were present only when cobalt was evaporated but their intensities were not proportional to the other bands assigned to ionisation of cobalt. Furthermore, they could not be assigned to any known ionisation of atomic cobalt or to a possible energy loss in atomic cobalt. It was thought, however, that under the conditions of the experiment, energy-loss processes are unlikely as the cobalt band at 12.91eV, corresponding to a $(3d)^{-1}$ ionisation, showed no evidence of any energy-loss features. Hence, although the bands marked 'X' in figures 5.A.3.(a) and 5.A.3.(b) cannot be definitely assigned at this stage, they are thought to be molecular in origin and will be investigated in future experiments in the Southampton p.e.s. group.

Photoelectron spectra of cobalt have also been recorded by Schmidt et al (24). The spectra were recorded at 63.0eV, this being the position of the dominant $3p^5(3d^8\ ^3F)4s^2\ ^4D \leftarrow 3p^6 3d^7 4s^2\ ^4F$ absorption. By analogy with the present study by HeI photoelectron spectroscopy, it was expected that both 3d and 4s ionisations would be observed. Unfortunately the expected 4s ionisations at 8.3eV and 9.1eV, corresponding to the $Co^+\ ^5F \leftarrow Co\ ^4F$ and $Co^+\ ^3F \leftarrow Co\ ^4F$ ionisations respectively, were buried in the high background. However, the expected band at 12.9eV corresponding to the $Co^+\ ^5D \leftarrow Co\ ^4F$ ionisation (removal of a 3d electron) was observed, in agreement with the present work described in this thesis.

The photoelectron spectrum of nickel is the most complex of the three spectra recorded. This complexity arises because the electronic ground state of nickel, the $(3d^84s^2)^3F$ state, is only $205cm^{-1}$ below the $(3d^94s)^3D$ state and the J manifolds of each state are overlapped (12). It is also expected that at the temperatures used for evaporation the $(3d^94s)^3D$ state will be appreciably populated. Two allowed ionisations should occur from the $(3d^84s^2)^3F$ state in the HeI region, corresponding to the $(4s)^{-1}$ ionisation processes $Ni^+(3d^84s)^4F$, $^2F \leftarrow Ni\ (3d^84s^2)^3F$. In contrast, seven allowed bands are expected from the $(3d^94s)^3D$ state. These correspond to the $(4s)^{-1}$ ionisation to the $(3d^9)^2D$ Ni^+ state and the $(3d)^{-1}$ ionisations to the $(3d^84s)^4F$, ^2F, ^2D, ^4P, ^2P and ^2D Ni^+ states.

Figure 5.A.5. shows the complete HeI photoelectron spectrum of nickel. The first band, band A of figure 5.A.5. was relatively weak and it was not possible to resolve any structure in this band. However, its maximum (7.61eV) was in good agreement with that expected for the $(3d^9)^2D_{5/2}$ $Ni^+ \leftarrow (3d^94s)^3D_3$ Ni ionisation. An expanded version of the 8.0-10.0eV ionisation energy region is shown in figure 5.A.6.(a). This shows structure arising from ionisation from both the $(3d^94s)^3D$ and $(3d^84s^2)^3F$ Ni states to the $(3d^84s)^4F$ and ^2F ionic states. The band centred at 8.67eV corresponds to ionisation to the $(3d^84s)^4F$ Ni^+ state whereas the smaller band centred at 9.31eV is associated with ionisation to the $(3d^84s)^2F$ Ni^+ state. For the more intense band in figure 5.A.6.(a), structure was observed at 8.67, 8.79, 8.89 and 8.96eV. On the basis of optical data (12), this structure was assigned to the ionisations $^4F_{9/2}$ $Ni^+ \leftarrow {}^3F_4$ Ni, Ni^+ $^4F_{7/2} \leftarrow {}^3F_4$ Ni, $^4F_{5/2}$ $Ni^+ \leftarrow {}^3F_4$ Ni and $^4F_{3/2}$ $Ni^+ \leftarrow {}^3F_4$ Ni. A small peak has also been observed at 8.56eV on the low IP side of the main band and has been assigned to the Ni^+ $^4F_{9/2} \leftarrow Ni$ $^3D_2$ ionisation. Similarly, a small component was observed at 9.20eV on the low ionisation energy side of the band at 9.31eV and this has been assigned to the process $^2F_{7/2}$ $Ni^+ \leftarrow {}^3D_2$ Ni. Although the band at 9.31eV can be assigned to the ionisation $^2F_{7/2}$ $Ni^+ \leftarrow {}^3F_4$ Ni, no evidence was obtained for the ionisation $^2F_{5/2}$ $Ni^+ \leftarrow {}^3F_4$ Ni expected at 9.49eV. The ratio of the experimental intensity (corrected for analyser transmission function) of the bands associated with the ^4F and ^2F ionic states was measured as (5.9±0.5):1.0, clearly much greater than the ratio of 2:1 expected on the basis of the number of components in the upper state.

An expanded version of the 10.0-11.0eV ionisation energy region is shown in figure 5.A.6.(b). Two peak maxima were clearly observed (peaks A and C in figure 5.A.6.(b)) at 10.47 and 10.71eV respectively corresponding to the processes $(3d^84s)^2D_{5/2}$ $Ni^+ \leftarrow (3d^94s)^3D_3$ Ni and $(3d^84s)^4P_{5/2,\ 3/2,\ \frac{1}{2}}$ $Ni^+ \leftarrow (3d^94s)^3D_3$ Ni. Of the two spectra shown in figure 5.A.6.(b), spectrum ii) has been recorded at about 200K higher than the temperature used to obtain spectrum i). Peak B at 10.56eV can be identified with the $(3d^84s)^2D_{3/2}$ $Ni^+ \leftarrow (3d^94s)^3D_3$ Ni ionisation, whereas at higher temperature a shoulder is seen on the low ionisation energy side of peak A which can be identified with the $(3d^84s)^2D_{5/2}$ $Ni^+ \leftarrow (3d^94s)^3D_2$ Ni process. Two other bands were also observed in the photoelectron spectrum of nickel associated with the ionisations $(3d^84s)^2G$ $Ni^+ \leftarrow (3d^94s)^3D$ Ni and $(3d^84s)^2P$ $Ni^+ \leftarrow (3d^94s)^3D$ Ni. In figure 5.A.6.(c) no structure is resolved in either of these bands although the ^2G $Ni^+ \leftarrow ^3D$ Ni band was clearly asymmetric to the low ionisation energy side. Since the splitting of the $^2G_{9/2}$ and $^2G_{7/2}$ levels in Ni^+ is very small, this asymmetry corresponds to unresolved structure arising from population of the J=3, 2, 1 levels of the ^3D initial state. A spectrum of this band recorded under improved resolution is shown in figure 5.A.7.(a) and the results of simulation of the observed band envelope using the method adopted previously for iron with a Gaussian band half-width of 65meV are shown in figure 5.A.7.(b). From these simulated spectra the temperature of the atomic beam was estimated as (1600±200)K and, as in the iron case, this is clearly less than the experimental furnace temperature.

The relative intensities of the bands labelled A to F in figure 5 have been measured and these are shown in table 5.A.3. As band D in figure 5 contains overlapping contributions from ionisation to the ^4P and $^2D(3d^84s)Ni^+$ states produced from the $(3d^94s)^3D$ state of neutral nickel and as bands B and C contain overlapping contributions from ionisation from the $(3d^84s^2)^3F$ and $(3d^94s)^3D$ states of neutral nickel to the $(3d^84s)^4F$ and $(3d^84s)^2F$ states of the nickel cation, it is difficult to use the intensities of these bands to estimate the $\sigma_{3d}:\sigma_{4s}$ HeI photo-ionisation cross-section ratio in neutral nickel. However, in figure 5.A.5. bands A and F correspond to the processes $(3d^9)^2D$ $Ni^+ \leftarrow (3d^94s)^3D$ Ni and $(3d^84s)^2G$ $Ni^+ \leftarrow (3d^94s)^3D$ Ni and hence

the corrected relative intensities of these bands can be used directly to provide an estimate of the $\sigma_{3d}:\sigma_{4s}$ cross-section ratio in nickel. The value obtained after allowing for the number of components in the ionic state is (3.1±0.3).

Schmidt et al (24) have recently recorded the ultraviolet photoelectron spectrum of nickel at a photon energy of 68.55eV corresponding to the $(3p^5 3d^9 4s^2\ ^3P,^3D)Ni \leftarrow (3p^6 3d^8 4s^2\ ^3F)Ni$ resonance transition. As in the HeI study reported here, an excited state of the neutral atom was appreciably populated (the $Ni(3d^9 4s)^3D$ state) at the elevated temperatures used for the experiment. Ionisations from both the ground and excited states of the atom would be expected to occur. This was in fact found to be the case in the autoionisation spectra reported in ref.(24). Three ionisations at 8.7eV, 10.6±0.1eV and 11.7±0.1eV ionisation energy were observed which corresponded to bands B, D and E/F of the HeI study described above. Evidence of bands A and C was not found by Schmidt et al (24) because they were weak relative to the other observed bands and were masked by the experimental background. Because of the complicated nature of the spectra recorded by Schmidt et al (24), it is not possible to calculate a value for the $\sigma_{4s}:\sigma_{3d}$ relative photoionisation cross-section ratio. In the HeI study, it was possible to calculate a $\sigma_{4s}:\sigma_{3d}$ value using the relative intensities of bands A and F, but this was not possible from the spectra of Schmidt et al because Band A was obscured by high experimental background.

For the work on the first-row transition metals described in this chapter, the 3d photoionisation cross-section is greater than the 4s photoionisation cross-section at the HeI (21.21eV) photon energy, as expected from theoretically computed partial 3d and 4s photoionisation cross sections (13,17). It would obviously be of interest to extend this investigation by measuring relative band intensities as a function of photon energy. It appears from theoretically predicted cross-sections as a function of free kinetic energy that, in the first row transition metals, the 3d photoionisation cross-section increases smoothly above threshold to a maximum and then decreases slowly. This is in contrast to the 4s photoionisation cross-section which varies rapidly just above threshold. In fact, it is expected that the 4s cross-

section is relatively large at threshold, where $\sigma_{4s} > \sigma_{3d}$, and then it decreases rapidly to a minimum just above threshold. This is followed by a gradual increase to a maximum whose height is typically one-tenth of the threshold value (17). These predictions are also consistent with some recently recorded photoelectron spectra for a series of first-row transition metal negative ions obtained with an ArII (2.54eV) photon source (18-21), where the bands derived from the $(4s)^{-1}$ ionisation are consistently more intense than those associated with the $(3d)^{-1}$ ionisation.

A further application of the results described in this chapter is in the assignment of the photoelectron spectra of transition-metal compounds (22, 23). Such spectra are commonly recorded in the vapour phase at the HeI photon energy. Hence the relative photoionisation cross-section ratios recorded in this study and in earlier work (6) (see also chapter 6 of this thesis) will probably be useful in interpreting relative experimental band intensities in the HeI photoelectron spectra of transition-metal compounds. Examples of this can be found in chapter 6 of this thesis in which experimental work on TiO, VO and CrO is described and assignment of the metal oxide spectra is assisted by the known band intensities and assignments in the corresponding metal spectra.

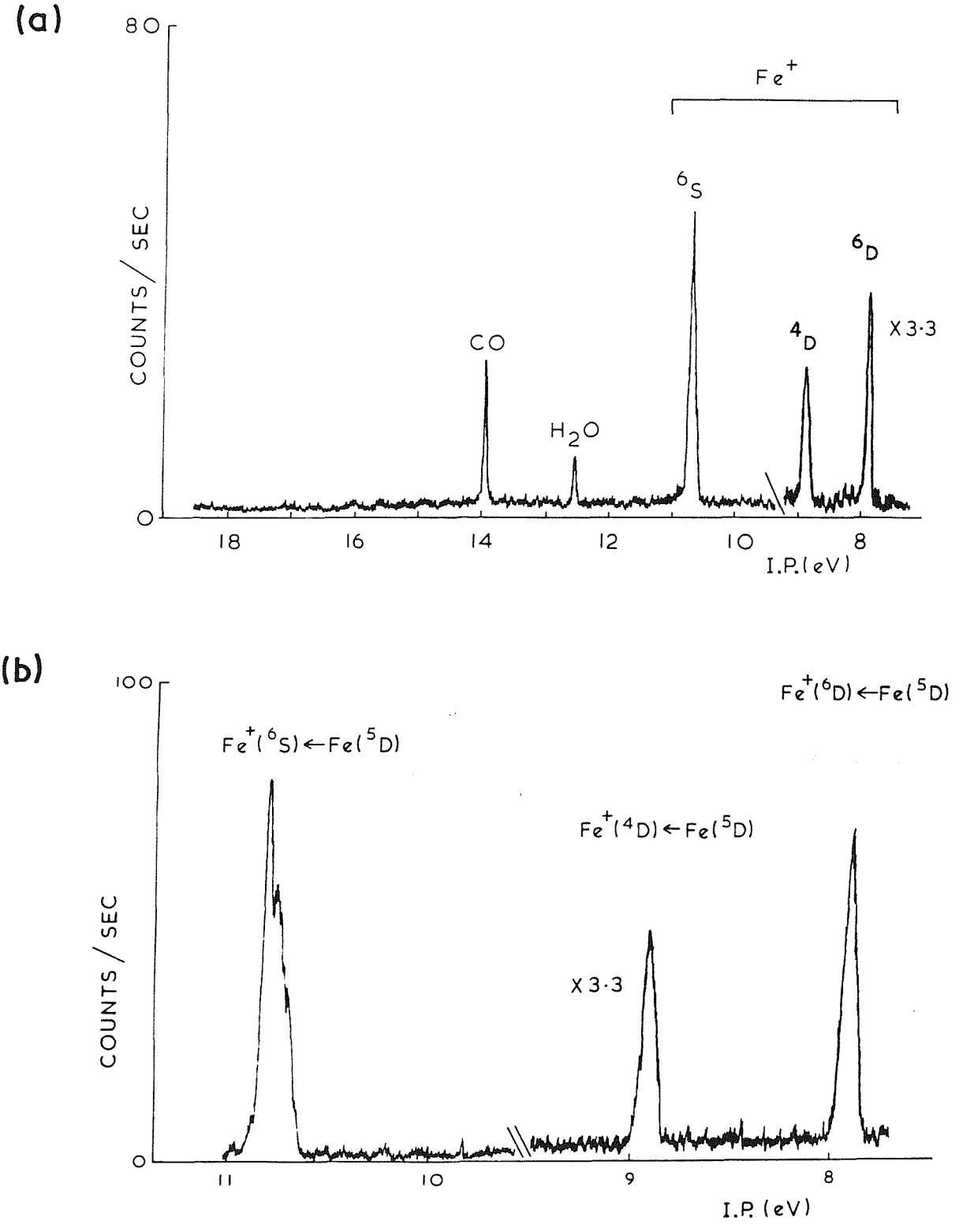
(a)
80
COUNTS / SEC
0
Fe+
6S
6D
4D
X 3·3
CO
H2O
18
16
14
12
10
8
I.P.(eV)
(b)
100
COUNTS / SEC
0
Fe+(6D)←Fe(5D)
Fe+(6S)←Fe(5D)
Fe+(4D)←Fe(5D)
X 3·3
11
10
9
8
I.P. (eV)

FIG 5A.1

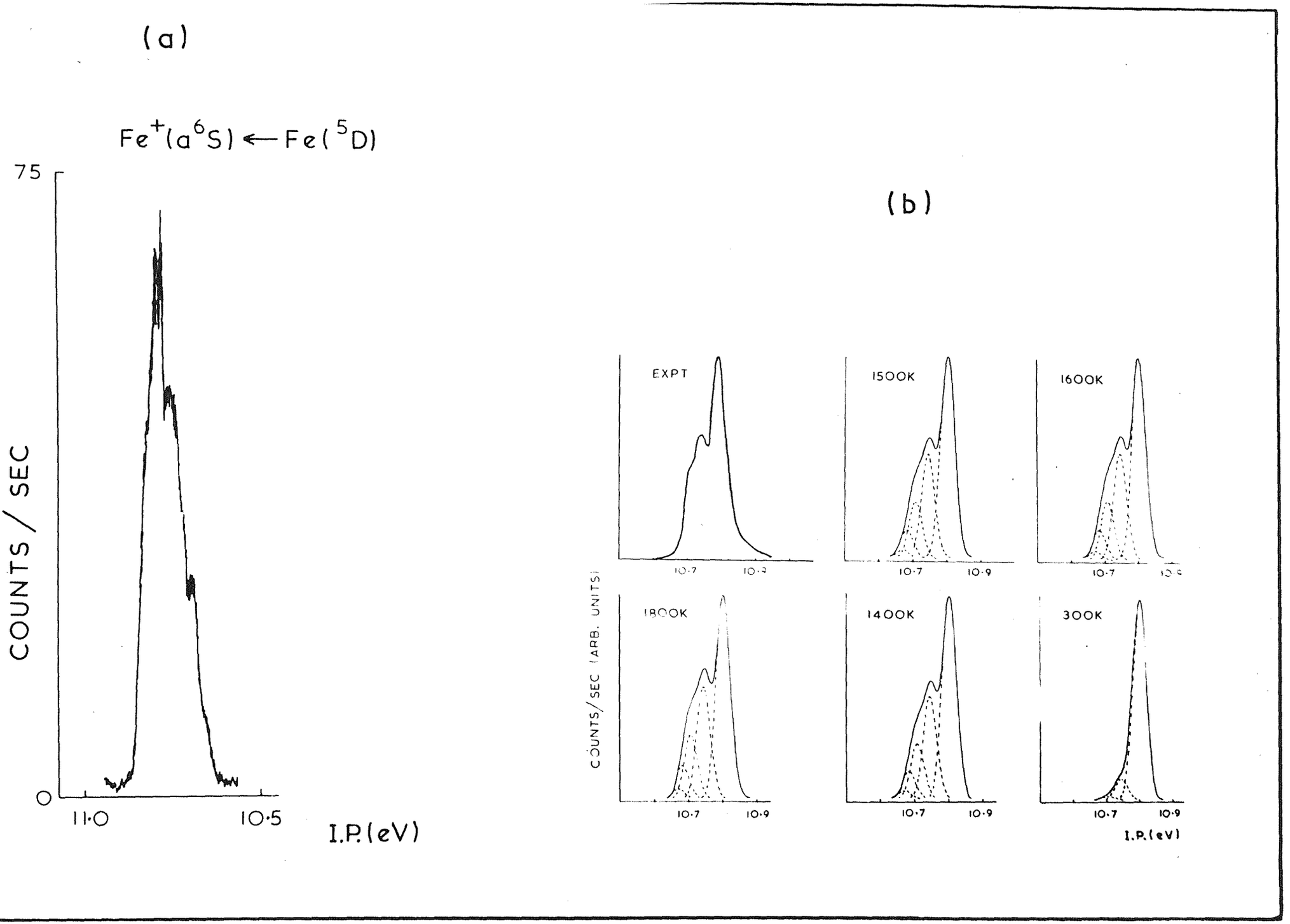
(a)
$Fe^+(a^6S) \leftarrow Fe(^5D)$
75
COUNTS / SEC
0
11·0
10·5
I.P.(eV)
(b)
EXPT
1500K
1600K
1800K
1400K
300K
10·7
10·9
COUNTS/SEC (ARB. UNITS)
I.P.(eV)

FIG 5A.2

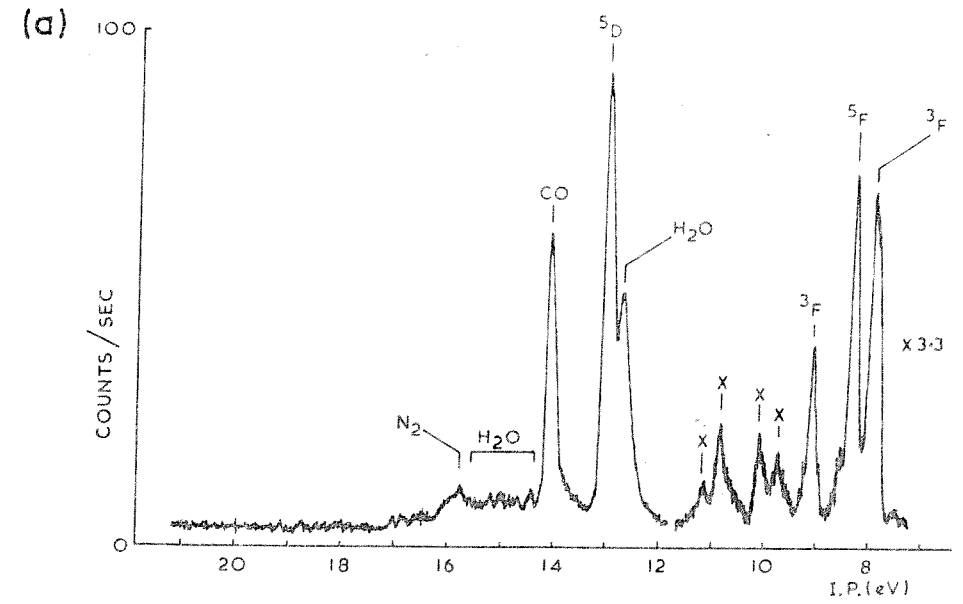
(a)
100
0
COUNTS / SEC
^5D
CO
H_2O
^5F
^3F
^3F
X 3·3
X
X
X
X
N_2
H_2O
20
18
16
14
12
10
8
I.P.(eV)

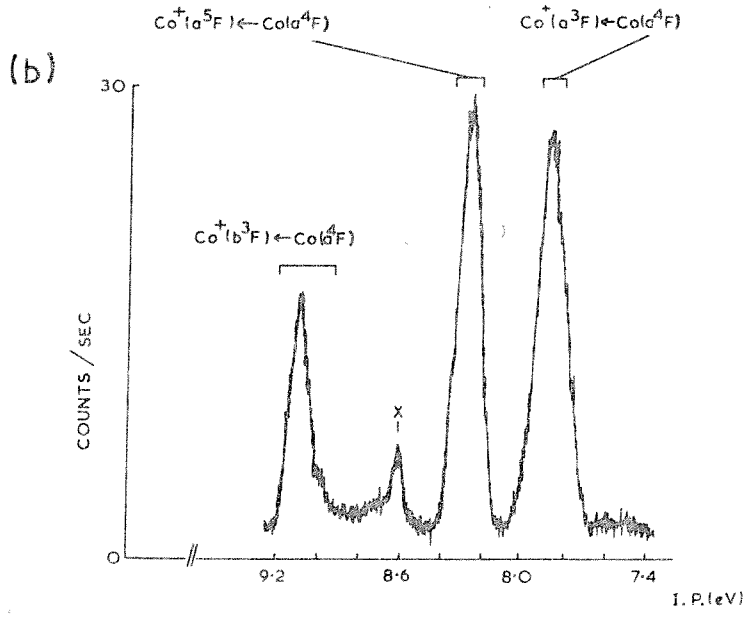
(b)
$Co^+(a^5F) \leftarrow Co(a^4F)$
$Co^+(a^3F) \leftarrow Co(a^4F)$
30
0
COUNTS / SEC
$Co^+(b^3F) \leftarrow Co(a^4F)$
X
9·2
8·6
8·0
7·4
I.P.(eV)

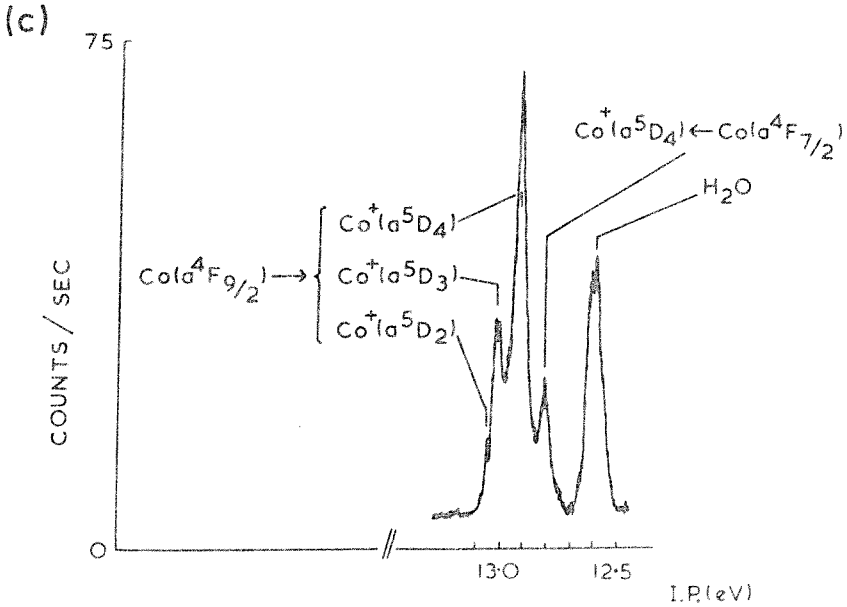
(c)
75
0
COUNTS / SEC
$Co^+(a^5D_4) \leftarrow Co(a^4F_{7/2})$
H_2O
$Co(a^4F_{9/2}) \rightarrow$
$Co^+(a^5D_4)$
$Co^+(a^5D_3)$
$Co^+(a^5D_2)$
13·0
12·5
I.P.(eV)

FIG 5A.3

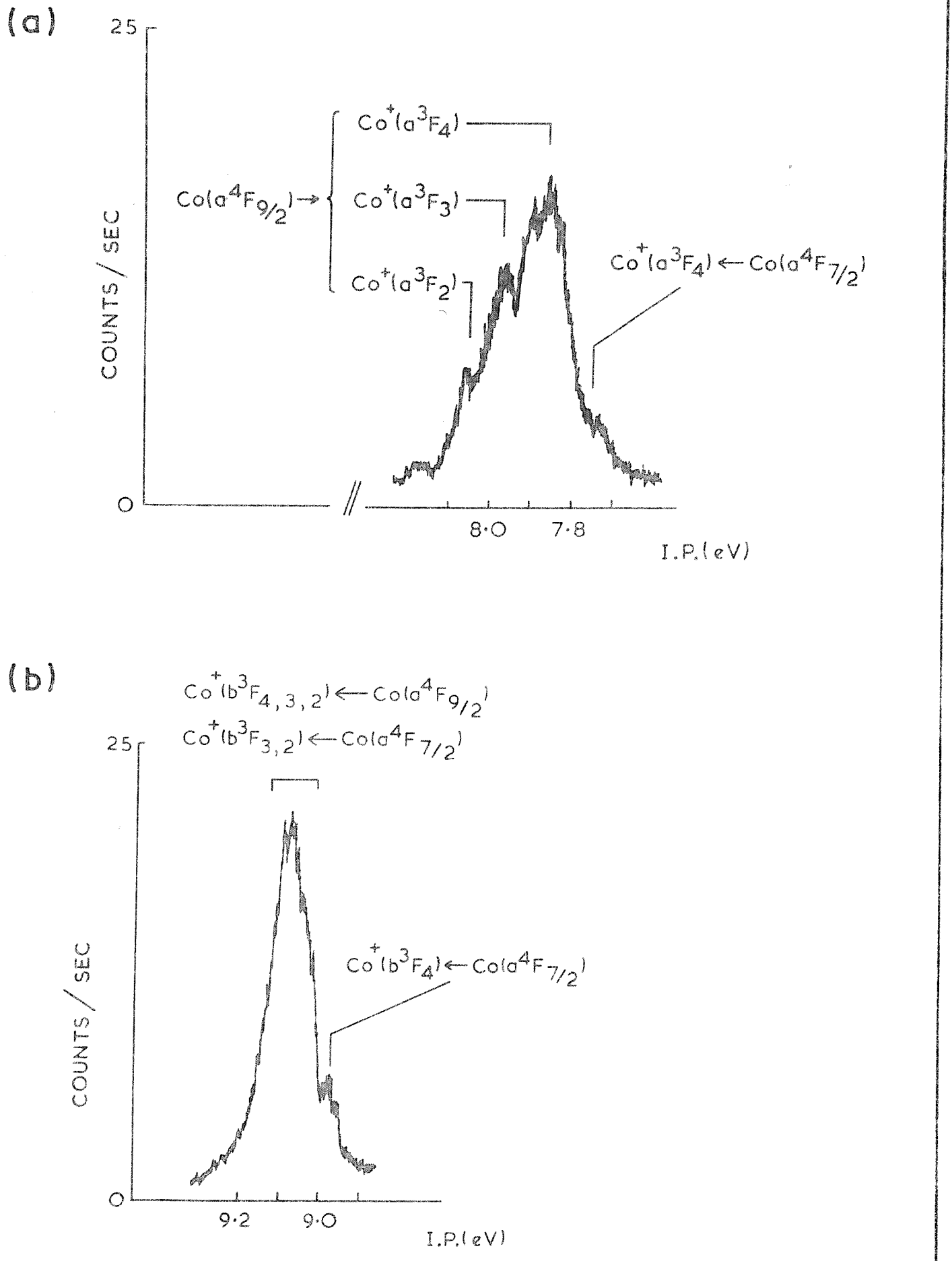
(a)
25
COUNTS / SEC
0
Co+(a3F4)
Co(a4F9/2) →
Co+(a3F3)
Co+(a3F2)
Co+(a3F4) ← Co(a4F7/2)
8·0
7·8
I.P.(eV)
(b)
Co+(b3F4,3,2) ← Co(a4F9/2)
Co+(b3F3,2) ← Co(a4F7/2)
25
COUNTS / SEC
Co+(b3F4) ← Co(a4F7/2)
0
9·2
9·0
I.P.(eV)

FIG 5A.4

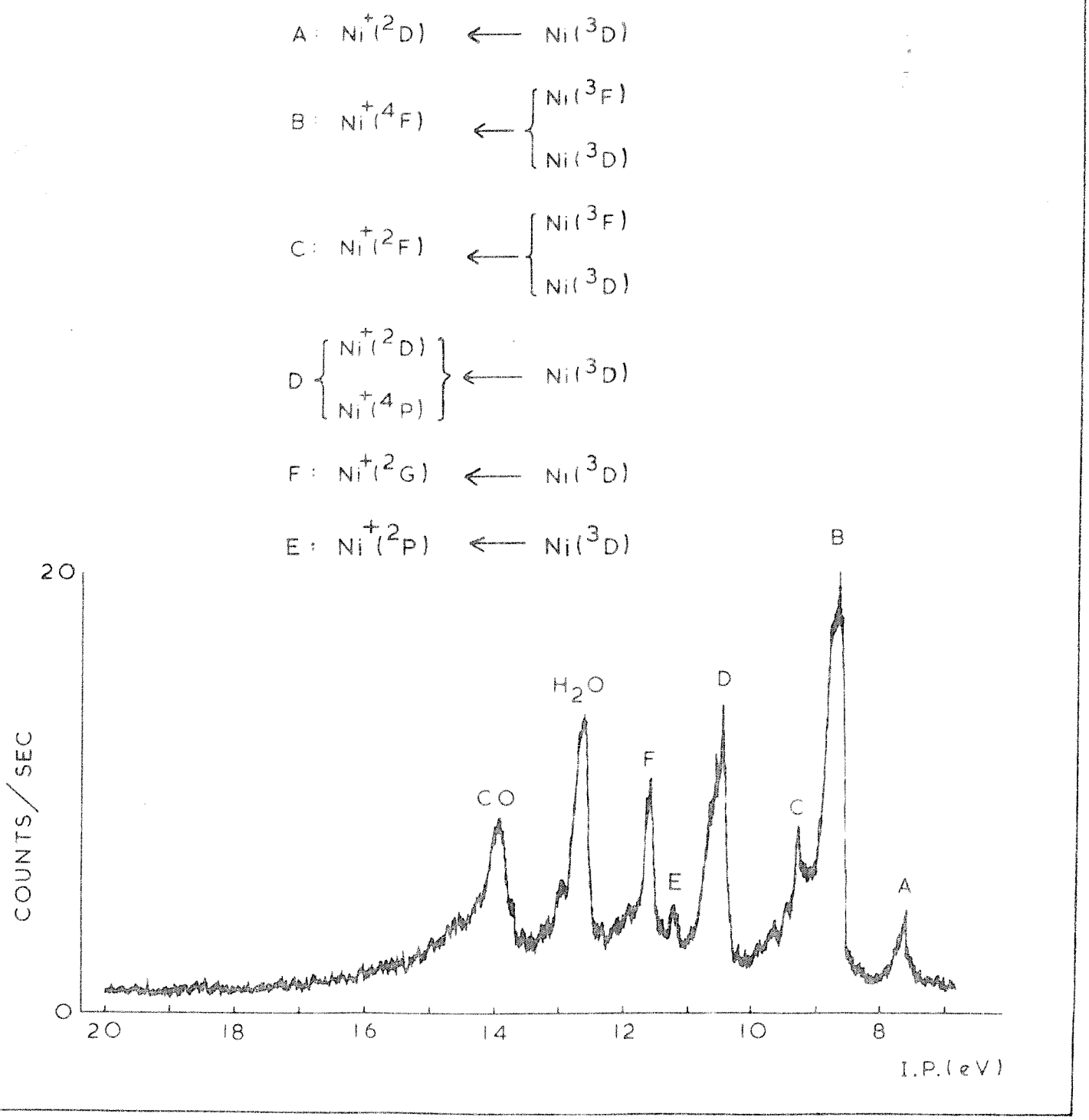
A : Ni+(2D) ← Ni(3D)
B : Ni+(4F) ← Ni(3F), Ni(3D)
C : Ni+(2F) ← Ni(3F), Ni(3D)
D { Ni+(2D), Ni+(4P) } ← Ni(3D)
F : Ni+(2G) ← Ni(3D)
E : Ni+(2P) ← Ni(3D)
20
0
COUNTS / SEC
CO
H2O
F
E
D
C
B
A
20
18
16
14
12
10
8
I.P.(eV)

FIG 5A.5

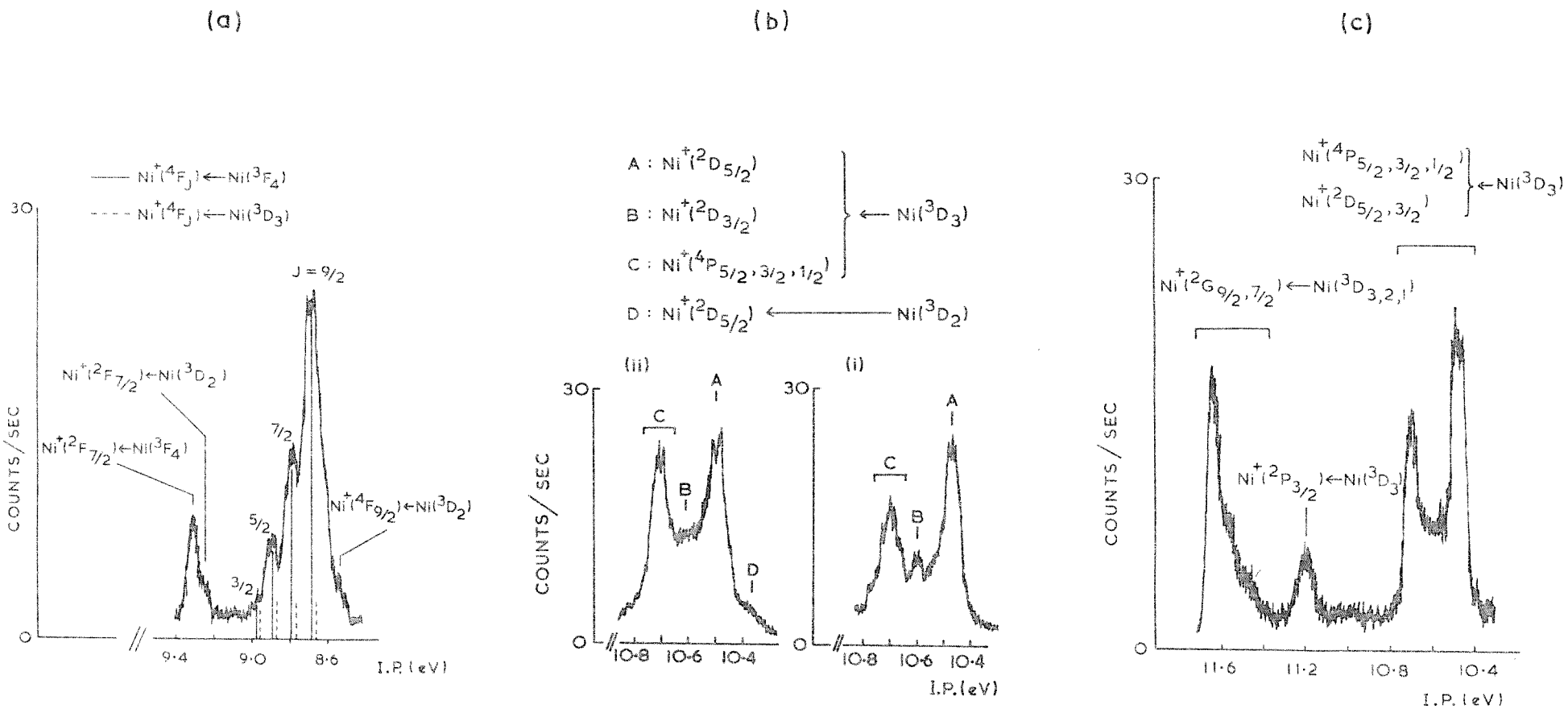
(a)
(b)
(c)
Ni+(4FJ)←Ni(3F4)
Ni+(4FJ)←Ni(3D3)
30
0
COUNTS/SEC
J = 9/2
Ni+(2F7/2)←Ni(3D2)
Ni+(2F7/2)←Ni(3F4)
7/2
5/2
3/2
Ni+(4F9/2)←Ni(3D2)
9·4
9·0
8·6
I.P. (eV)
A : Ni+(2D5/2)
B : Ni+(2D3/2)
C : Ni+(4P5/2,3/2,1/2)
← Ni(3D3)
D : Ni+(2D5/2) ← Ni(3D2)
(ii)
(i)
A
B
C
D
10·8
10·6
10·4
I.P. (eV)
Ni+(4P5/2,3/2,1/2)
Ni+(2D5/2,3/2)
←Ni(3D3)
Ni+(2G9/2,7/2)←Ni(3D3,2,1)
Ni+(2P3/2)←Ni(3D3)
11·6
11·2
10·8
10·4
I.P. (eV)

FIG 5A.6

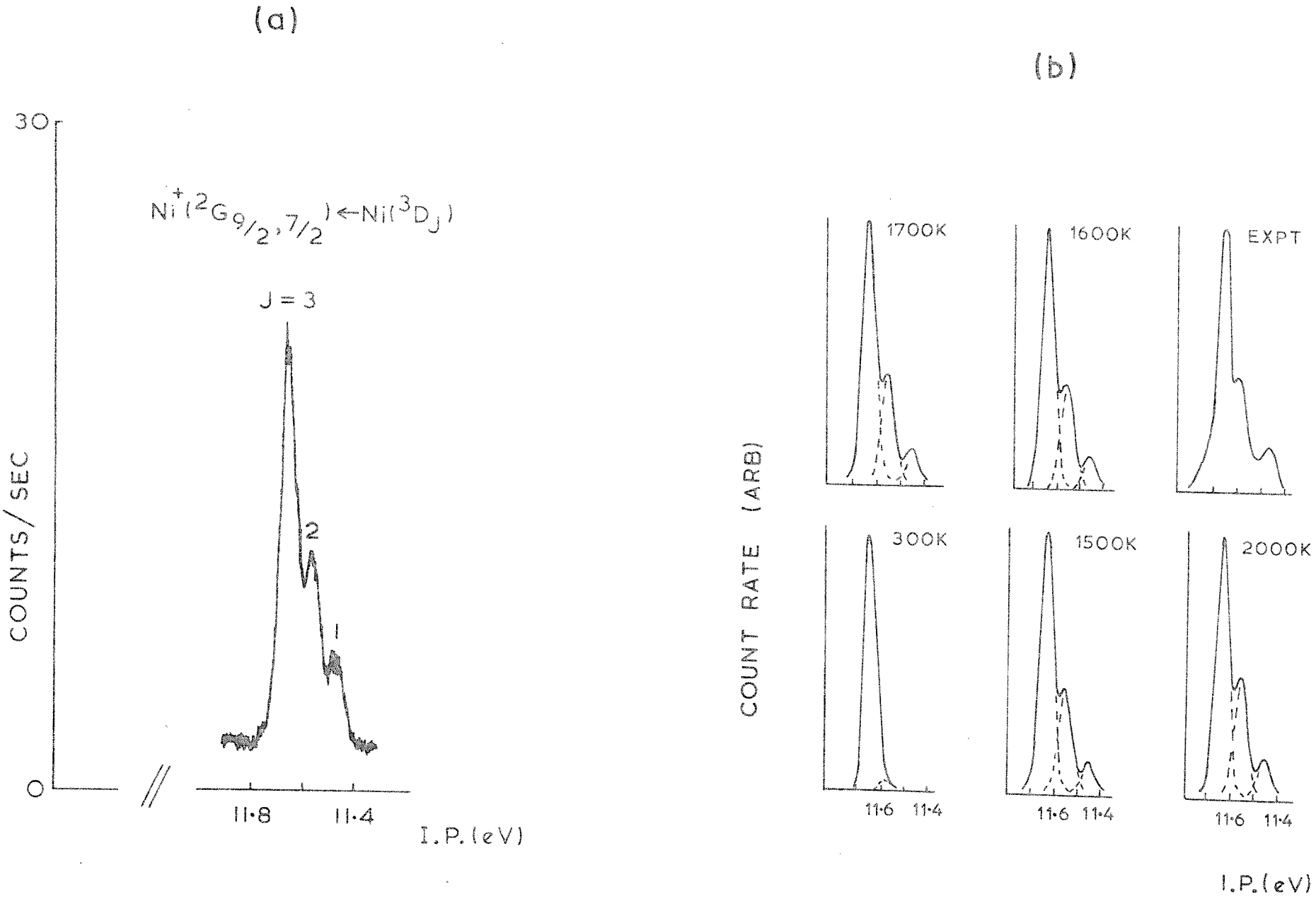
(a)
30
$Ni^+(^2G_{9/2,7/2}) \leftarrow Ni(^3D_J)$
J = 3
2
1
COUNTS / SEC
0
11·8
11·4
I.P. (eV)
(b)
1700K
1600K
EXPT
300K
1500K
2000K
COUNT RATE (ARB)
11·6 11·4
11·6 11·4
11·6 11·4
I.P. (eV)

FIG 5A.7

Table 5.A.1. Measurements obtained from the HeI photoelectron spectrum of iron

Orbital Ionised	Ionisation process $Fe^{+} \leftarrow Fe$	Measured ionisation potential (eV) of band maximum	Corrected experimental relative intensities
4s	$^{6}D \leftarrow ^{5}D$	7.90	1.4±0.2
4s	$^{4}D \leftarrow ^{5}D$	8.89	1.0
3d	$^{6}S \leftarrow ^{5}D$	10.79	7.3±0.7

Table 5.A.2. Measurements obtained from the HeI photoelectron spectrum of cobalt

Orbital Ionised	Ionisation process $Co^{+} \leftarrow Co$	Measured ionisation potential (eV) of band maximum	Corrected experimental relative intensities
4s electron ionised plus a 4s→3d transition	$a^{3}F \leftarrow ^{4}F$	7.86	1.9±0.2
4s	$a^{5}F \leftarrow ^{4}F$	8.27	1.9±0.2
4s	$b^{3}F \leftarrow ^{4}F$	9.08	1.0
3d	$a^{5}D \leftarrow ^{4}F$	12.91	12.2±1.5

Table 5A.3 Summary of the measurements obtained from the HeI photoelectron spectrum of nickel

Band lettering in figure 5	Orbital ionised	Ionisation process $Ni^{+} \leftarrow Ni$	Measured ionisation potential (eV) of band maximum	Corrected experimental relative intensities
A	4s	$a^{2} \leftarrow {}^{3}D$	7.61	0.50±0.05
B	(3d (4s	${}^{4}F \leftarrow {}^{3}D$ ${}^{4}F \leftarrow {}^{3}F$	8.67	5.90±0.5
C	(3d (4s	${}^{2}F \leftarrow {}^{3}D$ ${}^{2}F \leftarrow {}^{3}F$	9.31	1.0
D	3d	$b^{2}D$, $a^{4}D \leftarrow {}^{3}D$	10.47	3.7±0.3
E	3d	${}^{2}P \leftarrow {}^{3}D$	11.21	-*
F	3d	${}^{2}G \leftarrow {}^{3}D$	11.64	2.8±0.2

*Too weak for reliable intensity measurements to be made.

REFERENCES (5.A.)

1. Y. Baer, P.F. Heden, J. Hedman, M. Klasson, C. Nordling and K. Siegbahn, Phys. Scr. 1, 55 (1970).

2. D.E. Eastman, Electron Spectroscopy; Proc. Int. Conf. Pacific Grove, p.489 (1971).

3. C.N.R. Rao, D.D. Sharma, S. Vasudevan and M.S. Hedge, Proc. R. Soc. A, 367, 239 (1979).

4. G. Grenet, Y. Jugnet, T. Minh Duc and M. Kibler, J. Chem. Phys., 74, 2163 (1981).

5. G.C. Allen, P.M. Tucker and R.K. Wild, Oxidation Met., 13, 223 (1979).

6. J.M. Dyke, N.K. Fayad, A. Morris and I.R. Trickle, J. Phys. B., 12, 2985 (1979).

7. J.M. Dyke, N.K. Fayad, G.D. Josland and A. Morris, Mol. Phys., 41, 1051 (1980).

8. J.M. Dyke, G.D. Josland, R.A. Lewis and A. Morris, Mol. Phys., 44, 967 (1981).

9. A.N. Nesmeyanov, Vapour Pressures of the Chemical Elements, ed. R. Gary, Amsterdam (Elsevier) (1963).

10. O. Kubaschewski and E.L. Evans, Metallurgical Thermochemistry, Oxford (Pergamon) (1956).

11. R.E. Honig, R.C.A. Rev., 18, 195 (1957).

12. C. Moore, Atomic Energy Levels NBS Circular No. 467, Vol. 2 (Washington DC. US. Govt. Printing Office) (1952).

13. R.F. Reilman and S.T. Manson, Phys. Rev. A. 18, 2124 (1978).

14. S.T. Manson, Adv. Electron. Electron Phys., 44, 1 (1977).

15. S.T. Manson, J. Electron. Spectrosc. Rel. Phen., 9, 21 (1976).

16. E.K. Viinikka and Y. Ohrn, Phys. Rev. B, 11, 4168 (1975).

17. D.J. Kennedy and S.T. Manson, Phys. Rev. A, 5, 227 (1972).

18. R.R. Corderman, P.C. Engelking and W.C. Lineberger, J. Chem. Phys., 70, 4474 (1979).

19. P.C. Engelking and W.C. Lineberger, Phys. Rev. A, 19, 149 (1979).

20. C.S. Feigerle, R.R. Corderman, S.V. Bobashev and W.C. Lineberger, J. Chem. Phys., 74, 1580 (1981).

21. H. Hotop, R.A. Bennett and W.C. Lineberger, J. Chem. Phys., 58, 2373 (1973).

22. R.L. DeKock and D.R. Lloyd, Adv. Inorg. Radiochem., 16, 65 (1974).

23. R.L. Egdell and A.W. Potts, Specialist periodical Reports. Vol. 6 (1976).

24. E. Schmidt, H. Schroder, B. Sonntag, H. Voss and H.E. Wetzel, J. Phys. B, 16, 2961 (1983).

CHAPTER 5.B. RESULTS OBTAINED ON EVAPORATION OF A TRANSITION METAL ALLOY

5.B.1. Introduction

Stainless steels are of considerable importance commercially and industrially and this present investigation was undertaken as part of the collaboration between the Southampton p.e.s. group and the Berkeley Nuclear Laboratories of the C.E.G.B. The aim was to study via gas-phase p.e.s., an alloy previously studied by Auger Electron Spectroscopy (A.E.S.) at Berkeley (1-3). In the experiments performed at Berkeley (1-3) type EN58A stainless steel was annealed at temperatures between 770 and 1470K. During annealing, material lost from the stainless steel was collected on a cold finger and an elemental analysis of this deposit was carried out by A.E.S. The remaining surface of the stainless steel was also analysed by A.E.S. From analysis of the stainless steel surface, at temperatures up to 1200K, no significant variation between the annealed surface composition and the bulk was observed. Above 1200K, a rapid decrease in surface composition of chromium was observed together with a corresponding increase in nickel (1). From analysis of material deposited on the cold finger, as the annealing temperature was increased above 770K, chlorine and manganese were readily observed on the surface of the cold finger, but below 1020K manganese was the only metallic element which condensed in detectable quantities. On increasing the annealing temperature to 1120K, large quantitites of chromium and smaller amounts of iron as well as manganese and chlorine were condensed on the cold finger surface (1).

Following the successful study of iron, cobalt and nickel (discussed in the previous section) a sample of Cr/Ni/Nb stabilised steel of the type used in the C.E.G.B.'s Advanced Gas-Cooled Reactors (AGRs) (4) was supplied with the intention that it be studied by gas-phase p.e.s. at Southampton. It was hoped that it would be possible to perform direct vapour phase p.e.s. studies of the vapour effusing from a heated stainless steel sample and that there would be some similarities between the gas-phase p.e.s. studies and solid-phase studies of ref. (1).

5.B.2. Experimental

The supplied steel sample (denoted Sample A) was evaporated using a system identical to that used for the evaporation of iron, cobalt and nickel (see preceding section). The composition of the steel in wt. % was given as

Cr	Ni	C	Mn	Si	Nb	S	P	Co	Ti	Zr
19.8	24.5	0.035	0.55	0.59	0.50	0.005	0.005	0.004	0.05	0.05

Mo	Fe
0.02	Balance (∿55.0).

The RF voltage passed into the furnace was increased by 0.2 kV at a time and kept constant for two minutes during which time spectra were recorded over the 7.0eV to 11.0eV i.p. range. Temperatures were measured by focusing a calibrated optical pyrometer onto the hottest part of the furnace. The intensities of the metals evaporating (Fe, Co and Ni) were monitored by measuring the heights of the most intense bands in the iron, cobalt and nickel spectra i.e. the $Fe^{+6}S \leftarrow Fe^{5}D$, $Co^{+5}D \leftarrow Co^{4}F$ and $Ni^{+4}F \leftarrow Ni^{3}D/^{3}F$ bands. It was not possible to determine the proportion of any particular element in the effusing vapour because insufficient data is available on the relative photo-ionisation cross-sections of the metals. No bands attributable to manganese, chlorine or sulphur were observed during the course of this work.

5.B.3. Results and Discussion

The alloy studied in this work is similar to the EN58A stainless steel studied previously in references (1-3). In wt. % the composition of EN58A used in refs (1,2) has been determined as:

Cr	Ni	Mn	C	Si	S	P	Mo	Fe
18.3	9.0	1.17	0.05	0.04	<0.010	0.025	0.45	Balance (∿71.0).

The results of the gas-phase p.e.s. experiments on sample A are shown in the form of a graph of metal intensity against temperature

in Fig. 5.B.1. The three metals were observed over three different temperature ranges:

Cr	1600 - 2275°C (1870-2545K)
Fe	1650 - 2350°C (1920-2620K)
and Ni	1600 - 2500°C (1870-2770K)

The evaporation temperatures previously found for pure iron and nickel (see preceding section) were (1980±30)K and (2140±30)K respectively and (1760±30)K for pure chromium (see Chapter 6) in reasonable agreement with the temperature ranges quoted above. It should be noted that the temperature measurements performed previously for iron, nickel and chromium were carried out in exactly the same way as in this present study i.e. by focusing a calibrated optical pyrometer onto the hottest part of the furnace. An interesting point to note is that, in Fig. 5.B.1., the lower end of the evaporation temperature ranges for the three metals are within 50K of each other. Wild (1) has determined that a loss of material sufficient to produce 50% depletion to a depth of 10^{-6}m is not considered possible during a normal annealing period unless the equilibrium vapour pressure of the pure element exceeds 4×10^{-7} torr. The temperatures at which the vapour pressure is 4×10^{-7} torr for the individual main constituent elements, under equilibrium conditions, of the EN58A stainless steel have been given as (1)

Mn	870K
Cr	1225K
Fe	1280K
Ni	1320K

These temperatures correlated well with the temperatures at which depletion of the solid alloy was first observed in ref. (1). These actual "initial depletion temperatures" quoted in reference (1) are approximately 600K lower than those obtained in this study. This large discrepancy is obviously due to the relatively low sensitivity of the gas-phase p.e.s. technique. However, an interesting point to note is that the apparent vapourisation temperatures quoted by Wild (1)

are, for Fe, Cr and Ni, within 100K of each other in good agreement with the temperatures measured in this study. This p.e.s. experiment provides a useful opening for the new multidetector spectrometer. This spectrometer is capable of detecting smaller amounts of sample than the current single detector spectrometer and hence should be able to detect iron, chromium and nickel evaporation at lower temperatures than used in this work and possibly also manganese and chlorine. This present study failed to detect the evolution of manganese from the sample. However the concentration of manganese is fairly low in both the EN58A stainless steel (1.17%) used in reference (1) and the Cr/Ni/Nb stabilised steel (Sample A) used in this work (0.55%) and it should be possible for the Multidetector spectrometer to detect evolution of manganese where the single-detector spectrometer failed. Quite substantial evolution of manganese for a short period was noted in reference (1).

This study has obviously presented only preliminary results on the alloy (denoted Sample A). A measure of agreement has been obtained as far as evaporation characteristics are concerned. Leaving the evaporation of manganese aside, both studies show that the three metals Cr, Fe and Ni begin evaporating within 100K of each other. Further work however, is required to attempt to detect some of the elements present in the alloy in low concentration. It is hoped that the new multidetector spectrometer will allow this work to be carried out.

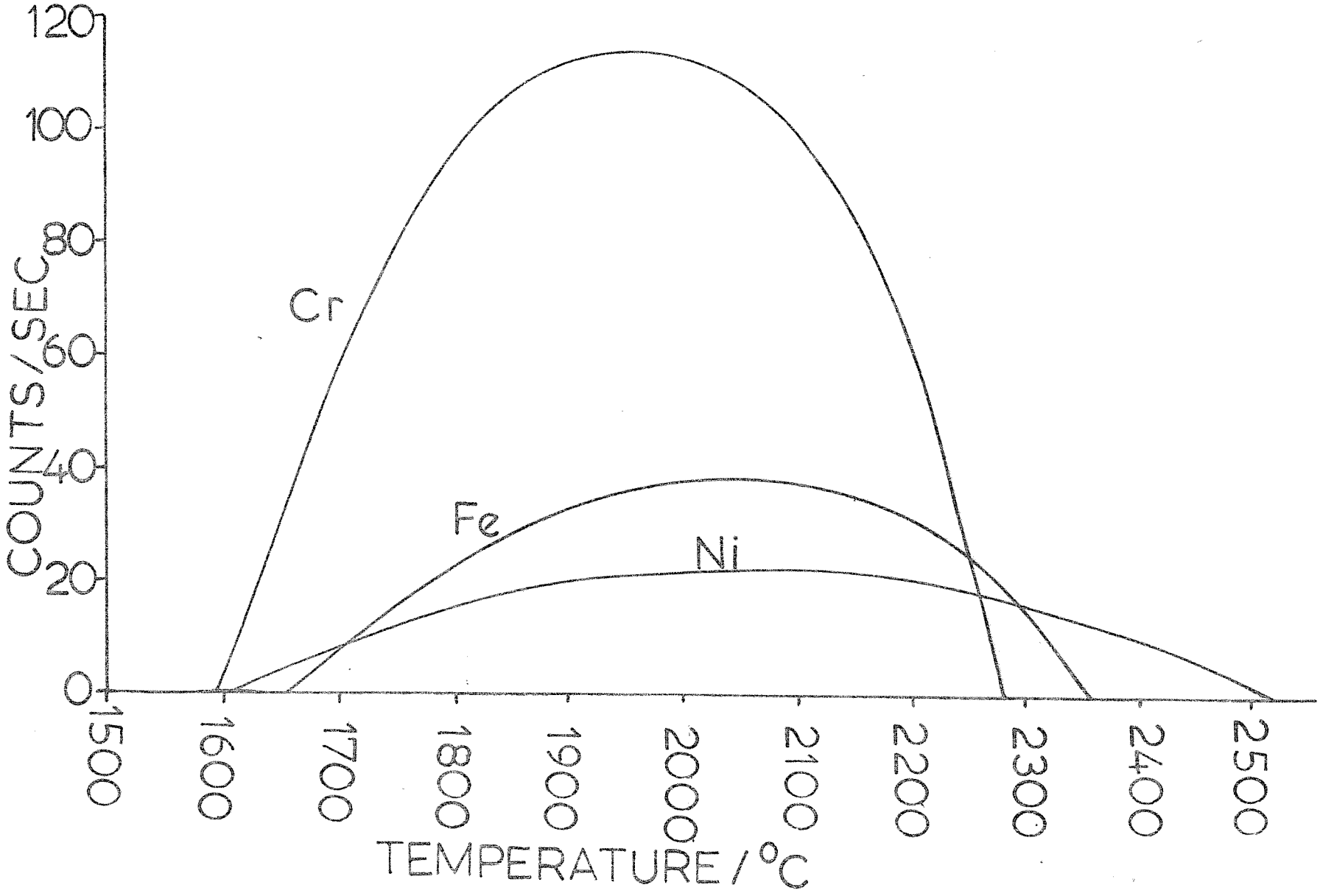

FIG 5B.1: Graph to show Fe, Cr, Ni intensities vs. temperature

REFERENCES

1. R.K. Wild, Corrosion Science, 14, 575 (1974).

2. R.K. Wild, Corrosion Science, 17, 87 (1977).

3. G.C. Allen and R.K. Wild, Can. J. Spectrosc., 28, 35 (1983).

4. R.K. Wild, Personal Communication.

CHAPTER SIX

CHAPTER 6.A. A THEORETICAL INTERPRETATION OF THE PHOTOELECTRON SPECTRUM OF TiO

6.A.1. Introduction

TiO is a molecule of considerable commercial and astrophysical importance (1, 2) and this prompted the recent experimental study on titanium and titanium monoxide at Southampton (3). Assignment of the experimental spectrum of atomic titanium was a relatively straightforward matter involving comparison with tabulated optical data (4). However, no such tabulated data exists for titanium monoxide. Work on AlF, CrO and VO (described in this thesis) has proved the value of ab initio ΔSCF CI calculations in facilitating the assignment of the photoelectron spectra of small molecules and, for this reason, it was decided to embark on a similar study on titanium monoxide in order to assign its experimental spectrum.

6.A.2. Computational Details

The ground electronic state of TiO is known from spectroscopic and theoretical studies (5-7) to be a $^3\Delta$ state which can be described in terms of the electronic configuration

$$----(8\sigma)^2(3\pi)^4(1\delta)^1(9\sigma)^1$$

where the 1δ level is essentially a Ti 3d atomic orbital and the 9σ molecular orbital is mainly Ti 4s in character. The 3π and 8σ levels are composed mainly of O2p atomic orbitals.

Previous ab initio calculations (5, 6) performed on TiO and TiO^+ using a minimum STO basis set with added Ti 4p and O3d polarisation functions suggest that the first ionisation potential of TiO corresponds to removal of an electron from the 9σ level to give the TiO^+ $^2\Delta$ state. Also, by evaluating the difference between the calculated minimum energies of the $TiO X^3\Delta$ and $TiO^+ X^2\Delta$ potential energy curves, an estimate has been made of the first adiabatic i.p. of TiO as 5.7eV (5).

In this work, a series of more extensive ab initio calculations have been performed on TiO and TiO^+ in order to estimate vertical ionisation energies for one electron ionisation from $TiO(X^3\Delta)$. All calculations were carried out at the experimental equilibrium bond length of $TiO(X^3\Delta)$ of 1.6203Å (8). Two basis sets were used for these calculations. Basis set I was a double-zeta STO basis taken from reference (9) with added polarisation functions with exponents O3d(2.10) and Ti4d(2.40), whereas basis set II was a contracted GTO basis composed of a [5s, 2p, 3d] set for titanium and a [3s, 2p] set for oxygen. This CGTO basis was constructed in exactly the same way as the corresponding VO and CrO basis sets, described in this chapter. For each basis set a number of one-electron processes were considered, namely the $(9\sigma)^{-1}$, $(1\delta)^{-1}$, $(8\sigma)^{-1}$ and $(3\pi)^{-1}$ ionisations and where more than one ionic state was produced on ionisation only the lowest state was considered in each case (10). SCF calculations were performed for these states of TiO^+ as well as for $TiO(X^3\Delta)$ and the corresponding ΔSCF vertical ionisation potentials derived from these calculations are listed in table 6.A.1.

In order to make some allowance for the correlation energy change on ionisation, limited configuration interaction calculations were performed for each ionic state as well as the neutral ground state.

For $TiO(X^3\Delta)$, a configuration interaction calculation was performed by considering all $^3\Delta$ states generated from the reference determinant computed with basis set II through single and double excitations with the constraint that only the orbitals 7σ to 13σ, 3π to 5π, 1δ and 2δ were open to orbital substitution. These were the orbitals whose energies were in the region -1.13a.u. to +1.12a.u. Exactly the same approach was adopted for the four TiO^+ states listed in table 6.A.1 with the same orbitals open to substitution.

As basis set II gave rise to a smaller number of functions and a lower total SCF energy than basis set I for any state of TiO or TiO^+ the SCF wave-functions obtained with basis set II were used in the configuration-interaction calculations performed in this work. The correlation energy corrected ΔSCF vertical ionisation potentials obtained by this approach are listed in table 6.A.1.

6.A.3. Results and Discussion

Two spectra recorded on vapourising stoichiometric TiO are shown in figure 6.A.1. These spectra were recorded recently by R.A. Lewis (3). For details of the experimental work reference (3) should be consulted. Spectrum (a) of fig. 6.A.1 shows the spectrum recorded between 6.0eV and 14.0eV while spectrum (b) shows an expanded version of the 5.0 to 10.0eV ionisation energy region. Two bands associated with TiO were observed in spectrum (b) at around 6.8eV and 8.4eV. In addition, a series of broad bands in the 10.0-12.0eV ionisation energy region were observed (spectrum (a)) which could also be attributed to TiO.

ΔSCF calculations performed in this work indicated that the first band of TiO (table 6.A.1) would correspond to a $(9\sigma)^{-1}$ ionisation while the second band would correspond to a $(8\sigma)^{-1}$ ionisation. However, as in the case of CrO and VO, it is not unusual for ΔSCF calculations to predict incorrectly the energy order of ionic states. For this reason, it was decided to perform limited configuration-interaction calculations on neutral TiO (the $TiO(X^3\Delta)$ ground state) and on a number of ionic states derived by one-electron ionisation from the neutral molecule, namely ionisations from the 9σ, 1δ, 8σ and 3π levels. The results of these calculations are also shown in table 6.A.1. The CI calculations predicted the first two bands of TiO to lie at 5.67eV and 7.58eV vertical ionisation energy corresponding to the two ionisations:

$$TiO^+(X^2\Delta) \leftarrow TiO(X^3\Delta)$$
$$TiO^+(^2\Sigma^+) \leftarrow TiO(X^3\Delta),$$

derived by $(9\sigma)^{-1}$ and $(1\delta)^{-1}$ ionisation respectively.

These calculated values show reasonable agreement with the experimentally derived values of 6.82±0.02eV and 8.20±0.01eV. Clearly, further more extensive CI calculations are needed to improve on these calculated values.

The CI calculations also predicted that the bands due to ionisation from the 8σ and 3π orbitals would appear at 9.21eV and 9.51eV respectively. Figure 6.A.1.(a) shows an expanded scan of the TiO

spectrum in which a series of bands with peak maxima of 10.57, 11.14, 11.48 and 11.78eV was observed. These bands cannot definitively be assigned at this stage but they are thought to be almost certainly due to ionisation to some of the states which arise from the $(8\sigma)^{-1}$ and $(3\pi)^{-1}$ ionisations. The $(8\sigma)^{-1}$ is expected to give three states ($^4\Delta$, $^2\Delta(2)$) and the $(3\pi)^{-1}$ ionisation is expected to give six states ($^4\Phi$, $^4\Pi$, $^2\Phi(2)$, $^2\Pi(2)$). These bands are expected in the 10.0-13.0eV ionisation energy region (10).

Mulliken analyses of the SCF wavefunctions were performed for all the states studied while Mulliken analyses of the CI natural orbitals were only performed for the $TiO(X^3\Delta)$, $TiO^+(^2\Sigma^+)$ and $TiO^+(^2\Delta)$ states. The results given in table 6.A.2 show that the $TiO^+(X^2\Delta)\leftarrow TiO(X^3\Delta)$ ionisation corresponds essentially to removal of an electron which is largely Ti4s in character whereas the $TiO^+(A^2\Sigma^+)\leftarrow TiO(X^3\Delta)$ ionisation corresponds to reduction of electron density from both the Ti3d and Ti4s atomic orbitals. This is essentially why the second band of TiO is much more intense than the first band. An exactly analogous result has also been obtained for the first two bands in the photoelectron spectrum of vanadium monoxide, described in this chapter. Hence, to summarise, the ΔSCF CI calculations performed in this work allow an assignment of the first two bands of the photoelectron spectrum of TiO to be made. Also, from these calculations it is possible to rationalise the relative intensities of these bands.

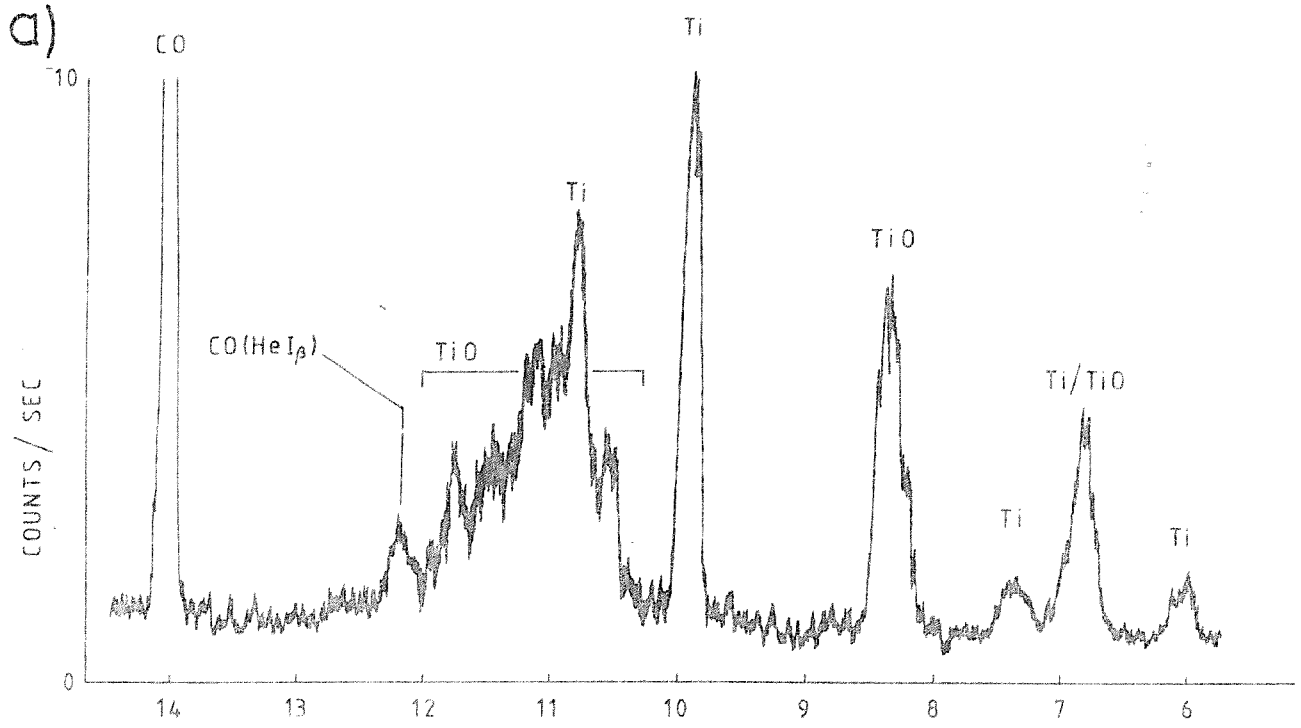
a)
CO
Ti
Ti
TiO
CO(HeIβ)
TiO
Ti/TiO
Ti
Ti
10
0
COUNTS / SEC
14
13
12
11
10
9
8
7
6

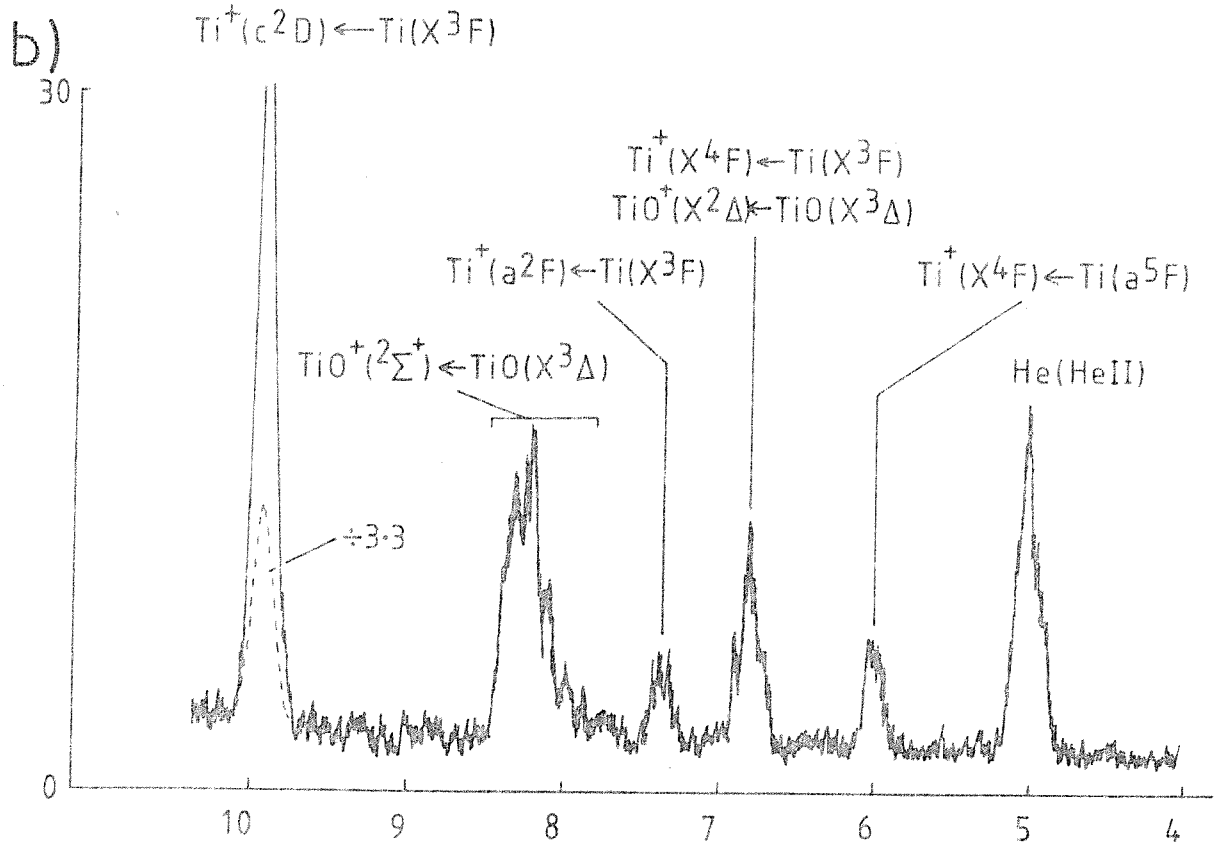
b)
Ti+(c2D)←Ti(X3F)
Ti+(X4F)←Ti(X3F)
TiO+(X2Δ)←TiO(X3Δ)
Ti+(a2F)←Ti(X3F)
Ti+(X4F)←Ti(a5F)
TiO+(2Σ+)←TiO(X3Δ)
He(HeII)
÷3·3
30
0
10
9
8
7
6
5
4
I.E.(eV)

FIG 6A.1

Table 6.A.1 Computed Vertical Ionisation Potentials (eV) of $TiO(X^3\Delta)$[a]

Ionisation[b]	Ionic state produced	ΔSCF value Basis I	ΔSCF value Basis II	ΔSCF+CI value Basis II	Experimental value
9σ	$^2\Delta$	5.81	6.03	5.67	6.82±0.02
1δ	$^2\Sigma^+$	7.92	8.36	7.58	8.20±0.01
8σ	$^4\Delta$	7.34	7.29	9.21	-
3π	$^4\Phi$	7.24	7.65	9.51	-

(a) See text for details of these calculations.

(b) One-electron ionisations were considered from the $TiO(X^3\Delta)(---8\sigma^2 3\pi^4 1\delta^1 9\sigma^1)$ configuration. Only the lowest energy ionic state arising from a particular configuration was considered in each case (10).

Table 6.A.2 Changes in Electron Density on Ionisation of $TiO(X^3\Delta)$ obtained from Ab Initio SCF Calculations[a]

Ionic State	Atomic Orbital[b]				
	Ti(s)	O(s)	Ti(p)	O(p)	Ti(d)
$TiO^+(^2\Delta)$	0.8467 (0.8767)	-0.0125 (-0.0102)	-0.0006 (-0.0009)	0.1108 (0.1015)	0.0567 (0.0328)
$TiO^+(^2\Sigma^+)$	0.5495 (0.4690)	-0.0201 (-0.0135)	-0.0085 (-0.0082)	0.1653 (0.1773)	0.3139 (0.3804)
$TiO^+(^4\Delta)$	0.6193	0.0170 CI DATA NOT AVAILABLE	-0.0077	0.1913	0.1802
$TiO^+(^4\Phi)$	0.5131	-0.0191 CI DATA NOT AVAILABLE	-0.0092	0.2671	0.2430

(a) These results were obtained with Basis II; similar results obtained with Basis I.

(b) Values in brackets obtained from CI calculations.

REFERENCES

1. (a) P.W. Merrill, A.J. Deutsch and P.C. Keenan, Astrophys. J., 136, 21 (1962).

   (b) H. Maerhara and Y. Yamashito, Publ. Astron. Soc. Jap., 28, 135 (1976).

2. (a) L.W. Ramsey, Astron. J., 86, 557 (1981).

   (b) H.R. Johnson, J.R. Mould and A.P. Bernat, Astrophys. J., 258, 161 (1982).

   (c) J.R. Mould and M.S. Bessell, Astrophys. J., 262, 142 (1982).

3. R.A. Lewis, Ph.D. Thesis, University of Southampton (1984).

4. (a) C.E. Moore, Atomic Energy Levels, NBS Circular No. 467 (Washington D.C., U.S. Govt. Printing Office, 1949).

   (b) C. Corliss and J. Sugar, J. Phys. Chem. Ref. Data, 8, 1 (1979).

5. K.D. Carlson and R.K. Nesbet, J. Chem. Phys., 41, 1051 (1964).

6. K.D. Carlson and C. Moser, J. Phys. Chem., 67, 2644 (1963).

7. C.W. Bauschlicher, P.S. Bagus and C.J. Melin, Chem. Phys. Letts., 101, 229 (1983).

8. (a) J.G. Phillips, Astrophys. J. Suppl. Series, 27, 319 (1974).

   (b) J.G. Phillips, Astrophys. J., 157, 449 (1969).

   (c) J.G. Collins, J. Physics B, 8, 304 (1976).

9. C. Roetti and E. Clementi, J. Chem. Phys., 60, 4725 (1974).

10. (a) J. Raftery, P.R. Scott and W.G. Richards, J. Phys. B, 5, 1293 (1972).

    (b) P.R. Scott, J. Raftery and W.G. Richards, J. Phys. B, 6, 881 (1973).

CHAPTER 6.B. THE He(I) PHOTOELECTRON SPECTRA OF VANADIUM AND VANADIUM MONOXIDE

6.B.1. Introduction

Gas-phase vacuum ultraviolet photoelectron spectra of the transition metals are important for a number of reasons. Firstly, the experimental spectra allow an estimate to be made of the relative photoionisation cross-sections of the outermost ns and (n-1)d shells at the photon energy used and this information is extremely useful in the interpretation of relative band intensities in the photoelectron spectra of transition metal compounds recorded at the same photon energy. Particular examples of this occur in the gas-phase HeI photoelectron spectra of CrO and TiO (described in this chapter) (37) where the spectra of atomic chromium and titanium proved useful in the assignment of the neutral metal monoxide spectra. Secondly, in recent years vacuum ultraviolet p.e.s. has proved to be a useful technique for investigating correlation and relativistic effects in atomic species and their ions (1-7). Atomic studies of this type are also important as a preliminary step for understanding changes in electronic structure which take place upon formation of molecules, polymeric species or solids from isolated atoms. The photoelectron spectrum of vanadium has been recorded during the course of this work using both single detector and multidetector spectrometers. This study has been an important test for the new spectrometer (briefly described in chapter 2 of this thesis) and has highlighted the advantages of multichannel detection over single channel detection. The photoelectron spectrum of vanadium has proved to be invaluable in the assignment of the photoelectron spectrum of VO, also recorded during the course of this work.

Several mass-spectrometric studies have been performed to study the vapour phase species present over the solids of VO and higher oxides such as V_2O_3. Berkowitz et al (8) have studied the molecules vapourising from $V_2O_5(s)$ and VO(s). The vapour over $V_2O_5(s)$ was found to contain $V_4O_{10}(g)$, $V_6O_{14}(g)$ and $V_6O_{12}(g)$ with some evidence for $V_4O_8(g)$ and $V_2O_4(g)$, whilst the vapour over VO(s) was found to contain V(g), VO(g) and $VO_2(g)$ with VO(g) being the largest vapour phase component.

Farber et al (9), in a similar study, found that the species in equilibrium with $V_2O_5(s)$ included $V_4O_{10}(g)$ and $V_4O_8(g)$. Also V_2O_3 was studied for the first time (9) showing that the main vapour phase components

were V(g), VO(g) and VO_2(g). In a series of studies by laser induced fluorescence spectroscopy (10-12), Merer et al produced VO by employing a 2450 MHz electrodeless discharge of a mixture of $VOCl_3$ and argon. This study produced an accurate value for the equilibrium bond length in the VO ground state which was subsequently used in the ab initio SCF calculations performed in this work. The bond length was obtained by rotational analysis of the observed spectrum. Kasai (13) employed another method to obtain VO. He used a mixture of V and V_2O_5 ($\sim$1:1 by weight) which gives rise to the reaction $3V + V_2O_5 \rightarrow VO$. Previous to this study there had been some doubt over the true ground state of neutral VO. It had been thought that it could be a $^2\Delta$ state arising from a $(\delta)^1(\sigma)^2$ configuration or a $^2\Sigma/^4\Sigma$ state arising from a $\delta^2\sigma^1$ configuration. Kasai (13) proved conclusively that the ground state was $^4\Sigma^-$ by isolating VO in an argon matrix and obtaining the e.s.r. spectrum of the molecule.

Lagerquist and Selin (14,15), have studied several electronic bands of VO observed in emission and have obtained reliable values for the equilibrium bond length of $VO(X^4\Sigma^-)$ and values for $\overline{\omega}_e$ and $\overline{\omega}_e x_e$ of 1011.56 cm^{-1} and 4.97 cm^{-1} for $VO(X^4\Sigma^-)$. It was hoped that values for $\overline{\omega}_e$ and r_e could be obtained for several states of VO^+ in this study.

All of the first row transition metals have now been studied via gas-phase p.e.s. (1,2) and a comparison of the photoionisation cross-section ratio $\sigma_{3d}:\sigma_{4s}$ across the series can now be made.

6.B.2. Experimental

Vanadium and vanadium oxide were produced in the gas-phase by vapourising the solids (99.9% Cerac Inc.) into flowing helium from tungsten furnaces (for details of furnace design see chapter two). Sufficiently high vapour pressures to record spectra of the species under investigation were obtained at furnace temperatures of (2030±30)K for vanadium and (2050±30)K for vanadium oxide. These temperatures were measured by focussing a calibrated optical pyrometer onto the hottest part of the furnace. In addition to the main experiments evaporations of V_2O_3, V_2O_5, $(V + V_2O_3)$ and $(3V + V_2O_5)$ were also carried out.

The photoelectron spectrometer and inductively heated furnace used in this study have both been described in detail in chapter 2 of this thesis. Spectral calibration was achieved using the HeIα and HeIβ spectra of methyl iodide and the He(II) ionisation of helium. The spectrum of vanadium proved to be an invaluable aid to the calibration of the vanadium oxide spectra. The transmission function of the analyser was calibrated using a standard method (16) and found to be linear within 5% of the electron kinetic energy for electron energies greater than 0.5eV. Observed ionisation energies agreed well with those obtained from optical spectroscopy (17) and are quoted to an estimated accuracy of ±0.01eV.

The vanadium spectra were recorded using both a single-detector spectrometer and the new multi-detector spectrometer (38) (described in chapter 2 of this thesis) allowing a comparison of the two methods of data acquisition to be made.

6.B.3. Computational Details

Ab initio SCF and configuration-interaction calculations were performed on a number of states of VO and VO^+ in order to estimate the ground state of VO^+ and vertical ionisation energies derived from one-electron ionisations from $VO(X^4\Sigma^-)$. All the calculations were carried out at the experimental equilibrium bond length of $VO(X^4\Sigma^-)$ of 1.5894Å (12). The basis set used was a contracted GTO basis. The vanadium (12s, 6p, 4d) basis set of Roos et al (32) was contracted to [5s, 2p, 2d] using the method of Raffenetti (33). The vanadium GTO basis was also augmented by a single diffuse d function, as specified by Hay (34), to give a total contracted GTO basis set of [5s, 2p, 3d]. For oxygen, the (7s,3p) GTO basis set of Roos and Siegbahn (35) was contracted to [3s, 2p].

The ground state of VO is known to be $X^4\Sigma^-$ (13) corresponding to the configuration

$$------(3\pi)^4(8\sigma)^2(1\delta)^2(9\sigma)^1$$

An SCF calculation was performed on the neutral molecule and on several ionic states derived by one-electron ionisation from the 9σ, 1δ, 8σ and 3π orbitals of the neutral molecule. Where more than one ionic state was

produced, only the position of the lowest state was calculated in each case (36). The results of the SCF calculations are given in table 6B.3.

Configuration Interaction calculations were performed on all the states of VO and VO^+ studied during the course of the SCF calculations. Assuming the dominant configuration of $VO(X^4\Sigma^-)$ to be $-----(3\pi)^4(8\sigma)^2(1\delta)^2(9\sigma)^1$ a calculation was performed by considering all $^4\Sigma^-$ configurations generated from the reference configuration through single and double excitations with the constraint that only the orbitals 8σ to 13σ, 3π to 5π and 1δ and 2δ were open to orbital substitution. These were the orbitals whose energies were in the energy range -1.15 to 1.31 au. This calculation showed that the $(3\pi)^4(8\sigma)^2(1\delta)^2(9\sigma)^1$ configuration is the main contributor to the groundstate of VO, with the coefficient of this configuration in the final CI wavefunction being 0.86. Following this calculation, some allowance for the correlation energy in the ionic state was made by performing CI calculations on states attainable by one-electron ionization from the 9σ, 1δ, 8σ, and 3π orbitals of neutral VO. In these calculations the same orbitals as used in the neutral CI calculations were open to substitution and all single and double excitations were considered in the CI expansions. The correlation corrected ΔSCF vertical ionization potentials obtained from these calculations are given in Table 6B.3.

6.B.4 Results and Discussion

The HeI photoelectron spectrum of atomic vanadium is shown in Figure 6.B.1. Six bands attributable to atomic vanadium are shown in this spectrum and have been labelled A to F. Although neutral vanadium has a $^4F_{3/2}$ ground state arising from the configuration $V(---3d^34s^2)$, other J-components (J=5/2, 7/2, 9/2) of this state will be populated at the temperatures used for evaporation (17). As a result, the observed spectra will contain contributions from ionisations from all four ^4F_J components. On the basis of known states and term values for V and V^+ (17), two formally allowed 4s ionisations and two formally allowed 3d ionisations are expected from the $V(a^4F, 3d^34s^2)$ ground state in the HeI energy range. These correspond to ionisation to the states $V^+(a^5F, 3d^34s^1)$, $V^+(a^3F, 3d^34s^1)$, $V^+(e^3F, 3d^24s^2)$ and $V^+(e^3P, 3d^24s^2)$.

As in the case of iron, cobalt and nickel (see chapter 5 of this thesis) an assumed temperature of ∿1800K (estimated from other p.e.s. studies of transition metals where the excitation temperature in the ionisation region is typically several hundred degrees lower than the furnace temperature) together with known optical data (17) may be used to calculate the position of the band maxima for the bands mentioned above. These positions were calculated as 7.06, 7.80, 11.46 and 12.79eV respectively, in good agreement with the corresponding peak maxima of bands B, C, E and F in figure 6.B.1. of 7.06, 7.78, 11.45 and 12.78eV. For bands B and C, the experimental intensity ratio was measured as 1.6±0.1:1.0 (corrected for analyser transmission) in good agreement with the ratio of 1.66:1 expected on the basis of the number of components in the ionic state whereas for bands E and F the corrected experimental intensity ratio was obtained as (9.8±1.6) in rather poor agreement with the ratio of 2.33:1 expected on the basis of upper state degeneracy. Clearly, band F is weaker than expected and has lost intensity by some mechanism such as final-state configuration interaction (18). However, use of the relative intensities of bands E and B, corrected for analyser transmission, leads to an estimate of the $\sigma_{3d}:\sigma_{4s}$ cross-section ratio at the HeI photon energy of (29.8±2.5) for atomic vanadium.

In addition to bands B, C, E and F, two other bands were observed in figure 6.B.1. which could be assigned to ionisation of atomic vanadium. These bands, labelled A and D in figures 6.B.1. and 6.B.2., were centred at 6.83 and 8.12eV respectively. The relative intensities of bands A to F are listed in table 6.B.1. On the basis of known atomic energy levels (17), bands A and D were assigned to 3d ionisations of a vanadium excited state (the a^6D state) which is approximately 0.27eV above the ground state. The ionisation processes involved are:

$V^+(a^5F,\ 3d^34s^1) \leftarrow V(a^6D,\ 3d^44s^1)$ (band A) and
$V^+(a^5P,\ 3d^34s^1) \leftarrow V(a^6D,\ 3d^44s^1)$ (band D).

The experimental ratio of these bands, corrected for analyser transmission, was measured at (2.2±0.2) in good agreement with the ratio of 2.33:1 expected on the basis of ionic state degeneracy. Also, assuming

a beam temperature of 1800K, their peak maxima were estimated from tabulated energy levels (17) as 6.83eV and 8.12eV in good agreement with the experimental values. One more band corresponding to a $(4s)^{-1}$ ionisation of the excited state should be observed at 6.47eV (17). However, using the value of $\sigma_{3d}:\sigma_{4s}$ derived in this work and taking account of degeneracy in the final states, this band would be expected to have an intensity of approximately $1/40^{th}$ of that of band A. Detailed examination of the spectra recorded during the course of this work did not yield definite evidence of this band. In most spectra the possible band did not have intensity above the normal base line and noise level.

As noted previously in a similar p.e.s. study of atomic titanium (19), bands associated with 3d ionisation of an excited state were of comparable intensity to bands associated with 4s ionisation of the ground state at the furnace temperature at which spectra were recorded. As can be seen from figure 6.B.2 and table 6.B.1, this also appears to be the case for the vanadium spectra recorded here. In the vanadium experimental spectra, the intensity of the $Va^4F(4s)^{-1}$ bands relative to the $Va^6D(3d)^{-1}$ bands is determined both by the 3d:4s photoionisation cross-section ratio and the relative population of the a^6D and a^4F neutral states. As a result, using the intensities of bands A and B (as these have the same final ionic states) and assuming the $\sigma_{3d}:\sigma_{4s}$ cross-section ratio of (29.8±2.5) derived earlier, a beam temperature at the point of photoionisation is obtained as (1940±260)K. This value is, as expected, slightly lower than the furnace temperature because of inefficient loss of electronic excitation energy by collisions of the excited metal atoms with the inert carrier gas before photoionisation occurs. An independent check of the above cross-section ratio can be obtained by using an electron excitation temperature of 1800K estimated from the known furnace temperature and from results obtained on other metals studied under similar conditions (1,2). At this temperature the relative population of the V a^6D and V a^4F levels will be 0.18, assuming a Boltzmann distribution between these levels, and use of the measured B:A band intensity ratio shown in table 6.B.1 leads to a value for $\sigma_{3d}:\sigma_{4s}$ of 31.6 in reasonable agreement with the more rigorously derived value of (29.8±2.5). This implies that the earlier assumption that band F has lost intensity by a mechanism such as final state configuration interaction is probably correct.

As well as bands A to F listed in table 6.B.1 another band was observed in most spectra centred at (10.47±0.02)eV ionisation energy. This has been marked 'X' in figure 6.B.1. This band was not proportional in intensity to the known atomic vanadium peaks and appeared at slightly lower furnace temperature than the bands attributed to atomic vanadium. Also this feature was only seen when vanadium was present in the furnace and it therefore almost certainly arises from a vanadium containing species. Although it cannot be positively identified this band could possibly be associated with the first ionisation potential of VO_2 which has been measured recently in an electron impact mass spectrometric study as (10.5±0.3)eV (20).

Figure 6.B.2 demonstrates one of the advantages of using a multi-detector photoelectron spectrometer compared with a single detector instrument, namely the improved data acquisition rate of the multidetector system. Figure 6.B.2(a) is a single scan of the 6.5-8.5eV i.p. region obtained on a single detector spectrometer in a time of 60 seconds whereas figure 6.B.2(b) is 150 scans of the same region in a total time of 9 seconds. From the statistics given in the figure, it can be estimated that the enhanced sensitivity of the multidetector form of detection, measured as a reduction in data acquisition time for a constant signal-to-noise ratio, is of the order of 50-60 for these experiments. Such an improvement in data acquisition speed is very valuable in high temperature photoelectron spectroscopy as it minimises problems associated with contamination of sensitive areas in the ionisation region which occur during the course of an evaporation. It should also be noted that the experimental relative intensities of the four bands A to D are, within experimental error, the same on both the multidetector and single detector spectrometers. This is because the furnace design, sample pumping speed, distance from the furnace to the photon source and temperature range over which spectra were recorded are very similar in both cases. There is, however, a significant improvement in the spectral resolution of figure 6.B.2(b) compared to figure 6.B.2(a). This is attributed mainly to an improved design of the heating system used in the multidetector spectrometer over that used in the single detector system which minimises the effects of electrical interference, as well as to the continuous monitoring capability of the TV-based multidetector system employed here.

The completion of this investigation on vanadium means that all the first row transition metals have now been studied in the gas-phase with photoelectron spectroscopy using the HeI photon source and a tabulation of the $\sigma_{3d}:\sigma_{4s}$ values derived from these studies is given in table 6.B.2. Although the values of $\sigma_{3d}:\sigma_{4s}$ for each element are dependent on the kinetic energy of the ejected electron and as a result the $\sigma_{3d}:\sigma_{4s}$ ratio varies slightly depending on the ionisation energies considered, the overall trend that is evident from table 6.B.2 is a decrease of $\sigma_{3d}:\sigma_{4s}$ with increasing atomic number. The main factor affecting photoionisation cross-sections which changes on going from scandium to zinc is the radial distribution of the 4s and 3d orbitals and this can be seen in table 6.B.2 where values of the radial expectation values $\langle r\rangle_{4s}$ and $\langle r\rangle_{3d}$, as calculated for the neutral transition metals with numerical relativistic Dirac-Fock calculations (21), are listed. As shown in this table, there is a disproportionate contraction of the 3d shell relative to the 4s shell as the atomic number increases. This occurs because each successive 3d electron is more effective in screening the 4s electrons from the added nuclear charge than in screening the remaining 3d electrons from this charge.

Qualitatively, comparison of measured $\sigma_{3d}:\sigma_{4s}$ ratios with values of $\langle r\rangle_{3d}$ and $\langle r\rangle_{4s}$ listed in table 6.B.2 implies that although both σ_{3d} and σ_{4s} at the HeI energy change on going from scandium to zinc, the main change occurs in σ_{3d} which decreases relative to σ_{4s} with increasing atomic number. Available photoionisation cross-section calculations (24-26) suggest that for the transition metals the 3d photoionisation cross-section will always be greater than or equal to the 4s photoionisation cross-section at the HeI(21.22eV) photon energy and higher photon energies. It appears from these calculations (24-26) that the 3d photoionisation cross-section as a function of electron kinetic energy increases smoothly above threshold to a maximum and then decreases slowly. The 4s cross-section, however, is relatively large at threshold where $\sigma_{4s}>\sigma_{3d}$. It then decreases rapidly to a minimum just above threshold before increasing slowly to a maximum whose height is typically one-tenth of the threshold value (26). This general behaviour is consistent with band intensities recorded in the photoelectron spectra of the first-row transition metal

negative ions obtained with an ArII(2.54)eV photon source (27-31) where the bands associated with $(4s)^{-1}$ ionisations are always more intense than those associated with $(3d)^{-1}$ ionisations.

The experimental spectrum obtained by vapourising stoichiometric VO is shown in figure 6.B.3. Apart from the four previously observed vanadium bands in the 6.0-9.0eV ionisation energy region (marked Av, Bv, Cv and Dv on the spectrum), two new bands were observed. On the basis of the ΔSCF calculations shown in table 6.B.3 these bands would be assigned to the

$$VO^+(^3\Sigma^-) \leftarrow VO(X^4\Sigma^-)$$

and

$$VO^+(^5\Sigma^-) \leftarrow VO(X^4\Sigma^-)$$ ionisations.

However the ground state electronic configuration of VO is known to be $....(8\sigma)^2(3\pi)^4(1\delta)^2(9\sigma)^1$. From this it might be expected that the first two observable bands would correspond to ionisations from the 9σ and 1δ orbitals to give $^3\Sigma^-$ and $^3\Delta$ states in the ion respectively. Subsequent CI calculations showed that this is in fact the case (similar behaviour was seen in the case of CrO also described in this chapter). Thus the two bands marked A_{VO} and B_{VO} in figure 6.B.3 are assigned to the $VO^+(X^3\Sigma^-) \leftarrow VO(X^4\Sigma^-)$ and $VO^+(A^3\Delta) \leftarrow VO(X^4\Sigma^-)$ ionisations respectively.

An expanded scan of the first band of VO is shown in figure 6.B.4. The sample used to obtain this spectrum must have had a slightly higher V:O ratio as this gave higher VO:V ratios than figure 6.B.3. The vertical ionisation potential of the first band was measured as (7.25±0.01)eV with the ΔSCF and ΔSCF + CI values of 6.54eV and 6.06eV being in reasonably good agreement. This band exhibited a clear vibrational series of three components derived by ionisation from the v''=0 level of the neutral molecule. In figure 6.B.4, it was noted that the band marked Bv was more intense relative to the band marked Av than expected. This can easily be seen by comparison of figures 6.B.1 and 6.B.4. The relative intensity of bands Av and Bv had been measured previously in the work on vanadium and closer examination revealed that the intensity of band Bv in the VO spectrum contained a contribution from ionisation

from the first vibrational level (v"=1) of neutral VO. Figure 6.B.4 shows both this "hot" band and the second band of vanadium in dotted form. Further evidence for the existence of this "hot" band is shown by the fact that the vibrational separation between it and the $VO^+(^3\Sigma^-, v'=0) \leftarrow VO(X^4\Sigma^-, v''=0)$ ionisation, measured as $(996\pm30)cm^{-1}$ is very close to $\bar{\omega}_e - 2\bar{\omega}_e x_e$ in the ground state neutral molecule of 1001.6 cm^{-1} (14,15). The vibrational separation in the ion was measured as 1060±50 cm^{-1} with $\bar{\omega}_e x_e$ being measured as $(5.0\pm10.0)cm^{-1}$. The corresponding value for $\bar{\omega}_e$ in the neutral molecule has been determined as $1011.56cm^{-1}$ (14,15). In view of this apparent increase in $\bar{\omega}_e$ on ionisation it is to be expected that there would be a corresponding decrease in the equilibrium bond length, r_e, in the ion. A series of Franck-Condon calculations can be used to estimate the equilibrium bond length in the ion. Firstly, ignoring the intensity of the "hot" band for the present, known values of r_e, $\bar{\omega}_e$ and $\bar{\omega}_e x_e$ in the neutral molecule (14,15) and the experimental values for $\bar{\omega}_e$ and $\bar{\omega}_e x_e$ determined in this work were used in a series of Franck-Condon calculations over a range of ionic equilibrium bond lengths. A value of r_e = 1.54±0.01Å for $VO^+(X^3\Sigma^-)$ was the value determined at this stage. Secondly, assuming a Boltzmann vibrational temperature of 875K by analogy with TiO (19,37), the relative populations in the first four vibrational levels of $VO(X^4\Sigma^-)$ were calculated. A further set of Franck-Condon calculations were then performed over a range of equilibrium bond lengths until good agreement with the observed envelope, including the presence of the "hot" band was obtained. Having assumed a temperature of 875K, the ionic equilibrium bond length was found to be essentially unchanged at r_e = 1.55±0.01Å. The value for r_e in the neutral molecule has previously been determined at 1.5894Å (12).

The second band of VO shown in figure 6.B.3 had a measured vertical ionisation potential of 8.42±0.01eV. The ΔSCF and ΔSCF + CI calculated v.i.p.s. of 8.01eV and 7.51eV respectively are both in reasonable agreement with the experimental value. However, it was mentioned earlier that the ΔSCF calculations failed to predict the correct ordering of ionic states. The correct ordering was only predicted when correlation was taken into account through a series of configuration interaction

calculations. No vibrational structure was observed on this band and this is probably due to spin-orbit splitting in the ionic $^3\Delta$ state and vibrational excitation in the neutral molecule making resolution of any structure very difficult.

The experimental relative intensities of the two VO bands have been measured at $5.63\pm0.44(^3\Delta):1(^3\Sigma^-)$ after correction for the transmission function of the analyser. This can be rationalised on the basis of the $\sigma_{3d}:\sigma_{4s}$ relative photoionisation cross-section ratio of (29.8±2.5) for vanadium quoted earlier. Table 6.B.4, which lists calculated changes in electron density on ionisation, shows that the main change on ionisation to the $VO^+(X^3\Sigma^-)$ state is in V(s) electron density while the corresponding changes on ionisation to the $VO^+(^3\Delta)$ state are in V(s) and V(d) electron density. In view of the greater change in V(d) electron density for the $VO^+(^3\Delta)$ state it is to be expected that the band due to the $(1\delta)^{-1}$ ionisation will be greater in intensity than that due to the $(9\sigma)^{-1}$ ionisation. This is, in fact, what is observed experimentally.

Despite a careful search of the high i.p. region (10eV upwards) no higher bands of VO were observed. On the basis of the CI calculations performed in this work it is quite likely that a higher band could be observed. This high i.p. region is currently being re-investigated using the new multidetector spectrometer at Southampton (described in chapter 2 of this thesis) and it is hoped that bands due to $(3\pi)^{-1}$ and $(8\sigma)^{-1}$ ionisation from the neutral molecule will be observed. It is also possible that the band 'X' in figure 6.B.1 will also be observed.

In addition to the main experiments on stoichiometric VO, test evaporations were carried out on two mixtures of vanadium with higher vanadium oxides. Figure 6.B.5 shows the spectrum obtained on evaporation of a 3:1 stoichiometric V/V_2O_5 mixture. This was useful in that the intensity of the vanadium bands was low relative to that of VO and hence made measurement of the intensity of the first band of VO less complicated. The general behaviour of the sample was very similar to that of a pure VO sample with a near identical vaporisation temperature. It was noticed, however, that pressure was rather high at low temperature and this is thought to be due to evolution of oxygen. An evaporation of a 1:1 V/V_2O_3

mixture as used by Kasai (13) was also carried out. This behaved almost identically to a pure VO sample with similar yields of vanadium and vanadium oxide and hence it was not thought necessary to present a spectrum here. It is interesting to note that, contrary to mass-spectrometric studies (8,9), no polymeric species were observed in the experiments on these mixtures. The new multidetector spectrometer will prove useful in detecting these species in future experiments since the evidence (8,9) shows that they should be readily observable. Figure 6.B.6 shows a spectrum derived from evaporation of a 1:1 V/VO mixture. This experiment was carried out to produce spectra of VO with more intense vanadium bands and this proved useful for calibration purposes. Again, as with the two other mixtures, sample behaviour was very similar to that of pure VO.

Clearly, further work would be useful to supplement the work on vanadium and vanadium oxide described in this chapter. It would obviously be useful to study all the first-row transition metals using a synchrotron source in order that relative band intensities can be systematically measured as a function of photon energy. In the case of vanadium oxide, it would be useful to study the higher i.p. region in the hope of finding higher bands of the molecule. Also, more extensive CI calculations are necessary to determine more accurate vertical ionisation potentials. The present calculations are obviously only relatively small CI calculations with only a limited number of single and double electron excitations considered. This was necessary because of the limits on computer time and storage space.

The work on vanadium monoxide discussed in this chapter has, as far as is known, produced the first ever directly measured value for the first ionisation potential of VO. Recent work by Balducci et al (20), using high temperature mass-spectrometry, has estimated the first i.p. of VO^+ as 8.4±0.3eV. This value corresponds to the second ionisation potential of 8.42±0.01eV determined in this work. The reason for this apparent discrepancy is that, as in the HeI spectrum, the intensity of the first ionisation process in VO on electron impact (in ref. (20) 70eV kinetic energy electrons were used) is very much weaker than the second ionisation process and Balducci et al (20) erroneously extrapolated their ion currents back to the second i.p. of VO.

The study by Balducci et al (20) has also produced an estimate of 10.5±0.3eV for the appearance potential of VO_2^+ and it would obviously be of interest to study the higher i.p. regions of the vapour above several oxides of vanadium to see if this band is observable with u.v. p.e.s.

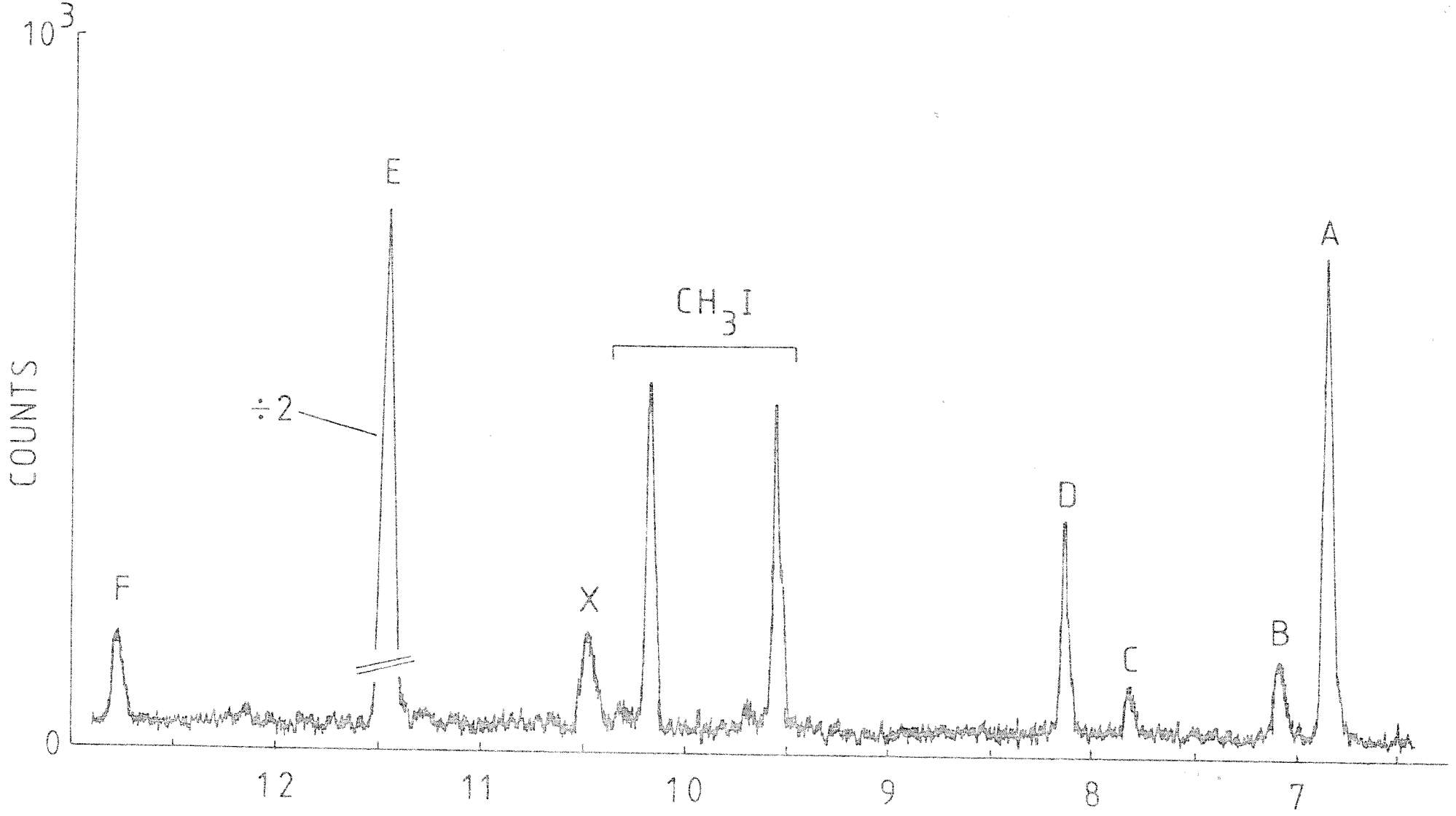

FIG 6B.1

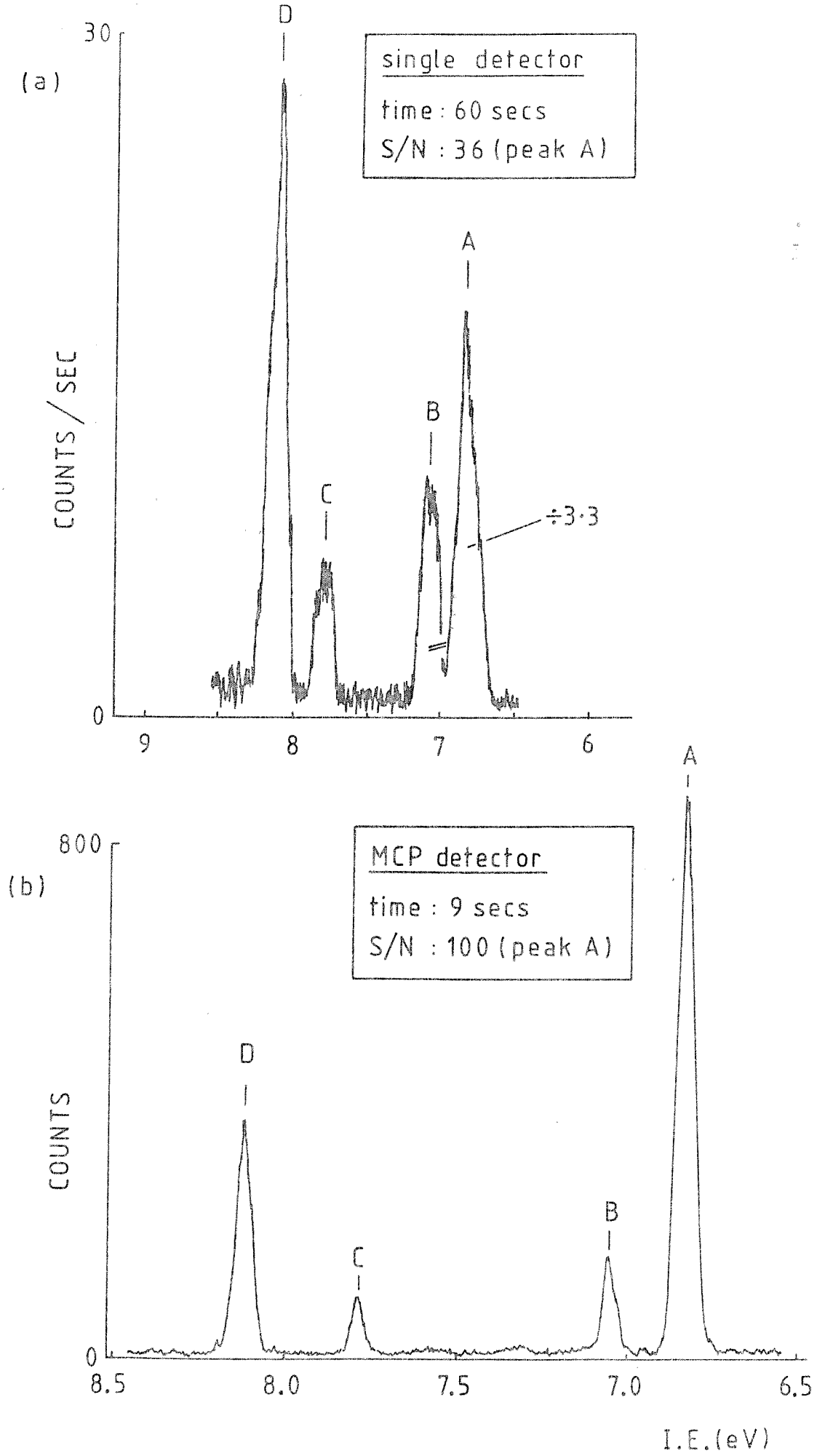
(a)
30
0
COUNTS / SEC
D
C
B
A
÷3·3
9
8
7
6
single detector
time : 60 secs
S/N : 36 (peak A)
(b)
800
0
COUNTS
D
C
B
A
8.5
8.0
7.5
7.0
6.5
I.E.(eV)
MCP detector
time : 9 secs
S/N : 100 (peak A)

FIG 6B.2

A_V : $V^+(a^5F) \leftarrow V(a^6D)$

B_V : $V^+(a^5F) \leftarrow V(a^4F)$

C_V : $V^+(a^3F) \leftarrow V(a^4F)$

D_V : $V^+(a^5P) \leftarrow V(a^6D)$

A_{VO}: $VO^+(X^3\Sigma^-) \leftarrow VO(X^4\Sigma^-)$

B_{VO}: $VO^+(A^3\Delta) \leftarrow VO(X^4\Sigma^-)$

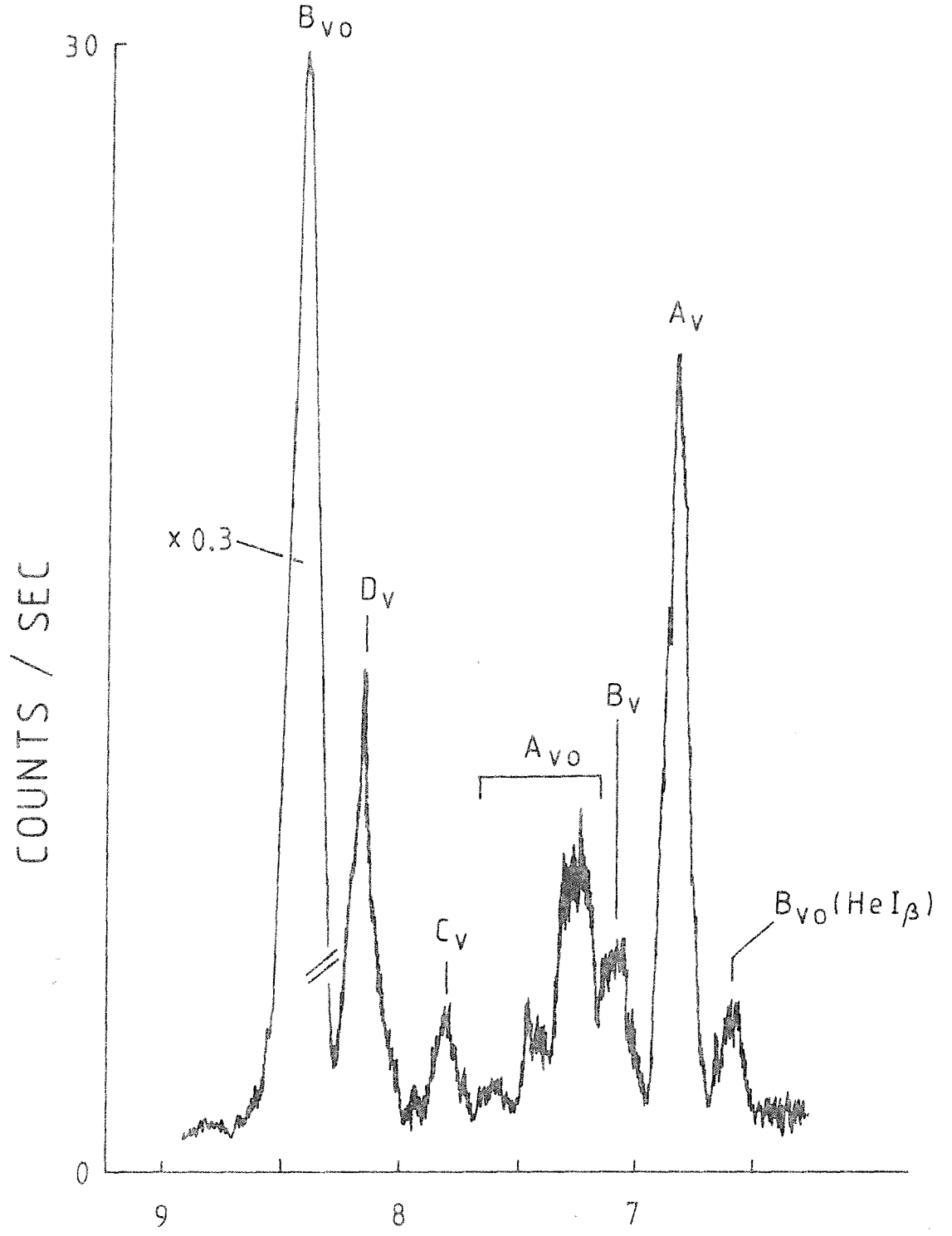

FIG 6B.3

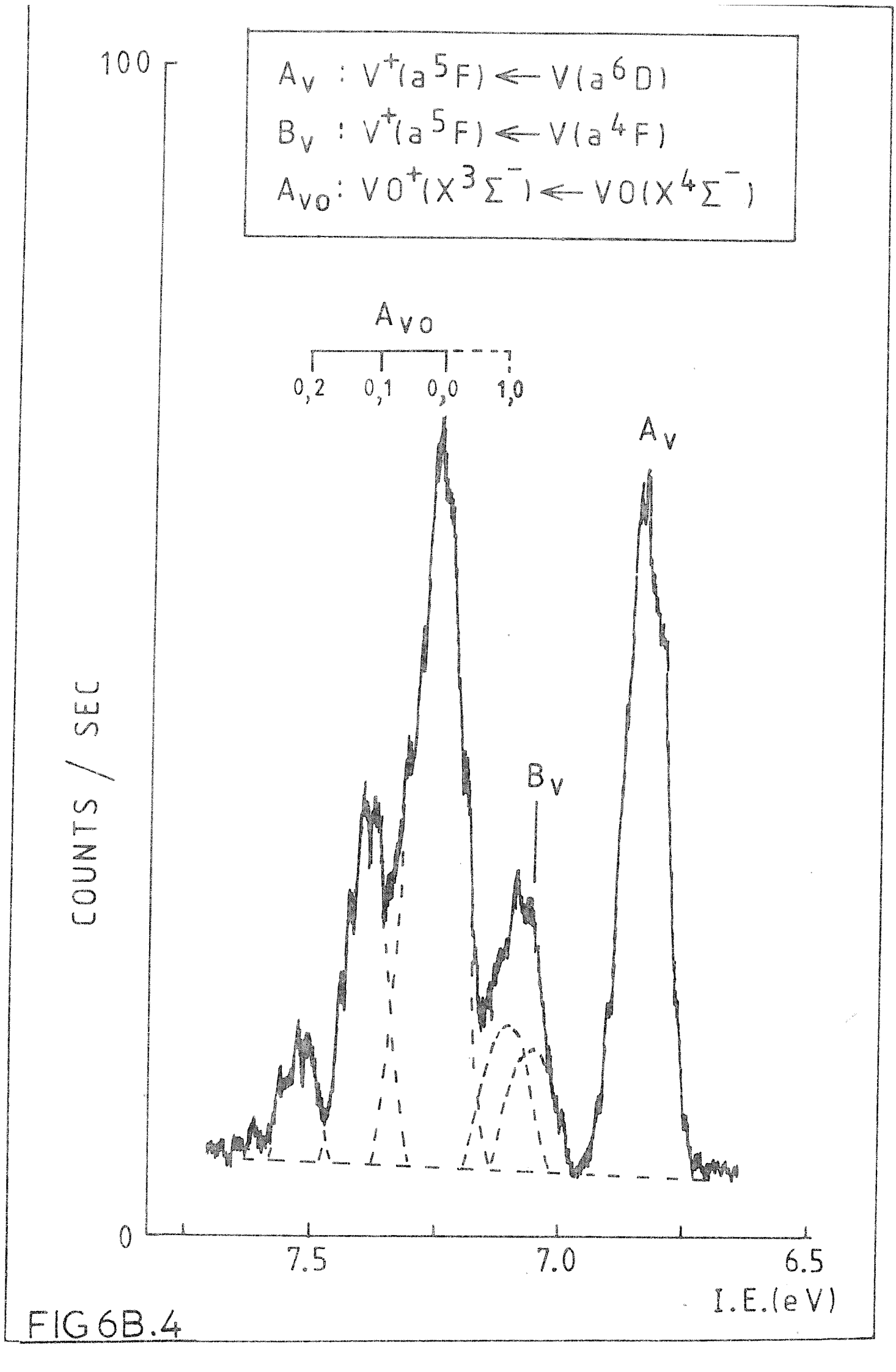
A_V : $V^+(a^5F) \leftarrow V(a^6D)$
B_V : $V^+(a^5F) \leftarrow V(a^4F)$
A_{VO}: $VO^+(X^3\Sigma^-) \leftarrow VO(X^4\Sigma^-)$
100
0
COUNTS / SEC
A_{VO}
0,2
0,1
0,0
1,0
A_V
B_V
7.5
7.0
6.5
I.E.(eV)

FIG 6B.4

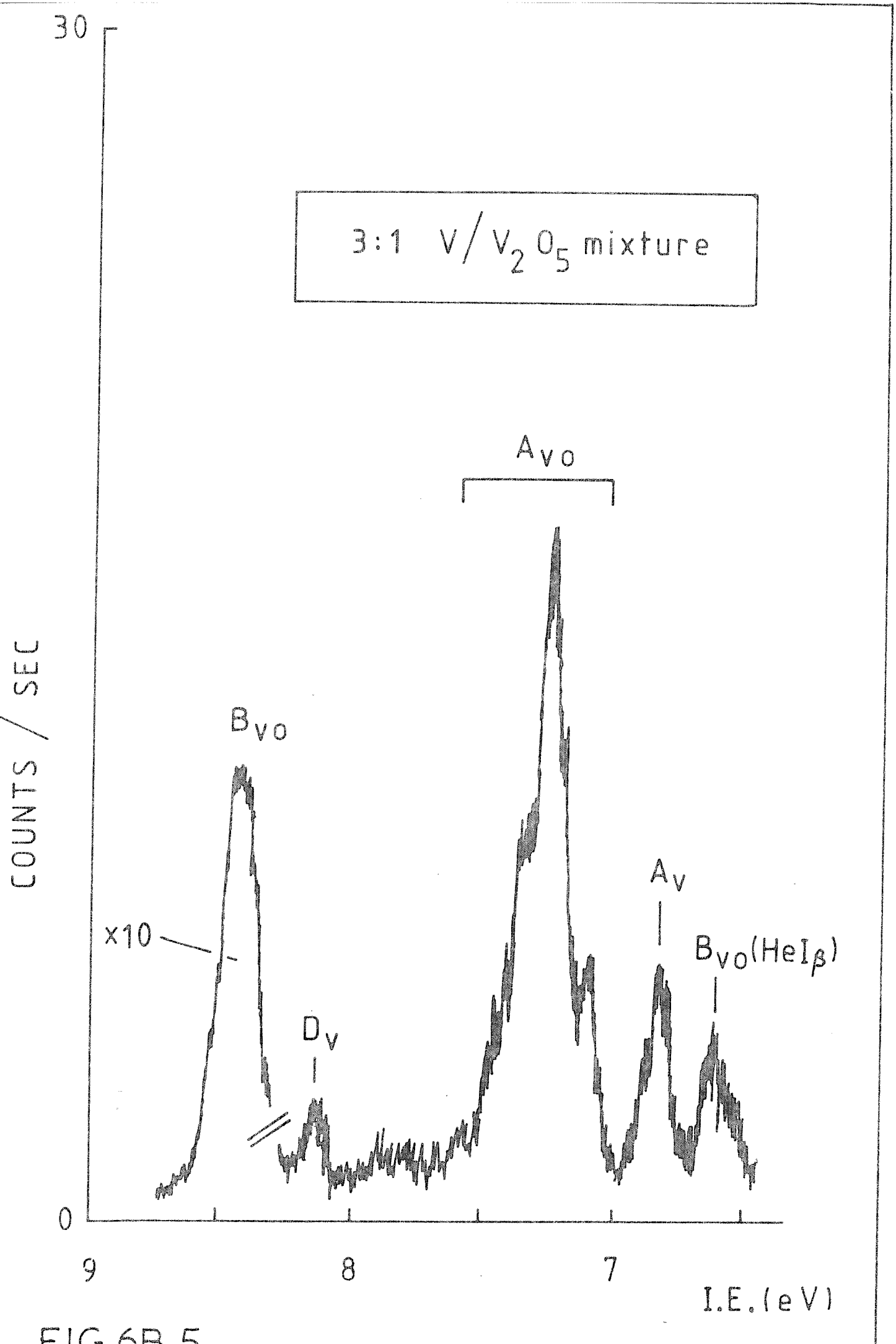
30
3:1 V/V2O5 mixture
AVO
BVO
AV
BVO(HeIβ)
DV
x10
COUNTS / SEC
0
9
8
7
I.E.(eV)

FIG 6B.5

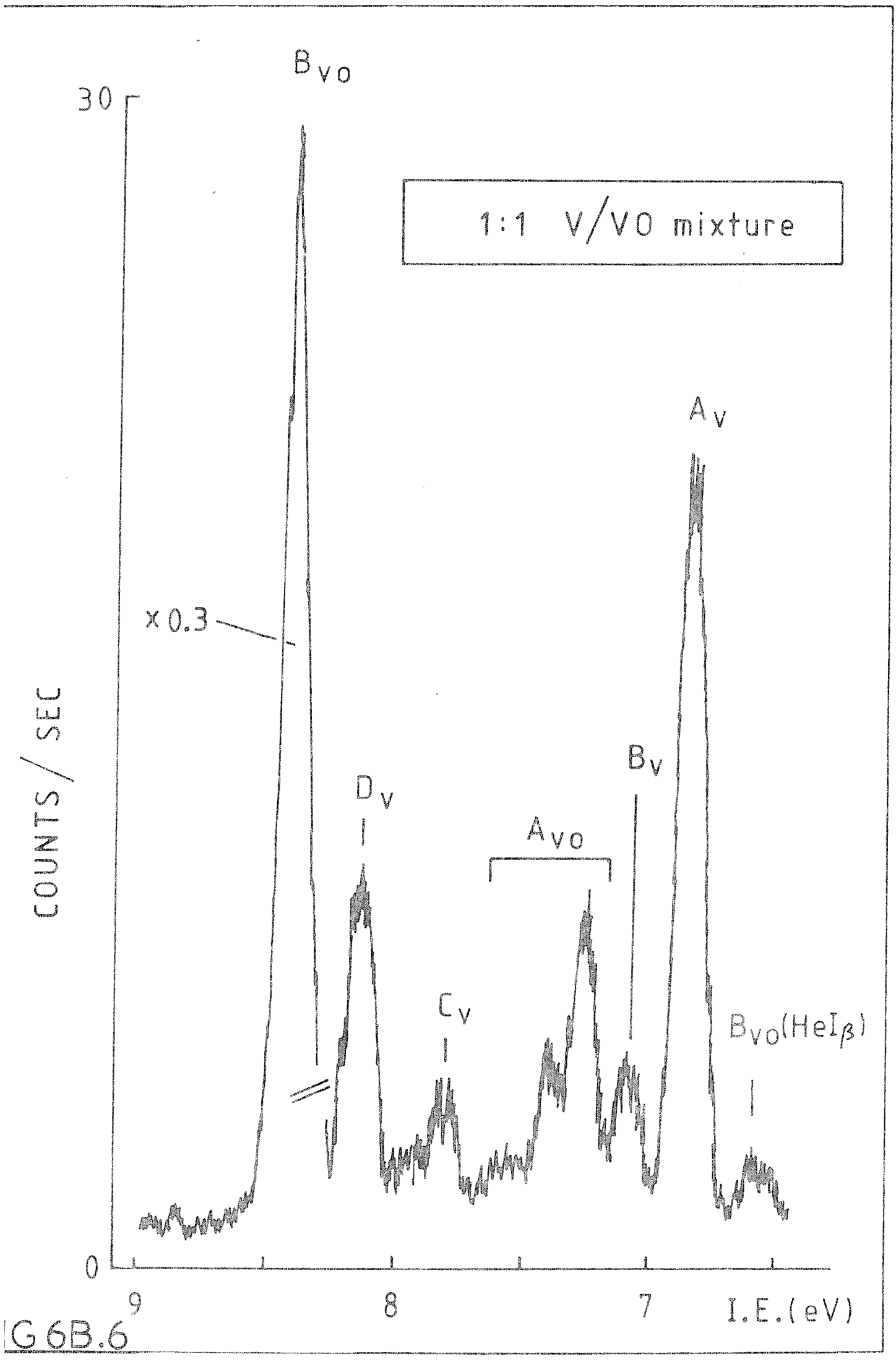
Bvo
30
1:1 V/VO mixture
Av
x 0.3
Dv
Bv
Avo
Cv
Bvo(HeIβ)
COUNTS / SEC
0
9
8
7
I.E.(eV)

G6B.6

Table 6.B.1

Measurements obtained from the HeI photoelectron spectrum of vanadium

Band Label in Figure 2	Orbital Ionized	Band Assignment	Measured Ionisation Potential (eV) of Band Maximum	Corrected Experimental Relative Intensities(a)
A	3d	$V^+(a^5F) \leftarrow V(a^6D)$	6.83	9.3±0.1
B	4s	$V^+(a^5F) \leftarrow V(a^4F)$	7.06	1.6±0.1
C	4s	$V^+(a^3F) \leftarrow V(a^4F)$	7.78	1.0
D	3d	$V^+(a^5P) \leftarrow V(a^6D)$	8.12	4.3±0.1
E	3d	$V^+(e^3F) \leftarrow V(a^4F)$	11.45	28.8±0.3
F	3d	$V^+(e^3P) \leftarrow V(a^4F)$	12.78	2.9±0.3

(a) Corrected for the transmission function of the analyser.

Table 6.B.2. Comparison of HeI $\sigma_{3d}:\sigma_{4s}$ cross-section ratios with computed radial expectation values (21) for the 3d and 4s orbitals in the first row transition metals

	Ground State Electronic Configuration	Experimental HeI $\sigma_{3d}:\sigma_{4s}$ ratio; this work and references (22, 23)	$\langle r_{3d} \rangle$ a.u. ref. (21)	$\langle r_{4s} \rangle$ a.u. ref. (21)
Sc*	$3d^1 4s^2$	57.1±9.0	1.69	3.94
Ti	$3d^2 4s^2$	30.0±5.9	1.50	3.74
V	$3d^3 4s^2$	29.8±2.5	1.36	3.58
Cr	$3d^5 4s^1$	9.1±2.0	1.41	3.79
Mn	$3d^5 4s^2$	3.2±0,4	1.16	3.31
Fe	$3d^6 4s^2$	25.5±1.5	1.09	3.20
Co	$3d^7 4s^2$	9.0±1.0	1.03	3.10
Ni	$3d^8 4s^2$	3.1±0.3	0.97	3.01
Cu	$3d^{10} 4s^1$	1.0±0.1	0.99	3.26
Zn	$3d^{10} 4s^2$	1.9	0.88	2.85

*M.P. Hastings, Personal Communication.

Table 6.B.3 Computed vertical ionisation potentials (eV) of $VO(X^4\Sigma^-)$ [a]

Ionisation [b]	Ionic State Produced	ΔSCF Value	ΔSCF + CI Value	Experimental Value	No. of Configurations generated [c]
-	$VO(X^4\Sigma^-)$	-	-	-	3693
$(9\sigma)^{-1}$	$VO^+(^3\Sigma^-)$	6.54	6.06	7.25±0.01	2611
$(1\delta)^{-1}$	$VO^+(^3\Delta)$	8.01	7.51	8.42±0.01	2618
$(3\pi)^{-1}$	$VO^+(^5\Pi)$	7.25	10.04	-	3970
$(8\sigma)^{-1}$	$VO^+(^5\Sigma^-)$	6.94	9.25	-	3618

(a) See text for details of these calculations.
(b) One-electron ionisations were considered from the $VO(X^4\Sigma^-)$ state. Only the lowest energy ionic state arising from a particular configuration was computed in each case.
(c) Configurations generated by one- and two-electron excitations from the reference configuration in each case.

Table 6.B.4 Changes in electron density on ionisation calculated from VO converged SCF wavefunctions[a]

State	Atomic Orbital				
	V(s)	O(s)	V(p)	O(p)	V(d)
$VO(X^4\Sigma^-)$	-	-	-	-	-
$VO^+(X^3\Sigma^-)$	0.7288 (0.7973)	-0.0122 (-0.0088)	-0.0015 (-0.0018)	0.1548 (0.1304)	0.1301 (0.0828)
$VO^+(^3\Delta)$	0.5526 (0.5283)	-0.0163 (-0.0142)	-0.0067 (-0.0058)	0.1492 (0.1384)	0.3212 (0.3533)
$VO^+(^5\Pi)$	0.5639	-0.0160 CI DATA NOT AVAILABLE	-0.0073	0.2371	0.2224
$VO^+(^5\Sigma^-)$	0.6190	0.0208 CI DATA NOT AVAILABLE	-0.0061	0.1699	0.1965

(a) Figures in brackets are the electron density changes derived from analysis of the CI natural orbitals.

REFERENCES

1. J.M. Dyke, G.D. Josland, R.A. Lewis and A. Morris, Molecular Physics, 44, 967 (1981).

2. J.M. Dyke, N.K. Fayad, G.D. Josland and A. Morris, Molecular Physics, 41, 1051 (1980).

3. S. Suzer, M.S. Banna and D.A. Shirley, J. Chem. Phys., 63, 3473 (1975).

4. N.S. Hush and S. Suzer, Chem. Phys. Letts., 46, 411 (1977).

5. E.P.F. Lee and A.W. Potts, J. El. Spec. Rel. Phen., 19, 65 (1980).

6. J. Berkowitz, J.L. Dehmer, Y.K. Kim and J.P. Desclaux, J. Chem. Phys., 61, 2556 (1974).

7. (a) S.T. Lee, S. Suzer, E. Matthias, R.A. Rosenberg and D.A. Shirley, J. Chem. Phys. 66, 2496 (1977).

   (b) S. Suzer, S.T. Lee and D.A. Shirley, J. Chem. Phys., 65, 412 (1976).

8. J. Berkowitz, W.A. Chupka and M.G. Inghram, J. Chem. Phys., 27, 87 (1957).

9. M. Farber, O.M. Uy and R.D. Srivastava, J. Chem. Phys., 56, 5312 (1972).

10. A.S.C. Cheung, R.C. Hansen, A.M. Lyyra and A.J. Merer, J. Mol. Spec., 86, 526 (1981).

11. A.S. C. Cheung, R.C. Hansen and A.J. Merer, J. Mol. Spec., 91, 165 (1982).

12. A.S. C. Cheung, A.W. Taylor and A.J. Merer, J. Mol. Spec., 92, 391 (1982).

13. P.H. Kasai, J. Chem. Phys., 49, 4979 (1968).

14. A. Lagerquist and L-E. Selin, Arkiv. Fysik, 11, 429 (1956).

15. A. Lagerquist and L-E. Selin, Arkiv. Fysik, 12, 553 (1957).

16. J.L. Gardner and J.A.R. Samson, J. El. Spec. Rel. Phen., 8, 469 (1976).

17. (a) C. Moore, Atomic Energy Levels NBS Circ. 467 Vol. 1 (Washington D.C., U.S. Govt. Printing Office, 1949).

   (b) J. Sugar and C. Corliss, J. Phys. Chem. Ref. Data, 7, 1191 (1978).

   (c) J. Sugar and C. Corliss, J. Phys. Chem. Ref. Data, 9, 473 (1980).

18. S.T. Manson, J. El. Spec. Rel. Phen., 9, 21 (1976).

19. R.A. Lewis, Ph.D. Thesis, University of Southampton (1984).

20. G. Balducci, G. Gigli and M. Guido, J. Chem. Phys., 79, 5616 (1983).

21. J.P. Desclaux, Atomic Data and Nuclear Data Tables, 12, 311 (1973).

22. J.M. Dyke, N.K. Fayad, A. Morris and I.R. Trickle, J. Phys. B., 12, 2985 (1979).

23. (a) S. Suzer, S.T. Lee and D.A. Shirley, Phys. Rev., A13, 1842 (1976).

(b) S. Suzer and D.A. Shirley, J. Chem. Phys., 61, 2481 (1974).

24. D.J. Kennedy and S.T. Manson, Phys. Rev., A5, 227 (1972).

25. S.M. Goldberg, C.S. Fadley and S. Kono, J.El. Spec. Rel. Phen., 21, 285 (1981).

26. R.F. Reilmann and S.T. Manson, Phys. Rev., A18, 2124 (1978).

27. W.C. Lineberger, Pure Applied Physics, 243, 239 (1982).

28. R.R. Cordermann, P.C. Engelking and W.C. Lineberger, J. Chem. Phys., 70, 4474 (1979).

29. P.C. Engelking and W.C. Lineberger, Phys. Rev. A19, 149 (1979).

30. C.S. Feigerle, Z. Herman and W.C. Lineberger, J. El. Spec. Rel. Phen., 23, 441 (1981).

31. C.S. Feigerle, R.R. Cordermann, S.V. Bobashev and W.C. Lineberger, J. Chem. Phys., 74, 1580 (1981).

32. B. Roos, A. Veillard and G. Vinot, Theor. Chim. Acta., 20, 1 (1971).

33. R.C. Raffenetti, J. Chem. Phys., 58, 4452 (1973).

34. P.J. Hay, J. Chem. Phys., 66, 4377 (1977).

35. B. Roos and P. Siegbahn, Theor. Chim. Acta., 17, 209 (1970).

36. (a) J. Raftery, P.R. Scott and W.G. Richards, J. Phys. B., 5, 1293 (1972).

(b) P.R. Scott, J. Raftery and W.G. Richards, J. Phys. B., 6, 881 (1973).

37. J.M. Dyke, B.W.J. Gravenor, R.A. Lewis and A. Morris, Molecular Physics (in Press).

38. These experiments were performed in collaboration with M.P. Hastings.

CHAPTER 6.C. THE FIRST IONISATION POTENTIAL OF THE $CrO(X^5\Pi)$ MOLECULE

6.C.1. Introduction

Very little is known about the low-lying electronic states of the monopositive ions of the diatomic first-row transition metal oxides and, in almost all cases, not even the ground electronic state is known with any certainty. In contrast, the ground electronic state of most of the corresponding neutral oxides is now well established as a result of spectroscopic studies which have been performed on several low-lying states of the neutral molecule (1-7).

In the case of chromium monoxide, the electronic ground state is known to be $CrO(X^5\Pi)$ and a number of spectroscopic constants for this state have been derived (8, 9). In addition, there have been various estimates of the first ionisation potential. The most recent values are 7.7±0.3eV, obtained by studying the translational-energy dependence of the reaction cross-sections of Cr^+ with N_2O and O_2 (10) and 8.2±0.5eV and 8.4±0.5eV, obtained from electron impact mass spectrometry (11, 12). Because the error limits associated with these ionisation energies are large, the present photoelectron spectroscopic study (p.e.s.) was undertaken to provide an improved value for the first adiabatic ionisation potential of CrO. It was also hoped that p.e.s. would facilitate characterisation of the accessible states of CrO^+ and assist with the determination of the electronic ground state of this ion.

6.C.2. Experimental

Chromium monoxide was produced in the gas-phase by reacting chromium atoms with either oxygen or ozone in the region just above the photoionisation zone of the spectrometer. A few experiments were also carried out with nitrous oxide as the oxidant but no reaction was observed. At first sight this may seem surprising as inspection of tabulated heats of formation (13) shows that the $Cr+N_2O$ reaction is more exothermic than the $Cr+O_2$ reaction, i.e.

$$Cr(^7S) + O_2(X^3\Sigma_g^-) \rightarrow CrO(X^5\Pi) + O(^3P) \quad \Delta H^\theta = 75.2 \text{ kJmol}^{-1} \qquad (1)$$

$$Cr(^7S) + N_2O(X^1\Sigma^+) \rightarrow CrO(X^5\Pi) + N_2(X^1\Sigma_g^+) \quad \Delta H^\theta = -173.1 \text{ kJmol}^{-1} \qquad (2)$$

$$Cr(^7S) + O_3(X^1A_1) \rightarrow CrO(X^5\Pi) + O_2(X^3\Sigma_g^-) \quad \Delta H^\theta = -315.7 \text{ kJmol}^{-1} \qquad (3)$$

It should be noted, however, that $N_2O(X^1\Sigma^+)$ does not correlate with $N_2(X^1\Sigma_g^+)$ and $O(^3P)$ but dissociates to $N_2(X^1\Sigma_g^+)$ and $O(^1D)$ (10, 14), unlike $O_3(X\,^1A_1)$ and $O_2(X^3\Sigma_g^-)$ which both dissociate to ground-state products when one bond is broken. More importantly, however, application of spin conservation shows that reaction (2) is spin-forbidden whereas reactions (1) and (3) are both partially allowed.

In this study, chromium atoms were produced in the vapour phase by evaporating chromium from a zirconia-lined molybdenum furnace (15). Ozone was prepared by high-voltage discharge of oxygen and stored by trapping on non-indicating silica gel at dry-ice temperature.

The photoelectron spectrometer and inductively heated furnace used in this study are both described in detail in chapter 2 of this thesis (16-18). Spectral calibration was achieved using the HeIα (21.22eV) spectra of methyl iodide and chromium atoms. The first band of CrO has also been recorded with NeIα radiation and calibration was achieved in this case using the first band of chromium atoms recorded with the NeIα 16.67eV and 16.85eV photon lines. No new spectral information was obtained from the NeI spectra although the measurements obtained were in good agreement with those obtained from the HeI spectra.

6.C.3. Computational Details

Ab initio SCF and configuration-interaction calculations were performed on a number of states of CrO and CrO^+ in order to estimate the ground state of CrO^+ and vertical ionisation energies derived from one-electron ionisations from $CrO(X^5\Pi)$. All calculations were carried out at the experimental equilibrium bond length of $CrO(X^5\Pi)$ of 1.6179Å (8). Two basis sets were used in these calculations. The first was a double-zeta STO basis set (19) whereas the second (Basis II) was a contracted GTO basis set. In this GTO basis, the chromium (12s, 6p, 4d) basis set of Roos et al (20) was contracted to [5s, 2p, 2d] using the method of Raffenetti (21). Also, as Hay (22) has recently reported improved results for calculations on transition metals using basis sets of this type in which an extra diffuse d function has been added, the chromium GTO basis was augmented by a single diffuse d function (with an exponent specified by Hay (22)) giving a total contracted GTO basis set of

[5s, 2p, 3d]. Also, for oxygen, the (7s,3p) GTO basis set of Roos and Siegbahn (23) was contracted to [3s, 2p]. Both basis sets I and II have been used in the SCF calculations performed in this work and in both cases the results obtained were very similar. However, as basis set II gave rise to a smaller total number of functions and a lower total energy for any state of CrO or CrO^+ than basis set I, this was the one used in the limited configuration-interaction calculations performed in this work. All the computed quantities quoted thus refer to basis set II, the CGTO basis.

Although the ground electronic state of CrO is known from spectroscopic evidence to be a $^5\Pi$ state (8, 9), the dominant electronic configuration (or configurations) of this state is not known. However, the electronic configuration of a number of first-row transition-metal oxides in their ground electronic states has been estimated previously by making use of a simple crystal-field model in which the molecules are represented formally as M^{2+} O^{2-} and the degenerate d orbitals of the metal are split by the field (7, 24). The ground state of Cr^{2+} has a d^4 configuration which would give the high-spin states $\sigma^1\pi^1\delta^2$, $^5\Pi$; $\sigma^1\pi^2\delta^1$, $^5\Delta$ and $\sigma^0\pi^2\delta^2$, $^5\Sigma^+$. On this basis the ground electronic configuration of $CrO(X^5\Pi)$ would be expected to correspond to the configuration

$$-----(8\sigma)^2(3\pi)^4(1\delta)^2(9\sigma)^1(4\pi)^1.$$

Assuming this to be the dominant configuration, an SCF calculation was performed on $CrO(X^5\Pi)$. A configuration-interaction calculation was then performed by considering all $^5\Pi$ states generated from the reference state through single and double excitations with the constraint that only the orbitals 8σ to 13σ, 3π to 5π, 1δ and 2δ were open to orbital substitution. These were the orbitals whose energies were in the region -0.37 a.u. to +1.50 a.u. This calculation indicated that the $(8\sigma)^2(3\pi)^4(1\delta)^2(9\sigma)^1(4\pi)^1$ configuration is the main contributor to the ground state of CrO, with the coefficient of this configuration to the final CI wavefunction being 0.87.

On the basis of this evidence, the low-lying ionic states of CrO accessible by one-electron ionisation from the neutral molecule could be determined. A number of one-electron processes were considered, namely the $(4\pi)^{-1}$, $(9\sigma)^{-1}$, $(1\delta)^{-1}$, $(3\pi)^{-1}$ and $(8\sigma)^{-1}$ ionisations, and where more than one ionic state was produced, only the position of the lowest state was calculated in each case (25). SCF calculations were performed for the states of CrO^+ obtained and the corresponding ΔSCF vertical ionisation potentials are presented in table 6.C.1. In order to make some allowance for the correlation energy error in these vertical ionisation potentials, limited configuration-interaction calculations were carried out for these ionic states following the same procedure as used for the neutral molecule. The resulting ΔSCF + CI computed vertical ionisation potentials are also shown in table 6.C.1. As can be seen from this table, at the SCF level the ground state of CrO^+ is expected to be a $^6\Delta$ state arising from the configuration

$$-----(8\sigma)^2(3\pi)^3(1\delta)^2(9\sigma)^1(4\pi)^1$$

whereas, when configuration interaction is taken into account, the ground state of the ion is predicted to be a $^4\Sigma^-$ state corresponding to the configuration

$$-----(8\sigma)^2(3\pi)^4(1\delta)^2(9\sigma)^1$$

This latter result is in agreement with the fact that VO, which is isoelectronic with CrO^+, is known to have a $^4\Sigma^-$ ground state arising essentially from the configuration $(8\sigma)^2(3\pi)^4(1\delta)^2(9\sigma)^1$ (1, 26-28).

6.C.4. Results and Discussion

The band associated with the first ionisation potential of CrO is shown in figures 6.C.1. (a) and (b). These spectra have both been recorded for the Cr + O_3 reaction but with slightly different partial pressures of ozone. Similar spectra have also been obtained by reacting chromium atoms with oxygen, although more intense spectra showing better signal-to-noise ratios and clear vibrational structure were observed using ozone as the oxidant. By recording spectra with different relative partial pressures of chromium atoms and ozone, it proved possible to subtract the chromium atom contribution arising from the $Cr^+(^6D) \leftarrow Cr(^7S)$ ionisation.

This procedure gave a vibrational envelope with a vertical ionisation energy of 8.16±0.01eV. Clear vibrational structure was observed in this band and measurement of the vibrational spacings allowed an estimate of the vibrational frequency, $\overline{\omega}_e$, in the ground state of the ion to be made. The value obtained, 640±30cm^{-1}, compares with the corresponding value in the ground state of the neutral molecule, CrO($X^5\Pi$), of 898.5cm^{-1} (8,9). The observed vibrational separations were regular and showed no signs of structure arising from excitation of the neutral molecule. As a result, the position of the first vibrational component, 7.85±0.02eV, is believed to be a reliable estimate of the first adiabatic ionisation potential of CrO($X^5\Pi$). This value is in reasonable agreement with a number of previous experimental estimates (10-12) and is closest to a value of 7.7±0.3eV obtained by studying the reaction cross-section of Cr^+ with N_2O and O_2(10). It should be noted that experimental estimates of the first ionisation potential of CrO_2 are in the range 10.3±0.5eV (11,12), implying that the observed band cannot be attributed to ionisation of CrO_2.

The vibrational band envelope observed in the first band of CrO can be used to estimate the equilibrium bond length, r_e, in the ground state of the ion. The procedure is described in detail in chapter 3 of this thesis and involved computing Franck-Condon envelopes for various trial ionic equilibrium bond lengths until good agreement with the experimental vibrational intensity distribution was obtained. Using this method, the equilibrium bond length, r_e, of $CrO^+(X^4\Sigma^-)$ was estimated as 1.79±0.01Å. Also, the dissociation energy, D_e, of $CrO^+(X^4\Sigma^-)$ was determined from the observed adiabatic first ionisation energy of CrO, the first ionisation potential of atomic chromium (29) and the known dissociation energy, D_e of CrO($X^5\Pi$) of 4.57±0.09eV (11). This was derived on the assumption that CrO($X^5\Pi$) dissociates to Cr(^{7}S) and O(^{3}P) and $CrO^+(X^4\Sigma^-)$ dissociates to $Cr^+(^6S)$ and O(^{3}P). The value obtained, 3.48±0.11eV, is in excellent agreement with a value of 3.49±0.10eV determined by studying the translational-energy dependence of the reaction cross-sections of the $Cr^+ + O_2$ and $Cr^+ + N_2O$ reactions (10).

The ionisation energy region above 10.0eV was partially masked by intense bands arising from the HeIα and HeIβ spectra of ozone and oxygen and a careful search of the experimental spectra recorded for the Cr + O_3 reaction in the ionisation energy region 8.5-10.0eV showed no further bands that could be attributed to CrO. This is surprising since it was anticipated, on the basis of the ionic states of CrO that are accessible from the ground state by one-electron ionisation, that a band associated with the $CrO^+(^4\Pi) \leftarrow CrO(X^5\Pi)$ ionisation would be observed. However, Mulliken analyses performed for the CI natural orbital wave-functions obtained for the $CrO(X^5\Pi)$, $CrO^+(X^4\Sigma^-)$ and $CrO^+(^4\Pi)$ states (shown in table 6.C.2.) showed that the reduction in chromium 3d electron density on ionisation is greater for the $(4\pi)^{-1}$ ionisation than for the $(9\sigma)^{-1}$ ionisation. In contrast, the reduction in chromium s electron density on ionisation is smaller for the $(4\pi)^{-1}$ ionisation than for the $(9\sigma)^{-1}$ ionisation. In the case of atomic chromium, the 3d photoionisation cross-section is much greater than the s photoionisation cross-section at the HeI photon energy (15), which probably explains why the band associated with the CrO^+ $(^4\Pi)$ state is not observed experimentally.

As can be seen from table 6.C.1. comparison of the first ionisation potential of CrO measured in this work with that computed by ΔSCF calculations corrected by a limited configuration-interaction procedure shows rather poor agreement, the computed value being ca 1.7eV too low. This discrepancy almost certainly arises from the rather modest configuration-interaction calculations that have been performed and which allowed only a partial correction for the change in electron correlation energy for each ionisation. Nevertheless, the calculations are useful in that they indicate that the ground state of CrO^+ is a $^4\Sigma^-$ state obtained from $CrO(X^5\Pi)$ via a $(4\pi)^{-1}$ ionisation. This result is in agreement with the known ground state (see preceding section 6.B.) of the isoelectronic molecule VO(1, 26-28). Clearly, however, further more sophisticated calculations and extra spectroscopic evidence are required to support this result, and it is hoped that this study will stimulate such theoretical and experimental investigations.

FIGURES

Fig. 6.C.1.

Two HeI photoelectron spectra recorded for the first band of CrO obtained from the reaction $Cr+O_3$. A: $Cr^+(^6D) \leftarrow Cr(^7S)$; B: $CrO^+(X^4\Sigma^-) \leftarrow CrO(X^5\Pi)$. (a) has a slightly larger Cr : CrO ratio than (b). The vibrational band envelope of the first band of CrO was obtained by subtracting the chromium atom contribution.

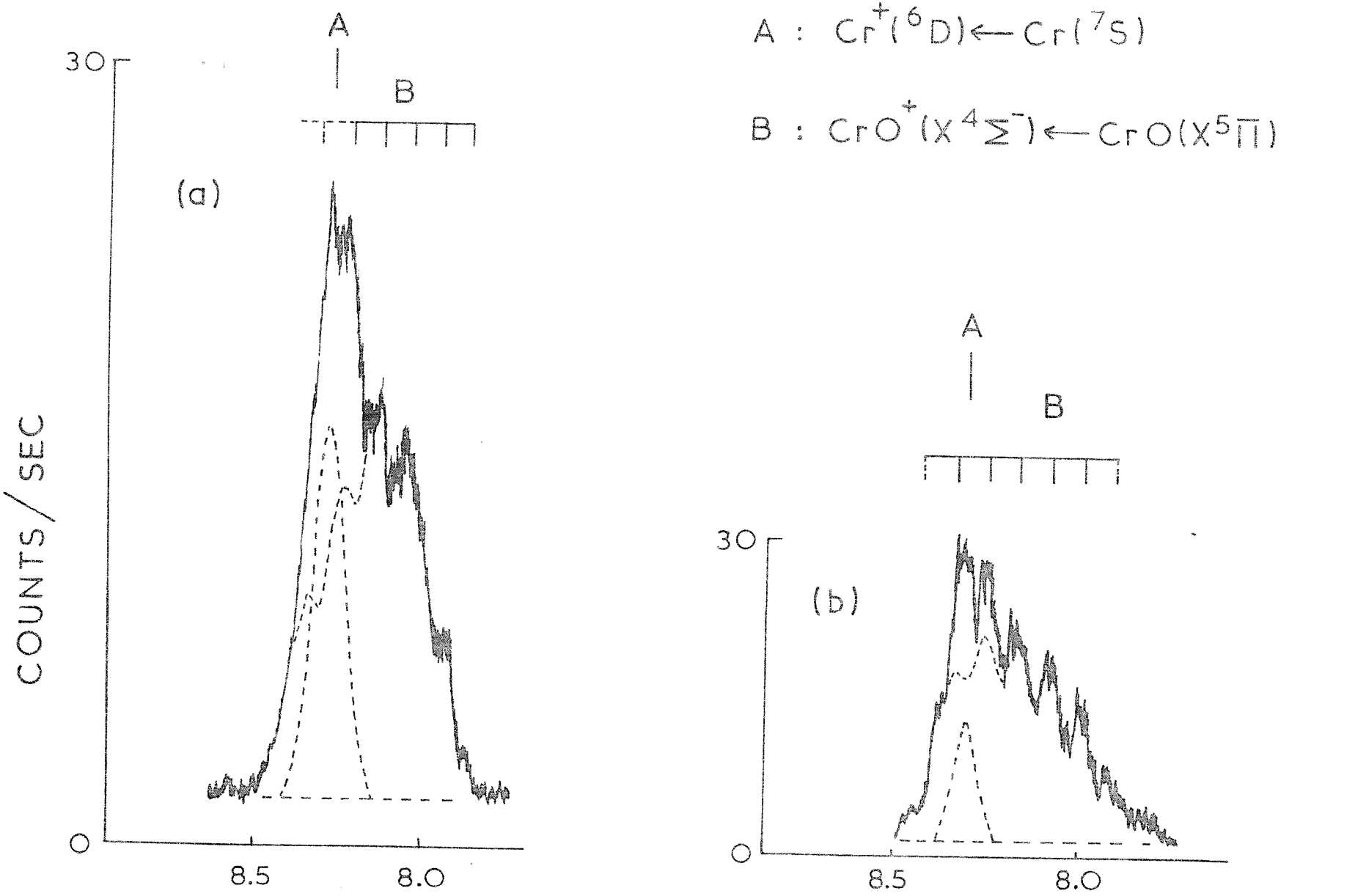
A : $Cr^{+}(^{6}D) \leftarrow Cr(^{7}S)$
B : $CrO^{+}(X\,^{4}\Sigma^{-}) \leftarrow CrO(X\,^{5}\Pi)$
A
B
(a)
(b)
30
0
COUNTS / SEC
8.5
8.0
I.P. (eV)

FIG 6C.1

Table 6.C.1. Computed Vertical Ionisation Potentials (eV) of $CrO(X^5\Pi)$[a]

Ionisation[b]	Ionic State Produced	ΔSCF Value	ΔSCF + CI Value	Experimental Value	No. of Configurations Generated[c]
-	$CrO(X^5\Pi)$	-	-	-	3231
$(4\pi)^{-1}$	$CrO^+(^4\Sigma^-)$	7.27	6.43	8.16±0.01	2588
$(9\sigma)^{-1}$	$CrO^+(^4\Pi)$	7.35	6.45	-	2386
$(1\delta)^{-1}$	$CrO^+(^4\Phi)$	9.90	8.52	-	2532
$(3\pi)^{-1}$	$CrO^+(^6\Delta)$	5.79	8.00	-	2521
$(8\sigma)^{-1}$	$CrO^+(^6\Pi)$	5.84	8.36	-	2508

(a) See text for details of these calculations.

(b) One-electron ionisations were considered from the $CrO(X^5\Pi)(---8\sigma^2 3\pi^4 1\delta^2 9\sigma^1 4\pi^1)$ configuration. Only the lowest energy ionic state arising from a particular configuration was computed in each case.

(c) Configurations generated by one- and two-electron excitations from the reference configuration in each case.

Table 6.C.2.(a) Results of a Mulliken Analysis on the CI Natural Orbitals (Basis II) for $CrO(X^5\Pi)$ and a number of states of CrO^+

State	Orbital Ionised	Atomic Orbital				
		Cr(s)	O(s)	Cr(p)	O(p)	Cr(d)
$CrO(X^5\Pi)$	-	6.7454	3.9741	11.9789	4.4805	4.8211
$CrO^+(X^4\Sigma^-)$	4π	6.1814	3.9886	11.9859	4.2731	4.5710
$CrO^+(^4\Pi)$	9σ	6.0144	3.9793	11.9814	4.3180	4.7069

Table 6.C.2.(b) Difference in Electron Density between the CrO($X^5\Pi$) Neutral Ground State and the Ionic States $^4\Sigma^-$ and $^4\Pi$

State	Orbital Ionised	Atomic Orbital				
		Cr(s)	O(s)	Cr(p)	O(p)	Cr(d)
$CrO^+(X^4\Sigma^-)$	4π	0.5640	-0.0145	-0.0070	0.2074	0.2501
$CrO^+(^4\Pi)$	9σ	0.7310	-0.0052	-0.0025	0.1625	0.1142

REFERENCES

1. R.J. Van Zee, C.M. Brown, K.J. Zeringue and W. Weltner, Acc. Chem. Res., 13, 237 (1980).

2. O. Appelblad, A. Lagerquist and I. Renhorn, Phys. Scr., 22, 603 (1981).

3. R.M. Gordon and A.J. Merer, Can. J. Phys., 58, 642 (1980).

4. (a) A.S.C. Cheung, N. Lee, A.M. Lyyra, A.J. Merer and A.W. Taylor, J. Mol. Spect., 95, 213 (1982).

   (b) P.C. Engelking and W.C. Lineberger, J. Chem. Phys., 66, 5054 (1977).

5. (a) W.H. Hocking, M.C.L. Gerry and A.J. Merer, Can. J. Phys., 51, 54 (1979).

   (b) J.G. Phillips, Astrophys. J. Suppl. Ser., 26, 313 (1973).

6. R. Stringat, C. Athenour and J.L. Fermenias, Can. J. Phys., 50, 395 (1972).

7. C.J. Cheetham and R.F. Barrow, Adv. High Temp. Chem., 1, 7 (1967).

8. W.H. Hocking, A.J. Merer, D.J. Milton, W.E. Jones and G. Krishnamurty, Can. J. Phys., 58, 516 (1980).

9. M . Ninomiya, J. Phys. Soc. Jpn., 10, 829 (1955).

10. P.B. Armentrout, L.F. Halle and J.L. Beauchamp, J. Am. Chem. Soc. 76, 2449 (1982).

11. G. Balducci, G. Gigli and M. Guido, J. Chem. Soc. Faraday Trans. 2, 77, 1107 (1981).

12. R.T. Grimley, R.P. Burns and M.G. Inghram, J. Chem. Phys., 34, 664 (1961).

13. JANAF Thermochemical Tables, Ed. D.R. Stull and H. Prophet (National Bureau of Standards, Washington D.C., 2nd Edn, 1971), Vol. 37.

14. (a) V.J. Troe and H.G. Wagner, Ber. Bunsenges Phys. Chem., 71, 946 (1967).

   (b) A.J. Lorquet, J.C. Lorquet and W. Forst, Chem. Phys., 51, 253 (1980).

15. J.M. Dyke, N.K. Fayad, A. Morris and I.R. Trickle, J. Phys. B, 12, 2985 (1979).

16. D. Bulgin, J.M. Dyke, F. Goodfellow, N. Jonathan, E. Lee and A. Morris, J. El. Spec. Rel. Phen., 12, 67 (1977).

17. J.M. Dyke, N. Jonathan and A. Morris, Electron Spectroscopy: Theory, Techniques and Applications (Academic Press, London, 1979), Vol. 3, p.189.

18. J.M. Dyke, N. Jonathan and A. Morris, Int. Rev. Phys. Chem., 2, 3 (1982).

19. C. Roetti and E. Clementi, J. Chem. Phys., 60, 4725 (1974).

20. B. Roos, A. Veillard and G. Vinot, Theor. Chim. Acta, 20, 1 (1971).

21. R.C. Raffenetti, J. Chem. Phys., 58, 4452 (1973).

22. P.J. Hay, J. Chem. Phys., 66, 4377 (1977).

23. B. Roos and P. Siegbahn, Theor, Chim. Acta, 17, 209 (1970).

24. (a) P.S. Bagus and H.J.T. Preston, J. Chem. Phys., 59, 2986 (1973).

    (b) P.S. Bagus, Publication RJ975 (IBM Research Library, San Jose, California, 1972).

25. (a) J. Raftery, P.R. Scott and W.G. Richards, J. Phys. B, 5, 1293 (1972).

    (b) P.R. Scott, J. Raftery and W.G. Richards, J. Phys. B., 6 881 (1973).

26. K.D. Carlson and C. Moser, J. Chem. Phys., 44, 3259 (1966).

27. P.H. Kasai, J. Chem. Phys., 49, 4979 (1968).

28. (a) A.S.C. Cheung, A.W. Taylor and A.J. Merer, J. Mol. Spec., 92, 391 (1982).

    (b) A.S.C. Cheung, R.C. Hansen and A.J. Merer, J. Mol. Spec., 91, 165 (1982).

29. C.E. Moore, Atomic Energy Levels, Natl. Bur. Stand,, Circ. 467 (U.S. Govt. Printing Office, Washington D.C., 1949), Vol. 1.

CHAPTER 6.D. PRELIMINARY STUDIES ON THE BARIUM MONOXIDE AND STRONTIUM MONOXIDE MOLECULES

6.D.1. Introduction

The molecules barium monoxide and strontium monoxide are important molecules in flame chemistry (1) and have been the subject of atmospheric release experiments (2,3). This work presents preliminary results on the uv-photoelectron spectra of both molecules.

Hocking et al (4) in a microwave study of the alkaline earth metal oxides have produced SrO and BaO by reacting barium and strontium, entrained in argon carrier gas, with oxygen or nitrous oxide. The reason for using an oxidation reaction to obtain the oxides, rather than using direct evaporation, was that, as the alkaline earth group is ascended progressively higher temperatures are required to vapourise the solid oxide. As higher temperatures are used, the tendency towards dissociation on evaporation increases. The study of Hocking et al (4) did, however, state that the vapour above BaO at 2200K consisted largely of diatomic BaO while the vapour above SrO at 2500K was estimated to contain only 5% diatomic SrO (5). Thus direct evaporation seemed the best method to use in this work for BaO while even 5% diatomic SrO in the gas-phase should provide sufficient partial pressure of the metal monoxide for a photoelectron spectrum to be obtained. MgO and CaO dissociate completely on heating and would thus have to be produced via a cross-beam reaction for a photoelectron spectroscopic study.

Several studies have been performed on BaO and SrO using the method of direct evaporation. Wharton et al (6) and Kaufman et al (5), in a microwave study, produced beams of SrO and BaO using an iridium furnace while Farber et al (7) in a mass-spectrometric study produced a beam of SrO by evaporation from an alumina cell. Murad (8), however, successfully used a molybdenum Knudsen cell to evaporate SrO. Several mass-spectrometric studies have yielded estimates for the first ionisation potentials of SrO and BaO. For SrO Murad (4) quotes (6.1±1.0)eV. This was an early study and more recent work by high-temperature mass-spectrometry (8) has yielded a value of (7.0±0.2)eV.

Further more recent work by Murad (10) has also determined a value of (7.0±0.2)eV via reaction of Sr^+ ions with oxygen. In view of the agreement between these latter two studies (8, 10) it is likely that the first ionisation potential of SrO is in the region of 7.0eV. The first ionisation potential of BaO^+ has been estimated on two occasions. Rauh et al (11) have estimated (6.85±0.1)eV while Murad (8) estimates (6.8±0.2)eV. Both studies were carried out mass-spectrometrically.

6.D.2. Experimental

Vapours containing diatomic BaO and SrO were obtained by evaporating the solids (Cerac Inc., >99.9%) from a molybdenum furnace of the type described in Chapter 2. The photoelectron spectrometer used in the study has also been described previously in Chapter 2. Spectral calibration was achieved using the HeIα (21.21eV) photoelectron spectrum of methyl iodide, the HeIβ spectrum of methyl iodide and the HeII spectrum of helium. Also, known atomic peaks were used once their positions had been established using MeI and the HeII(He) line.

6.D.3. Results and Discussion

The HeI photoelectron spectra of the vapours derived from evaporation of solid SrO and BaO are shown in figures 6.D.1. and 6.D.2. respectively.

The HeI photoelectron spectrum of strontium in the i.p. region of interest, 5.0eV to 7.5eV, is expected to consist of one sharp band at 5.69eV ionisation energy (12) arising from a $(5s)^{-1}$ ionisation from the ground state of the atom i.e.

the $Sr^+(...4s^24p^65s^1,\ ^2S) \leftarrow Sr(...4s^24p^65s^2,\ ^1S)$ ionisation.

Fig. 6.D.1. shows the spectrum recorded from a sample of SrO. The $(5s)^{-1}$ ionisation of strontium is clearly seen at a calibrated position of (5.69±0.01)eV. In addition, a band can be seen centred at around 6.90eV which is absent on evaporating strontium alone and it is therefore thought to be associated with the first ionisation

potential of SrO (7, 8, 10). Several spectra were recorded and the position of the band maximum of this feature has been found to be (6.94±0.04)eV. Unfortunately this band was weak and, consequently, a more accurate position could not be established. During some experiments the spectra were obscured by a very high background which was present even when the HeI source was switched off. It is thought that this effect is due to contamination of the sample by water, present either in the sample itself or in the ionisation chamber, giving rise to the reaction $Sr + H_2O \rightarrow SrOH^+ + H + e^-$ first studied by Padley et al (13). Thus reaction of water with strontium atoms could give rise to free electrons masking the bands of Sr and SrO in the photoelectron spectrum.

In experiments which did not suffer from this background electron problem, bands due to ionisation of strontium were observed in the higher i.p. region. These were observed at 7.52eV ionisation energy arising from the $Sr^{+2}D_{3/2}$, $_{5/2} \leftarrow Sr^2S$ ionisation and at 8.62/8.75eV ionisation energy arising from the $Sr^{+2}P_{\frac{1}{2}}$, $_{3/2} \leftarrow Sr^2S$ ionisation.

The HeI photoelectron spectrum of barium has been studied by Suzer et al (10). It is notable in that it is one of the few atomic p.e.s. spectra which show strong effects of autoionisation at the HeI photon energy. Five bands were observed in the region of interest, 5.0 to 10.0eV ionisation energy, arising from ionisation from the ground state of neutral barium. The ionisations and their ionisation energies are given below:

$Ba^{+2}S$	←	Ba^1S	5.21eV
$Ba^{+2}D_{3/2}$	←	Ba^1S	5.81eV
$Ba^{+2}D_{5/2}$	←	Ba^1S	5.92eV
$Ba^{+2}P_{\frac{1}{2}}$	←	Ba^1S	7.70eV
$Ba^{+2}P_{3/2}$	←	Ba^1S	7.92eV

The HeI photoelectron spectrum of the vapour obtained from vapourisation of solid BaO is shown in Fig. 6.D.2. All five of the bands mentioned above are clearly visible. In addition, a band centred at around 6.90eV is also visible which could possibly be due to BaO. At the present time insufficient data exists to allow the position of

this band to be determined accurately. Several early runs were carried out without problems. In later runs, however, a high background electron problem was encountered, similar to that observed in the SrO study. This prevented any bands of BaO to higher i.p. from being detected.

By analogy with the TiO and VO studies described in this Chapter, the first bands of SrO and BaO will almost certainly show evidence of vibrational excitation in the neutral molecule. Hence care will be needed in resolving vibrational structure in the region of the leading edge of the bands, particularly in view of the fact that the vibrational frequencies in the ground state of SrO and BaO are relatively low; $\bar{\omega}_e$ in BaO $X^1\Sigma^+$ = 669.76 cm^{-1}, $\bar{\omega}_e$ in SrO $X^1\Sigma^+$ = 653.5 cm^{-1} (15).

Further more intensive, experimental work is required on both SrO and BaO. Work is needed to surmount the background electron problem for both molecules as well as to improve the signal-to-noise ratio of the spectra. However, preliminary spectra of BaO have already been recorded on the new Multidetector spectrometer by M.P. Hastings. Detailed molecular orbital calculations will also be required to assign the photoelectron spectra of the two molecules.

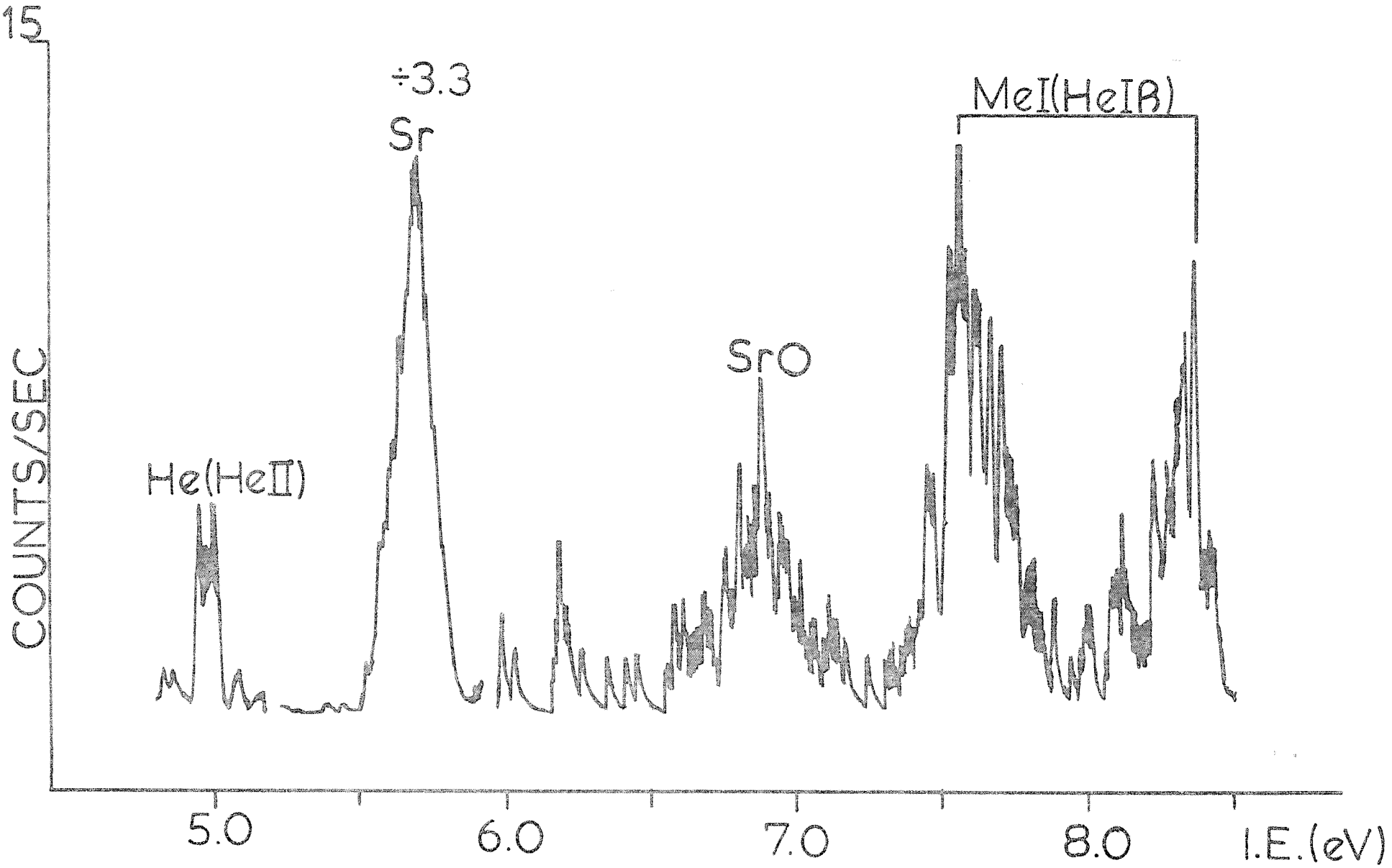

FIG 6D.1

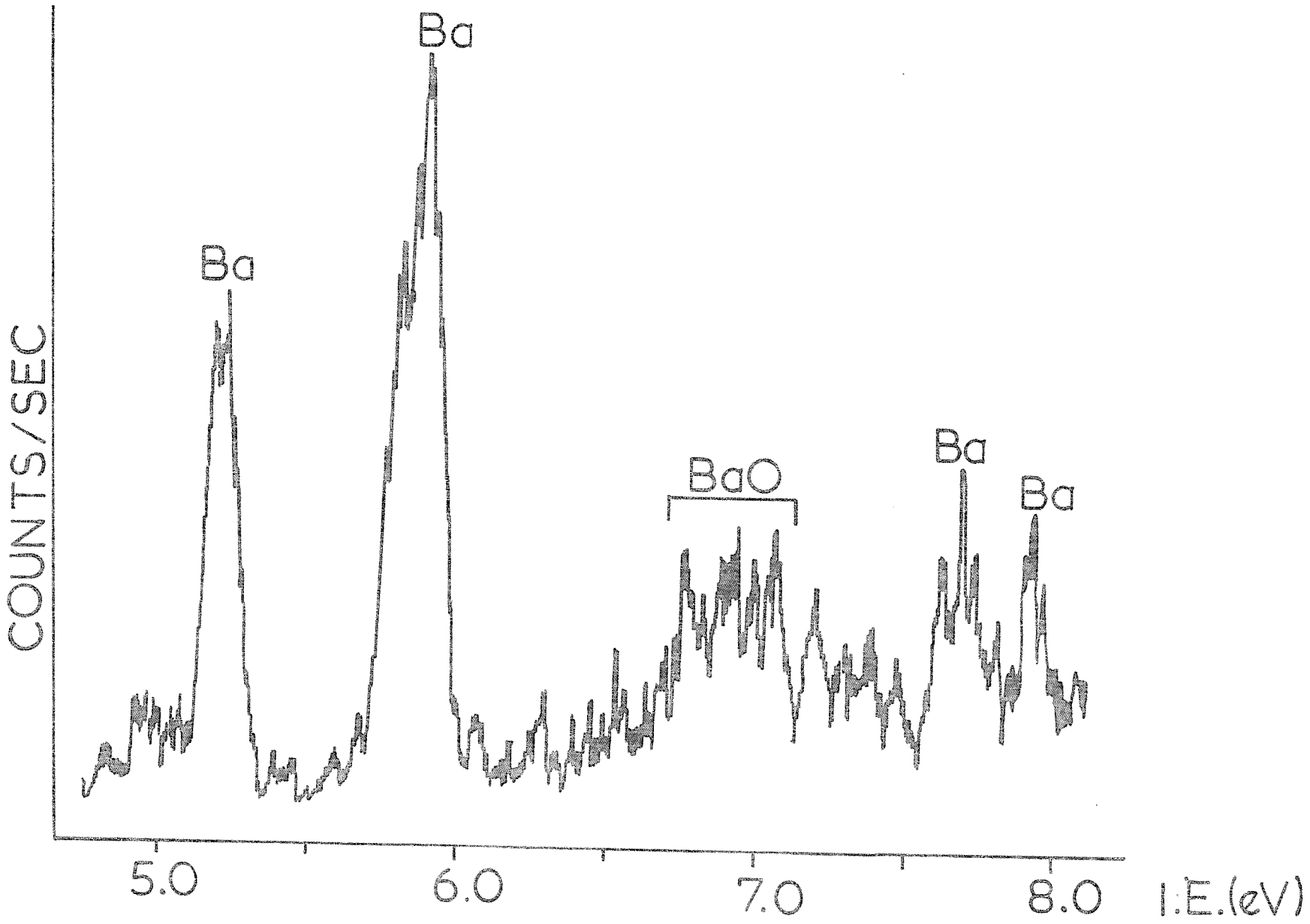

FIG 6D.2

REFERENCES

1. J.W. Hastie in High Temperature Vapours - Science and Technology (Academic Press, New York, 1975).

2. E. Murad and W. Swider, Geophys. Res. Lett., 6, 929 (1979).

3. E. Murad, W. Swider and S.W. Benson, Nature, 289, 273 (1981).

4. W.H. Hocking, E.F. Pearson, R.A. Creswell and G. Winnewisser. J. Chem. Phys., 68, 1128 (1978).

5. M. Kaufman, L. Wharton and W. Klemperer, J. Chem. Phys., 43, 943 (1965).

6. M. Wharton and W. Klemperer, J. Chem. Phys., 38, 2705 (1963).

7. M. Farber and R.D. Srivastava, High Temp. Sci. 8, 73 (1976).

8. (a) E. Murad, J. Chem. Phys., 75, 4080 (1981).

   (b) E. Murad, J. Chem. Phys., 73, 1381 (1980).

9. E. Murad, Air Force Geophysics Laboratory (USAF), Environmental Research Paper No. 610 (AFGL-TR-77-0235, 1977).

10. E. Murad, J. Chem. Phys., 78, 6611 (1983).

11. E.G. Rauh and R.J. Ackermann, J. Chem. Phys., 60, 1396 (1974).

12. C.E. Moore, Atomic Energy Levels, NBS, Circ. 467 (U.S. Govt. Printing Office, Washington D.C.) Vol. II (1952).

13. P.J. Padley, F.M. Page and T.M. Sugden, Trans. Far. Soc., 57, 1552 (1961).

14. S. Suzer, S-T. Lee and D.A. Shirley, Phys. Rev. A, 13, 1842 (1976).

15. K.P. Huber and G. Herzberg, Constants of Diatomic Molecules (Van Nostrand, New York, 1979).

CHAPTER 6.E. A STUDY OF THE SODIUM PLUS OZONE REACTION

6.E.1. Introduction

This thesis has dealt mainly with the uv-photoelectron spectra of metals and metal oxides. It is experimentally preferable in a study of this kind if an oxide can be evaporated directly into the gas-phase and a spectrum recorded as in the case of vanadium oxide (Chapter 5). However, as in the case of FeO (1), dissociation of the metal oxide into the metal and oxygen may occur on heating. Under these circumstances, in order to generate the metal monoxide in the vapour phase in sufficient concentrations for p.e.s. detection it is necessary to use a cross-beam reaction of a metal with an oxidant such as N_2O, O_2 or O_3. For a cross-beam reaction to be successful the primary reaction needs to be fairly rapid and any secondary reactions which remove the metal monoxide should ideally be slow. In the case of sodium, discussed in this section, the $Na+O_3 \rightarrow NaO+O_2$ reaction is known to be rapid with a calculated rate constant at room temperature of 3.3×10^{-10} cm^3 $molecule^{-1}$ s^{-1} (2,3). The exothermicity of this reaction is 35Kcal mol^{-1} (4). Knowing this information it was decided to carry out a cross-beam study of sodium with ozone.

A study of NaO is imporant for a number of reasons. The molecule is an important constituent of the earth's upper atmosphere. Meteors, containing sodium, entering the earth's atmosphere may react to produce oxides. Sodium reacts with the ozone layer to produce NaO which may then be ionised by ultra-violet radiation (4-6). The NaO^+ may then be involved in a number of chemical reactions. For these reasons it would be useful to carry out the $Na+O_3$ reaction in the laboratory to study the photoionisation of NaO. Sodium is also important as a coolant in fast breeder nuclear reactors (7). In these reactors liquid sodium is contained at temperatures above the ignition temperature of the metal and spillages will therefore lead to fires. A study of the burning rates of sodium pool fires has already been carried out (7) and one of the products of sodium combustion has been found to be NaO. Thus a study of the $Na+O_3$ reaction in the laboratory from this point of view would also be interesting.

6.E.2. Experimental and Results and Discussion

Sodium metal was evaporated from a graphite furnace with a tantalum capillary and crossed with a beam of ozone in the region just above the photoionisation zone of the spectrometer. The reaction system was very similar to that used in Chapter 5. The ozone was produced and stored in the same way as in the $Cr+O_3$ study (see Chapter 5).

The HeI photoelectron spectrum of sodium which is unpublished, consists of one sharp band at an i.p. of 5.11eV corresponding to the $Na^+(...2p^63s^0, {}^1S) \leftarrow Na(...2p^63s^1, {}^2S)$ ionisation. On crossing with the ozone beam, there was some evidence of chemiluminescence in the ionisation chamber though the spectra obtained did not show any evidence of the presence of NaO. However, the relative proportion of oxygen relative to that of ozone in the spectrum was slightly increased with respect to that observed in the spectrum of the ozone sample. This indicated that a small amount of reaction was taking place but unfortunately the oxide was not present in detectable amounts. A possible explanation for this may be that NaO^+ dissociates in the gas-phase. Using the expression $IP(NaO) + Do(NaO^+) = Do(NaO) + IP(Na)$ and taking values of $IP(NaO) = (7.4\pm0.4)eV$ and $D_o(NaO)=(2.61\pm0.2)eV$ from Murad's tables (8), the dissociation energy, D_o, of NaO^+ may be calculated as $(0.35\pm0.6)eV$. Thus it is quite possible that $D_o(NaO^+)$ is negative and that NaO^+ in its ground electronic state is dissociative. Under these circumstances it would not be expected that a photoelectron spectrum of NaO would be observed.

This preliminary study has paved the way for a more detailed study of the $Na+O_3$ reaction by gas-phase photoelectron spectroscopy. The rate constant of the reaction is favourable and the reaction is known to be exothermic. A similar situation exists in the case of the $Al+O_3$ reaction (9). The reaction is known to be exothermic and, on the basis of an experimental rate constant of 3×10^{-11} cm^3 $molecule^{-1}$ s^{-1} for the $Al+O_2 \rightarrow AlO+O$, is expected to be rapid (9). The problem with the $Na+O_3$ reaction is that very little NaO is produced in the gas-phase which is, at present, undetectable using a single-detector spectrometer.

Further work must concentrate on increasing the proportion of NaO in the gas-phase, by using a more efficient mixing system, and on recording spectra with good signal-to-noise ratios with the new multidetector spectrometer.

REFERENCES

1. D.L. Hildenbrand, Chem. Phys. Letts., 34, 352 (1975).

2. S.C. Liu and C.G. Reid, Geophys. Res. Letts., 6, 283 (1979).

3. C.E. Kolb and J.B. Elgin, Nature, 263, 488 (1976).

4. E.E. Ferguson, Geophys. Res. Letts., 5, 1035 (1978).

5. E. Murad, J. Geophys. Res., 83, 5525 (1978).

6. E. Murad and W. Swider, Geophys. Res. Letts., 6, 929 (1979).

7. R.N. Newman and J.F.B. Payne, Combustion and Flame, 33, 291 (1978).

8. E. Murad, Air Force Geophysics Lab. (USAF), Environmental Research Paper No.610 (AFGL-TR-77-0235, 1977).

9. W. Felder and A. Fontijn, J. Chem. Phys., 64, 1977 (1976).

CHAPTER 7

A study of the Photoelectron Spectra of Aluminium Monofluoride, AlF and Trifluoride, AlF_3

7.1 Introduction

In recent years the Southampton pes group has had links with the Berkeley Nuclear Laboratory of CEGB. Part of this collaboration has involved the study of the processes occurring during ignition of alloys used for canning uranium fuel elements in Magnox nuclear reactors. These alloys are normally resistant to oxidation but there are circumstances, however improbable, when an alloy could ignite. As a result attention has been focussed on how to extinghuish or inhibit such a fire.

Compounds thought to be potentially useful for this purpose include boron trifluoride, nitrogen and sulphur hexafluoride. Magnox alloys consist essentially of magnesium and aluminium and the aim of the collaboration with the CEGB is to establish the processes occurring in a fire and to examine, spectroscopically, the products of such a fire. These include oxides, fluorides and oxyfluorides of the constituent metals of the alloy as well as molecular fragments derived from the extinguishants. Earlier work (1) has described the HeI photoelectron spectrum of BF while this present work describes the photoelectron spectra of AlF and AlF_3. The photoelectron spectrum of MgF_2 has also been recently recorded by M.P. Hastings in the Southampton pes group.

Aluminium monofluoride has been the subject of a number of previous spectroscopic studies (2-7), probably because it can be produced fairly readily in the vapour phase at only moderately high temperatures ($\sim$1000K) (8,9). However, although a number of Rydberg states of AlF have been observed (3), no Rydberg series has yet been described and hence it has not been possible to determine an accurate first ionisation potential (ip) of this molecule from optical spectroscopic studies. The only experimental estimates of the first adiabatic ip of AlF come from electron impact mass spectrometry and are consistent with a value of (9.70±0.50)eV (10-12). In the work to be discussed in this Chapter, the photoelectron spectrum of gaseous AlF has been investigated with the aim of providing an improved adiabatic first ionisation potential of this molecule. It was also hoped to assign the observed bands with the aid of ab initio quantum mechanical PNO-CEPA calculations (for details of the method see Chapter 3)

and ΔSCF ab initio molecular orbital calculations. It was also proposed to determine spectroscopic constants (r_e, $\bar{w}_e$, D_e) of the corresponding states of AlF^+. As AlF was produced in the vapour phase by heating a stoichiometric mixture of aluminium and aluminium trifluoride, the photoelectron spectrum of AlF_3 has been recorded. It has been assigned by comparison with the well established photoelectron spectrum of BF_3 (13-16) and on the basis of ab initio molecular orbital calculations performed for BF_3 and AlF_3.

7.2 Experimental

AlF was produced in the vapour phase by heating a stoichiometric mixture of aluminium powder and aluminium trifluoride which had been carefully mixed and pressed into pellets. The pellets were loaded into a graphite furnace, details of which may be found in Chapter 2 of this thesis. The mixture was slowly warmed to ∿500K to remove any traces of water. Once this was achieved, the temperature was slowly raised to (1050±20)K (as measured with a chromel-alumel thermocouple in contact with the furnace) and a photoelectron spectrum recorded. This was attributed to AlF as studies of the vapour composition above Al/AlF_3 mixtures suggest that AlF is the predominant vapour phase species in this temperature range whereas AlF_3 is a minor component (8,9).

The HeI photoelectron spectrum of AlF_3 was recorded by heating solid AlF_3 in a graphite furnace, identical to that used for the Al/AlF_3 mixture at (1050±20)K. Of the aluminium trihalides the fluoride appears to be exceptional in that, at any given temperature, its vapour pressure is several orders of magnitude lower than that of the other halides (17,18). Also, for AlF_3, the dimer concentration is much lower than that of the monomer for all temperatures up to the normal sublimation point. In the cases of the other aluminium trihalides, the vapour consists predominantly of dimeric species at the sublimation point (17-19).

The photoelectron spectrometer and inductively heated furnace used in this study have been described in Chapter 2 of this thesis (20, 21). For the conditions under which AlF and AlF_3 spectra were observed, the usual resolution was 30-35 meV (f.w.h.m.) as measured for argon

ionised by HeI radiation. Spectra were calibrated using methyl iodide, carbon monoxide, nitrogen and argon.

7.3. Computational Details

The electronic ground state configuration of AlF($X^1\Sigma^+$) may be written as:

$$(1\sigma)^2(2\sigma)^2(3\sigma)^2(4\sigma)^2(1\pi)^4(5\sigma)^2(6\sigma)^2(2\pi)^4(7\sigma)^2$$

and at least bands associated with the $(6\sigma)^{-1}$, $(2\pi)^{-1}$ and $(7\sigma)^{-1}$ ionisations are expected in the HeI region.

Three types of calculation have been performed in order to assign the observed spectrum of AlF.

(a) Ab initio ΔSCF vertical ionisation potentials have been calculated for the $(6\sigma)^{-1}$, $(2\pi)^{-1}$ and $(7\sigma)^{-1}$ ionisations using the Hartree-Fock SCF method. The ATMOL3 suite of programs (22) was used for both the neutral molecule and the three ionic states under consideration. The basis set used (Basis I) was a double-zeta STO basis set taken from those of Roetti and Clementi (23) with added polarisation functions (the exponents used were Al4s (1.00), 4p (1.00) 3d(1.35) and F3d(2.01)). All of the calculations were performed at the experimental equilibrium bond length of AlF $X^1\Sigma^+$ of 1.6544Å (4-7).

(b) HFS LCAO calculations have also been performed on AlF using the method outlined in Chapter 3 of this thesis. In these calculations the basis set used (Basis II) was of triple-zeta quality with the atomic cores kept frozen and the aluminium 3s and 3p and fluorine 2s and 2p orbitals being treated as valence orbitals. Vertical ionisation potentials were estimated by Slaters' transition-state method. The results from these HFS calculations and the ab initio ΔSCF calculations are summarised in table 7.1.

(c) The potential energy functions of the $X^2\Sigma^+$, $A^2\Pi$ and $B^2\Sigma^+$ states and the $X^1\Sigma^+$ state of AlF have also been calculated from highly correlated PNO-CEPA electronic wavefunctions (these calculations were performed by Drs. Rosmus and Klein in Frankfurt, West Germany).

In these calculations on AlF a GTO basis set with 12s, 9p, 2d functions for Al and 10s, 6p, 2d functions for F was used (Basis III) (23). Only the innermost 5s and 4p functions for Al and 4s and 3p functions for F were contracted. The electronic wavefunctions have been calculated by the pseudonatural orbital CI(PNO-CI) method described in Chapter 3 (24). In these calculations all valence electrons have been correlated. Previous experience (25) with atomic orbital basis sets of similar size as used in this study suggests that about 75% of the valence correlation energies have been accounted for in the electronic states considered. The vertical ionisation potentials and spectroscopic constants obtained from the PNO-CI calculations are summarised in tables 7.2 and 7.3.

As an aid to identification of the spectrum of AlF, the vibrational envelope of the first photoelectron band has been computed via two methods. Firstly, the PNO-CEPA potential energy functions were used as input in a solution of the radial Schrodinger equation of nuclear motion allowing vibrational wavefunctions to be calculated. From these, Franck-Condon factors were calculated for ionisation from the v"=0 vibrational level of $AlF(X^1\Sigma^+)$ to the v'=0, 1 and 2 levels of $AlF^+(X^2\Sigma^+)$ as 1.00, 0.69 and 0.19. Secondly, ab initio Hartree-Fock SCF wavefunctions and total energies were computed with the STO double-zeta basis set mentioned earlier (Basis I). For the AlF $X^1\Sigma^+$ and AlF^+ $X^2\Sigma^+$ states within ± 0.2Å of the potential-energy minimum and points were fitted to a fourth order polynomial in $(r-r_e)$. This led to predicted values of r_e and $\bar{w}_e$ in the AlF $X^1\Sigma^+$ and AlF^+ $X^2\Sigma^+$ states which are listed in table 7.4. As expected for a calculation of this type (26) which neglects electron correlation, comparison of the computed values for AlF $X^1\Sigma^+$ with those known experimentally shows that the calculated r_e values are somewhat low whereas the computed $\bar{w}_e$ values are slightly high . These calculated spectroscopic parameters were then used in a Franck-Condon calculation to simulate the vibrational envelope of the first band of AlF, using the method outlined in Chapter 3 of this Thesis. The Franck-Condon factors obtained in this way for ionisation from the v"=0 vibrational level of $AlF(X^1\Sigma^+)$ to the v'=0, 1 and 2 levels of $AlF^+(X^2\Sigma^+)$ were 1.00, 0.47 and 0.11. Although the ab initio calculations used in this procedure suffer from a neglect of electron correlation,

the vibrational band envelopes previously predicted in this way have proved useful in the assignment of photoelectron bands of a number of diatomic molecules (1, 27, 28). The vibrational band envelope computed via the PNO-CEPA method takes account of electron correlation and is thus more likely to be in better agreement with experiment than the band envelope computed using ab initio SCF calculations (Basis I). An impression of the good agreement between the PNO-CEPA vibrational band envelope and the experimental vibrational band envelope may be gained by comparing figures 7.3 and 7.4.

A series of ab initio single determinantal SCF calculations using the STO double-zeta basis set (Basis I) were also performed for the AlF^+ $A^2\Pi$ state over a wide range of bond lengths (1.6-2.7Å). The potential energy curve obtained was found to be dissociative, consistent with results of similar calculations on the $A^2\Pi$ states of BF^+ and $AlCl^+$ (1, 29) and with results of the PNO-CEPA calculations performed for AlF^+ $A^2\Pi$ in this work.

As AlF is isoelectronic with CS and since the photoelectron spectrum of CS is known to show evidence of strong correlation effects (21), the above calculations have also been supplemented by configuration interaction calculations on both the neutral molecule and a number of ionic states. These calculations were performed using the ATMOL-SPLICE suite of programs (30). From the SCF wavefunction of AlF $X^1\Sigma^+$, obtained from the configuration $----(5\sigma)^2(6\sigma)^2(2\pi)^4(7\sigma)^2$ with Basis I, a configuration interaction calculation was carried out by considering all $^1\Sigma^+$ states generated from this reference configuration through single and double excitations with the constraint that only the orbitals 5σ to 13σ and 2π to 6π were open to orbital substitution. The calculations indicated that the $----(5\sigma)^2(6\sigma)^2(2\pi)^4(7\sigma)^2$ configuration is the main contributor to the ground state of AlF with its coefficient in the final CI wavefunction being 0.96. Similar calculations with the same orbitals open to substitution were also performed for the lowest three AlF^+ $^2\Sigma^+$ and $^2\Pi$ states. The results of these calculations are listed in table 7.1. Comparison of the results of the CI calculations and PNO-CEPA calculations described in this work will be made later.

Ab initio Hartree-Fock SCF calculations have also been performed for AlF_3 using the same STO double-zeta basis set (Basis I) as used for AlF and the experimental photoelectron spectrum has been assigned on the basis of Koopmans' Theorem applied to the orbital energies obtained for the neutral molecule. Similar calculations were also performed for BF_3 using the basis set of reference (1). For both molecules, geometries derived from gas-phase electron diffraction studies were used (31-33). The results of these calculations are summarised in table 7.5.

7.4. Results and Discussion

The HeI photoelectron spectrum obtained on evaporating a stoichiometric mixture of aluminium and aluminium trifluoride is shown in figure 7.1. It shows three bands which were in the same intensity ratio on varying the helium carrier gas pressure and furnace temperature as well as a broad weak feature centred at (16.10±0.05)eV. This spectrum has also been reproduced on heating Al/AlF_3 mixtures containing excess aluminium, except that the band positioned at 16.10eV was much weaker under these conditions. The photoelectron spectrum of AlF_3 has also been recorded (see figure 7.2). By comparison of the spectra obtained and knowledge of the main species present in each case from vapour pressure measurements, it was concluded that the spectrum shown in figure 7.2 arises solely from AlF_3, the first three bands in figure 7.1 are due to ionisation of AlF and the weak feature centred at (16.10±0.05)eV in figure 7.1 arises from AlF_3.

The first band of AlF is the only one which shows resolvable vibrational structure (see figure 7.3). The adiabatic and vertical ionisation potentials of this band coincide at (9.73±0.01)eV. This band is assigned on the basis of the calculated ionisation energies (see tables 7.1 and 7.2) to the $AlF^+ X^2\Sigma^+ \leftarrow AlF\ X^1\Sigma^+$ ionisation. The difference between the ΔSCF and the experimental vertical ips shown in tables 7.1 and 7.2 gives the correlation correction to the ionisation energy. As expected, since the correlation energy in the $X^2\Sigma^+$ state is lower than that in the $X^1\Sigma^+$ state the ΔSCF values are lower than the experimental vertical ip and the PNO-CEPA (Basis III) and ΔSCF plus CI (Basis I) values are also lower than this value by 0.3 eV and 0.49 eV

respectively. This is because the PNO-CEPA method only accounts for ∿75% of the correlation energy (25) in the $X^2\Sigma^+$ and $X^1\Sigma^+$ states while the ΔSCF plus CI (Basis I) method only makes allowance for single and double excitations in a molecule or ion and ignores higher order excitations.

In the first band of AlF, as well as the adiabatic vibrational component, at least three other vibrational peaks were observed to higher ionisation energy and measurement of their separations gave a value of $\bar{w}_e = (1040\pm40)\,cm^{-1}$ in the ionic state, a value which compares with 802 cm^{-1} in the ground state of the neutral molecule (4-7). A similar increase in vibrational frequency on ionisation occurs in the BF case (1). This increase in bond strength has been rationalised previously in terms of an ionic bonding scheme, which has been found more appropriate than a covalent approach in describing the bonding in the group III monohalides and their ions (1, 29, 34-36). The ab initio SCF calculations (Basis I) performed in this work indicate that the first ionisation process in AlF corresponds to removal of an Al 3s electron with a net strengthening of the ionic band in the cation. The relative intensities of the three main vibrational components shown in figure 7.3, corresponding to the ionisations v' = 0, 1 and 2, $AlF^+\ X^2\Sigma^+ \leftarrow v'' = 0$, AlF $X^1\Sigma^+$, were measured as 1.00:0.82±0.03:0.35±0.05 in reasonably good agreement with the relative intensities predicted by the PNO-CEPA method of 1.00:0.69:0.19. Using the method outlined in Chapter 3 and assuming no vibrational excitation of the neutral molecule, these experimental vibrational relative intensities have been used with a series of Franck-Condon calculations to estimate the equilibrium bond length in the $AlF^+\ X^2\Sigma^+$ state as (1.58±0.01)Å. However, in all experimental spectra, one vibrational component was observed on the low ionisation energy side of the $v' = 0 \leftarrow v'' = 0$ component (see figure 7.3) and its position was consistent with that expected for the "hot band" due to the ionisation process $v' = 0$, $AlF^+\ X^2\Sigma^+ \leftarrow v'' = 1$, AlF $X^1\Sigma^+$. The presence of contributions from vibrationally excited AlF in the band makes analysis of the experimental vibrational intensities somewhat difficult because, within the resolution of the experiment, overlap will occur between the following pairs of $v' \leftarrow v''$ transitions: $0 \leftarrow 0$ and $1 \leftarrow 1$,

$1 \leftarrow 0$ and $2 \leftarrow 1$, and $2 \leftarrow 0$ and $3 \leftarrow 1$. This obviously means that the intensities of the three main vibrational components in figure 7.3 cannot be used directly to estimate the equilibrium bond length in the ion. Nevertheless, as the contribution from the v" = 1 and v" = 2 AlF $X^1\Sigma^+$ levels in figure 7.3 was small, the following approximate procedure was adopted. Use of the computed Franck-Condon factors for the $v' = 0 \leftarrow v'' = 0$ and $v' = 0 \leftarrow v'' = 1$ transitions (calculated with $\bar{w}_e = 1040\ cm^{-1}$ and $r_e = 1.58\mathring{A}$ in the ion) with the corresponding experimental component intensities (1:0.25±0.05) leads to an estimated AlF $X^1\Sigma^+$ vibrational temperature of (950±50)K, a value which is slightly lower than the furnace temperature of (1050±20)K probably because of collisional deactivation of the AlF molecules before ionisation. This effective vibrational temperature together with the computed Franck-Condon factors for the ionisations v" = 0 and v" = 1 to v' = 0, 1, 2 and 3 allows a small correction to be made to the experimental band intensities to yield a more accurate estimate of the experimental intensity ratio of the processes $v' = 0, 1, 2 \leftarrow v'' = 0$. These modified intensities then led, via a further series of Franck-Condon calculations, to a new estimate of the equilibrium bond length in the AlF^+ $X^2\Sigma^+$ state which was slightly increased from the original value to $(1.59\pm0.01)\mathring{A}$. The vibrational temperature of AlF $X^1\Sigma^+$ was also redetermined using Franck-Condon factors re-calculated at this ionic bond length together with the experimental vibrational intensity ratio and found to be essentially unchanged from the initial value of (950±50)K. Table 7.4 shows that the values of r_e and $\bar{w}_e$ in the $AlF^+(X^2\Sigma^+)$ state obtained via ab initio SCF calculations (Basis I) are in good agreement with the values derived experimentally.

The vibrational band envelope of the first AlF band was also calculated using the PNO-CEPA method. To do this, theoretical vibrational envelopes of the first photoelectron band have been calculated from the PNO-CEPA potential energy curves for the $v' \leftarrow v'' = 0$ and $v' \leftarrow v'' = 1$ progressions and both envelopes are shown schematically in figure 7.4. In constructing these envelopes the calculated Franck-Condon factors have been used with Gaussian line shapes with a width at half height of 75 meV determined by the experimental resolution. It can be seen immediately from the figure that the $v' \leftarrow v'' = 1$ progression exhibits a rather irregular envelope largely because of the small overlap between

the v" = 1 and v' = 1 vibrational wavefunctions. However, if both envelopes are added together with a weighting factor of 1:0.25 the resulting theoretical spectrum (figure 7.4) is in very good agreement with the experimental envelope (figure 7.3).

The quality of the PNO-CEPA potential energy function for both $AlF(X^1\Sigma^+)$ and $AlF^+(X^2\Sigma^+)$ states can also be judged from the computed spectroscopic constants (r_e and $\bar{w}_e$) for the $AlF(X^1\Sigma^+)$ state for which very accurate experimental values are available (4-7). In general, single determinantal Hartree-Fock type SCF molecular orbital calculations predict the potential energy of a diatomic molecule (43) to lie above the experimental potential energy curve with the potential minimum at slightly lower bond length. At the single-determinantal SCF level, this results in calculated values of r_e being frequently too low and $\bar{w}_e$ being too high relative to the experimentally derived parameters. This is because electron correlation is neglected in these calculations. However, when electron correlation is taken into account via a method such as the PNO-CEPA approach, predicted and experimental potential energy curves become closer. As a result, the calculated values of r_e will increase slightly while those of $\bar{w}_e$ will decrease slightly.

Two types of basis set (Basis I and III) were used for the calculations on $AlF(X^1\Sigma^+)$ and $AlF^+(X^2\Sigma^+)$ but, nevertheless a broad measure of agreement was achieved. This can be shown by comparing the calculated ΔSCF value of the first vertical ip of AlF obtained using Basis I (8.51 eV; table 7.1) and that obtained using Basis III (8.53 eV; table 7.2). Detailed comparison is also possible between tables 7.3 and 7.4. At the SCF level with both basis sets I and III, for the AlF $X^1\Sigma^+$ and AlF^+ $X^2\Sigma^+$ states, the computed values of r_e are too low and the computed values of $\bar{w}_e$ are too high, as expected because of neglect of electron correlation (43). However, allowance for most of the correlation in the AlF $X^1\Sigma^+$ and AlF^+ $X^2\Sigma^+$ states by the PNO-CEPA method gives values of $\bar{w}_e$ and r_e in each state which are much closer to experiment. For the AlF $X^1\Sigma^+$ state, (see PNO-CEPA calculations (table 7.3)), the theoretical equilibrium bond length, r_e, is overestimated by 0.009Å while the theoretical vibrational frequency is higher than the experimental value by 2 cm^{-1}. For the AlF^+ $X^2\Sigma^+$ state, r_e is over-

estimated by 0.01Å and $\bar{w}_e$ is underestimated by 80 cm^{-1} (calculated as 960 cm^{-1} and measured experimentally as (1040±40)cm^{-1}). However, since the PNO-CEPA calculations are expected to predict $\bar{w}_e$ for the AlF^+ $X^2\Sigma^+$ state to within ±50 cm^{-1}, the experimentally measured value of (1040±40)cm^{-1} for $\bar{w}_e$ may be a slight overestimate due to uncertainties in measurement of vibrational separations in an envelope which contains contributions from ionisation of vibrationally excited AlF. As a result, an average of theoretical PNO-CEPA and experimental values is probably the most reliable estimate for $\bar{w}_e$ of AlF^+ $X^2\Sigma^+$ i.e. $\bar{w}_e$ = (1000±40)cm^{-1}.

Another parameter which can be determined from the first band of AlF is the dissociation energy in the ground state of the ion. Assuming, as seems likely, that AlF $X^1\Sigma^+$ dissociates to $Al(^2P)$ and $F(^2P)$ and AlF^+ $X^2\Sigma^+$ dissociates to $Al^+(^1S)$ and $F(^2P)$ then the first adiabatic ionisation energy of AlF, (9.73±0.01)eV, can be used with the known dissociation energy, D_o, of AlF $X^1\Sigma^+$, (6.89±0.13)eV (11), and the first ionisation energy of aluminium, 5.98eV (37), to estimate the dissociation energy, D_o in AlF^+ $X^2\Sigma^+$ as (3.14±0.14)eV.

The second band of AlF, shown in figure 7.1, is broad and no vibrational structure was resolved. The band onset and maxima were measured at (13.65±0.02)eV and (14.75±0.02)eV respectively. Both the ΔSCF plus CI calculations (table 7.1) and the PNO-CEPA calculations (table 7.2) indicate that the band is due to both $(2\pi)^{-1}$ and $(6\sigma)^{-1}$ ionisations. By analogy with CS and SiO (38-41), the band due to the $(2\pi)^{-1}$ ionisation should appear to be broad with the adiabatic ionisation potential not equal to the vertical ionisation potential. However, unlike the CS and SiO examples, no vibrational structure was observed which could indicate that this band is complicated by the presence of the $(6\sigma)^{-1}$ ionisation. Figure 7.5 shows that both the $A^2\Pi$ and $B^2\Sigma^+$ states of AlF^+ are expected in the region of the second experimentally observed band. The parts of the potential energy functions necessary for an assignment to be made are also shown in figure 7.5 as computed via the PNO-CEPA method. The $B^2\Sigma^+$ state of AlF^+ dissociates to Al^+ (^3P) + $F(^3P)$ and the $X^2\Sigma^+$ state dissociates to Al^+ (^1S) + $F(^2P)$. Close to the equilibrium internuclear distance of the $X^2\Sigma^+$ state, the 7σ orbital exhibits the approximate occupancy (Al) 3s 3pσ whereas at larger distances it becomes

(Al) $3s^2$. The reverse occupancy change occurs for the 6σ molecular orbital. Therefore, there is an avoided crossing of the X and B states of AlF^+ at larger internuclear distances due to the changes of the 7σ and 6σ molecular orbital characters. For this reason, the $B^2\Sigma^+$ potential curve is rather shallow and its equilibrium internuclear distance is larger than that of the $X^2\Sigma^+$ state by 0.47Å (see table 7.3). The $A^2\Pi$ state is calculated to be repulsive and to lie below the $B^2\Sigma^+$ state (see figure 7.5). An energy range of 13.6-15.0eV may be calculated for the AlF^+ $A^2\Pi \leftarrow AlF$ $X^1\Sigma^+$ ionisation from these PNO-CEPA potential energy curves and in view of the fact that the vertical ip of the AlF^+ $B^2\Sigma^+ \leftarrow AlF$ $X^1\Sigma^+$ ionisation is calculated to be 14.67eV (see table 7.2), the second broad band in the photoelectron spectrum of AlF corresponds to ionisation to both the $A^2\Pi$ and $B^2\Sigma^+$ states of AlF^+. This assignment is also supported by the results of the other calculations performed in this work which are summarised in table 7.1. For the AlF^+ $A^2\Pi \leftarrow AlF$ $X^1\Sigma^+$ and AlF^+ $B^2\Sigma^+ \leftarrow AlF$ $X^1\Sigma^+$ ionisations, vertical ionisation energies of 14.23eV and 15.93eV are obtained by the HFS transition state method and 13.44eV and 15.13eV via the ΔSCF plus CI (Basis I) method. Both these methods make some allowance for electron correlation and thus may be directly compared with the PNO-CEPA results.

There is still one problem remaining in the spectrum of AlF. The sharp band observed in the spectrum at 15.33eV, as yet unassigned, must be due to a shake-up state of AlF^+ since no other formally allowed bands are expected in the HeI region.

The CI calculations performed in this work indicate that this band is due to a formally forbidden $^2\Sigma^+$ state arising from the configuration $(2\pi)^{-1}$ $(7\sigma)^{-1}$ $(3\pi)^{+1}$. The band gains intensity through interaction of the $(2\pi)^{-1}$ $(7\sigma)^{-1}$ $(3\pi)^{+1}$ configuration with a configuration which is obtained by a one-electron ionisation from the neutral molecule. The CI calculation on the AlF^+ $B^2\Sigma^+$ state (see table 7.1) indicated that, as well as the expected ionisation at 15.13eV having appreciable intensity, a root to higher energy containing the $(2\pi)^{-1}$ $(7\sigma)^{-1}$ $(3\pi)^{+1}$ configuration as the dominant configuration should also be observed in an experimental spectrum. Table 7.1 shows that this band would have an intensity of 0.09 relative to the AlF^+ $B^2\Sigma^+$ intensity of 0.87, as estimated from squares of

coefficients of formally allowed contributions to the CI eigenvectors. Fig. 7.1 shows that the fourth band of AlF is of appreciable intensity and this is in agreement with the known photoelectron spectrum of CS (39-41) and with the CI calculations on CS described in Chapter 4 of this thesis.

The calculated value for the fourth ip of ALF of 18.34eV is rather high relative to the experimentally measured value of 15.33eV. This is partly because, with the SPLICE package, problems are often encountered in obtaining convergence for higher roots of a given state (see Chapter 3) and in the CI procedure a higher than normal convergence criterion had to be used for the $C^2\Sigma^+$ state (0.05 instead of 0.001). Also, for a more reliable estimate of the fourth ip to be obtained, further more extensive CI calculations are required on both AlF and AlF^+. Further details of the CI calculations performed in this work, summarised in table 7.1, are given in Chapter 4.

It is reassuring that the general features of the AlF spectrum described in this Chapter are in good agreement with that known for the HeI photoelectron spectra of the thallium and indium monohalides (29, 34-36). For these molecules, as in the AlF case, three bands were observed with the first and third bands being sharp and the second band being very broad. In view of the assignment of the second band in AlF, it seems likely that the second band in the spectra of the thallium and indium monohalides also arises from ionisation to both the $A^2\Pi$ and $B^2\Sigma^+$ states. The assignment of the photoelectron spectrum of AlF_3 (summarised in table 7.5) has been achieved with the aid of SCF calculations performed for both BF_3 and AlF_3 using STO double-zeta plus polarisation function basis sets and by comparison with the known photoelectron spectrum of BF_3. In neutral BF_3, the three outermost filled molecular orbitals are of $1a_2'$, 1e" and 4e' symmetry. The $1a_2'$ and 1e" orbitals are composed of linear combinations of F2p orbitals whereas the 4e' molecular orbital is composed of F2p symmetry combinations with small contributions from B2p atomic orbitals. The next two molecular orbitals, the $1a_2"$ and 3e' levels, are also mainly F2p in character. A similar situation also arises in AlF_3 where the outermost five molecular orbitals are also mainly F2p in character. In the HeI photoelectron spectrum of

BF_3, the first three bands arise from ionisation of the $1a_2'$, 1e" and 4e' levels (at experimental vertical ionisation potentials of 15.95, 16.67 and 17.14eV respectively (13,14)) with the $(4e')^{-1}$ band being the most intense and the $(1e")^{-1}$ band being the weakest. On this basis and from the computed ionisation energies in table 7.5, the photoelectron spectrum of AlF_3 is assigned in the following way. Band B in figure 7.2 is attributed to the $(5e')^{-1}$ ionisation whereas band A is attributed to two unresolved bands arising from the $(1e")^{-1}$ and $(1a_2')^{-1}$ ionisations. The other observed bands in the AlF_3 spectrum, bands C and D, are assigned as shown in table 7.5.

Perhaps one of the more significant measurements to be forthcoming from this work is an improved estimate of the first adiabatic ionisation energy of AlF. The value obtained, (9.73±0.01)eV is in agreement with the value expected from electron impact mass spectrometry, (9.70±0.50)eV (10-12), but the error limits have been drastically reduced. Although a number of Rydberg states of AlF have previously been observed by Barrow and coworkers (3), detailed analysis of these states was not possible because an accurate value of the first ionisation potential of AlF was not available. A preliminary analysis was nevertheless presented (3) based on a value of the AlF ionisation energy (9.92eV) estimated by analogy with known Rydberg series in BF. However, the more reliable ionisation potential of AlF determined in this work allows a re-determination of the quantum defects of the Rydberg states observed by Barrow and coworkers (3) assuming that the atomic character of the observed excited states ($C^1\Sigma^+$, $D^1\Delta$, $E^1\Pi$, $G^1\Sigma^+$, $F^1\Pi$ and $H^1\Sigma^+$) are unchanged from that given in reference (3). This latter assumption is supported for the $D^1\Delta$ state by recent ab initio molecular orbital calculations (42). The results of the re-analysis are presented in table 7.6 with the original values of Barrow et al (3) given in brackets. Clearly, identification of other Rydberg states of AlF would be extremely useful and would lead to a further improvement in the first ionisation energy of AlF. It is therefore to be hoped that the work described in this Chapter will generate further interest in this problem and lead to further spectroscopic studies on AlF.

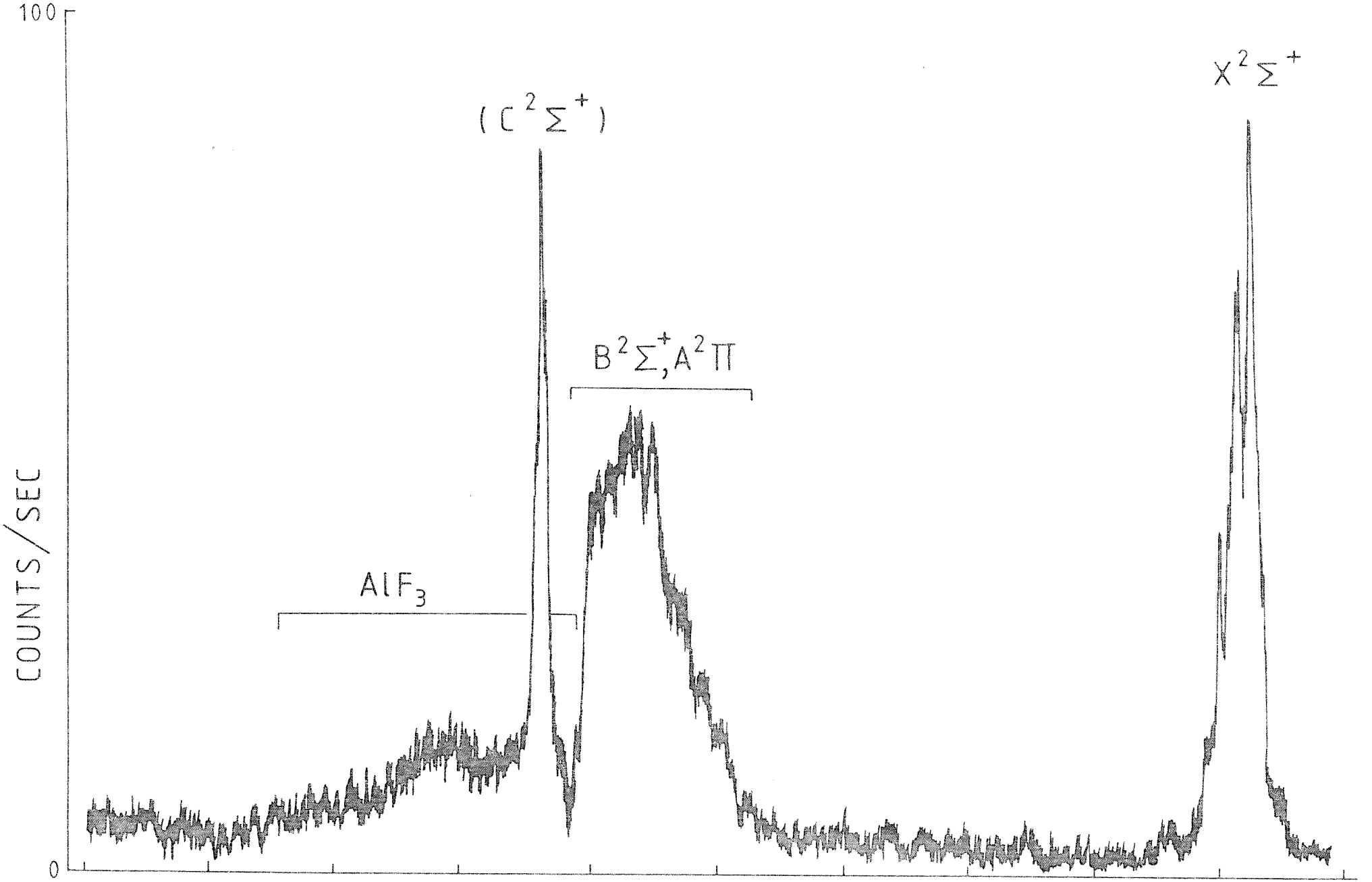
100
0
COUNTS/SEC
$(C^2\Sigma^+)$
$X^2\Sigma^+$
$B^2\Sigma^+, A^2\Pi$
AlF_3
18
16
14
12
10
I.E.(eV)

FIG 7.1

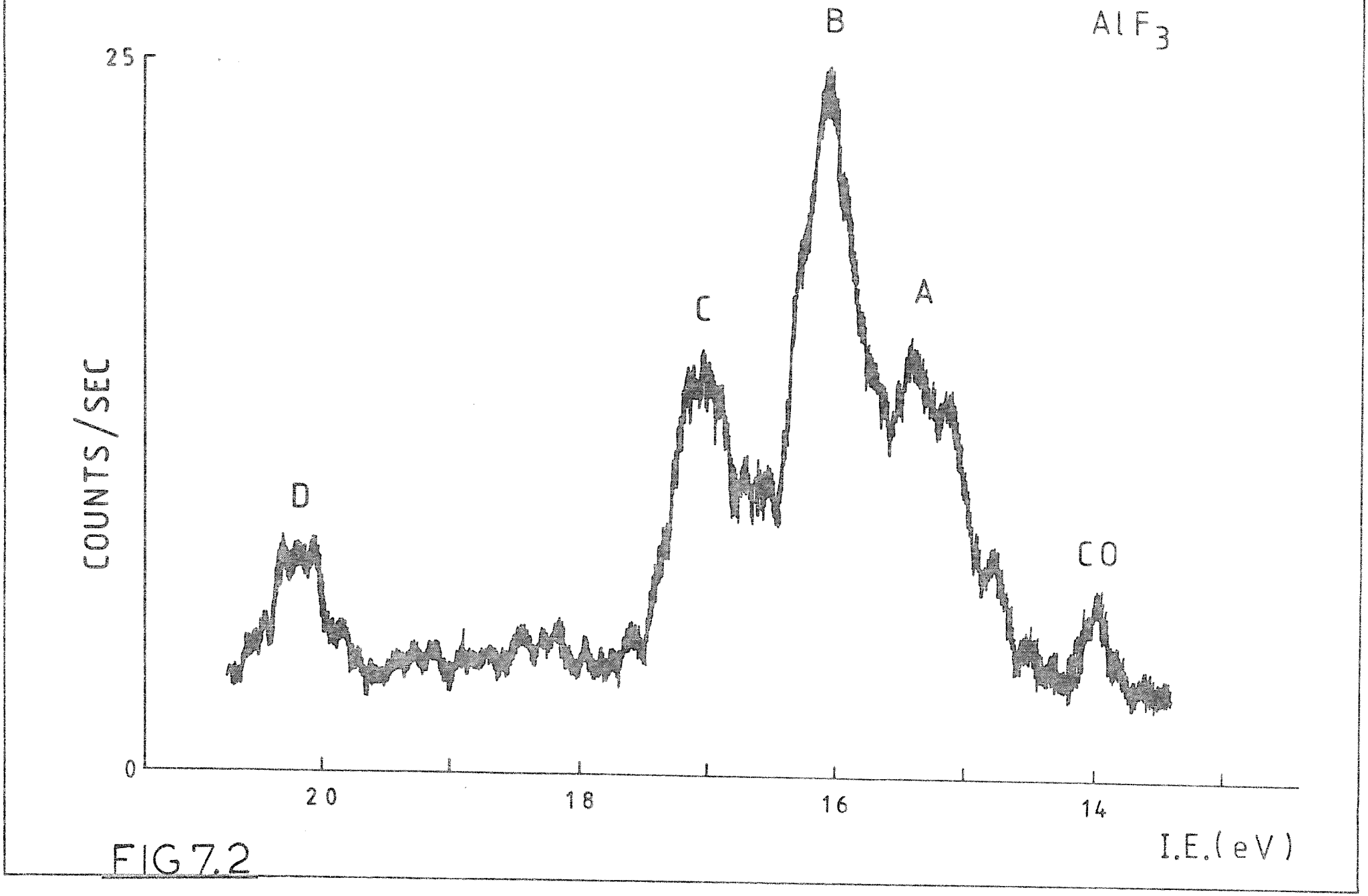

FIG 7.2

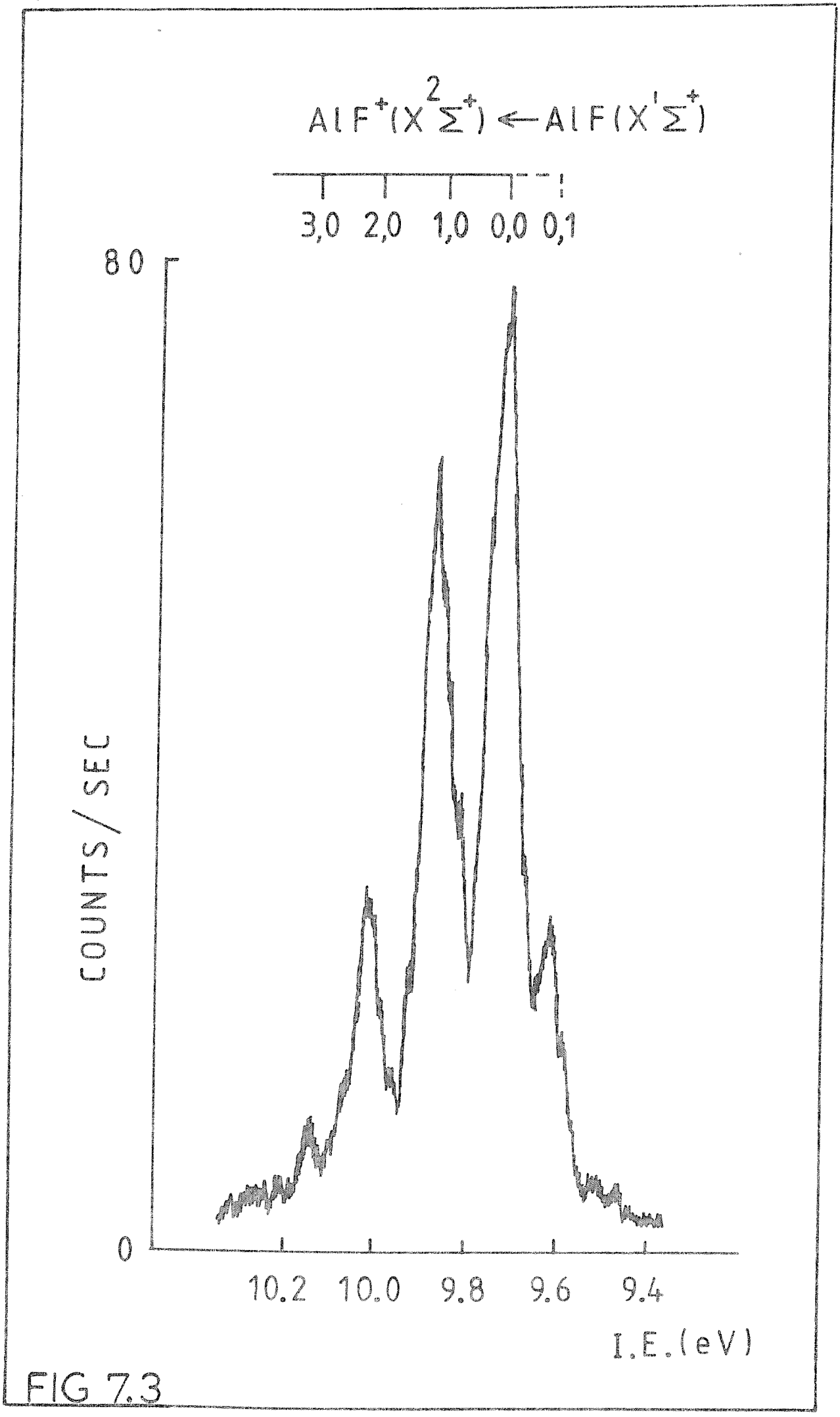

FIG 7.3

Simulated vibrational envelopes of the ALF first band via the PNO-CEPA method.

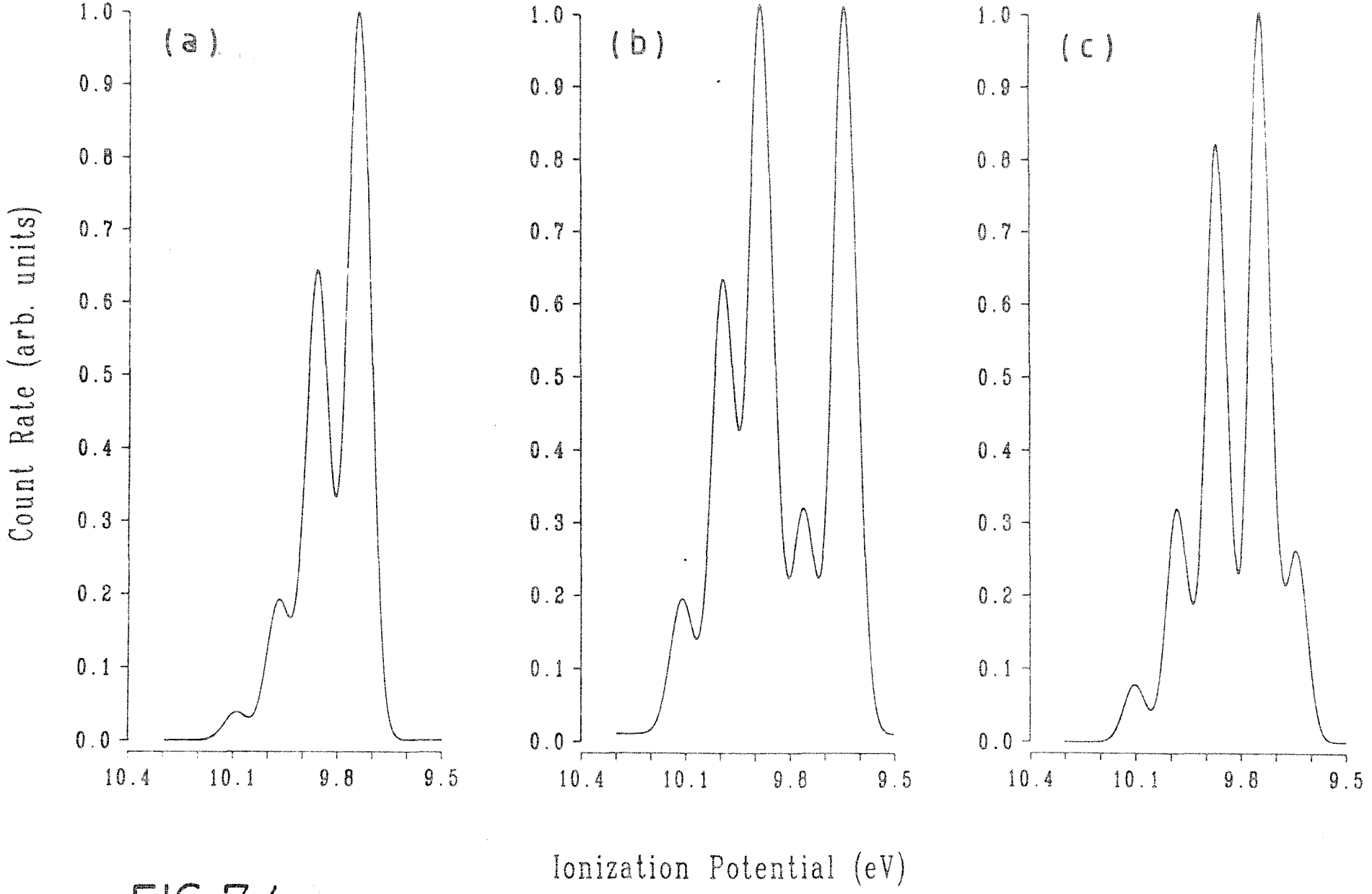

FIG 7.4

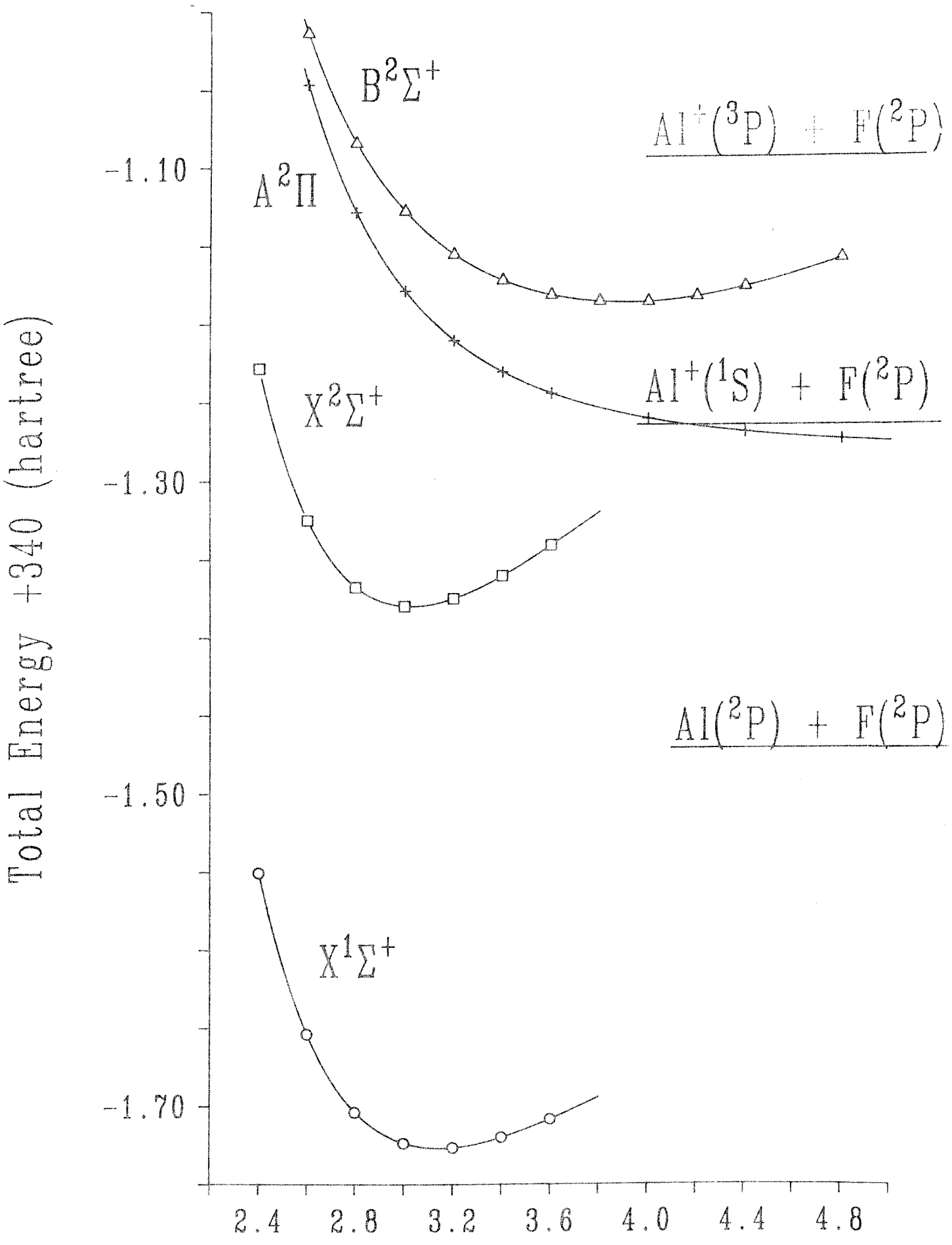
Total Energy +340 (hartree)
-1.10
-1.30
-1.50
-1.70
$B^2\Sigma^+$
$A^2\Pi$
$X^2\Sigma^+$
$X^1\Sigma^+$
$Al^+(^3P) + F(^2P)$
$Al^+(^1S) + F(^2P)$
$Al(^2P) + F(^2P)$
2.4
2.8
3.2
3.6
4.0
4.4
4.8
Internuclear Distance (bohr)

FIG7.5

Table 7.1 Computed Vertical Ionisation Potentials of $AlF(X^1\Sigma^+)$[a]

Orbital Ionised	Ionic State	HFS[b] Transition State	Koopmans'[c] Theorem	ΔSCF value[c]	ΔSCF plus CI[c]	Experimental value
7σ	$X^2\Sigma^+$	9.36	9.01	8.51	9.24(0.96)[e]	9.73±0.01
2π	$A^2\Pi$	14.23	16.45	12.99	13.44(0.92)	13.6-15.2
6σ	$B^2\Sigma^+$	15.93	18.02	15.28	15.13(0.87)	
-	$(C^2\Sigma^+)$	-	-	-(d)	18.34(0.09)	15.33±0.01

(a) All calculations were performed at the experimental equilibrium bond length of $AlF(X^1\Sigma^+)$ of 1.6544 Å (4-7).

(b) HFS calculations were performed using Basis II; see text for details.

(c) Calculations performed using Basis I; see text for details.

(d) See text for assignment of this band.

(e) Values in brackets are the sum of coefficients of formally allowed contributions to the final CI wavefunctions.

Table 7.2 Computed Ionisation Potentials (eV) of AlF($X^1\Sigma^+$)[a]

Orbital Ionised	Ionic State	ΔSCF value[e] vertical ip	ΔPNO-CEPA[e] vertical ip	Experimental vertical ip
7σ	$X^2\Sigma^+$	8.53	9.43	9.73±0.01
2π	$A^2\Pi$	-	13.6-15.0[b]	13.6-15.2[c]
6σ	$B^2\Sigma^+$	14.69	14.67	13.6-15.2[c]
-	($C^2\Sigma^+$)	-	-	15.33±0.01[d]

(a) From the total energies of the particular states at the theoretical Re's (cf. Table 7.3).

(b) Obtained for the classical turning points of v''=0 in AlF $X^1\Sigma^+$ as a vertical cut on the repulsive $A^2\Pi$ potential energy functions (cf. Figure 7.5).

(c) Experimental range of the second PE-band of AlF.

(d) See text for assignment of this band.

(e) Calculations performed using Basis III; see text for details.

Table 7.3 Theoretical Spectroscopic Constants[a] of AlF and AlF^+

States	Method	E[b] (a.u.)	Re(Å)	Be(cm^{-1})	αe(cm^{-1})	$\bar{w}_e$(cm^{-1})	$w_e x_e$(cm^{-1})
AlF $X^1\Sigma^+$	RHF[d]	-341.47193	1.641	0.561	0.004	838	5
	PNO/CEPA[d]	-341.72686	1.663	0.546	0.004	804	4.3
	Exp.[c]		1.6544	0.5524	0.00498	802.2	4.77
AlF^+ $X^2\Sigma^+$	RHF[d]	-341.15888	1.576	0.609	0.004	1019	4.2
	PNO/CEPA[d]	-341.38047	1.601	0.590	0.004	960	3.7
	Exp. this work		(1.59±0.01)	-	-	(1040±40) (1000±40)[e]	-
AlF^+ $B^2\Sigma^+$	RHF[d]	-340.93153	1.983	0.385	0.002	440	1
	PNO/CEPA[d]	-341.18709	2.071	0.352	0.005	467	1

(a) Calculated from polynomial fits.

(b) Total energies at calculated equilibrium distances.

(c) References (4-7).

(d) Calculations performed using Basis III; see text for details.

(e) Final recommended value.

Table 7.4 Experimental and Calculated Spectroscopic Constants[c] for $AlF(X^1\Sigma^+)$ and $AlF^+(X^2\Sigma^+)$

	$AlF(X^1\Sigma^+)$		$AlF^+(X^2\Sigma^+)$	
	Experimental[a]	Calculated[a]	Experimental[b]	Calculated[b]
Equilibrium Bond Length r_e, Å.	1.6544	1.636	1.59±0.01	1.582
Vibrational Frequency $\bar{w}_e$, cm^{-1}.	802.2	886	(1040±40) (1000±40)[d]	1037

(a) See refs. (4-7).

(b) This work; see text for details.

(c) Calculations performed using Basis I; see text for details.

(d) Final recommended value.

Table 7.5 Computed and Experimental Vertical Ionisation Potentials (eV) of BF_3 and AlF_3

i) BF_3[a][b]

Orbital	Computed Vertical Ionisation Potential via Koopmans' Theorem	Experimental v.i.p. ref. (17,18)
$3a_1'$	44.96	-
$2e'$	43.82	-
$4a_1'$	22.88	21.50±0.05
$3e'$	21.76	20.09±0.02
$1a_2''$	20.43	19.13±0.02
$4e'$	18.66	17.14±0.01
$1e''$	18.32	16.67±0.01
$1a_2'$	17.59	15.95±0.02

ii) AlF_3[a][c]

Orbital	Computed Vertical Ionisation Potential via Koopmans' Theorem	Experimental v.i.p. ±0.02eV	Band letter in Figure 7.2
$4a_1'$	42.00	-	-
$3e'$	41.64	-	-
$5a_1'$	19.55	20.09	D
$4e'$	18.38	17.07	C
$2a_2''$	17.73		
$5e'$	17.49	16.10	B
$1e''$	17.21	15.45	A
$1a_2'$	16.72		

(a) The experimental geometries used for these calculations are taken from references (31-33).

(b) Calculations performed using basis of reference (1).

(c) Calculations performed using Basis I; see text for details.

Table 7.6 Re-determination of the quantum defects of a number of singlet Rydberg states of AlF[a]

State	Character of the excited electron from ref.(3)	To from ref.(3)/eV	n-δ[b]	n	δ[b]
$H^1\Sigma^+$	4pσ	8.405	3.204 (2.998)	4	0.79 (1.00)
$F^1\Pi$	4pπ	8.216	2.997 (2.827)	4	1.00 (1.17)
$G^1\Sigma^+$	3dσ	8.282	3.065 (2.884)	3	-0.06 (0.12)
$E^1\Pi$	3dπ	7.953	2.767 (2.631)	3	0.23 (0.37)
$D^1\Delta$	3dδ	7.647	2.555 (2.447)	3	0.45 (0.55)
$C^1\Sigma^+$	4sσ	7.210	2.323 (2.241)	4	1.67 (1.76)

(a) The To values listed in this table are taken from Table VI of ref.(3). The parameters (n-δ) and δ are derived assuming i.p. (AlF) = 9.73 eV, as determined in this work.

(b) The (n-δ) and δ values shown in brackets are derived on the assumption that i.p. (AlF) = 9.92 eV (see ref.(3)).

References

1. J.M. Dyke, C. Kirby and A. Morris, J.C.S. Faraday II, 79, 483 (1983).

2. J.M. Brown, I. Kopp, C. Malmberg and B. Rydh, Physica Scripta, 17, 55 (1978).

3. R.F. Barrow, I.Kopp and C. Malmberg, Physica Scripta, 10, 86 (1974).

4. (a) D.R. Lide, J. Chem. Phys., 42, 1013 (1965).

   (b) D.R. Lide, J. Chem. Phys., 38, 2027 (1963).

5. A.G. Maki and F.J. Lovas, J. Mol. Spectry., 95, 80 (1982).

6. F.C. Wyse, W. Gordy and E.F. Pearson, J. Chem. Phys., 52, 3887 (1970).

7. J. Hoeft, F.J. Lovas, E. Tiemann and T. Torring, Z. Naturforsch, 25A, 1029 (1970).

8. H. Kvande, High Temperatures High Pressures, 14, 245 (1982).

9. T. Matsushima, T. Ito and K. Ono, Sci. Rept. Inst. Tohuku University, 415, 195 (1964).

10. J.C. Ehlert, G.D. Blue, J.W. Green and J.L. Margrave, J. Chem. Phys., 41, 2250 (1964).

11. E. Murad, D.L. Hildenbrand and R.P. Main, J. Chem. Phys., 45, 263 (1966).

12. R.F. Porter, J. Chem. Phys., 33, 951 (1960).

13. (a) P.J. Bassett and D.R. Lloyd, J.C.S. Chem. Commun., 36 (1970).

    (b) P.J. Bassett and D.R. Lloyd, J.C.S. (A), 1551 (1971).

14. E. Haller, H. Koppel, L.S. Cederbaum, W. von Niessen and G. Bieri, J. Chem. Phys., 78, 1359 (1983).

15. A.W. Potts, H.J. Lempka, D.G. Streets and W.C. Price, Phil. Trans. Roy. Soc., A268, 59 (1970).

16. G.H. King, S.S. Krishnamurthy, M.F. Lappert and J.B. Pedley, Faraday Disc. Chem. Soc., 54, 70 (1972).

17. R.F. Porter and E.E. Zeller, J. Chem. Phys., 33, 858 (1960).

18. JANAF Thermochemical Tables, 2nd Edn. NSRDS-NBS37; Editors D.R. Stull and H. Prophet (US. Govt. Printing Office, Washington D.C., 1971).

19. R.F. Krause and T.B. Douglas, J. Phys. Chem., 72, 475 (1968).

20. D.K. Bulgin, J.M. Dyke, F. Goodfellow, N. Jonathan, E.P.F. Lee and A. Morris, J. Elect. Spec. Rel. Phen., 12, 67 (1977).

21. (a) J.M. Dyke, N. Jonathan and A. Morris, Electron Spectroscopy: Theory, Techniques and Applications (Academic Press, New York, 1979), vol. 3, p.189.

(b) J.M. Dyke, N. Jonathan and A. Morris, Int. Rev. Phys. Chem., 2, 3 (1982).

22. V.R. Saunders and M.F. Guest, ATMOL 3 Reference Manual (SERC, Rutherford Appleton Laboratory, 1976).

23. (a) C. Roetti and E. Clementi, J. Chem. Phys., 60, 4725 (1974).

(b) S. Huzinaga, Technical Rept., Univ. Alberta, Approximate Atomic Functions (1973).

24. W. Meyer, J. Chem. Phys., 58, 1017 (1973).

25. R. Klein and P. Rosmus, Personal Communication.

26. W.G. Richards, J. Raftery and R.K. Hinkley, Theoretical Chemistry (Specialist Periodical Report, The Chemical Society, London), vol. 1, p.1 (1974).

27. J.M. Dyke, A. Morris and A. Ridha, J.C.S. Faraday II, 78, 2077 (1982).

28. J.M. Dyke, A. Morris and I.R. Trickle, J.C.S. Faraday II, 73, 147 (1977).

29. J. Berkowitz and J.L. Dehmer, J. Chem. Phys., 57, 3194 (1972).

30. M.F. Guest and W.R. Rodwell, RL-77-110B. The Bonded Function CI Program, Rutherford Appleton Laboratory, SERC (1977).

31. P.A. Akishin, N.G. Rambidi and E.Z. Zasorin, Kristallografiya, 4, 186 (1959).

32. G. Shanmugasundaram and G. Nagarajan, Z. fur Phys. Chemie., 240, 363 (1969).

33. K. Kuchitsu and S. Konaka, J. Chem. Phys., 45, 4342 (1966).

34. J. Berkowitz, J. Chem. Phys., 56, 2766 (1972).

35. J.L. Dehmer, J. Berkowitz and L.C. Cusachs, J. Chem. Phys., 58, 5681 (1973).

36. J. Berkowitz and T.A. Walter, J. Chem. Phys., 49, 1184 (1968).

37. C.E. Moore, Atomic Energy Levels, Natl. Bur. Stand. Circ., 467 (1949).

38. E.A. Colbourn, J.M. Dyke, E.P.F. Lee, A. Morris and I.R. Trickle Molec. Phys., 35, 873 (1978).

39. (a) N. Jonathan, A. Morris, M. Okuda, D.J. Smith and K.J. Ross, Chem. Phys. Letts., 13, 334 (1972).

(b) N. Jonathan, A. Morris, M. Okuda, K.J. Ross and D.J. Smith, Disc. Faraday Soc., 54, 48 (1972).

40. (a) G.H. King, H.W. Kroto and R.J. Suffolk, Chem. Phys. Letts., 13, 457 (1972).

(b) D.C. Frost, S.T. Lee and C.A. McDowell, Chem. Phys. Letts. 17, 153 (1972).

41. J. Schirmer, W. Domcke, L.S. Cederbaum and W. von Niessen, J. Physics B, 11, 1901 (1978).

42. S.P. So and W.G. Richards, J. Physics B, 14, 1973 (1974).

43. W.G. Richards and J.A. Horsley, "Ab initio Molecular Orbital Calculations for Chemists", Clarendon Press, Oxford (1970).